# Integrated autothermal reactor concepts for combined oxidative coupling and reforming of methane

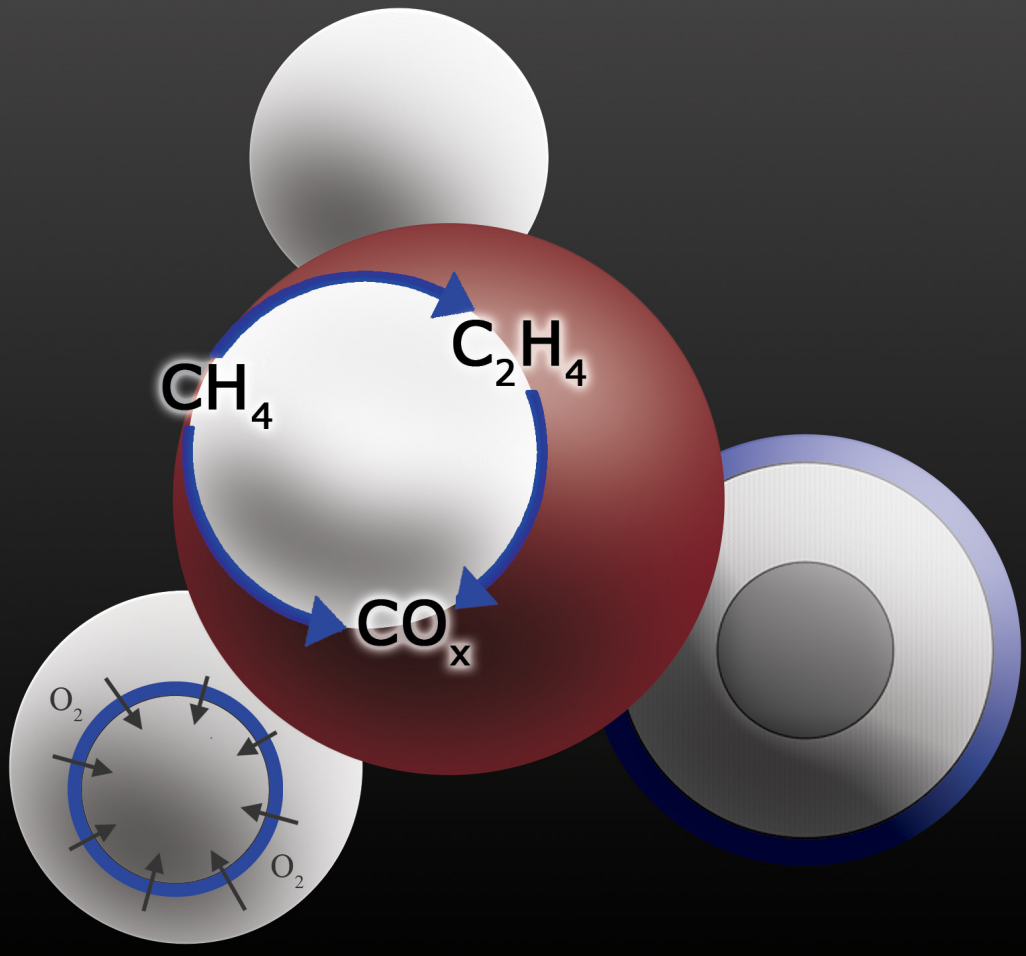


T.P. Tiemersma

# Integrated autothermal reactor concepts for oxidative coupling and reforming of methane

Samenstelling promotiecommissie:

| | |
|---|---|
| Prof. dr. G. van der Steenhoven, voorzitter | Universiteit Twente |
| Prof. dr. ir. J.A.M. Kuipers, promotor | Universiteit Twente |
| Dr. ir. M. van Sint Annaland, assistent-promotor | Universiteit Twente |
| Prof. dr. ir. L. Lefferts | Universiteit Twente |
| Prof. Dr.-Ing. A. Seidel-Morgenstern | Otto-von-Guericke Universität Magdeburg |
| Prof. E. Drioli | University of Calabria |
| Prof. dr. F. Kapteijn | Technische Universiteit Delft |
| Prof. dr. ir. A. Nijmeijer | Universiteit Twente |
| Dr. ir. D.W.F. Brilman | Universiteit Twente |
| Dr. ir. A. Zwijnenburg | Johnson Matthey |


This work is part of the research programme Advanced Sustainable Processes by Engaging Catalytic Technologies (ASPECT), which is financially supported by NWO/ACTS under project number 053.62.008.



Printed by:
Ipskamp Drukkers B.V., P.O. Box 333, 7500 AH, Enschede, The Netherlands
ISBN 978-90-365-2985-3, DOI 10.3990/1.9789036529853

# INTEGRATED AUTOTHERMAL REACTOR CONCEPTS FOR OXIDATIVE COUPLING AND REFORMING OF METHANE

PROEFSCHRIFT

ter verkrijging van
de graad van doctor aan de Universiteit Twente,
op gezag van de rector magnificus,
prof. dr. H. Brinksma,
volgens besluit van het College voor Promoties
in het openbaar te verdedigen
op vrijdag 5 maart 2010 om 16.45 uur

door

Tymen Petrus Tiemersma

geboren op 14 januari 1979
te Kollumerzwaag

Dit proefschrift is goedgekeurd door de promotor

**Prof.dr.ir. J.A.M. Kuipers**

en de assistent-promotor

**Dr.ir. M. van Sint Annaland**

# Contents

# Summary

With the inevitable increase of industrial development and growth of global welfare, the demand for industrial chemicals, such as ethylene, will increase while the resources available per capita are decreasing. Anticipating that fossil fuels will remain an important source of primary energy and bulk chemicals, reserves will be decreasing and it is therefore essential to search for alternative production methods based on different feedstocks and with significantly enhanced efficiencies. For ethylene production, a direct method of converting natural gas into higher hydrocarbons is the heterogeneously catalyzed oxidative coupling of methane (OCM), however, only with hydrocarbon yields limited to 30-35% despite enormous efforts to optimize the catalysts. By combining OCM with a secondary process, namely steam reforming of methane (SRM), the methane conversion can be increased significantly while improving temperature control and simultaneously producing valuable synthesis gas. In this thesis, the focus will lie on the integration of the exothermic OCM and endothermic SRM reactions to an overall autothermal process, so that the OCM process is effectively cooled and the generated reaction energy is efficiently used to produce synthesis gas.

The integration of the OCM and SRM reactions is most optimally achieved on the catalyst particle scale, which would eliminate the need for heat exchange with a cooling medium inside the reactor and opens up the possibility to use a membrane reactor for distributive oxygen dosing with which much higher product yields can be achieved. Because the chemical reactions occurring on both types of catalytic active sites interfere, it is proposed to use a dual function catalyst particle in which the two chemical processes are physically separated by an inert, porous layer, such that additional diffusional resistances are intentionally created. The reforming activity is located in the particle center, while the oxidative coupling catalyst is present only in the outer shell of the particle. The performance of this dual-function catalyst particle integrating the exothermic OCM and endothermic SRM has been designed and studied by detailed numerical simulations. Compared to conventional OCM, the introduction of a reforming activity significantly increases the methane conversion without deteriorating the productivity towards the desired ethylene and ethane. Moreover, the presence of an intra-particle heat sink enables local autothermal operation which greatly simplifies the reactor design. The structuring of the catalytic functions inside a single catalyst particle yields many advantages over conventional indirect coupling of exothermic and endothermic reactions in different reactor compartments, especially because the intra-particle heat transfer resistance is much smaller than the heat transfer resis-

tance between different reactor compartments. It has been demonstrated by means of numerical simulations that at low oxygen concentration (representing conditions in a packed bed membrane reactor), the internal mass transfer limitations can be effectively utilized to regulate the total reforming reaction rates and to prevent oxygen from reaching the reforming catalyst. Additionally, the size of the reforming catalytic core can, together with the effective diffusion properties inside the particle (viz. particle porosity and tortuosity) and the bulk gas phase concentrations, be used to tune the process to local autothermal operation, opening the possibility to couple these reactions in a packed bed membrane reactor with improved product yield. The integral performance of the designed dual function catalyst particles, which were placed in a packed bed reactor equipped with porous membranes for distribute feeding of oxygen, was studied with numerical simulations. It was confirmed that with distributive oxygen feeding via membranes indeed the local oxygen concentration in the packed bed membrane reactor can be kept low, which combined with a high Thiele modulus for oxidative coupling (i.e. strong oxygen concentration profiles inside the catalyst particle) makes dual function catalysis possible. Using a reforming core diameter of approximately 50-100 $\mu$m, the steam reforming and oxidative coupling reaction rates could be effectively tuned to achieve autothermal operation at the reactor scale, while the methane conversion was enhanced from 44% to 55%. The decrease of the $C_2$ production rates was not detrimental and mainly caused by a lower selectivity of the oxidative coupling catalyst at higher conversions, leading to losses to $C_2$ reforming lower than 40%. In addition, it was shown that the temperature profiles in the reactor can be strongly reduced with the dual function process and that the use of axial oxygen membrane flux profiles enables the use of a single particle configuration to approach autothermal operation in the entire reactor.

An alternative integrated process can be achieved by combining OCM and SRM in a heat exchange reactor comprising of two separate reaction chambers which are thermally coupled. The OCM is carried out in packed bed reverse flow membrane reactor tubes submerged into a fluidized bed where the unconverted methane and by-products, from which the valuable $C_2$ components have been separated, are reformed together with some additional steam, thus producing synthesis gas and consuming the reaction heat liberated by the exothermic OCM. This novel reactor concept with autothermal operation has been developed and studied by detailed modeling to gain insight in the complex behavior of the reactor. On basis of detailed simulations it has been shown that indeed the exothermic OCM and endothermic SRM can be very efficiently coupled permitting close to autothermal operation with cyclic steady state $C_2$ yields up to 30% at full methane conversion with a $CH_4/O_2$ ratio of 2-2.5 and a

$H_2O/CH_4$ ratio of 3 in the SRM fluidized bed reactor.

Although this reactor concept was studied by means of numerical simulations, experimental confirmation of the feasibility is required. Because of the application of reverse flow operation for OCM, a stable catalyst is essential, and it was found based on a literature study that $Mn/Na_2WO_4$ is a suitable catalyst. The rates of the main reactions prevailing during the OCM were measured under differential conditions in a quartz micro-catalytic fixed bed reactor. Because the catalyst is a reducible metal oxide, it was found with Thermal Gravity Analysis (TGA) that catalyst pre-treatment with oxygen is required to obtain a high $C_2$ selectivity of about 85%, and that a low oxygen partial pressure during the OCM reactions is already sufficient to maintain the catalyst stable in the oxidized state. Because the kinetic models for OCM over a $Mn/Na_2WO_4/SiO_2$ in the literature are not suitable for application in numerical reactor models, the overall reaction orders and rate constants of the primary reactions were determined by measuring the intrinsic reaction rates at different methane and oxygen inlet concentrations. The reaction rate constants of the secondary ethane and ethylene oxidation reactions were estimated assuming first order in both the hydrocarbon and in oxygen from the experimental data published by Takanabe (2008) for the same catalyst. It was found that the reaction order in $O_2$ for the coupling reaction is 0.38, while the reaction order in $O_2$ for $CH_4$ oxidation approaches unity, indicating that low $O_2$ concentration levels are beneficial for obtaining a high $C_2$ selectivity (up to 80-90%). Based on the experiments and least-squares minimization, a simplified reaction mechanism is proposed, where the dependency of the $C_2H_6$ (coupling) and $CO_2$ (oxidation) production rates and the secondary $C_2H_4$ production and $C_2$ oxidation rates are described with power-law type reaction rate expressions.

The feasibility of the concept in which OCM and SRM are combined in a single reactor with separate compartments is supported by experiments of oxidative coupling of methane on a $Mn/Na_2WO_4/SiO_2$ catalyst in a packed bed membrane reactor equipped with a modified $Al_2O_3$ porous membrane, based on its relatively good stability at high temperatures and its low fluxes. The applied porous membranes were characterized via measurements of the pore size and mole fluxes. The influence of several relevant parameters on oxidative coupling of methane was investigated in a small scale membrane reactor, with a limited amount of catalyst. The effects of distributed feed of oxygen on the hydrocarbon yield and the axial temperature profiles were also studied in a reactor with a relatively large amount of catalyst, so that effects of larger scale could be studied. The fluidized bed reactor, in which steam reforming reactions are performed, was emulated by a fluidized sand bed which was heated by means of an electrical oven. Experiments with OCM and distributed feed of air in

both reactors, demonstrated that with OCM a $C_2$ yield of 25-30 % can be achieved, which is comparable with results published in the literature. Comparison with OCM experiments with pre-mixed feed of air showed that the obtained yield is only higher if very diluted flow is applied, at less diluted conditions the relatively high oxygen membrane flux at the end of the reactor results in high secondary oxidation reaction rates and concomitant temperature rise. This was confirmed by measurements of the axial and radial temperature profiles and qualitative simulations with a reactor model that included the reaction rate expressions which were experimentally determined in Chapter 5. In order to minimize the temperature increase downstream, a non-uniform membrane permeation flux profile could be applied. It was also determined that the optimization of the required heat removal, especially when using higher methane inlet concentrations becomes increasingly important and is essential for a feasible process. By selecting a better method of heat removal, i.e. by application of longer membrane tubes with lower fluxes, the increase of the temperature can be moderated even further. It can be concluded that an OCM packed bed membrane reactor which is immersed into a fluidized bed reactor, can produce acceptable $C_2$ yields and that distributed feed of oxygen is optimal for the combined OCM/SRM reactor concept.

# Samenvatting

De vraag naar industriële bulk chemicaliën, zoals etheen, zal de komende jaren blijven stijgen door de toenemende ontwikkeling en welvaartsgroei, terwijl de beschikbare grondstoffen en energie per hoofd van de wereldbevolking zullen afnemen. Omdat fossiele brandstoffen een belangrijke rol zullen blijven spelen voor de korte en middellange termijn, is het essentieel dat alternatieve productieprocessen met meer geschikte fossiele grondstoffen en met een veel hogere efficiëntie worden ontwikkeld.

Een veelbelovend (heterogeen gekatalyseerd) proces om direct etheen te produceren uit aardgas (methaan) is de oxidatieve koppeling van methaan (OCM). Ondanks de vele pogingen om de opbrengst van etheen te verhogen, heeft de omzetting van methaan in hogere koolwaterstoffen via OCM een opbrengst die in de praktijk gelimiteerd is tot 30-35%. De totale conversie van methaan kan echter aanmerkelijk worden verbeterd door de OCM te combineren met een secundair proces, namelijk het stoom-reformen van methaan (SRM). Door de combinatie van deze twee processen kan de temperatuur van het exotherme OCM proces beter worden beheerst, terwijl er met het endotherme SRM proces een waardevol extra reactieproduct, synthesegas, wordt geproduceerd. In dit proefschrift zijn de mogelijkheden tot integratie van het exotherme OCM en het endotherme SRM proces onderzocht, leidend tot een proces met een hogere energie-efficiëntie, zodanig dat OCM effectief wordt gekoeld en de geproduceerde reactiewarmte nuttig wordt gebruikt voor de omzetting in synthesegas.

De optimale methode om de twee processen te integreren is de combinatie van OCM en SRM in een enkel katalysatordeeltje, omdat temperatuursbeheersing door een interne koeling wordt gerealiseerd. Tevens wordt het mogelijk om het gecombineerde proces uit te voeren in een membraanreactor, waarmee beduidend hogere opbrengsten kunnen worden gehaald door het gebruik van distributieve zuurstofdosering. Vanwege de storende werking van de SRM reacties op de opbrengst van etheen, is het echter noodzakelijk om een katalysator te gebruiken waarbij de OCM en SRM processen gescheiden zijn door een inerte poreuze laag, zodanig dat de opzettelijk gecreeërde diffusieweerstand de reactiesnelheid zal bepalen. De actieve sites van de SRM katalysator zijn gelocaliseerd in het midden van het deeltje, terwijl de actieve sites van het OCM proces alleen aan de buitenkant van het deeltje zijn aangebracht. Het ontwerp en het gedrag van dit katalysatordeeltje is bestudeerd met geavanceerde numerieke simulaties. Ten eerste is gebleken dat de methaanconversie aanmerkelijk wordt verhoogd door de combinatie van het OCM en SRM proces in een enkel deeltje, terwijl de etheen en ethaan productie grotendeels intact blijft. Tevens kan het reactorontwerp sterk worden vereenvoudigd, door de aanwezigheid van de interne koeling ten gevolge van

de endotherme SRM reacties. De gestructureerde OCM/SRM katalysator heeft vele voordelen ten opzichte van de conventionele koppeling van exotherme en endotherme reacties, voornamelijk omdat het warmtetransport binnen een poreus deeltje een veel lagere weerstand kent vergeleken met warmtetransport door reactorwanden en binnen reactorcompartimenten. De numerieke simulaties hebben aangetoond dat het mogelijk is om interne diffusielimiteringen te gebruiken voor het reguleren van de reforming reacties, en dat bij lage zuurstofconcentraties (vergelijkbaar met de omstandigheden in een gepakt bed membraanreactor) contact van zuurstof met de SRM katalysator vermeden kan worden. Bovendien is aangetoond dat het proces verder lokaal kan worden geoptimaliseerd door het wijzigen van de afmetingen van de SRM katalysator, de interne diffusieweerstanden (bijvoorbeeld de porositeit en tortuositeit van het deeltje) en de samenstelling van de gasfase, zodat het mogelijk wordt om het katalysatordeeltje toe te passen in een gepakt bed membraanreactor.

Het gedrag van de gecombineerde OCM/SRM katalysatordeeltjes is in een gepakt bed membraanreactor bestudeerd, met behulp van numerieke simulaties. De berekeningen hebben bevestigd dat het distributief doseren van zuurstof via membranen, waarmee de lokale zuurstofconcentratie in het gepakte bed aanzienlijk wordt verlaagd, in combinatie met een hoge Thiele modulus voor oxidatieve koppeling (sterke concentratieprofielen van zuurstof in de deeltjes) de juiste condities gecreëerd kunnen worden om het gecombineerde OCM/SRM katalysatordeeltje toe te passen in de gehele reactor. Uit de berekeningen blijkt dat met een diameter van de SRM kern van ongeveer 50-100 $\mu$m, de reactiesnelheden van OCM en SRM zodanig op elkaar aangepast kunnen worden dat autotherme opereratie mogelijk wordt, en dat bovendien de methaanconversie toeneemt van 44% naar 55%. De afname van de $C_2$ productiesnelheden is hierbij minder dan 40%, omdat deze voornamelijk gerelateerd is aan de lagere selectiviteit van de OCM katalysator vanwege de lagere methaanconcentraties en niet ten gevolge van verliezen door reforming reacties. Naast de toegenomen conversie worden de axiale temperatuurprofielen eveneens sterk verlaagd door gebruik te maken van de gecombineerde OCM/SRM katalysator. Door daarnaast slim gebruik te maken van axiale profielen in de zuurstofmembraanflux is het mogelijk om het proces autotherm uit te voeren met een OCM/SRM katalysatordeeltje met een enkele configuratie.

Een andere mogelijkheid om OCM en SRM te combineren, is om een enkele reactor uit te rusten met verschillende compartimenten die onderling warmte uitwisselen. De oxidatieve koppeling wordt uitgevoerd in een reverse flow gepakt bed membraanreactor, die ondergedompeld is in een wervelbedreactor waarin de reformingreacties worden uitgevoerd. In het eerste reactorcompartiment wordt de stromingsrichting peri-

odiek omgekeerd (reverse flow), zodat kostbare externe recuperatieve warmteuitwisseling overbodig wordt. In het tweede reactorcompartiment wordt het productgas van het OCM proces (bestaande uit niet omgezette methaan en de bijproducten ontdaan van de gewenste $C_2$ componenten) samen met extra stoom gebruikt als grondstof voor het SRM proces, waarbij synthesegas wordt geproduceerd en de overtollige warmte van het OCM proces wordt geconsumeerd. Dit nieuwe autotherme reactorconcept is ontwikkeld en bestudeerd door middel van gedetailleerde numerieke simulaties om inzicht te verkrijgen in het complexe gedrag van deze reactor. De berekeningen hebben aangetoond dat het mogelijk is om de OCM en SRM processen op de voorgestelde manier thermisch te koppelen. In de cyclisch stationaire toestand is het mogelijk om een theoretische $C_2$ opbrengst van 30% te halen bij een volledige methaan omzetting, indien een $CH_4/O_2$ ratio van 2-2.5 voor OCM en een $H_2O/CH_4$ ratio van 3 in de SRM wervelbedreactor wordt toegepast.

Hoewel dit reactorconcept in detail is bestudeerd door middel van numerieke simulaties, is een experimentele bevestiging van de haalbaarheid noodzakelijk. De meest stabiele en geschikte katalysator voor het toepassen van reverse flow voor oxidative koppeling van methaan is op dit moment $Mn/Na_2WO_4$ op $SiO_2$. De snelheden van de belangrijkste reacties van oxidatieve koppeling op deze katalysator zijn daarom gemeten onder differentiële condities in een kleine gepakt bed reactor van kwartsglas, omdat de huidige modellen beschikbaar in de literatuur niet compleet zijn en daardoor niet geschikt voor toepassing in numerieke reactormodellen. Door middel van Thermal Gravimetry Analysis (TGA) is vastgesteld dat de katalysator (een reduceerbare metaaloxide) met zuurstof voorbehandeld dient te worden om een voldoende hoge $C_2$ selectiviteit van ongeveer 85% te halen, maar dat een lage zuurstofconcentratie gedurende de OCM reactie al voldoende is om de katalysator stabiel te houden. Na deze voorbehandeling zijn de reactiesnelheidsconstantes en de reactie-ordes van de primaire reacties vastgesteld, door de reactiesnelheden te meten bij verschillende methaan en zuurstofconcentraties. De reactiesnelheden van de secundaire reacties, de oxidatie van etheen en ethaan, zijn geschat op basis van gepubliceerde experimentele data voor dezelfde katalysator door Takanabe (2008) en door eerste orde afhankelijkheid van de koolwaterstof- en zuurstofconcentraties aan te nemen. Op basis van de verzamelde experimentele gegevens is een vereenvoudigd reactiemechanisme opgesteld, waarin de afhankelijkheid van de productiesnelheden van ethaan (oxidatieve koppeling) en kooldioxide (verbranding) en de consumptiesnelheden van de $C_2$ componenten door middel van power-law reactiesnelheidsvergelijkingen kan worden beschreven. Het is gevonden dat de reactieorde van zuurstof van de primaire koppelingsreactie gelijk is aan 0.38, terwijl de reactieorde van zuurstof van de

methaanoxidatie gelijk is aan 1, wat bevestigt dat lage zuurstofconcentraties gunstig zijn voor een hoge $C_2$ selectiviteit (80-90%).

De haalbaarheid van het reactorconcept waarin OCM en SRM zijn ondergebracht in verschillende compartimenten, is deels geverifieerd door middel van experimenten met OCM op de $Mn/Na_2WO_4/SiO_2$ katalysator in een gepakt bed membraanreactor, uitgerust met poreuze $Al_2O_3$ membranen, vanwege de relatief hoge stabiliteit bij hoge temperatuur en de lage permeabiliteit. De wervelbedreactor, waar de SRM reacties plaatsvinden, is vervangen door een verwarmd gefluïdiseerd zandbed om een constante temperatuur te waarborgen. De invloed van verschillende relevante parameters op de oxidatieve koppeling is gemeten in een gepakt bed membraanreactor met een relatief kleine hoeveelheid katalysator. De invloed van het distributief doseren van zuurstof en schaaleffecten op zowel de $C_2$ opbrengst als de axiale temperatuurprofielen is bestudeerd in een reactor met een grotere hoeveelheid katalysator. In beide reactoren is aangetoond dat een $C_2$ opbrengst van 25-30% haalbaar is, indien zuurstof wordt gedoseerd via een membraan, dat goed overeenkomt met gepubliceerde opbrengsten in vergelijkbare systemen. De hoge $C_2$ opbrengst is zowel met voorgemengde als axiaal gedoseerde zuurstof mogelijk indien het reactiemengsel sterk wordt verdund. Bij hogere concentraties van de reactanten leidt de hoge zuurstofflux aan de uitgang van de membraanreactor tot een hoge oxidatiesnelheid van etheen en ethaan en bijbehorende hoge temperaturen. Deze resultaten zijn bevestigd door middel van metingen van de radiale en axiale temperatuurprofielen in de membraanreactor en door kwalitatieve numerieke simulaties met een reactormodel, waarin het experimenteel vastgestelde vereenvoudigde reactiemechanisme was geïmplementeerd. De sterk gestegen temperatuur aan het eind van de reactor kan worden verlaagd door een niet uniforme zuurstofverdeling toe te passen. De temperatuurstijging kan verder worden verlaagd en geoptimaliseerd door langere membraanbuizen te gebruiken, waardoor de zuurstof geleidelijker wordt toegediend. Dit wordt belangrijker en essentieel voor een haalbaar proces voor hogere ingangs-concentraties van methaan. De conclusie is dat oxidatieve koppeling van methaan in een gepakt bed membraanreactor, die gekoeld wordt door een wervelbed reactor, geschikt is om acceptabele $C_2$ opbrengsten te realiseren en dat voor het gecombineerde OCM/SRM reactorconcept axiaal doseren van zuurstof het meest optimaal is.

# 1 Introduction


## Abstract

With the ever increasing industrial development and growth of global welfare, the demand for industrial chemicals, such as ethylene, will increase while the resources available per capita are decreasing. Anticipating that fossil fuels will remain an important resource of primary energy and resources in the coming century, it is essential to search for alternative production methods and to increase the efficiency of these processes. A direct method of converting natural gas into higher hydrocarbons is oxidative coupling of methane (OCM), however, only with hydrocarbon yields limited to 30-35% despite the enormous efforts to optimize the catalysts. By combining OCM with a secondary process, namely steam reforming of methane (SRM) the methane conversion can be increased significantly while simultaneously producing valuable synthesis gas. In this thesis, the focus will lie on the integration of the exothermic OCM and endothermic SRM reactions to an overall autothermal process, so that the OCM process is effectively cooled and the generated reaction energy is efficiently used to produce synthesis gas. The integration can be achieved on the reactor scale by compartmentiliazation of the OCM and SRM reactions in separate sections of a heat exchange reactor, but is most optimally achieved on the catalyst particle scale. Integration on the particle scale would eliminate the need for heat exchange inside the reactor and opens up the possibility to use a membrane reactor for distributive oxygen dosing with which much higher product yields can be achieved.

## 1.1 Energy efficiency in the chemical industry

In the 20$^{th}$ century, the fast development of the (chemical) industry has led to affordable bulk chemicals and energy which have been key drivers for global economic growth and its associated welfare in a large part of the world. In the current century, it is expected that the industrial development will increase even at a faster pace, particularly in Asia and South America. With the growing awareness about the influence of greenhouse gas emissions on the world climate and the shrinking resources per capita it is essential to reduce and optimize the use of energy and resources such that a sustainable future can be ensured.

For the coming 30 years, it is projected that 94% of the global increase in industrial energy consumption is to occur in manufacturing (non-OECD[1]) economies such as Brazil, Russia, India and China (EIA, 2009). Keeping in mind the short time-scale at which this will take place, it would be utopic to think that a transition to only sustainable primary energy sources and technology is feasible. For this reason all the energy outlooks project that fossil fuels in the form of oil, coal and gas will remain the main source of raw materials for the industry in the coming century. This means that for existing (capital-intensive) processes, increasing the energy efficiency in all its aspects will offer the biggest scope for cutting emissions (IEA, 2009).

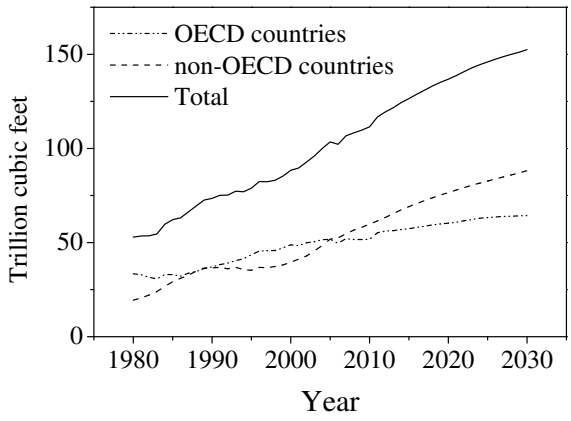


**Figure 1.1:** Historical and projected natural gas consumption figures for OECD (Organisation for Economic Co-operation and Development) and non-OECD countries (source: International Energy Outlook 2009 (EIA, 2009)).

[1]OECD (Organisation for Economic Co-operation and Development). Members: Austria, Belgium, Czech Republic, Denmark, Finland, France, Germany, Greece, Hungary, Iceland, Republic of Ireland, Italy, Luxembourg, Netherlands, Norway, Poland, Portugal, Slovakia, Spain, Sweden, Switzerland, Turkey, UK, Australia, Canada, Japan, Mexico, New Zealand, South Korea, US.

Because the world's oil reserves are limited, alternative sources of primary energy and resources have to be considered to arrive at a more sustainable energy mix for the future. Because of the abundant coal reserves in e.g. the United States and China, coal has been the fastest growing primary energy source for six years (BP, 2009) and it might be logical that future organic chemicals and liquid fuels will be produced via syngas obtained from coal (see e.g. Levenspiel, 2005). Next to coal-based processes, the transition from oil-based economy to a much cleaner natural gas may offer more opportunities, particularly because methane (the main compononent of natural gas) may also originate from bio-based resources. Natural gas can therefore serve as a transition fuel in between the fossil and a possibly more bio-based fuel industry. It is therefore expected that natural gas consumption (for industrial use and electricity generation) will increase at growth rates between 1-2 % per year (Fig. 1.1).

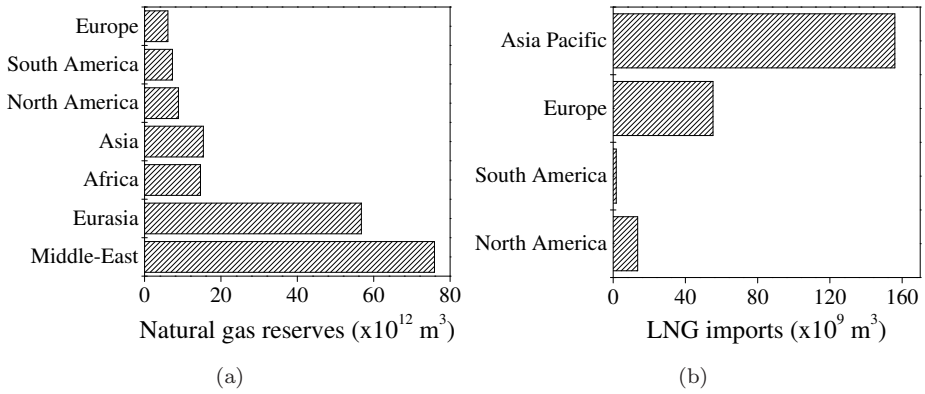


**Figure 1.2:** LNG imports (Source: BP Statistical Review of World Energy BP (2009)).

As shown in Fig. 1.2, almost 75% of the natural gas reserves are located in the Middle East, Russia and Quatar (BP, 2009; EIA, 2009). Hence, as industrial energy supply and demand are geographically separated, transportation of natural gas is required. Because of its low volumetric energy density liquefaction or on-site conversion methods are necessary for economical transportation. As can be seen in Fig. 1.2b, there is already a large movement of liquefied natural gas (LNG) around the world which will be steadily increasing because one of the main drivers of the increase of natural gas consumption is the demand for power generation, which typically is produced near the site of consumption to avoid energy losses in high-voltage cable lines. Conversion on-site is also gaining more attention; large industrial complexes are currently built close to large natural gas fields, so that the gas can be utilized in large-scale GTL (Gas-To-Liquid) processes for production of synthetic fuels and bulk

chemicals. In the following section, the possibility of producing one of the largest world bulk chemicals, ethylene, from natural gas is outlined.

## 1.2 Ethylene production

The most important application of ethylene ($C_2H_4$) is the production of bulk-chemicals such as polyethylene and ethylene oxide, which are used for the packaging and coolants market. The industrial production of ethylene, one of the major bulk petrochemicals with a global production of more than 120 MMTPA (Nakamura, 2007), is mostly carried out via steam cracking of light hydrocarbons. Depending on location and availability, the feedstock for steam cracking can vary from naphtha (mostly European refineries) to ethane (mostly US refineries), but ethane is principally preferred because higher ethylene yields can be achieved and smaller quantities of heavier olefins (e.g. propylene) are produced (Ullmann 2006). In addition, industrial cracking furnaces require large amounts of heat to run the endothermic process, which is carried out by using costly direct fired tubular reactors operating at high temperatures (T = 850°C). Both feedstocks are thus intermediate products that require pre-processing, which could be circumvented if natural gas could be converted into $C_2H_4$ directly. Because of the rising raw materials prices, depletion of oil and the demand for cleaner and more energy-efficient processes, alternative process concepts for the production of $C_2H_4$ are investigated.

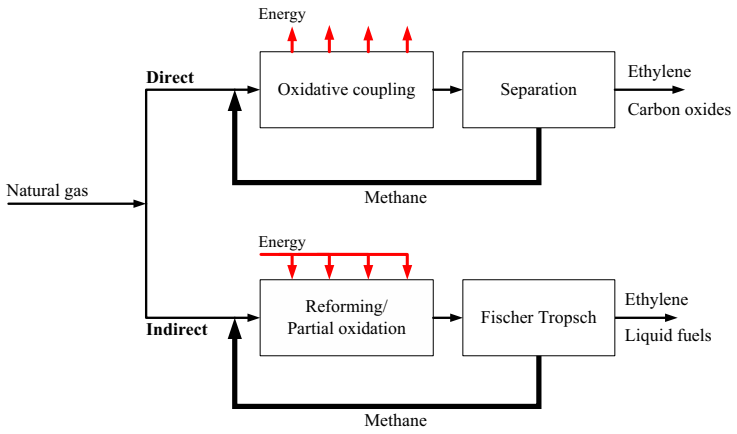


**Figure 1.3:** Direct and indirect pathways to ethylene and liquid fuels.

An alternative hydrocarbon source for ethylene is natural gas, which can be converted into $C_2H_4$ indirectly by first producing synthesis gas (CO and $H_2$) via partial oxidation or steam reforming of methane, and subsequent production of higher hydrocarbons via the well-known Fischer Tropsch synthesis which occurs at low or high temperature, depending on the desired products (Fig. 1.3). With the low temperature Fischer Tropsch process, the hydrocarbon waxes produced can be fed to a conventional steam cracker, which produces a.o. $C_2H_4$. However, it is generally accepted that the best way of producing linear olefins indirectly from natural gas is the high temperature Fischer Tropsch process, which typically produces a mixture of liquid fuels (gasoline/diesel/naphtha) and light olefins (Dry, 2002). The mixture of light olefins is then separated into the desired products, and a methane-rich offgas is sent as fuel gas or burnt for energy production. The main disadvantage is the relatively high yield of light gases and the corresponding large recycle stream of particularly $CH_4$ (a high $C_2H_4$ selectivity unfortunately goes together with a high $CH_4$ selectivity), thus, more efficient direct conversion processes are preferred for ethylene production from natural gas.

## 1.3 Oxidative coupling and steam reforming of methane

A direct route for the production of ethylene from natural gas in a single step is the oxidative coupling of methane (OCM), which involves conversion of natural gas together with oxygen at high temperature (>750 °C) into the selective product $C_2H_4$ and the undesired unselective by-products CO and $CO_2$.

$$2\,CH_4 + O_2 \longrightarrow C_2H_4 + 2\,H_2O \qquad \Delta H^0_{298} = -141 \text{ kJ/mole } CH_4 \qquad (1)$$

$$CH_4 + 2\,O_2 \longrightarrow CO_2 + 2\,H_2O \qquad \Delta H^0_{298} = -803 \text{ kJ/mole } CH_4 \qquad (2)$$

$$C_2H_4 + 3\,O_2 \longrightarrow 2\,CO_2 + 2\,H_2O \qquad \Delta H^0_{298} = -1323 \text{ kJ/mole } C_2H_4 \qquad (3)$$

Like with all selective oxidation reactions this results in the typical conversion-selectivity problem, meaning that a high $CH_4$ conversion (i.e. feeding a relatively large amount of $O_2$) automatically leads to a poor product selectivity and a large yield of undesired combustion products like $CO_2$. In addition, the highly reactive intermediate $C_2H_4$ may easily react to the unwanted and thermodynamically favored oxidation products at too high $O_2$ concentrations. The yield of higher hydrocarbons ($C_2$ and higher) generally is not sufficient for the development of an economically attractive industrial process, because the production of higher hydrocarbons in conventional reactors will always be a trade-off between high $CH_4$ conversion and high $C_2$ selectivity. Since the 1980's, it has therefore been attempted to develop suitable

OCM catalysts, to increase the $C_2$ yield. The main findings are that alkaline earth metals promoted by rare earth oxides most effectively catalyze the coupling reaction, resulting in some of the most promising catalysts Li/MgO (Keller and Bhasin, 1982; Korf et al., 1989), $La_2O_3$/CaO (Sofranko et al., 1987) and Mn/$Na_2WO_4$/$SiO_2$ (Pak et al., 1998). Although optimization of the catalyst and application of various different reactor types has led to improved performance of the process, however, a single pass $C_2$ yield above 30-35% has never been achieved (e.g. Makri and Vayenas, 2003).

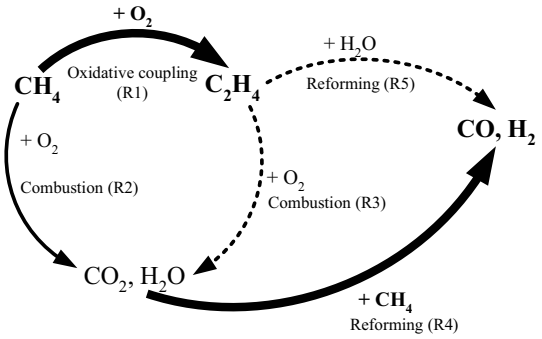


**Figure 1.4:** Overall reaction scheme for the combined production of synthesis gas and ethylene via oxidative coupling and reforming of methane.

Because of the relatively low $CH_4$ conversions that are achieved, various reactor concepts have been developed to increase the overall product yield by recycling of the reactants to the reactor, and separating the selective products formed by the primary reactions from the product mixture. Makri and Vayenas (2003) suggested to apply a fixed bed with integrated separation of $C_2H_4$ by absorption on molsieves. Fluidized bed reactor concepts have been studied by Baerns and Buyevskaya (1998). Although these reactor concepts are a promising lead to industrial scale operation, the large scale production of $C_2H_4$ will always involve a large recycle of $CH_4$, quite similar to the Fischer Tropsch process (see Fig. 1.3), while the by-products CO and $CO_2$ will lead to a significant decrease of the carbon efficiency. Thus, the direct conversion of $CH_4$ into $C_2H_4$ is still high on the industrial wish-list, but it remains a major scientific and technological challenge.

In this work, it is proposed to improve the methane conversion and the feasibility of the OCM process by integration of steam reforming of methane (SRM). If the by-products and the unconverted $CH_4$ from the OCM could be used as reactants

for steam/dry reforming of methane, the conversion could be significantly increased thereby avoiding or decreasing the requirement for a $CH_4$ recycle, while simultaneously producing synthesis gas ($CO/H_2$) and hydrocarbons directly from natural gas (see Fig. 1.4). As most steam reforming catalysts are also excellent oxidation catalysts, and are catalytically active for $C_2H_4$ reforming, the combination of OCM and SRM in a single multifunctional reactor is a technological challenge.

$$CH_4 + H_2O \rightleftharpoons CO + 3\,H_2 \qquad \Delta H^0_{298} = 206 \text{ kJ/mole } CH_4 \qquad (4)$$

$$C_2H_4 + 2\,H_2O \rightleftharpoons 2\,CO + 4\,H_2 \qquad \Delta H^0_{298} = 210 \text{ kJ/mole } C_2H_4 \qquad (5)$$

Next to the increase of the $CH_4$ conversion, another significant additional advantage of the combination of OCM and SRM investigated in this work, is that the large amount of heat generated by the exothermic oxidative coupling is consumed by the endothermic reforming, creating the opportunity to achieve an overall autothermal process.

### 1.3.1 Membrane reactors

An important aspect of the oxidative coupling reaction (and many other selective oxidation reactions), which can be exploited to maximize the total product yield is the $O_2$ reaction order of the preferred reaction, which is typically smaller than the $O_2$ reaction order of the unselective (total) oxidation reactions. As a consequence, the hydrocarbon selectivity increases at lower $O_2$ partial pressures, however, at the expense of the total $CH_4$ conversion which decreases because of the lower $O_2$ concentrations.

With co-feed of the reactants to the (catalytic) reactor compartment (Fig. 1.5a), the high reactant inlet concentrations and the concomitantly large reaction rates lead to low selectivity and characteristic high temperature peaks close to the reactor inlet. The need for low $O_2$ concentration interferes with the demand for a high $CH_4$ conversion level, which can be overcome by using a redox-type catalyst (like $Mn/Na_2WO_4$), however with this mode of operation many problems such as deposition of carbonaceous deposits and reactor stability were observed (Lafarga et al., 1994). Distributed feed is a better solution, which can be applied in different configurations to suppress undesired oxidation of products and/or reactants by keeping the local $O_2$ concentration low. Closest to conventional operation is the installation of a series of packed bed reactors with inter-staged feeding of one of the reactants, which is quite similar to a recycle or loop reactor, however, without intermediate separation of reaction products (see Fig. 1.5b). The total feed of $O_2$ is divided into $n$ parts, which is fed to the separate stages. A relatively high yield can be achieved by this interstaged feeding,

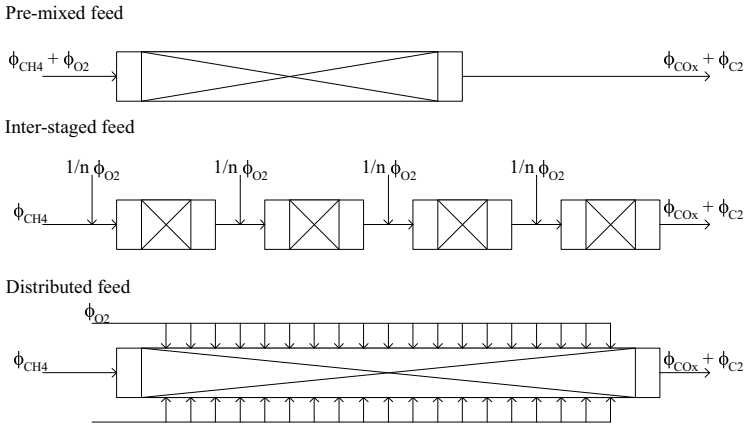


**Figure 1.5:** Feeding modes of $O_2$ to packed bed reactors.

because the local selectivity is higher and the heat production is reduced. Optimal performance is achieved when the number $n$ of inter-staged feeding points approaches infinity, so that the reactants are uniformly distributed, which can be accomplished with a membrane (Fig. 1.5c). In a membrane reactor, a single reactor compartment (instead of multiple staged reactors) is used where the reactant is fed to the catalytic compartment by either (multiple) porous or dense membranes. As can be imagined, the degree of complexity of the reactor itself is somewhat higher, because multi-tubular reactors are required, however the separate stages and inter-staged cooling and feed of $O_2$ is no longer required. For oxidative coupling, numerous types of dense perovskite membranes (Akin and Lin, 2002; Yang et al., 2005) and porous membrane tubes (Coronas et al., 1994a; Kao et al., 2003; Lu, Dixon, Moser, Ma and Balachandran, 2000) have been tested, leading to increased insight in the behavior, stability and performance of OCM under these conditions. With the current state-of-art, the highest $C_2$ yields obtained with membrane reactors are limited to 25-30% which were all obtained with diluted reactant flow, which also limits the temperature rise. In this study, the purpose of using distributed feed of $O_2$ is two-fold. First, it is attempted to increase the overall $C_2$ selectivity by using a low $O_2$ membrane flux, which will be investigated in a small-scale micro-catalytic fixed bed reactor (to determine the $O_2$ reaction orders) and a somewhat larger membrane reactor in which the integral effects of oxidative coupling will be studied. Second, for better thermal control of the combined OCM/SRM process, and to achieve overall autothermal conditions, it is preferred to have a rather uniform heat generation along the reactor length.

### 1.3.2 Thermal coupling of OCM and SRM

Also for better thermal control of exothermic reactions, controlled dosing of $O_2$ by using membrane reactors is beneficial. As the reaction heat is now released along the reactor length, it becomes possible to implement SRM along with OCM. The amount of methane that needs to be reformed relative to the amount of methane reacted via oxidative coupling in order to achieve autothermal operation can be calculated, based on overall reaction schemes. In the idealized case, it can be assumed that the by-product $CO_2$ only result from unselective oxidation reactions which can be lumped into a single reaction. The overall reaction can then be written as:

$$(1 + x + y_1)\,CH_4 + (\frac{1}{2} + 2y_1)\;O_2 + (x - 1 - 2y_1 + 2y_2)\,H_2O \longrightarrow$$
$$(\frac{1}{2} - y_2)\;C_2H_4 + (x + 2y_1 + 2y_2)\,CO + (3x + 2y_1 + 4y_2)\,H_2$$

Where $x$ represents the amount of methane reforming (SRM) relative to OCM, $y_1$ the extent of methane combustion/dry reforming relative to OCM and $y_2$ the extent of $C_2H_4$ lost to reforming reactions relative to OCM (SRE). For various settings of $y_1$, which is a parameter for the $CO_x$ selectivity of the OCM catalyst, and $y_2$, it can be calculated that overall autothermal operation can be achieved when:

$$x\Delta H_{SRM} + y_2\Delta H_{SRE} = \Delta H_{OCM} + y_1\,(\Delta H_{PROX})$$

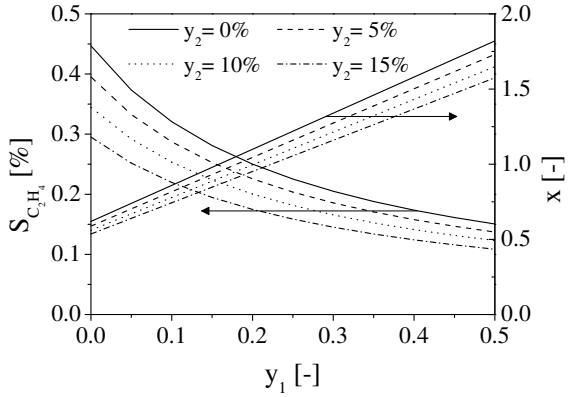


**Figure 1.6:** Maximum $C_2H_4$ selectivity that can be achieved at full $CH_4$ conversion and required amount of steam reforming ($x$) to obtain autothermal operation for various amounts of $C_2H_4$ reforming.

In the idealized case where no combustion products are formed ($y_1 = 0$), overall autothermal operation can be achieved by coupling the OCM with reforming

(SRM/SRE) using x = 0.62, which would result in an ethylene selectivity of 45% (and a synthesis gas selectivity of 55%). Obviously, this situtation will never occur due to $CH_4$ oxidation and consecutive oxidation of the formed $C_2$ 's, into CO or $CO_2$. In order to maintain autothermal operation at these conditions, some additional methane steam reforming is required to compensate for the net heat production. At $y_1 = 0.2$ autothermal operation can be realized with $x = 1.1$, which yields an overall ethylene selectivity of 25% (see Fig. 1.6). When both OCM and SRM are performed in the same catalytic reactor compartment, consecutive reforming of $C_2H_4$ will decrease the overall $C_2$ selectivity. This is illustrated by variation of the parameter $y_2$, and it is shown that at $y_1$=0.2 the $C_2$ selectivity decreases to 20% if 10% of the formed $C_2H_4$ is consumed via reforming. Because of the endothermic $C_2$ reforming, the required amount of $CH_4$ steam reforming is somewhat lower.

To achieve autothermal operation, additional catalyst optimization and tuning of the process to optimal operating conditions (in a membrane reactor) is essential. Two important issues have to be solved as the SRM catalyst is an excellent deep oxidation catalyst (see e.g. Trimm and Lam, 1980) and ethylene reforming is difficult to prevent along with methane reforming reactions (Graf et al., 2007). First, to prevent the presence of oxygen on the SRM catalyst, it is required to separate the OCM and SRM catalytic functions and second the extent of $C_2H_4$ reforming has to be minimized. This has led to the idea of separating the two catalytic functions, which has been worked out in two reactor concepts, in which OCM and SRM can operate autothermally, namely on the scale of a single catalyst particle and on the scale of the reactor by compartmentalization of OCM and SRM catalysts.

## 1.4 This thesis

In the first concept to combine OCM and SRM, on the scale of a single catalyst particle, the interference of OCM and SRM reactions can be prevented by using a catalyst particle in which the two processes are physically separated by an inert, porous layer, such that additional diffusional resistances are intentionally created. By locating the reforming activity in the particle center, the SRM reaction rates are controlled by these diffusion limitations. The presence of oxygen on the SRM catalyst is effectively prevented because the oxygen is converted on a very active oxidative coupling catalyst, which is present only in the outer shell of the particle. The concept of integrating an exothermic and an endothermic reaction on the scale of a catalyst particle, and tuning of the reactions by diffusional limitations may also be more generic, and suitable for other reaction systems. In this study, however, the effect of integration of SRM in

a OCM catalyst particle has been studied by detailed numerical modeling, in order to derive design criteria for the catalyst particle to achieve optimal heat integration (Chapter 2). Subsequently the performance of a packed membrane reactor filled with this dual function catalyst is studied in great detail, coupling the particle model to a heterogeneous packed bed membrane reactor model (Chapter 3).
In the second concept the combination of OCM and SRM on the reactor scale, the OCM is carried out in a packed bed reverse flow membrane reactor tubes submerged into a fluidized bed where the unconverted methane and by-products, from which the valuable $C_2$ components have been separated, are reformed together with some additional steam, thus producing synthesis gas and consuming the reaction heat liberated by the exothermic OCM. The two different reactor concepts for combined oxidative coupling and steam reforming of methane have been investigated in detail, to optimize simultaneous ethylene and syngas production in an overall autothermal process. The thermal coupling of OCM and SRM via two different reactor compartments is studied. Chapter 4 involves the proposal of this novel reactor concept, which is investigated with numerical simulations. Chapter 5 deals with an experimental study of OCM on a $Mn/Na_2WO_4$ catalyst, which was used to derive a (lumped) kinetic model for OCM which can be applied for reactor modeling studies. In Chapter 6, the feasibility of OCM in a membrane reactor was investigated, especially focusing on the axial temperature profiles. Finally, the epilogue of this thesis discusses the findings and the possibilities for application of this combined process on industrial scale.

## Acknowledgement

The authors gratefully acknowledge the financial support by the Netherlands Organisation for Scientific Research (NWO/ACTS) under the research theme of Advanced Sustainable Processes by Engaging Catalytic Technologies (ASPECT) (project 053.62.008).

## Nomenclature

| | | |
|---|---|---|
| $\Delta H$ | kJ/mol | Reaction enthalpy |
| $\phi_i$ | mole/s | Molar flow of component i |
| $S$ | % | Selectivity |
| $x$ | - | Amount of reforming reactions relative to OCM |
| $y_1$ | - | Amount of oxidation reactions relative to OCM |
| $y_2$ | - | Amount of $C_2H_4$ reforming reactions relative to OCM |

*Subscripts*

| | | |
|---|---|---|
| OCM | - | Oxidative coupling of methane |
| PROX | - | Partial oxidation of methane |
| SRE | - | Steam reforming of ethylene |
| SRM | - | Steam reforming of methane |

# 2

# Design of a dual-function OCM/SRM catalyst particle


## Abstract

A dual-function catalyst particle which integrates the exothermic oxidative coupling and endothermic steam reforming of methane for the simultaneous autothermal production of ethylene and synthesis gas has been designed and studied by detailed numerical simulations. Compared to conventional oxidative coupling of methane, the introduction of a reforming activity significantly increases the methane conversion without deteriorating the productivity towards the desired ethylene and ethane. Moreover, the presence of an intra-particle heat sink enables local autothermal operation which greatly simplifies the reactor design, opening the possibility to couple these reactions in a packed bed membrane reactor with improved product yield. Because the chemical reactions occurring on both types of catalytic active sites interfere, it is proposed to use a catalyst particle in which the two processes are physically separated by an inert, porous layer, such that additional diffusional resistances are intentionally created. The reforming activity is located in the particle center, while the oxidative coupling catalyst is present only in the outer shell of the particle.

The structuring of the catalytic functions inside a single catalyst particle yields many advantages over conventional indirect coupling of exothermic and endothermic reactions in different reactor compartments, especially because the intra-particle heat transfer resistance is much smaller than the heat transfer resistance between different reactor compartments. It has been demonstrated by means of numerical simulations that at low oxygen concentration (representing conditions in a packed bed membrane reactor), the internal mass transfer limitations can be effectively utilized to regulate the total reforming reaction rates and to prevent oxygen from reaching the reforming catalyst. Additionally, the size of reforming catalytic core can, together with the effective diffusion properties inside the particle (viz. particle porosity and tortuosity) and the bulk gas phase concentrations, be used to tune the process to local autothermal operation.

## 2.1 Introduction

The ideal configuration of a dual-function catalyst particle to couple non-interfering exo- and endothermic processes is a uniformly distributed catalytic activity inside the porous structure for both the exothermic and endothermic reaction systems, mainly because conventional preparation methods such as impregnation can be applied and the development of the particle is rather straightforward. A second best option is to use a homogenized mixture of particles with catalytic activity for either the exothermic or the endothermic reactions. In this case intra- and/or extraparticle heat transfer resistances may cause temperature differences between the different particles. In the specific case of combining oxidative coupling (OCM) and steam reforming of methane (SRM), the catalysts used for steam reforming (such as $Ni/Al_2O_3$ or $Pt/Al_2O_3$) are also active for unselective oxidation reactions, thus using a uniform catalyst layout as indicated in Fig. 2.1a would lead to a non-feasible, non-selective, highly exothermic process. In addition, both $C_2H_4$ and $C_2H_6$ are susceptible for steam reforming, resulting in a major loss of valuable hydrocarbons.

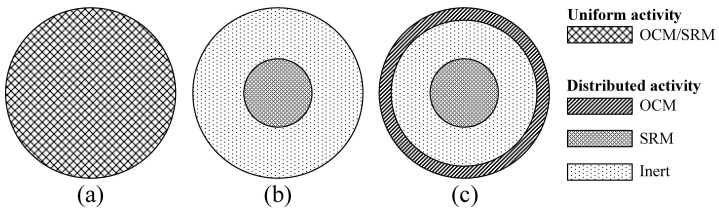


**Figure 2.1:** Configuration of catalytic activity in a dual-function catalyst particle for combined production of $C_2H_4$ and synthesis gas.

Interference of both processes is strongly reduced by locating the reforming activity in the particle center (Fig. 2.1b) and subsequently adding the oxidative coupling activity at the outer layer of the particle (Fig. 2.1c). Due to transport limitations introduced by a porous, inert layer located between the OCM and SRM catalytic functions, the extent of $C_2$ reforming on the SRM catalyst is minimized. Provided that an OCM catalyst with sufficiently large activity is used (such as $La_2O_3/CaO$ (Stansch et al., 1997)), the presence of intra-particle diffusion limitations, reflected by a large value of the Thiele modulus, results in total conversion of oxygen in the outer (OCM) catalyst layer, thereby avoiding the presence of molecular $O_2$ at the SRM catalyst.

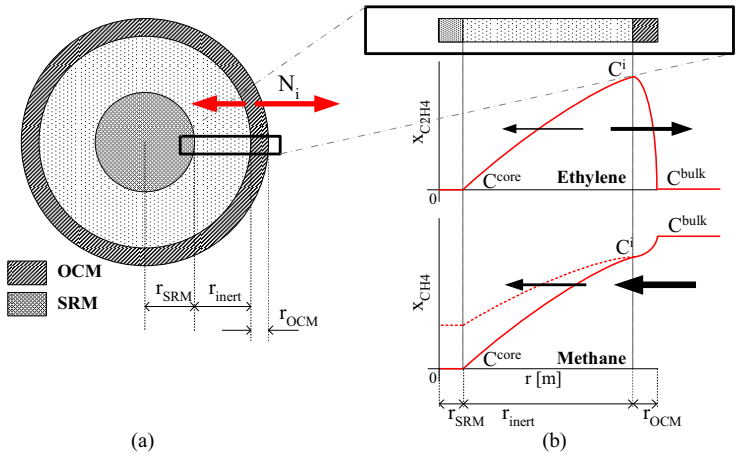


**Figure 2.2:** (a) Schematic layout of dual-function catalyst particle and (b) typical $CH_4$ and $C_2H_4$ intraparticle mole fraction profiles (symbols explained in the symbols list).

The design of a dual function catalyst for autothermal operation requires the calculation of the dimensions of e.g. the SRM core diameter ($r_{SRM}$), the thickness of the OCM layer ($r_{OCM}$) and the thickness ($r_{inert}$) and properties (viz. particle porosity and tortuosity) of the inert layer in order to locally balance the heat generation and consumption by OCM and SRM without deteriorating the $C_2$ productivity. Because inside the porous particle, transport of mass is governed by molecular and/or Knudsen diffusion, modification of the porous structure influences the ratio of OCM and SRM reactions and thereby the degree of autothermicity. Increasing the extent of intra-particle mass transfer limitations, i.e. decreasing the effective diffusivity $D_{eff}$ or increasing the diffusion path length $r_{inert}$, reduces the inward mass flux of $C_2H_4$ and $C_2H_6$ so that less valuable hydrocarbons are lost via SRM reactions (see Fig. 2.2). Next to the $C_2$ flux, however, the $CH_4$ fluxes and hence syngas production are also limited by mass transfer, which in turn influences the degree of autothermal operation and the synthesis gas yield.

In the first part of this chapter it is determined by means of numerical simulations under which conditions synthesis gas can be produced together with higher hydrocarbons on a single catalyst particle. It will be shown how intra-particle mass transfer limitations can be effectively used to influence the ratio of OCM and SRM reaction rates and achieve autothermal operation. Because of axial concentration profiles prevailing in the reactor, the local required energy consumption rate by reforming reactions in the catalyst particles will be dependent on the extent of secondary $C_2$

combustion reactions. Obviously this changes the design criteria for the particles and optimization of the desired configuration of the catalyst particle (i.e. core diameter, inert layer thickness and particle structure) is principally required for each location in the reactor. Therefore, the influence of intra-particle temperature gradients and bulk gas phase composition (representing different axial locations in the reactor) are quantitatively investigated in the final part of this chapter, resulting in the formulation of criteria required for the design of a multi-functional autothermal catalyst particle for OCM and SRM. The integral performance of a packed bed membrane reactor with a dual function OCM/SRM catalyst is studied in Chapter 3.

## 2.2 Numerical model

To study the temperature and concentration profiles for a multicomponent reaction mixture inside a catalyst particle with distributed catalytic activity, a particle model was developed that is capable of solving multicomponent mass transport and energy transport in a porous structure. The model is based on numerical simulation of the phenomena occurring inside porous particles for gas-solid and/or catalyzed reactions as described by many researchers (e.g. Apecetche et al., 1973; Weisz and Hicks, 1962).

### 2.2.1 Model Equations

The unsteady state, one-dimensional pseudo-homogeneous mass and energy conservation equations have been listed in a general form in Table 2.1, describing the concentration and temperature profiles inside a catalyst particle for a flat plate ($\alpha = 0$), cylindrical ($\alpha = 1$) or spherical ($\alpha = 2$) particle. It is assumed that only diffusive transport of mass and energy is taking place, which can be described by generalized Fick's law of diffusion. Furthermore, isobaric conditions are assumed, based on the work of Veldsink et al. (1995). Although reactions with a net change in moles, such as steam reforming, in principle will lead to pressure and gas density changes in the particle it was verified that pressure gradients are negligible for small particles with a point of symmetry, which greatly simplifies the required modeling approach. Finally, the ideal gas law can be applied because at high temperatures the non-ideal behavior of gases is strongly reduced, as can be derived from generalized compressibility charts in Poling et al. (2007).

The source terms (Table 2.1) are calculated with typical representative OCM and SRM reaction kinetics taken from the literature. A relatively complete reaction scheme for the oxidative coupling of methane is the kinetic scheme derived for a

**Table 2.1:** One-dimensional equations for the intra-particle reaction model.

*Continuity equation*

$$\varepsilon_g \frac{\partial \rho_g}{\partial t} = -\frac{1}{r^\alpha}\frac{\partial}{\partial r}(r^\alpha n_{tot})$$

*Component mass balance*

$$\varepsilon_g \rho_g \frac{\partial \omega_i}{\partial t} = -\frac{1}{r^\alpha}\frac{\partial}{\partial r}(r^\alpha n_i) + s_{r,i} M_i$$

with source term: $s_{r,i} = (1-\varepsilon_g)\rho_s \sum_{j=1}^{N_{reac}} \nu_{i,j} r_j$ for i = 1..N

and fluxes: $n_i = j_i + \omega_i n_{tot} = -\rho_g \sum_{k=1}^{N-1} d^0_{eff,i,k} \frac{\partial \omega_k}{\partial r} + \omega_i n_{tot}$ for (N-1) components

and $j_N = -\sum_{i=1}^{N-1} j_i$

*Energy balance*

$$(1-\varepsilon_g)\rho_s C_{p,s} \frac{\partial T}{\partial t} = -\frac{1}{r^\alpha}\frac{\partial}{\partial r}(r^\alpha \lambda_{eff,s} \frac{\partial T}{\partial r}) + s_h$$

with source term: $s_h = (1-\varepsilon_g)\rho_s \sum_{j=1}^{N_{reac}} r_j \Delta H_{r,j}$

*Boundary conditions*

| *Location* | *Mass balance* | *Energy balance* |
|---|---|---|
| $r = 0$ | $\frac{\partial \omega_i}{\partial r} = 0$ | $\frac{\partial T}{\partial r} = 0$ |
| $r = r_p$ | $-\sum_{k=1}^{N-1} d^0_{eff,i,k} \frac{\partial \omega_i}{\partial r} = k^\bullet_{g\to s}(\omega_{i,bulk} - \omega_i) + n_{tot}$ | $-\lambda_{eff,s}\frac{\partial T}{\partial r} = \alpha^\bullet_{g\to s}(T_{bulk} - T)$ |

$La_2O_3$/CaO catalyst by Stansch et al. (1997). These rate expressions for OCM were determined by experiments in a micro-catalytic fixed bed reactor in the temperature range of interest (700-955°C), $p_{CH_4}$ =10-95 kPa and $p_{O_2}$ =1-20 kPa. For the steam reforming and the water-gas-shift reaction, reaction rate expressions developed for a $Pt/Al_2O_3$ catalyst have been taken from Xu and Froment (1989). The reaction rate constants for $C_2H_6$ and $C_2H_4$ were found to be a factor 2 and 10 respectively higher than $CH_4$ reforming at 500°C, as has been established experimentally by Graf et al. (2007). See Appendix 2.A for a more detailed description of reaction rate expressions.

#### Intra-particle diffusive mass transport

Diffusive transport of mass is calculated by Fick's generalized law, which basically involves the Maxwell-Stefan equations with the assumption of linearized gradients. The application of Maxwell-Stefan equations greatly increases the complexity of the numerical solution because of the strong coupling between the equations, but unfortunately multicomponent diffusion can only be described accurately by means of an effective diffusion coefficient for all species if the mixture is either very dilute or when the species are of similar nature. This approach would reduce the diffusivity matrix $[D^0]$ to a scalar and thereby would greatly simplify the numerical solution of the equations. However, in non-diluted gas mixtures containing components with largely differing diffusion coefficients (e.g. $H_2$ and $CH_4$ ), as studied in this work, the interaction between components strongly influences the concentration profiles, and the conventional approach of one single (Fickian-based) diffusion coefficient for all components introduces a large error in the calculation results. Therefore, the intraparticle mass diffusion fluxes $n_i$ are calculated by means of the linearized Maxwell-Stefan equations for (N-1) independent equations (Taylor and Krishna, 1993). According to the Fick formulation with a square matrix $[D]$ containing Maxwell-Stefan diffusivities for N-1 components in the molar average velocity frame, this can be written as:

$$[D] = [B]^{-1}[\Gamma] \quad \text{with} \quad \Gamma_{i,j} = \mathbf{I}_{i,j} + x_i \left.\frac{\partial ln\phi_i}{\partial x_j}\right|_{T,P,x_k,k\neq j=1\cdots N-1} \tag{2.1}$$

For ideal gas mixtures the matrix of thermodynamic correction factors [Γ] reduces to the identity matrix and $[B]^{-1}$ consists solely of binary diffusion coefficients and the component interaction coefficients, as defined in Table 2.2. In the derivation of $[B]$ (see Appendix 2.B) it can be seen that this method of calculating multicomponent diffusion coefficients is particularly advantageous, because it implicitly accounts for the constraint on the weight fractions to sum up to unity, so that the system of strongly coupled equations only needs to be solved for (N-1) components.

**Table 2.2:** Calculation of Maxwell Stefan diffusivities.

*Definition of* $[B]$ *in molar average reference velocity frame*

$$[B] = \begin{bmatrix} b_{1,1} & b_{1,2} & \cdots & b_{1,N-1} \\ b_{2,1} & b_{2,2} & \cdots & b_{2,N-1} \\ \vdots & \vdots & b_{i,i} & \vdots \\ b_{N-1,1} & b_{N-1,2} & \cdots & b_{N-1,N-1} \end{bmatrix}$$

$$\text{with } b_{i,i} = \frac{x_i}{Đ_{i,N}} + \sum_{\substack{k=1 \\ k\neq i}}^{N-1} \frac{x_k}{Đ_{i,k}} \quad b_{i,j} = -x_i \left( \frac{1}{Đ_{i,j}} - \frac{1}{Đ_{i,N}} \right)$$

*Conversion to mass average reference velocity frame*

$$[D^0] = [B^{ou}][\omega][x]^{-1}[D][x][\omega]^{-1}[B^{ou}]^{-1}$$

$$\text{with } B^{ou}_{i,k} = \mathbf{I}_{i,k} - \omega_i \left( 1 - \frac{x_k \omega_N}{\omega_k x_N} \right)$$

The elements of $[B]$ contain the diffusion coefficients of the binary pairs $Đ_{i,j}$, which can be calculated with correlations based on the kinetic theory of gases found in e.g. Poling et al. (2007). The inverted matrix of $[B]$ is a matrix $[D]$ containing diffusion coefficients based on the molar averaged reference velocity frame. However, the mass balances are calculated in the mass averaged reference velocity frame, which simplifies the component continuity equations, but requires conversion of $[D]$ to the mass averaged reference velocity frame. In Table 2.2, the algorithm is listed with which this is achieved and the result of the multiplication is a matrix $[D^0]$ of (N−1) order, which is the inverted matrix of binary diffusion coefficients corrected for the mass averaged reference velocity frame. In Appendix 2.C the relevance of the conversion from mole to mass averaged reference velocity frame is discussed in more detail.

#### Interphase mass and energy transfer

Mass and energy transport between the bulk gas phase and the catalyst surface is often calculated based on a single transfer coefficient for all components. However, to account for the interaction between the components in an undiluted multi-component system, the method of Toor, Stewart and Prober is applied here to calculate the mass transfer coefficient under zero flow conditions and to correct the coefficient for non-equimolar diffusion through the boundary layer (Stewart and Prober, 1964; Taylor

and Krishna, 1993; Toor, 1964a,b).

$$\begin{aligned}(n)|_{r=r_p} &= \rho_g \left[k_{g\to s}\right]\left((\omega_{bulk}) - (\omega)\right) + (\omega)\, n_{tot} \\ &= \rho_g \left[k^{\bullet}_{g\to s}\right]\left((\omega_{bulk}) - (\omega)\right) \end{aligned} \tag{2.2}$$

The matrix of finite mass transfer coefficients $[k^{\bullet}_{g\to s}]$, which can be interpreted as the correction of the mass flux $j_i$ for a net total mass flux $n_{tot}$ to obtain $n_i$, is calculated with Sylvesters' expansion formula (Taylor and Krishna, 1993).

$$\left[k^{\bullet}_{g\to s}\right] = \sum_{i=1}^{m} \hat{k}_{g\to s,i} \left( \prod_{\substack{j=1 \\ j\neq 1}}^{m} \left( \left[D^0\right] - \hat{D}^0_j \mathbf{I} \right) / \prod_{\substack{j=1 \\ j\neq 1}}^{m} \left( \hat{D}^0_i - \hat{D}^0_j \right) \right) \tag{2.3}$$

Where $m$ is the number of distinct eigenvalues of the $[D]$ matrix ($m \leq N-1$). The vector containing the eigenvalues (e.g. Taylor and Krishna, 1993) of the mass transfer coefficients ($\hat{k}_{g\to s}$) under condition of zero mass flux ($n_{tot} = 0$) can be calculated using an appropriate Sherwood correlation, which can be found in e.g. the VDI Heat Atlas (1993). In this work, however, limiting values of Sh have been taken to illustrate the influence of interphase mass transfer.

Once the eigenvalues of the mass transfer coefficient under zero mass flux ($\hat{k}_{g\to s}$) are known, a correction for the contribution of $n_{tot}$ is performed via the following correction factor (assuming the film model (Bird et al., 2002)), to obtain $[k^{\bullet}_{g\to s}]$.

$$\Xi_m = \frac{\Phi_m}{(exp(\Phi_m) - 1)} \text{ with } \Phi_m = \frac{n_{tot}}{\rho_g \hat{k}_{g\to s,m}} \tag{2.4}$$

Depending on the direction of the total flux, it can be verified that the drift flux $n_{tot}$ will enhance or decrease the mass transfer coefficient and therewith influences the component flux $n_i$.

Analogous to the calculation of the mass transfer coefficients, the heat transfer coefficient obtained with a Nusselt correlation should be corrected for non-equimolar diffusion. The heat transfer correction factor $\Xi_h$ is calculated completely analogous to equation 2.4, however with:

$$\Phi_h = \frac{-\sum_{i=1}^{N} n_i \bar{H}_i / M_i}{\alpha_{g\to s,0}} \quad \text{so that} \quad \alpha^{\bullet}_{g\to s} = \Xi_h \alpha_{g\to s,0} \tag{2.5}$$

In this work the heat transfer coefficient $\alpha_{g\to s,0}$ is calculated from limiting values of Nu to investigate the importance of interphase heat transfer. The corrected mass and heat transfer coefficients are used in the boundary conditions listed in Table 2.1.

### 2.2.2 Numerical solution

For the numerical solution of the equations summarized in Table 2.1, fully implicit schemes are preferred because the numerical stability of an explicit scheme is constrained by a maximum time step which is, in case of multicomponent diffusion, related to magnitude of the diffusivity coefficients and the grid size. Fourier analysis gives the following well-known (Von Neumann) criterion for numerical stability for explicit discretization schemes (Wesseling, 2001):

$$\frac{D_{i,max}\Delta t}{\Delta r_{min}^2} < \frac{1}{2} \tag{2.6}$$

Because diffusion coefficients typically vary around $10^{-5}$ $m^2/s$, the maximum time step for small catalyst particles (0.1–5 mm) lies in the order of milliseconds, leading to long calculation times to achieve steady state operation. To enable the use of (much) larger time steps the equations are discretized and solved via an implicit discretization scheme.

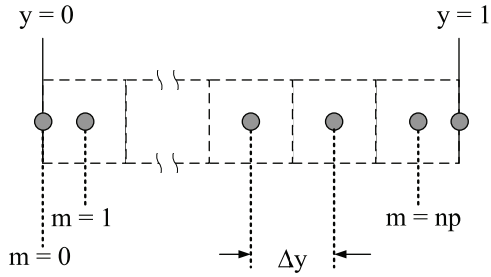


**Figure 2.3:** Equidistant mesh in the numerical y-space in which equations are solved.

The time derivative of the equations listed in Table 2.1 is calculated with a conventional first order Euler step, and adaptive time stepping is applied by evaluating the accuracy of the solution at each time step. The mass and energy balances are solved on a staggered numerical grid where the mass fractions and the temperature are evaluated at the grid points (m=2 .. np−1) (see Fig. 2.3), while the total molar flux $n_{tot}$ is evaluated at the cell faces. The diffusional fluxes are discretized with a standard $2^{nd}$ order centered difference scheme. A transformation function has been implemented to achieve a higher grid resolution near the particle surface, transforming the diffusive terms in the mass and energy balances into:

$$\frac{1}{r^\alpha}\frac{\partial}{\partial r}\left(r^\alpha \beta \frac{\partial u}{\partial r}\right) = \frac{1}{\psi^\alpha \psi'}\frac{\partial}{\partial y}\left(\frac{\psi^\alpha}{\psi'}\beta\frac{\partial u}{\partial y}\right) \tag{2.7}$$

The numerical grid can now be locally refined by applying a suitable transformation function. The following transformation function has been used in this work:

$$r = \psi(y) = r_{particle}\left[1 - \left((1-p_\psi)(1-y)^2 + p_\psi(1-y)\right)\right] \qquad with \qquad p_\psi = 0.01 \quad (2.8)$$

For example, the above function increases the number of grid cells near the particle boundary, so that steep gradients near the boundary can be accurately solved on a refined grid, while the remainder of the computational domain is solved on a grid which is more coarse. The numerical code has been extensively tested with cases for which an analytical solution was available and the results of the model validation can be found in Appendix 2.D.

### 2.2.3 Outline and model settings

The criteria for autothermal operation along the reactor length will change because of changing bulk gas phase concentrations, and losses of valuable $C_2$ hydrocarbons by secondary oxidation and by reforming reactions will increase. Therefore, the integration of reforming and oxidative coupling on catalyst scale was investigated for single particles for different bulk compositions mimicking different axial locations. Reactor inlet conditions, of which the default values are listed in Table 2.3, will be used to demonstrate the performance of the dual function catalyst and illustrate how to arrive at autothermal operation at the particle level.

**Table 2.3:** Default parameters for the particle model.

| Parameter | Value | Parameter | Value |
|---|---|---|---|
| $T$ [K] | 1073.15 | $x_{\mathrm{CH_4}}$ [-] | 0.5 |
| $p_{tot}$ [kPa] | 150 | $x_{\mathrm{H_2O}}$ [-] | 0.1-0.4 |
| $r_p$ [m] | $0.025 - 5 \cdot 10^{-3}$ | $x_{\mathrm{O_2}}$ [-] | 0.001-0.01 |
| $r_{OCM}$ [m] | $0.25 \cdot 10^{-3}$ | $x_{\mathrm{N_2}}$ [-] | balance |
| $r_{SRN}$ [m] | $0.5 \cdot 10^{-3}$ | | |

First, oxidative coupling of methane is studied separately. The influence of the intra-particle concentration gradients and the effect of varying gas phase bulk concentration and temperature was investigated. Because intra-particle concentration gradients are essential for the feasibility of the dual function catalyst, it was assessed whether external mass and heat transfer limitations negatively influence the performance. Second, it was investigated at which conditions the steam reforming reaction rates are governed by internal mass transfer limitations. Finally, the feasibility of the

dual function catalyst was demonstrated by deriving the required dimensions from criteria determined from the OCM simulations. At isothermal and non-isothermal conditions, the effective diffusivity, different $CH_4$ conversion levels (representing different axial locations in the reactor), the bulk gas phase concentration and the particle diameter were used to tune the process to autothermal operation, resulting in guidelines for particle design.

## 2.3 Only oxidative coupling of methane

The development of a dual function catalyst particle for the combined OCM and SRM requires that first the characteristics of the oxidative coupling process are investigated, because the design of the catalyst is largely determined by the (mass transfer limited) OCM reaction rates.

### 2.3.1 Particle effectiveness factors

The minimum thickness of the catalyst layer for OCM ($r_{OCM}$) was determined from calculations using the numerical particle model for multicomponent systems and compared with an approximate analytical solution for the particle effectiveness factor. Generally, analytical expressions for the particle effectiveness factor are only available for single reactions but an expression for the effectiveness factor for the OCM system with multiple reactions can be derived, provided that $CH_4$ is in large excess compared to $O_2$ and that the oxidative coupling can be approximated as a system of reactions occurring in parallel with respect to $O_2$.

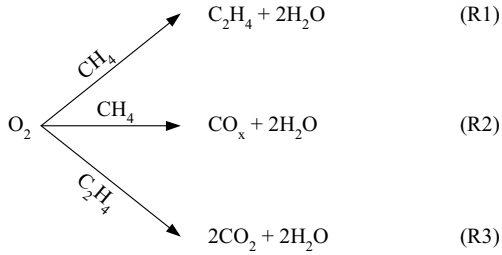


With the limiting component $O_2$ reacting via one selective (R1) and multiple unselective reactions (R2 & R3), the influence of intra-particle mass transfer limitations in a spherical particle can be written in terms of a particle effectiveness factor for the

consumption of $O_2$:

$$\eta_{O_2} = \frac{\int_{r=0}^{r=r_p} R_{j,local} 4\pi r^2 dr}{R_{j,bulk} V_p} \tag{2.9}$$

Analogous to van Sint Annaland et al. (2007a), a characteristic Thiele modulus is defined which is related to the consumption and mass transfer of oxygen. Under the assumption of absence of external mass transfer limitations ($Sh = \infty$) and conversion dominated by $O_2$ concentration profiles the modified Thiele modulus can be defined as:

$$\phi'_{O_2} = \frac{r_p}{3} \sqrt{\frac{\sum_{j=1}^{N_{reac}} \frac{n_j + 1}{2} k_j c_{O_2,bulk}^{n_j - 1}}{D_{eff,O_2}}} \tag{2.10}$$

Assuming that the hydrocarbon concentrations are relatively high, which is the case for OCM, an overall (lumped) reaction rate constant $k_j$ (in 1/s) can be derived from the reaction kinetics, based on the overall reaction rate of $O_2$:

$$R_{O_2,total} = j_{O_2}\big|_{r=r_p} a_s = \sum_{j=1}^{N_{reac}} k_j c_{O_2,bulk}^{n_j} \tag{2.11}$$

Note that the influence of the concentrations of the hydrocarbons is lumped in the reaction rate constants $k_j$. The extent of internal diffusion limitations and their influence on the catalyst performance was investigated by varying the particle diameter using uniformly distributed OCM activity, thereby varying the modified Thiele modulus. From the intraparticle radial $O_2$ concentration profiles, which are depicted in Fig. 2.4a, it can be concluded that for larger particle diameters the $O_2$ conversion rate becomes completely dominated by intraparticle mass transfer. In general, intraparticle mass transfer limitations and hence low catalyst utilization are considered as disadvantageous because of the additional required reactor and catalyst volume, but Fig. 2.4b shows that intra-particle mass transfer limitations are actually slightly beneficial for the $C_2$ selectivity (=$C_2H_4$+$C_2H_6$ selectivity), provided that $CH_4$ is present in excess and that $C_2$ concentrations are low. At increasing Thiele modulii ($\phi'_{O_2} > 1$), the $C_2$ selectivity calculated with the particle model can be up to 2-3% higher than the maximum achievable bulk gas phase selectivity, depending on the bulk $O_2$ concentration. Because of the low local $O_2$ concentration, the strong concentration gradients caused by the intra-particle mass transfer limitations and the lower reaction order of $O_2$, the selective reactions are preferred leading to increased $C_2$ selectivity (Fig. 2.4a).

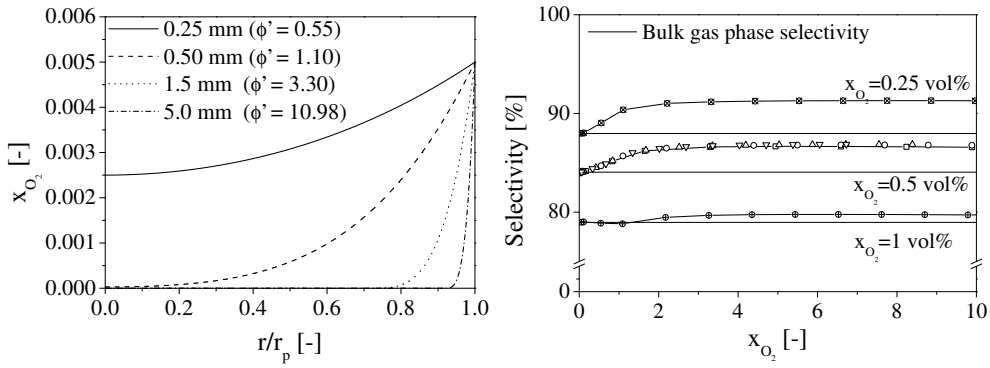


(a) (b)

**Figure 2.4:** Influence of the Thiele modulus on the intraparticle concentration profiles of $O_2$ (a) and on the corresponding $C_2$ selectivity (b) for OCM ($x_{CH_4}$=0.5, $x_{H_2O}$=0.4, $x_{O_2}$=0.005, $\varepsilon/\tau$=0.10, T=800 °C and p=150 kPa).

The numerically calculated effectiveness factor was compared with the well-known solution of the effectiveness factor for a first order irreversible reaction.

$$\eta_{exact} = \frac{3\phi' - tanh(3\phi')}{3(\phi')^2 tanh(3\phi')} \tag{2.12}$$

Results of this comparison are depicted in Fig. 2.5, where it is shown that the catalyst effectiveness factor for oxidative coupling can be very well described by the solution for a first order reaction, confirming results obtained by van Sint Annaland et al. (2007a), who investigated the influence of intra-particle diffusion limitations for a general selective oxidation reaction consisting of 2 reactions.

Because the particle properties, such as the particle porosity and tortuosity, influence the available reactive surface area ($a_s$ and the bulk particle density), the modified Thiele modulus adequately captures the effects of the particle properties and the effectiveness factor is not influenced.

The analytical solution for a first order reaction using the modified Thiele modulus is thus a valuable tool to give initial design conditions for the OCM catalyst. From Fig. 2.5 it can be seen that at $\phi'_{O_2} > 1$ concentration profiles already start to develop in the catalytic particle and with a maximum effectiveness factor for OCM of 30%, corresponding to $\phi'_{O_2} \approx 4$, it can be derived that a particle diameter larger than 2 mm is satisfactory to allow implementation of SRM activity in the particle center in order to eventually obtain autothermal operation and simultaneous production of synthesis gas and ethylene.

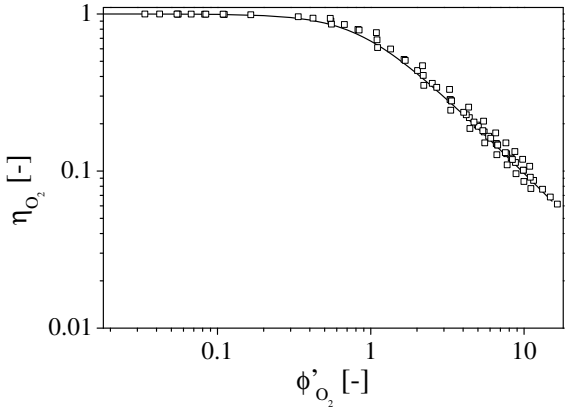


**Figure 2.5:** Effectiveness factor for the consumption of oxygen ($\eta_{O_2}$) as a function of the modified Thiele modulus for $\varepsilon/\tau = 0.05, 0.10, 0.15$ and 0.20 (the solid line indicates analytical solution for a first order reaction using the modified Thiele modulus) at $x_{CH_4}$= 0.5, $x_{H_2O}$=0.4, $x_{O_2}$=0.005, T=800 °C and p=150 kPa.

### 2.3.2 External mass transfer limitations

The presence of external mass and heat transfer limitations can be detrimental for the performance of the dual function catalyst particle, because component surface concentrations and hence the reaction rates may be altered and hence intra-particle concentration profiles may even disappear, so that $O_2$ may reach the SRM core and undesired oxidation reactions in the particle core may deteriorate the selectivity. The diffusion path length for oxidative coupling compared to steam reforming is much smaller, resulting in a higher sensitivity of OCM for external mass and heat transport limitations. In addition, if the transport rate of the reaction products from the particle surface to the gas bulk is restricted, possibly the deep-oxidation of valuable $C_2$ components is enhanced and the $C_2$ selectivity may decrease due to external mass transfer limitations.

Assuming, quite reasonably, that internal heat transfer limitations can be ignored and that the particle can be considered virtually isothermal, mass transfer coefficients for zero net flow in the form of Sherwood numbers ranging from 2 (which can be considered as a limiting case) to 10 were estimated from various empirical correlations (see for an overview Iordanidis (2002)). To account for the drift fluxes, the mass transfer coefficients were corrected via the method of Toor, Stewart and Prober as described in section 2.2.1. In Fig. 2.6 it can be seen that the influence of the external mass transfer limitations on the particle performance cannot be neglected, however,

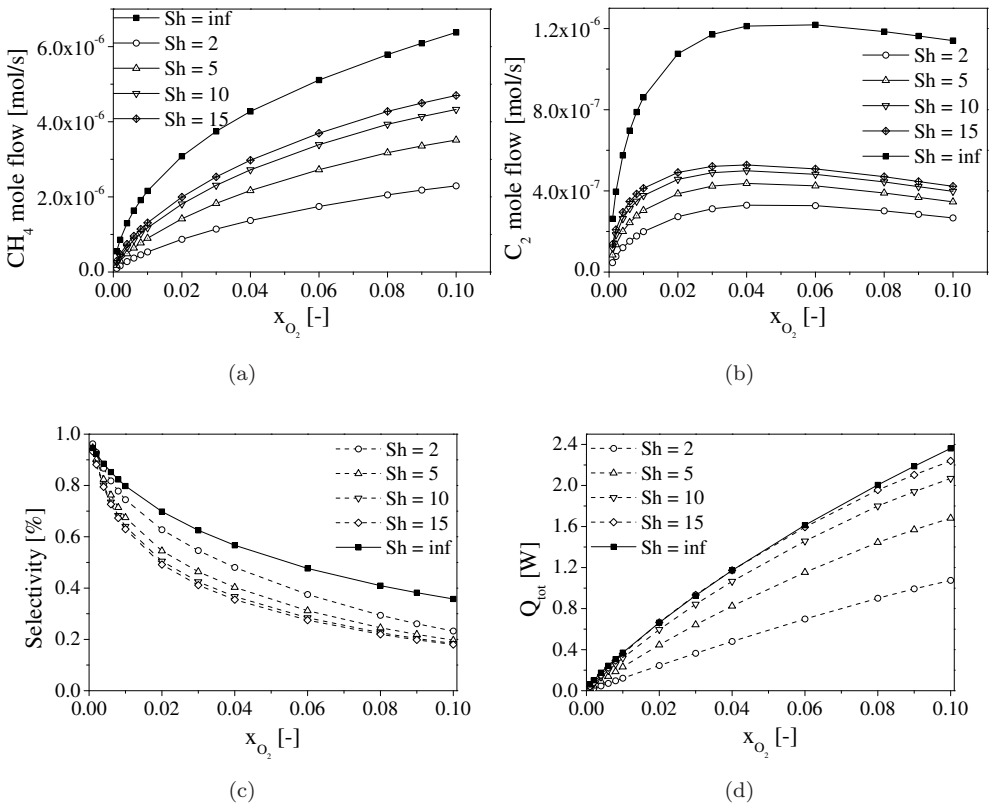


**Figure 2.6:** Influence of external mass transfer limitations at isothermal conditions for different oxygen bulk gas phase concentrations ($x_{CH_4}$ =0.5, $x_{H_2O}$ =0.4, $\varepsilon/\tau$=0.10, $T_{bulk}$=800 °C and p=150 kPa).

even for the selected large particle diameter the overall effect is limited. The total $CH_4$ conversion and the production of $C_2$ products is (obviously) decreased when mass transfer limitations become more pronounced, requiring larger reactor volumes (Fig. 2.6a/b). At $O_2$ concentrations below 1 vol. % and $Sh = 15$, the $C_2$ selectivity is still higher than 60% which is quite an acceptable performance. With increasing external mass transfer resistances, however, it turns out that the $C_2$ selectivity is actually enhanced, which is related to the surface concentrations of the individual components, especially $O_2$ and $C_2$ components. Due to the external mass transfer limitations, the mass transfer coefficients vary for each component, depending on the bulk concentration, the $CH_4/O_2$ ratio at the particle surface increases from about 50 in the bulk gas phase to more than 200 at the catalyst surface, so that the maximum $C_2$ selectivity is achieved at $Sh = 2$ (Fig. 2.6c). In addition to the increased $CH_4/O_2$

ratio, the $C_2$ concentrations at the surface have increased which leads to secondary reactions that influence the $C_2$ fluxes and the selectivity. At higher values of Sh, the surface $O_2$ concentration is higher thus more $C_2H_6$ is converted into $C_2H_4$ which is easily oxidized to CO and $CO_2$. Therefore the $C_2$ selectivity increases if Sh is decreasing. At infinitely high Sh, however, the $C_2$ surface concentration is assumed to be equal to the bulk concentration (which is zero) so that secondary reactions do no influence the (much higher) selectivity. The influence of higher $C_2$ concentrations in the bulk will be examined in section 2.7.3.

From these calculations, it can be concluded that despite influence of external mass transfer limitations, intra-particle concentration profiles still exist inside the catalyst particle, which is vital for the feasibility of the dual function catalyst particle, because $O_2$ should not reach the particle center. Additionally, it is demonstrated that even for the lowest values of Sh and at low $O_2$ concentration, the $C_2$ selectivity is only slightly influenced. The external mass transfer limitations may even enhance the $C_2$ selectivity.

### 2.3.3 Operating conditions

At a bulk gas phase concentration of 50% $CH_4$, 40% $H_2O$ and balance $N_2$ and isothermal reactor inlet conditions, the influence of the oxygen bulk gas phase concentration (the most important operating parameter for OCM) on the intra-particle concentration profiles was investigated. It was already demonstrated in the previous section that at an $O_2$ bulk concentration of 0.5 vol% the use of a low effective diffusion coefficient combined with high catalyst activity result in strong intra-particle concentration profiles.

In Fig. 2.7a/b it is shown that very similar results are obtained for a wide range of bulk gas phase $O_2$ concentrations. This may also be expected from the definition of the modified Thiele modulus for a first order reaction, which is independent of the $O_2$ concentration, meaning that the particle utilization ($\eta_{O_2}$) will not change. Because here the reaction rate constant is calculated from the complex reaction kinetics there is a small dependency of the Thiele modulus on the bulk gas phase $O_2$ concentration, so that the catalyst effectiveness factor is somewhat influenced and the penetration depth of $O_2$ increases slightly for higher bulk concentrations. Because the $O_2$ reaction order of the coupling reaction is lower than the unselective oxidation reactions, the $C_2$ flux is dominating the production of carbon oxides at $O_2$ concentrations lower than 2 vol%, leading to a $C_2$ selectivity as high as 95% (Fig. 2.7c). On the other hand, the $CO_2$ selectivity rises proportionally with the $O_2$ concentration but the CO selectivity increases less pronounced because of the low oxygen reaction order of

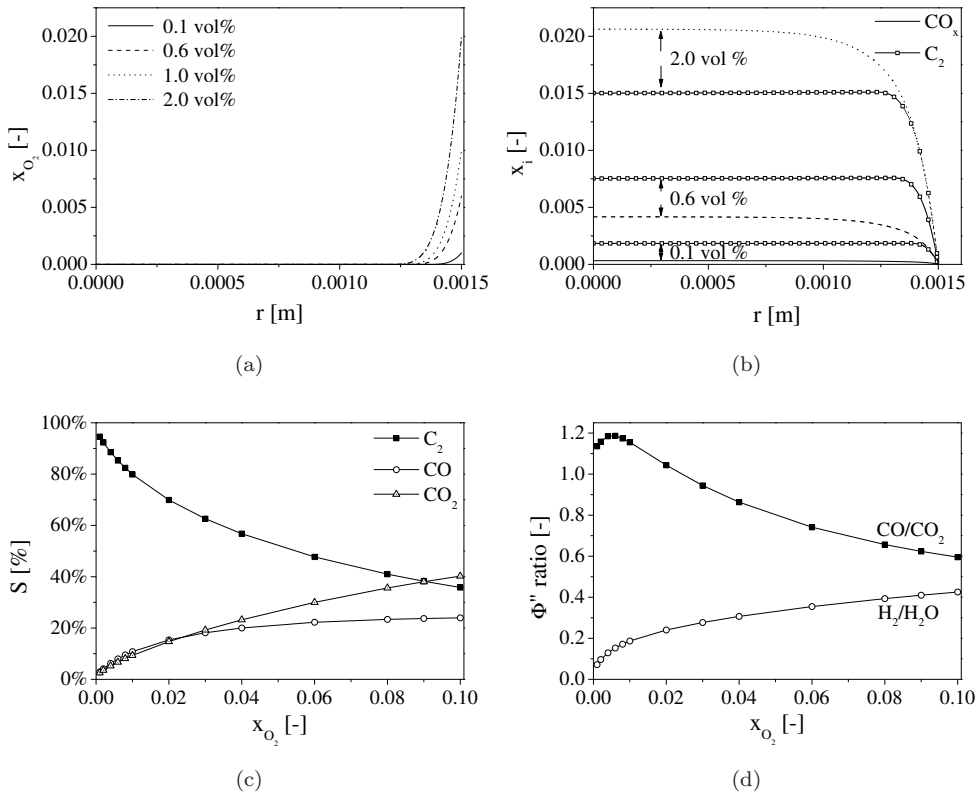


**Figure 2.7:** Influence of bulk gas phase $O_2$ concentration on (a) radial $O_2$ concentration profile, (b) radial $CO_x$ and hydrocarbon concentration profiles, (c) $C_2$ selectivity and (d) CO:$CO_2$ and $H_2$:$H_2O$ mole fraction ratios ($\varepsilon/\tau = 0.1$, T=800°C and p=150 kPa).

0.55 for the CO oxidation. At sufficiently low $O_2$ concentrations the selectivity to CO production will therefore increase relatively, which is reflected in the $CO/CO_2$ product ratio (Fig. 2.7d), which becomes larger than unity at $O_2$ concentrations lower than 1 vol%. Hence, if carbon monoxide is a preferred reaction product next to ethylene, the process should be operated at low $O_2$ concentrations. However, the production of $H_2$ is rather low at these conditions (Fig. 2.7d), in contrast to the CO production. Because the main sources of $H_2$ during OCM are thermal dehydrogenation of $C_2H_6$ and the water gas shift reaction, more $H_2O$ is produced compared to $H_2$ when the $O_2$ concentration is smaller than 1 vol%. Thus, to enable the combined production of synthesis gas and ethylene, a secondary process such as steam reforming is required.

### 2.3.4 Temperature effects

Because the particle effectiveness factor is small and a low $O_2$ concentration is used for OCM, excessive temperature increases will not occur at non-isothermal conditions. In Fig. 2.8a, the intra-particle temperature profiles illustrate that for an $O_2$ bulk gas

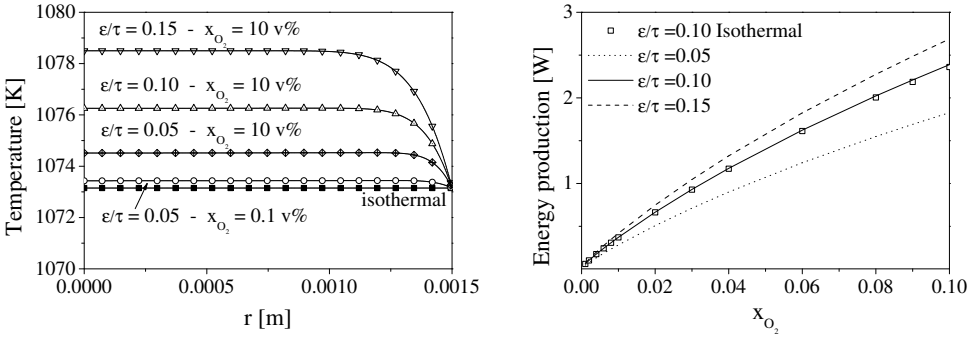


(a) (b)

**Figure 2.8:** Intra-particle temperature profiles (a) and overall reaction enthalpies (b) for different particle porosity over tortuosity ratios at T=800 °C and p=150 kPa.

phase concentration of 10 vol% the total temperature increase in a particle of 3 mm diameter does not exceed 10°C. The $C_2$ selectivity of OCM thus remains relatively uninfluenced by the heat of reaction, leading to similar results as displayed in Fig. 2.7c. Because most reactions take place near the catalytic surface the reaction heat is quickly removed to the bulk gas phase. Since most materials have a relatively high thermal conductivity between 5-20 W/m/K, the average temperature rise for other catalyst support materials than CaO ($\lambda_{eff,s} \approx 7 - 8$ W/m/K) will not differ significantly. Despite the fact that the temperature increase is negligible on the particle scale, the total heat production on the particle scale amounts approximately 0.4 W at an $O_2$ concentration of 1 vol% (Fig. 2.8b), which corresponds to a heat load of approximately 1.7 $MW_{th}/m^3_{reactor}$. Hence, efficient cooling of the reactor is very crucial to prevent excessive temperatures and unselective reaction products.

The influence of the external heat transfer limitations on the intraparticle concentration profiles is expected to be small when the local $O_2$ concentration and therewith the heat production per $m^3$ reactor are low. From the *Biot* number for heat transport ($Bi_h$) it can be derived that for the limiting case of Nu=2, $Bi_h$ will be roughly equal to 0.02 (based on $\lambda_p/\lambda_g = 10$). Analytical criteria suggest that for values of $Bi_h$ lower than 10, external heat transfer limitations are likely dominate intra-particle

heat transfer limitations. From the criterion originally derived by Anderson (1963), it can be inferred that significant temperature gradients in the particle will not develop because of the relatively low reaction rates (Mears, 1971a, 1973).

$$\frac{|\Delta H_r|\, R_{tot} r_p^2}{\lambda_p T_{bulk}} < 0.75 \frac{R T_{bulk}}{E_a} \tag{2.13}$$

A similar expression can be applied to evaluate the influence of external heat transfer limitations (Mears, 1971a, 1973).

$$\frac{|\Delta H_r|\, R_{tot} r_p^2}{\alpha^{\bullet}_{g \rightarrow s} T_{bulk}} < 0.15 \frac{R T_{bulk}}{E_a} \tag{2.14}$$

Evaluation of this analytical criterion based on an average reaction enthalpy of 300 kJ/mol supported by additional numerical simulations, showed that the presence of external heat transfer limitations will not significantly influence the performance of OCM at low $O_2$ concentrations and investigation of only mass transfer limitations is a safe assumption.

## 2.4 Only steam reforming of methane

If the OCM catalyst activity is sufficiently high ($\phi'_{O_2} > 2$), a SRM catalytic activity can be implemented in the core of the particle without the risk of $O_2$ reaching SRM catalytically active sites. Consequently, the production of $C_2H_4$ and synthesis gas can be tuned by modification of the SRM reaction rates either via the effective diffusion coefficients in the inert layer and/or the SRM core diameter. For accurate control over the reaction rates, it is preferred that the steam reforming reactions, occurring in the particle center, are totally governed by molecular diffusion. With conventional very active steam reforming catalysts, such as $Ni/Al_2O_3$ or $Pt/Al_2O_3$ this is typically the case. To verify the presence of diffusion limitations for steam reforming, different catalytic activity levels were applied by multiplying the reaction rates calculated with the kinetic model by Xu and Froment (1989) with a factor ranging from 0.01-10. The initially high bulk $H_2O$ concentration of 40% is required to obtain a high intra-particle $CH_4$ conversion and to prevent the deposition of carbonaceaous species; at lower bulk $CH_4$ concentrations (i.e. higher overall conversion) $H_2O$ still needs to be present in excess but the concentration can be lower than 40%. Indeed it is shown in Fig. 2.9a for $\varepsilon/\tau = 0.1$ and a catalytic activity parameter of 100% and higher, that the $CH_4$ concentration profiles are independent of the kinetic reaction rates and $CH_4$ conversion is completely limited by internal mass transfer limitations. The high reaction temperature (800°C) drives the thermodynamic equilibrium of steam

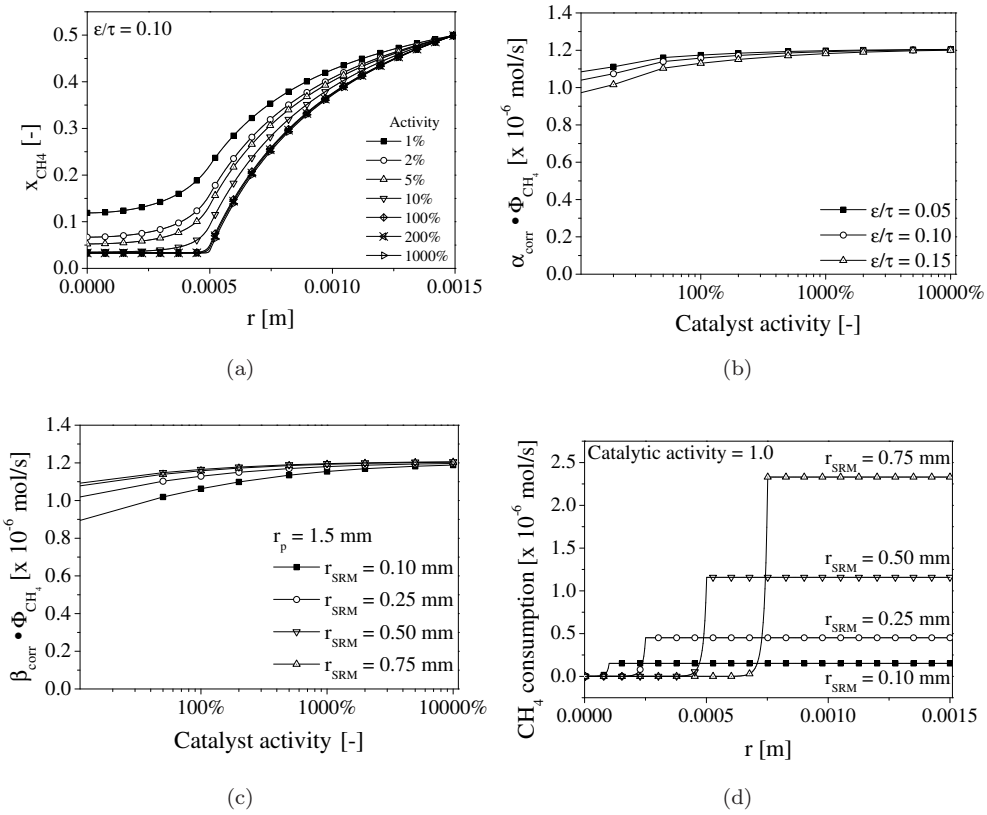


**Figure 2.9:** Influence of SRM catalytic activity on intraparticle $CH_4$ concentration profiles (a), corrected $CH_4$ flows for varying $\varepsilon/\tau$ (b) and influence of SRM catalytic core diameter on $CH_4$ flow (c) and corrected methane flow (d).

reforming towards nearly complete $CH_4$ conversion, maximizing the synthesis gas production. Because the effective diffusion coefficients will be utilized to control the reaction rates, it was also verified that the SRM reactions are controlled by diffusion by varying $\varepsilon/\tau$. If the $CH_4$ conversion is limited by internal mass transfer, the (scaled) $CH_4$ mole flow $\Phi_{CH_4}$ at the particle boundary, representing the overall $CH_4$ reaction rate, should be proportional to $\varepsilon/\tau$:

$$\alpha_{corr} = \frac{\varepsilon/\tau_{act}}{\varepsilon/\tau_{ref}} \tag{2.15}$$

Comparing the results from Fig. 2.9a and b, it can be inferred that for a catalytic activity factor of 100% or larger, the intraparticle $CH_4$ concentration profiles are constant, indicating the reaction rates are sufficiently high compared to the effective

diffusion rate. Calculation of the corrected $CH_4$ mole flow with the above equation confirms that for various $\varepsilon/\tau$ (Fig. 2.9b), 100% catalyst activity already results in approximately constant $CH_4$ consumption rates which are directly proportional to $\varepsilon/\tau$. Especially with somewhat larger $\varepsilon/\tau$, the totally diffusion limited regime can only be achieved with higher catalyst activity.

Alternatively to variation of the effective diffusion parameters, the core diameter of the steam reforming activity can be adjusted to modify the extent of reforming reactions. Still, the system utilizes mass transfer limitations, although this method might be an attractive alternative because the core diameter could be better controllable than $\varepsilon/\tau$. The mole flux in the diffusion controlled regime at the external particle surface can then be approximated with:

$$J_{\mathrm{CH_4}} = \frac{D_{eff} r_{SRM}}{r_p(r_p - r_{SRM})} \left(c_{\mathrm{CH_4},i} - c_{\mathrm{CH_4},SRM}\right) \tag{2.16}$$

and the calculated flux compared to a reference case is given by:

$$\beta_{corr} = \frac{r_{SRM}}{r_{SRM,ref}} \frac{(r_p - r_{SRM,ref})}{(r_p - r_{SRM})} \tag{2.17}$$

Similar to the case with variation of $\varepsilon/\tau$, variation of the SRM activity diameter results in a $CH_4$ flow changes proportional to the parameter $\beta_{corr}$ in Equation 2.17 and the SRM catalyst core diameter (Fig. 2.9c). For a larger core diameter (i.e. smaller $r_p - r_{SRM}$, larger $CH_4$ concentration gradients prevail, so that higher $CH_4$ flows can be achieved, which is shown in Fig. 2.9d where the $CH_4$ consumption rate is displayed as a function of the radial position for different SRM core diameters.

Using the catalytic activity equal to or higher than the catalyst used by Xu and Froment, the conversion rates on the SRM catalyst are totally limited by mass transfer which means that synthesis gas and energy consumption can be effectively tuned to obtain autothermal operation and increase the overall $CH_4$ conversion in a particle in the combined process.

## 2.5 Dual function catalyst particle

Based on the performed simulations, an initial design for the dual-function OCM and SRM catalyst particle can be made. If the total OCM reaction rate and hence the total heat production rate is known, the core radius $r_{SRM}$ required for autothermal operation can be calculated analytically, with the assumption of total conversion of $CH_4$ in the particle center (i.e. $C_{CH_4,core}$=0). The required reforming reaction rate is then based on the overall energy balance:

$$J_{SRM,required} 4\pi r_p^2 \equiv \frac{1}{\Delta H_{SRM}} \sum_{j=1}^{N_{reac}} \int^{V_p} R_j(-\Delta H_{OCM,j}) dV_p \tag{2.18}$$

At large excess of $CH_4$ and low $O_2$ concentrations, the influence of the OCM reaction rates on the local $CH_4$ concentration profile is negligible, so that the interface concentration $C_{CH_4,i}$ can be replaced by the $CH_4$ bulk gas phase concentration to estimate the required core radius. Rewriting Equation 2.16 for $r_{SRM}$ then yields:

$$r_{SRM} = r_p \frac{Y}{1+Y} \quad \text{with} \quad Y = \frac{\sum_{j=1}^{N_{reac}} \int_0^{V_p} R_j(-\Delta H_{OCM,j}) dV_p}{\Delta H_{SRM} D_{eff} 4\pi r_p (C_{CH_4,bulk} - C_{CH_4,core})} \tag{2.19}$$

Fig. 2.10 illustrates the influence of the $O_2$ consumption rate, represented by a modified Thiele modulus ($\phi'_{O_2}$), on the required SRM core radius for autothermal operation at several $CH_4$ bulk concentrations assuming isothermal conditions. It is shown that as the OCM heat production rate increases, a higher steam reforming reaction rate and thus a larger core radius is required to achieve autothermal conditions. Obviously, the calculated core radius is dependent on the bulk gas phase $CH_4$ concentration, because of the change in driving force for $CH_4$ transport. The strong dependency on the $CH_4$ concentration indicates that $r_{SRM}$ should therefore change along the reactor length. However, the use of different particle configurations in a single reactor compartment is complicated, so that in practice an average $r_{SRM}$ will be applied to achieve approximate overall autothermal operation, where small axial temperature gradient is accepted.

The influence of changing the effective diffusion coefficients via modification of the particle properties, specifically the ratio of the porosity over tortuosity, is demonstrated in Fig. 2.10 only for the case with a bulk $CH_4$ concentration of 50 vol%. Contrary to the results obtained with varying bulk $CH_4$ concentration, the effective diffusion parameter $\varepsilon/\tau$ does not influence the required reforming core diameter, which is related to the fact that both (diffusion limited ) OCM and SRM are influenced to the same extent because $\varepsilon/\tau$ was varied for the entire particle uniformly.

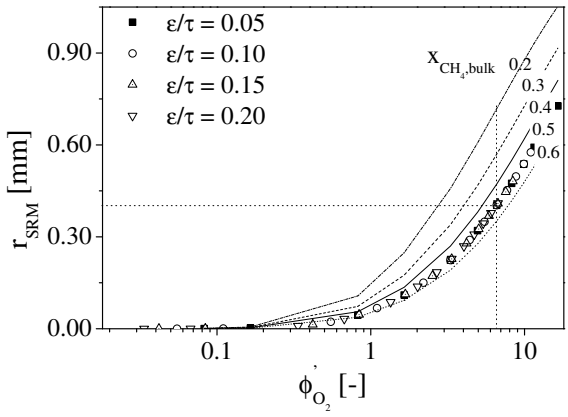


**Figure 2.10:** Required core radius for SRM activity for different $CH_4$ bulk gas phase concentrations and $\varepsilon/\tau$ ratios as a function of the the modified Thiele modulus for oxygen consumption $\phi'_{O_2}$ at isothermal conditions (T=800 °C, $r_p$=1.5 mm).

Thus, the results demonstrate that with relatively simple calculations the layout for the dual function OCM/SRM particle can be established. For a standard particle diameter of 3 mm and a modified Thiele modulus of approximately 6.6 (which is the case at reactor inlet conditions), it can be discerned that the required $r_{SRM}$ approximately amounts to 0.4 mm ($r_{SRM}/r_p \approx 0.27$). Although a default particle diameter of 3 mm was used here, it can easily be verified that these criteria can be derived analogously for different particle diameters and bulk concentrations. More detailed numerical simulations should, however, give insight in the exact influence of concentration and temperature profiles, additional reactions and the loss of $C_2$ components because of reforming reactions, which are investigated in detail in the next sections.

### 2.5.1 Proof of principle

The performance of the dual-function catalyst particle especially focusing on the extent of $C_2$ reforming reaction rates and syngas production is investigated at various bulk gas phase concentrations. To account for inaccuracies in the approximation of $r_{SRM}$, a value of 0.5 mm has been selected for further calculations. In this section, only the influence of the steam reforming reaction rates on the concentration profiles is evaluated, the heat effects of the endothermic SRM reactions on the performance will be discussed in a separate section.

Compared to a catalyst with only activity for the oxidative coupling of methane, the dual function catalyst particle with a core with SRM activity has significantly different concentration profiles for all components (Fig. 2.11(a)). The concentration of $CH_4$

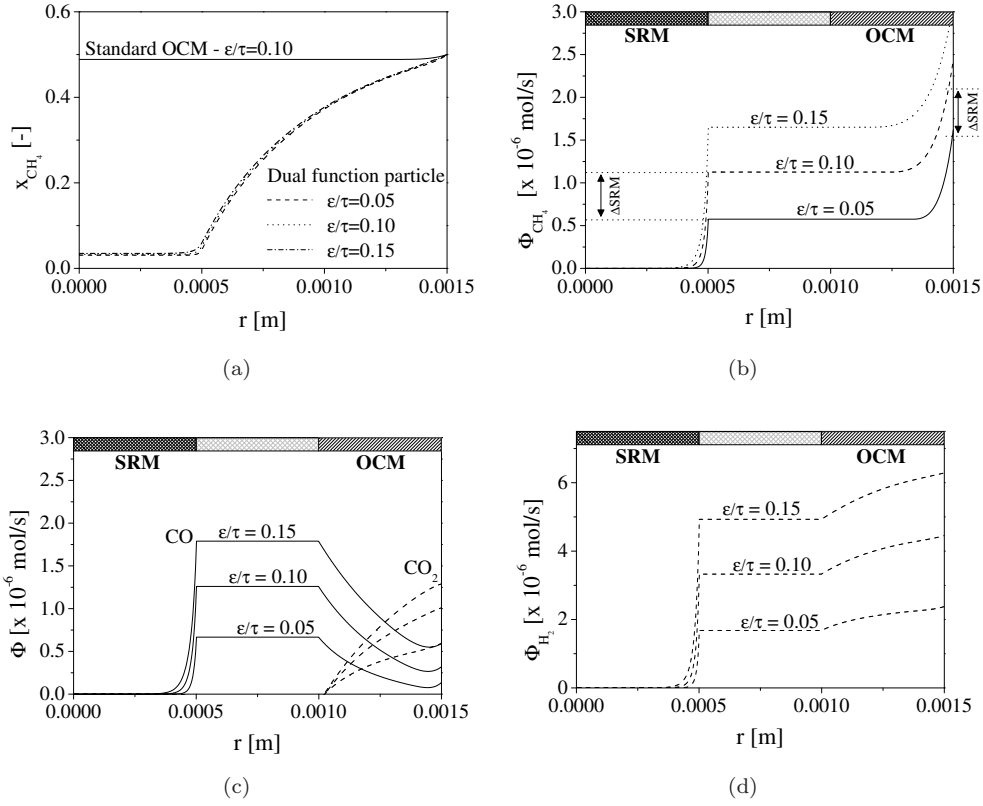


**Figure 2.11:** Intraparticle concentration profiles in combined OCM/SRM particle for different $\varepsilon/\tau$ for $CH_4$ (a) and $CH_4$ (b) CO and $CO_2$ (c) and $H_2$ (d) mole flow profiles ($x_{CH_4}$=0.5, $x_{O_2}$=0.005, $x_{H_2O}$=0.4, $r_P$=1.5 mm, $r_{SRM}$=0.5 mm, $r_{OCM}$=0.5 mm).

in the center of the dual function catalyst particle has dropped to almost zero, thus leading to a significantly enhanced $CH_4$ conversion rate and hence increased synthesis gas production. The calculations were performed for different $\varepsilon/\tau$, demonstrating that the reforming process operates in the diffusion limited regime. This can be discerned from the $CH_4$ concentration profiles, but becomes even more apparent from the $CH_4$ mole flow profiles displayed in Fig. 2.11(b), which increases proportionally with increasing $\varepsilon/\tau$.

From the displayed intraparticle $CH_4$ mole flow profiles it can also be concluded that approximately 50% of $CH_4$ is converted via steam reforming to synthesis gas and that compared to conventional OCM the conversion is indeed largely increased. Provided that sufficient steam is available, significant quantities of synthesis gas are produced

via steam reforming (Fig. 2.11(c) & 2.11(d)). The CO and $H_2$ mole flows increase in the particle center to a $H_2$/CO ratio of approximately 2.5, which would be suitable for further downstream processing via e.g. Fischer Tropsch synthesis. However, when the reaction products from the SRM activity diffuse through the OCM catalyst layer at high bulk gas phase $H_2O$ concentrations, the CO is partially converted into $CO_2$ via the water-gas-shift reaction. Although the $H_2$/CO ratio is further increased in this way, the undesired and unselective reaction product $CO_2$ is formed leading to lower carbon efficiency. The $CO_2$ production can be further decreased because the OCM catalytic layer ($r_{OCM} = 0.5$ mm) is not fully utilized for oxidative coupling (a safety margin is built in to ensure total $O_2$ conversion). If the OCM catalytic layer would be reduced to e.g. 0.25 mm the water-gas-shift reaction can already be significantly reduced. The partial conversion to $CO_2$ can be further circumvented by lowering the steam concentration, however this will also affect the degree of autothermal operation (i.e. steam reforming reactions) and the possible formation of carbonaceous species in the catalyst particle.

### 2.5.2 Hydrocarbon production and reforming

The results with the dual-function catalyst particle clearly demonstrate the theoretical feasibility of the combination of oxidative coupling and steam reforming of methane. To investigate the influence of the operating conditions on the losses of higher hydrocarbons due to reforming reactions, the intra-particle concentration profiles of $C_2H_4$ and $C_2H_6$ were evaluated at different bulk gas phase compositions. First, simulations were performed representing reactor inlet conditions, where the $C_2$ product concentration is virtually zero and the reactant concentration is maximal, corresponding to the most optimal conditions for a combined process for OCM and SRM.

It can be seen from the intraparticle concentration profiles of the higher hydrocarbons shown in Fig. 2.12a that the $C_2$ concentration is practically zero in the particle core because of the fast reforming reactions, consuming all valuable hydrocarbons in the particle center. Although this looks detrimental for the process performance, from the small $C_2$ flow to the particle center (Fig. 2.12b) it can be discerned that losses of $C_2H_4$ and $C_2H_6$ are very small because of the relatively small concentration gradients. The net production of $C_2$ products is for this case approximately 0.6 $\mu$mol/s, while the losses are 0.01 $\mu$mol/s. Even at higher $\varepsilon/\tau$ total losses of $C_2$ do not exceed 3%, therefore it can be concluded that because of the much larger concentration gradient and the shorter diffusion path length, the driving force for $C_2$ transport to the bulk gas phase is much higher, and therefore the influence of SRM activity on the $C_2$ production can be neglected at reactor inlet conditions.

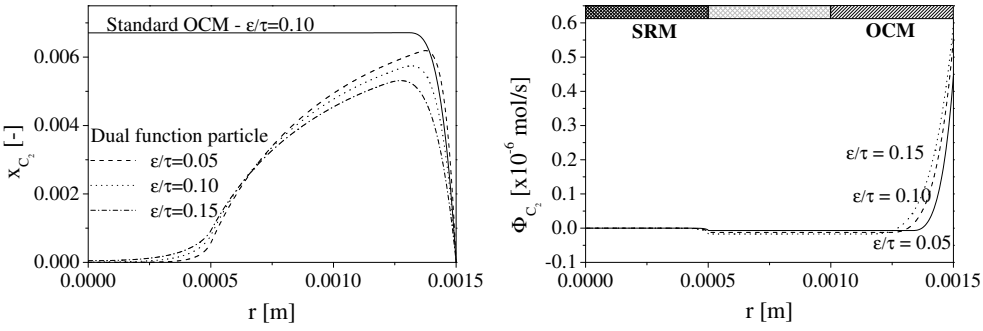


(a) (b)

**Figure 2.12:** Influence of steam reforming reactions and intra-particle diffusion limitations on (a) $C_2H_4$ and $C_2H_6$ concentration profiles and (b) mole flux profiles (T=800 °C, p=150 kPa, $x_{CH_4}$=0.5, $x_{O_2}$=0.005, $x_{H_2O}$=0.4, $r_{SRM}$=0.5 mm, $r_{OCM}$=0.25 mm, $r_P$=1.5 mm).

At higher $CH_4$ conversion however, i.e. further along the axial reactor coordinate, the losses will increase because of the decreasing $CH_4$ and increasing $C_2$ concentrations, promoting secondary oxidation reactions (e.g. $C_2H_4$ oxidation) and additional reforming reactions. To qualitatively determine the influence of the $CH_4$ conversion, the $C_2$ concentration was varied between 0 - 5 vol% for both OCM and the OCM/SRM particle at 3 different $CH_4$ bulk concentration levels (representing higher conversion levels).

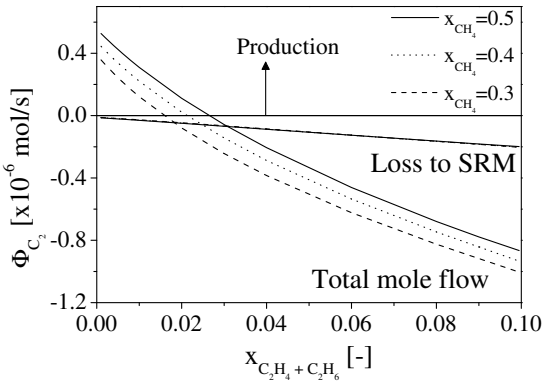


**Figure 2.13:** Total $C_2H_4$ and $C_2H_6$ mole flow at the particle surface and the losses to SRM reactions as a function of the $C_2$ bulk mole fraction ($x_{H_2O}$ =0.4, $x_{O_2}$ =0.005, $x_{C_2H_4}$=$x_{C_2H_6}$, $r_{SRM}$=0.5 mm, $\varepsilon/\tau = 0.1$).

At lower $CH_4$ bulk concentrations (i.e. higher conversion) and already at relatively low $C_2$ bulk concentrations, the influence of reforming on the $C_2$ losses starts to increase, because of the lower formation rate of higher hydrocarbons and the increased losses via the secondary oxidation reactions (decreased transfer rate of $C_2$ toward the particle surface). Compared to a bulk $C_2$ concentration of zero, the total $C_2H_4$ and $C_2H_6$ production (Fig. 2.13) diminishes and even starts to be consumed at $C_2$ concentrations higher than 2.5 vol%. Interestingly, at high $C_2$ concentrations the contribution of the SRM catalyst to the losses of $C_2H_4$ and $C_2H_6$ is quite small; as expected the total reaction rate of $C_2$ components is only (linearly) dependent on the driving force between the particle center and the OCM catalytic layer, which only marginally increases at higher bulk $C_2$ concentrations. At excess steam concentration, the contribution of the SRM catalyst to the total loss of $C_2$ components is independent of the $CH_4$ concentration and is limited to a maximum of approximately 5% (Fig. 2.13). Concluding, the losses of $C_2$ are not caused by the incorporation of SRM activity in the core of the dual function catalyst. The influence of secondary oxidation reactions is much larger, because these reactions occur near the catalyst surface. Therefore, at $C_2$ bulk mole fractions of about 0.04 and larger, most $C_2$ products are already converted via secondary oxidation reactions in the OCM catalytic layer, thereby decreasing the concentration in the particle and strongly lowering the driving force to the SRM catalyst compared to the bulk concentration. The $C_2$ losses are largely determined by the $C_2$ bulk concentration, the availability of $O_2$ and the extent of secondary oxidation reactions, which is a common feature seen in all processes involving oxidative coupling, and can only be reduced by optimization of the catalyst or by decreasing the $O_2$ concentration along the reactor length by applying distributed feeding of $O_2$ e.g. in a membrane reactor. This will be investigated in Chapter 3.

## 2.6 Autothermal operation

The dual-function catalyst particle produces $C_2H_4$ and $C_2H_6$ via OCM and simultaneously increases the $CH_4$ conversion yielding the value-added product synthesis gas. Next to the increased synthesis gas production, an important goal is create an autothermal process. Therefore, the heat effects of the exo- and endothermic reactions in the combined OCM/SRM catalyst particle were investigated at various conditions such that energy integration is optimized.

The optimization of the dual function process first requires a relatively low heat production of OCM, which is preferably generated uniformly along the reactor length so that a uniform particle configuration can be used. When $O_2$ and $CH_4$ are fed in premixed flow, the heat production per particle (2.5 W at 10 vol% $O_2$ ) is far too high to be balanced with heat consumption by steam reforming in the dual function process. By applying distributed feed of $O_2$, however, the local heat production rate can be significantly decreased and the reaction rates are sufficiently low to allow integration of SRM in the particle core. Fig. 2.14 (closed symbols) illustrates that indeed the intra-particle temperature profiles for OCM are smaller and total heat production is lowered if distributed feed of $O_2$ is used. For bulk gas phase $O_2$ concentrations ranging from 0.1-0.5 vol%, the maximum total heat production does not exceed 0.5 W and it further decreases when intra-particle mass transfer limitations become more pronounced (lower $\varepsilon/\tau$, Fig. 2.14a). However, the adiabatic temperature rise in the reactor is still more than 200 °C, requiring more efficient methods to remove and utilize excess reaction heat.

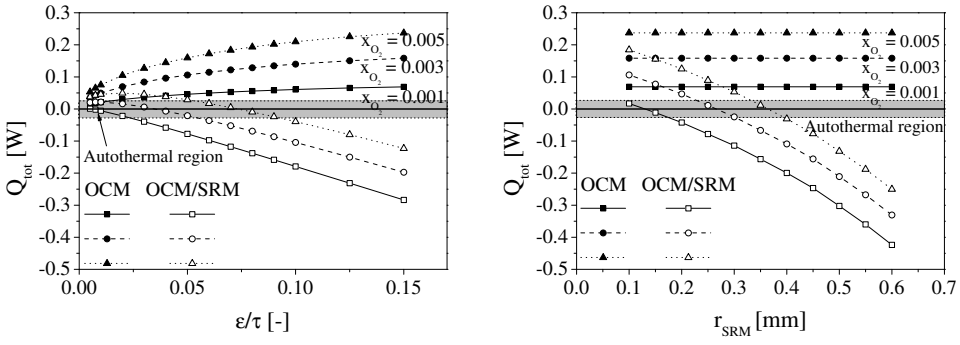


(a) (b)

**Figure 2.14:** Total reaction heat for a single OCM and OCM/SRM (dual function) particle for various (a) $\varepsilon/\tau$ ($r_{SRM} = 0.5$ mm) and (b) $r_{SRM}$ ($\varepsilon/\tau = 0.15$) at $x_{CH_4}$=0.5, $x_{H_2O}$=0.4, T=800°C, $r_p$=3.0 mm.

Autothermal operation is possible at low $O_2$ concentrations, by utilizing the mass-transfer limited steam reforming reactions and tune the overall energy balance. The energy production in a particle is calculated by integrating the overall reaction heat over the particle volume:

$$Q_{tot} = \sum_{j=1}^{N_{reac}} \Delta H_{r,j} \int_{r=0}^{r_p} R_{j,local} 4\pi r^2 dr \quad [\mathrm{W}] \tag{2.20}$$

At steady state and autothermal operation, the overall reaction heat is zero and by definition the energy flux at the particle boundary (i.e. the net heat production inside the particle) is zero and thus $\lambda \frac{\partial T}{\partial r}\big|_{r=r_p} = 0$. In principle a condition for autothermal operation ($Q_{tot} = 0$) can be found for all $O_2$ bulk gas phase concentrations investigated. The following parameters to tune the system to autothermal operation via their influence on the intra-particle mass diffusion were investigated:

- Effective diffusivity / reforming core diameter
- Particle diameter
- Steam concentration

### 2.6.1 Effective diffusivity / reforming core diameter

To demonstrate the principle, the reaction rates (and heats) are first tuned via the intra-particle mass transfer limitations, which can be adjusted via modification of $\varepsilon/\tau$ or $r_{SRM}$. The conditions for autothermal operation can be determined from Fig. 2.14, where the total reaction heat produced in the dual-function particle (open symbols) is compared with the heat produced in the particle with only OCM (closed symbols). It can be discerned that the heat production is strongly influenced by the added catalytic SRM function and that a considerable part of the exothermic reaction heat is consumed via steam reforming. Depending on the $O_2$ bulk concentration, the catalyst particle can operate practically autothermally with $\varepsilon/\tau$ varying from 0.01 to 0.08 for the selected SRM core and particle diameter.

The extremely low values required for $\varepsilon/\tau$ seems to be somewhat impractical because preparation of such a particle will become increasingly difficult. Therefore, the SRM core diameter can be changed alternatively, resulting in more feasible conditions for autothermal operation. For example, selecting $\varepsilon/\tau = 0.15$, then for 0.1 vol% $O_2$ in the bulk gas phase a core diameter of approximately 0.15 mm is required to obtain autothermal conditions (see Fig. 2.14b), which can be realised easily by standard catalyst preparation methods (in contrary to realization of $\varepsilon/\tau < 0.05$).

It can be seen that the total reaction heat $Q_{tot}$ is a non-linear function of $\varepsilon/\tau$ and $r_{SRM}$ for the dual function process. In Fig. 2.14a, where $\varepsilon/\tau$ is used to tune the SRM reaction rates to the OCM reaction rates, the non-linearity in the heat production of OCM is related to the penetration depth of $O_2$, changing the $C_2$ selectivity and the produced reaction heat. This non-linearity leads to a maximum in reaction heat for the dual function process, which is most visible at higher $O_2$ concentrations ($> 0.5$ vol%). If the SRM core diameter is varied instead of effective diffusivity, non-linearity in overall reaction heat produced is also expected because of the non-linear dependence of the fluxes to the SRM catalyst (according to Equation 2.17, Fig. 2.14b). The simulation results, however, demonstrate that autothermal operation is in principle feasible, the sensitivity of the particle performance for changes in operating conditions (especially bulk concentrations) will eventually be decisive how the dual-function particle should be applied at reactor scale, which will be studied in detail in the next chapter.

### 2.6.2 Particle diameter

In Figure 2.15, where the energy production is shown in particles of different diameters, where the SRM core diameter was used to tune to autothermal operation (fixing $\varepsilon/\tau$ to 0.15). For each applied particle diameter, the total oxygen flux is comparable, which means that the performance of OCM is virtually the same for all these cases. Although there are some differences resulting in a small improvement of the total $C_2$ selectivity for larger particle diameters, it can be inferred that the total heat production by OCM reactions only in the particle increases proportionally with the external surface area resulting in a 4 times higher heat production when the diameter increases from 5 to 10 mm.

When the dual function catalyst particle is used, and the particle diameter is again increased, it can be discerned that for all investigated particle diameters autothermal operation is possible (Fig. 2.15a) with feasible dimensions of the SRM core diameter. Remarkably, the required $r_{SRM}$ increases with only a factor 3 instead of 4, because of the interference of OCM and SRM processes ($r_p$=2.5 mm, $r_{SRM}$=1 mm vs. $r_p$=5 mm, $r_{SRM}$=3 mm). As a result of e.g. reforming of $C_2H_4$ and $C_2H_6$ (endothermic) and shift reactions (exothermic) the total heat production is influenced, thereby changing the required SRM diameter (Fig. 2.15a). The main components produced are $CO_x$ and $C_2$ in a ratio varying from 2.5 - 3.0 at autothermal conditions (Fig. 2.15b). From the $CO/CO_2$ product ratio it can however be concluded that a large part (nearly 50 %) of the CO produced on the SRM catalyst is shifted to $CO_2$. As already indicated earlier, the amount of CO which is converted to $CO_2$ via the water-gas-shift

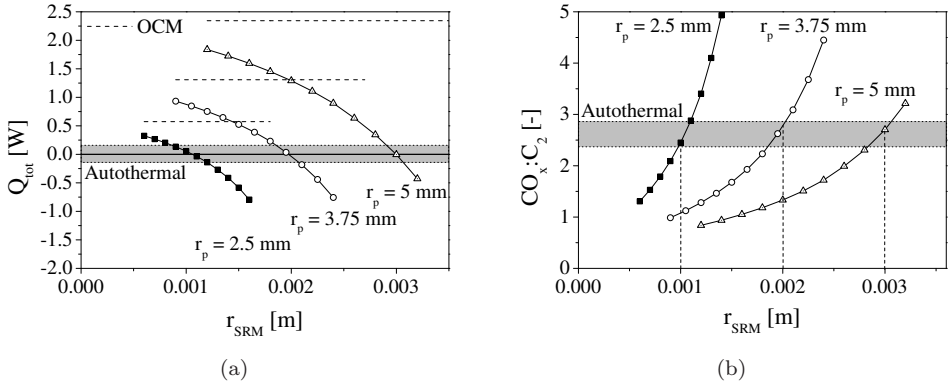


(a) (b)

**Figure 2.15:** Influence of the SRM core radius on (a) the nett energy production and (b) the $CO_x$ /$C_2$ product ratio for different particle diameters (T=800 °C, p=150 kPa, $x_{CH_4}$=0.3, $x_{H_2O}$=0.5, $x_{O_2}$=0.005, $\varepsilon/\tau$=0.15).

reactions could be minimized by modification of the OCM catalyst, or alternatively by optimization of the total OCM catalyst volume (i.e. by modification of $r_{OCM}$).

### 2.6.3 Steam concentration

The $H_2O$ concentration can be used to (fine-)tune the SRM reaction rates, which can overcome the necessity for changing $\varepsilon/\tau$ or $r_{SRM}$ along the reactor length and hence enables the application of a single (or only a few different) particle configuration(s). Because the oxidative coupling is relatively insensitive to the $H_2O$ concentration, increase of the $H_2O$ concentration will result in an increase of the energy consumption by reforming. Hence, the required bulk gas phase $H_2O$ concentration to obtain autothermal operation ($Q_{tot}$=0) was calculated for a bulk gas phase $O_2$ concentration ranging from 0.1-0.5 vol%, and for different effective diffusion coefficients ($\varepsilon/\tau$=0.05-0.15). It can be seen in Fig. 2.16a, that the bulk $O_2$ concentration determines the extent of exothermic reactions and hence the required $H_2O$ concentration varies from 5 to 40 vol% to balance the OCM reaction heat. Because the required bulk $H_2O$ concentration to obtain autothermal operation depends on the intra-particle mass transfer limitation, variation of $\varepsilon/\tau$ results in different 'iso-lines' for autothermal operation. Although a $CH_4$ concentration of 50 vol% is relatively high, autothermal operation is possible within a wide range of concentrations. At a lower bulk $CH_4$ concentration, similar results were obtained (Fig. 2.16b), except that because of the decreased $CH_4$ partial pressure the OCM reaction rates are lower and hence less heat is produced. Remarkably, from the slope of the 'iso-lines' it can be seen that when

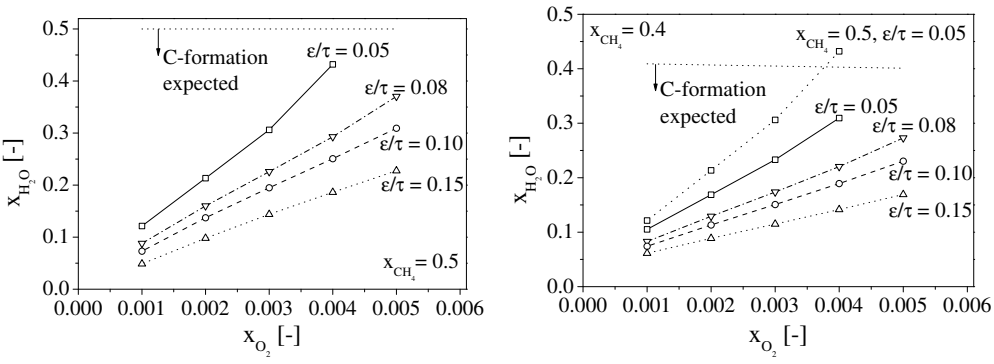


**Figure 2.16:** Required bulk $H_2O$ concentration to obtain autothermal operation with the dual function catalyst particle for various $\varepsilon/\tau$ at (a) $x_{CH_4}$ =0.5 and (b) $x_{CH_4}$ =0.4 (T=800°C, p=150 kPa, $d_p$=3 mm, $r_{SRM}$=0.5 mm).

the bulk gas phase $O_2$ concentration increases, in both cases the relative increase in required $H_2O$ concentration is larger at low $\varepsilon/\tau$, indicating that more heat consumption is required to attain autothermal operation. Although at low $\varepsilon/\tau$ the $C_2$ selectivity actually increases, resulting in less heat production and theoretically less $H_2O$ required for autothermal operation, the actual required steam concentration is higher because some $H_2O$ is also consumed by the exothermic water-gas-shift reaction. Although varying the $H_2O$ concentration could be relatively easily achieved, the lower $H_2O$ concentration limit is most likely to be constrained by the requirement to avoid the formation of carbonaceous species. Especially at lower $O_2$ concentration and $\varepsilon/\tau$ of e.g. 0.15, autothermal operation can in principle already be achieved at $x_{H_2O}$ =0.05 (Fig. 2.16a), obviously with high risk of coke formation. By decreasing the core diameter, the problem of too low H:C ratios can be solved, because autothermal operation can be already achieved at higher bulk $H_2O$ concentration (as demonstrated in Section 2.6.2). Therefore, the influence of $r_{SRM}$ was investigated as well at a relatively high $\varepsilon/\tau$ of 0.2 (which is quite standard for a porous particle) keeping the particle diameter fixed at 3 mm. Similar to the variation of the $\varepsilon/\tau$ in the previous section, a line can be drawn through the points at which autothermal operation is achieved. As shown in Fig. 2.17, the obtained autothermal lines require indeed a higher $H_2O$ concentration when the mass transfer limitation is increased because of the increased diffusion path length. With a SRM core radius varying between 0.3 and 0.4 mm, the exothermic reactions are fully balanced by endothermic steam reforming in a wide range of operating conditions at a more feasible $\varepsilon/\tau$ of 0.2. Hence, depending on

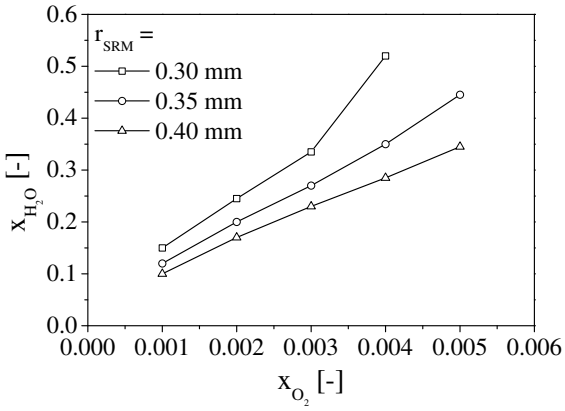


**Figure 2.17:** Autothermal operation at different bulk gas phase composition ($x_{O_2}$, $x_{H_2O}$) for various SRM core diameter at ($x_{CH_4}$ =0.5, T=800°C, p=150 kPa, $r_p$ =1.5 mm, $r_{OCM}$ =0.25 mm).

the particle production method, both approaches can be applied to construct a dual function catalyst particle.

### 2.6.4 Increased $C_2H_4$ and $C_2H_6$ concentration

The SRM core diameter was varied from 0.3-0.9 mm at different bulk gas phase concentrations of $C_2H_4$ and $C_2H_6$ while keeping $\varepsilon/\tau = 0.15$ constant. A $C_2$ bulk concentration of total 2.5, 5 and 10 vol% was selected, which lie well in the range of $C_2$ concentrations that can be expected along the axial direction of a membrane reactor. A bulk gas phase $O_2$ concentration of 0.5 vol% was used for these simulations, although similar results can be obtained at different $O_2$ concentration levels. For excluding (theoretical) formation of carbonaceous species, the H:C ratio can be increased somewhat by applying a $CH_4$ concentration of 30% and a $H_2O$ concentration of 40%. Previous simulations have shown the feasibility of the dual function catalyst

**Table 2.4:** Reaction enthalpies for most important oxidation reactions during oxidative coupling of methane (T=25 °C, p=100 kPa).

| Reaction | $\Delta H^0_{298}$ [kJ/mol] |
|---|---|
| $CH_4 + \frac{1}{4}O_2 \longrightarrow \frac{1}{2}C_2H_6 + \frac{1}{2}H_2O$ | -88 kJ/mol $CH_4$ |
| $CH_4 + 2\,O_2 \longrightarrow CO_2 + 2\,H_2O$ | -802 kJ/mol $CH_4$ |
| $C_2H_4 + 3\,O_2 \longrightarrow 2\,CO_2 + 2\,H_2O$ | -1323 kJ/mol $C_2H_4$ |
| $C_2H_6 + \frac{7}{2}O_2 \longrightarrow 2\,CO_2 + 3\,H_2O$ | -1429 kJ/mol $C_2H_6$ |

at reactor inlet conditions, here the influence of the secondary oxidation reactions and reforming reactions is elucidated. The presence of $C_2$ components in the bulk gas phase and the accompanied thermal effects of the secondary oxidation reactions can have a detrimental effect on the autothermal operation of the process. Because the reaction enthalpy of the deep oxidation reactions is excessively higher than the OCM reaction (see Table 2.4), the total heat production may increase significantly. The relatively low heat of reaction of methane steam reforming ($\Delta H_0^{298}$=205 kJ/mol $CH_4$) compared to the (secondary) combustion reactions taking place is disadvantageous, because most of the heat emerged by the exothermic processes needs to be consumed by $CH_4$ reforming, so that the ratio of required reforming compared to $C_2$ oxidation will be very high.

For a bulk gas phase $C_2$ concentration of zero (i.e. at inlet conditions), the $CH_4$ reforming rate is governed by intra-particle diffusion limitations for all SRM core diameters investigated (see Fig. 2.18a). If the $C_2$ bulk concentration is increased, $C_2$ reforming reactions are gaining importance next to $CH_4$ reforming. Because the amount of $O_2$ becomes deficient for total oxidation, $C_2H_4$ and $C_2H_6$ is left for the reforming reactions but the losses of $C_2$ due to reforming are much lower than the amount which is lost due to the unselective oxidation reactions.

In Fig. 2.18b, where the impact of the reforming activity on the energy balance is displayed, it can be observed that at a $CH_4$ concentration of 30%, the endothermic reactions are in all cases easily able to consume the heat generated by the OCM reactions. At reactor inlet conditions, the required $r_{SRM}$ is small ($\approx$ 0.4 mm). At increased $C_2$ concentration autothermal operation can be achieved if the required SRM core radius is about doubled (compared to reactor inlet conditions). The increased $C_2$ concentration means for OCM that secondary oxidation reactions may consume (part of) the present $C_2$ components, however, because of the interference between OCM and SRM, the dual function process is actually slightly beneficial for $C_2H_4$ and $C_2H_6$ production. In Fig. 2.18c it is shown that for the lowest bulk $C_2$ concentrations and small $r_{SRM}$, the total consumption of $C_2H_4$ and $C_2H_6$ (due to e.g. oxidation reactions) has actually decreased by maximally 30%. The production of synthesis gas via $CH_4$ steam reforming thus reduces the oxidation reactions and has a positive influence on the $C_2$ selectivity because of the water-gas-shift reaction and the $CO_2$ adsorption enthalpy in the OCM reaction kinetics. The positive contribution of reforming activity is obviously lower at higher $C_2$ bulk concentrations, because both $C_2$ reforming and oxidation starts to become increasingly important and the positive influence of $CO_2$ adsorption vanishes. If an average $r_{SRM}$ of 0.6-0.7 mm would be used at 0.5 vol.% $C_2$ concentration, the increase in the $C_2$ consumption does not

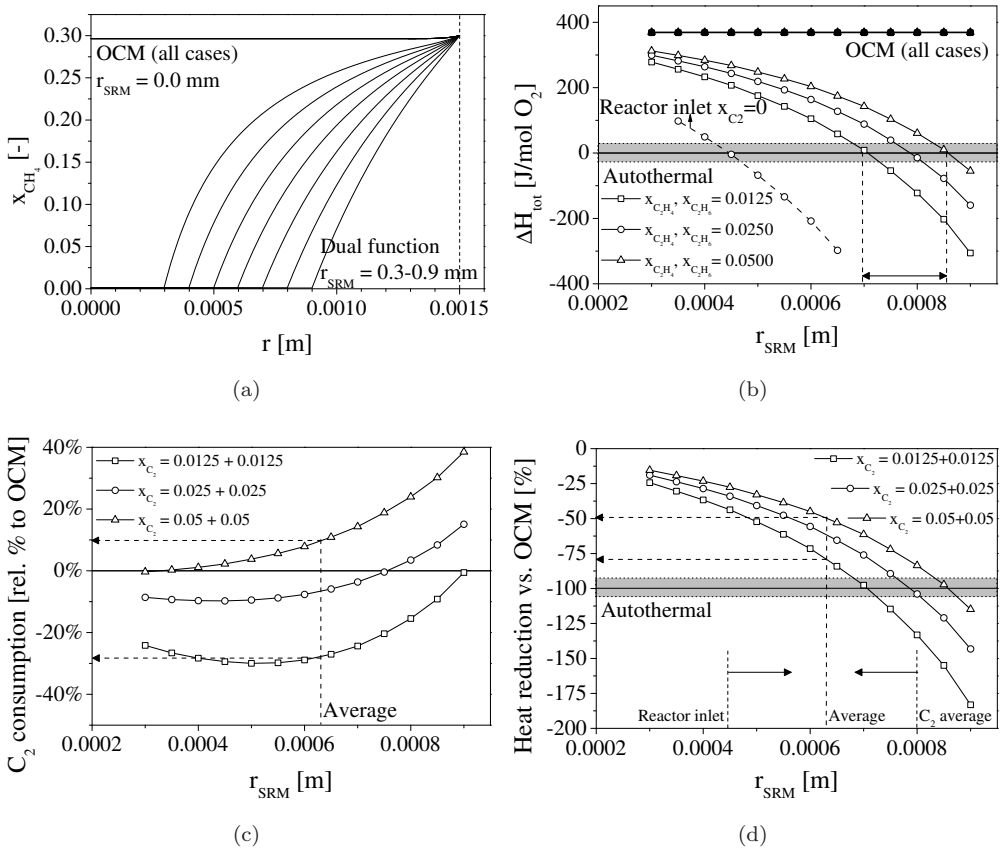


**Figure 2.18:** Influence of increased $C_2$ bulk gas phase concentration on (a) $CH_4$ mole fraction profile, (b) overall reaction enthalpy, (c) relative $C_2H_4$ and $C_2H_6$ consumption and (d) reduction of heat production for various $r_{SRM}$ ($x_{CH_4}$ =0.3, $x_{H_2O}$ =0.4, $x_{C_2H_4}$=$x_{C_2H_6}$ T=800°C, p=150 kPa). For reference also the performance of a catalyst with only OCM activity is included.

exceed 10%, which is very acceptable because valuable synthesis gas is produced and the total heat production is significantly decreased (50-80%).

The consequence of this principally large variation of required core diameter is that the particle configuration (or the bulk gas phase concentrations) should be varied along the reactor length to balance the exothermic and endothermic reactions. To prevent this, an average required core radius should be calculated, based on the insight in the axial profiles in the reactor. Fig. 2.18d illustrates that using an average core radius (at a constant $H_2O$ and $O_2$ concentration) of about 0.6 mm would already result in 50% to 75% reduction (instead of 100%) of the produced heat, which may

be already sufficient to avoid external cooling in the reactor in view of the fact that some axial temperature variations may be tolerated. For example, at the maximum bulk $C_2$ concentration of 5 vol.%, the dual function process produces 50% less heat at $r_{SRM}$ of 0.6 mm.

### 2.6.5 Temperature profiles

The operating conditions determining autothermal operation for the dual function catalyst particle can be summarized with the 'iso-lines' depicted in e.g. Fig. 2.16 (for different $\varepsilon/\tau$), 2.17 (for different $r_{SRM}$) and Fig. 2.18 (for different $C_2$ bulk gas phase concentrations). The overall synthesis gas yield and the corresponding intra-particle temperature and concentration profiles were elucidated with the bulk gas phase concentrations derived from these graphs and an average SRM core radius of 0.5-0.6 mm.

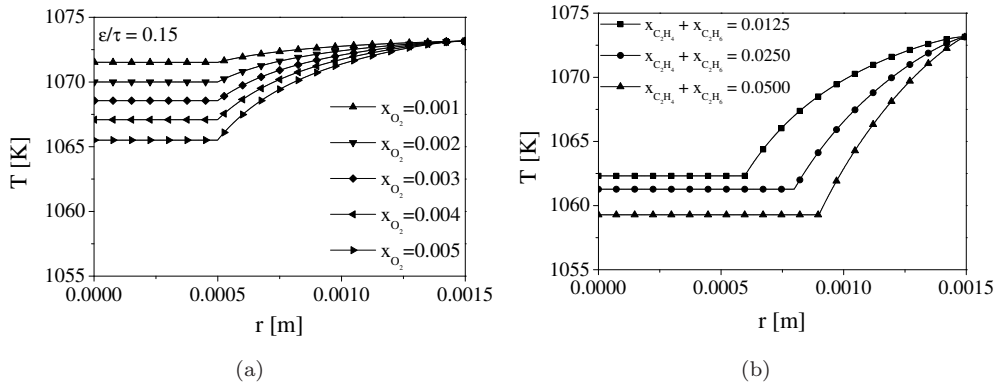


(a) (b)

**Figure 2.19:** Temperature profiles at autothermal conditions for (a) reactor inlet conditions with $x_{H_2O}$ as tuning parameter ($x_{CH_4}$=0.5) and (b) increased $C_2$ bulk gas phase concentration ($x_{CH_4}$=0.3, $x_{H_2O}$=0.5, $x_{O_2}$=0.005) with $r_{SRM}$ as tuning parameter.

The conditions required for the calculation of the temperature profiles depicted in Fig. 2.19a were obtained from simulations shown in Fig. 2.16. Clearly, the temperature in the particle center has dropped somewhat compared to conventional OCM. Because the solids heat conductivity is sufficiently high ($\lambda_{eff} \approx 5 - 10$ W/m/K), the large reaction rates and the accompanied heat transport limitation cause a temperature difference of not more than 10 °C. If the $C_2$ bulk gas phase concentration is increased and $r_{SRM}$ is adjusted to achieve autothermal operation, it can be seen

that the temperature difference does not increase significantly (Fig. 2.19b). In a particle of 3 mm diameter, this temperature difference is small and can be tolerated without consequences for particle stability. If the $CH_4$ conversion and thus the $C_2$ bulk concentration increases, the temperature differences between bulk gas phase and particle center slightly increase. The conditions for these simulations were obtained from results shown in Fig. 2.18, for an average $r_{SRM}$ of 0.6 mm. The temperature difference increases to approximately 15 °C, which is somewhat higher than at reactor inlet conditions. Although autothermal operation can be achieved, at these concentrations the $C_2$ components will already be consumed by the secondary oxidation as demonstrated in the previous paragraph, which can only be solved by applying an oxygen distribution profile in the reactor (i.e. a lower bulk $O_2$ concentration) so that the influence of secondary oxidation reaction is greatly minimized.

## 2.7 Conclusions

The theoretical feasibility of combining oxidative coupling and steam reforming of methane on the scale of a single catalyst particle in order to achieve autothermal conditions was demonstrated provided that the bulk oxygen concentration is kept low, as e.g. in a packed bed membrane reactor with distributive oxygen feeding. Within a wide range of operating conditions, the energy and the carbon efficiency (compared to conventional OCM) is significantly increased, as was demonstrated by means of detailed numerical simulations with a model describing chemical reactions and molecular diffusion by means of the linearized Maxwell-Stefan equations in a porous non-uniform catalytic particle.

Because of the mutual interference of the reforming catalyst and the oxidative coupling catalyst, the catalytic activity was structured into two catalytic sections separated by an inert, porous part. The internal mass transfer limitations are utilized to regulate the total reforming reaction rates and thus the energy consumption. It was found that the implementation of the SRM catalytic activity and the concomitant $C_2$ reforming reactions do not influence the overall performance of the combined process at reactor inlet conditions. However, the losses to $C_2$ reforming start to become more significant at higher $C_2$ bulk concentrations. Because of the increased $C_2$ bulk concentration, the lower methane concentration and the more pronounced highly exothermic $C_2$ oxidation, a relatively large amount of endothermic steam reforming is required to maintain autothermal operation leading to higher losses of ethylene and ethane. A slightly different particle configuration can be used to reduce $C_2$ losses significantly at the expense of small deviations from autothermal operation.

Simulations showed that the dual function catalyst particle is able to efficiently consume 100% of the reaction heat emerged from the OCM reactions, if the diameter of the SRM activity, or the effective diffusivity, or the bulk steam concentration is tuned such that autothermal operation is achieved. To avoid installing different particles at different axial positions, in practice, a single particle configuration ($r_p$=1.5 mm, $r_{SRM}$=0.5-0.6 mm, $r_{OCM}$=0.25-0.5 mm) may be applied in the entire reactor, which can consume more than 50-75% of the OCM reaction heat at elevated methane conversion, while still acceptable syngas to ethylene ratios can be achieved.

## Acknowledgement

The authors gratefully acknowledge the financial support by the Netherlands Organisation for Scientific Research (NWO/ACTS) under the research theme of Advanced Sustainable Processes by Engaging Catalytic Technologies (ASPECT) (project 053.62.008).

## Nomenclature

*Roman letters*

| | | |
|---|---|---|
| $a_s$ | $m^2/m^3$ | specific surface catalyst |
| $[B]$ | | inverse diffusion matrix |
| $b_{i,k}$ | | element of matrix $[B]$ |
| $Bi_h$ | | Biot number $= \alpha r_p/\lambda$ |
| $C$ | $mol/m^3$ | concentration |
| $C_p$ | kJ/kg/K | heat capacity |
| $[D]$ | $m^2/s$ | diffusion matrix in the molar average reference velocity frame |
| $[D^0]$ | $m^2/s$ | diffusion matrix in the mass average reference velocity frame |
| $[\hat{D}^0]$ | $m^2/s$ | Eigenvalues of the diffusion matrix $[D^0]$ |
| $[D^0_{eff}]$ | $m^2/s$ | effective diffusion matrix in the mass average reference velocity frame |
| $d^0_{eff,i,k}$ | $m^2/s$ | element of matrix $[D^0_{eff}]$ |
| $d_p$ | m | particle diameter |
| $Đ_{i,j}$ | $m^2/s$ | binary diffusivity of component $i$ |
| $E_a$ | J/mol | activation energy |
| $[I]$ | - | identity matrix |

| | | |
|---|---|---|
| $j_i$ | kg/m$^2$/s | diffusive mass flux of component i |
| $J_i$ | mol/m$^2$/s | diffusive mole flux of component i |
| $k_{0,j}$ | 1/s | pre-exponential factor |
| $k_j$ | 1/s | first order reaction rate constant |
| $k_{g\to s}$ | m/s | mass transfer coefficient under zero mass flux |
| $k^{\bullet}_{g\to s}$ | m/s | finite flux mass transfer coefficient |
| $K$ | - | thermodynamic equilibrium constant |
| $\hat{k}_{g\to s}$ | m/s | Eigenvalues of $k_{g\to s}$ |
| $M_i$ | kg/mol | mole mass of component i |
| $n_i$ | kg/m$^2$/s | mass flux of component $i$ |
| $n_j$ | - | reaction order of reaction $j$ |
| $n_{tot}$ | kg/m$^2$/s | drift flux |
| $p$ | Pa | (partial) pressure |
| $p_\psi$ | - | grid refinement parameter |
| $Q$ | W | heat |
| $r$ | m | radial coordinate |
| $r_{OCM}$ | m | thickness of the OCM catalytic layer |
| $r_{inert}$ | m | thickness of the inert porous layer |
| $r_{SRM}$ | m | thickness of the SRM catalytic layer |
| $r_p$ | m | particle radius |
| $r_j$ | mol/kg$_{\text{cat}}$/s | reaction rate of component j |
| $R_j$ | mol/m$^3$/s | reaction rate of component j |
| $s_{r,i}$ | mol/m$^3$/s | source term mass balance |
| $s_h$ | J/m$^3$/s | source term energy balance |
| $Sh$ | - | Sherwood number $= k_g d_p / D_{eff}$ |
| $t$ | s | time |
| $T$ | K | temperature |
| $T_{bulk}$ | K | temperature of the bulk gas phase |
| $V$ | m$^3$ | volume |
| $x$ | - | mole fraction |
| $y$ | - | dimensionless radial coordinate |

*Greek letters*

| | | |
|---|---|---|
| $\alpha$ | - | geometrical shape parameter |
| $\alpha_{g\to s,0}$ | W/m$^2$/K | heat transfer coefficient at zero flux |
| $\alpha^{\bullet}_{g\to s}$ | W/m$^2$/K | finite flux heat transfer coefficient |
| $\varepsilon$ | - | porosity |

| | | |
|---|---|---|
| $\phi_i$ | - | fugacity coefficient of component i |
| $\phi'$ | - | Thiele modulus |
| $\Phi_i$ | mol/s | mole flow of component i |
| $\psi$ | - | transformation function radial coordinate |
| $\Delta H_{r,j}$ | J/mol | reaction enthalpy of reaction j |
| $\overline{H}_i$ | J/mol | partial molar enthalpy of component i |
| $\eta$ | - | effectiveness factor |
| $\Xi_m$ | - | correction factor for mass flux |
| $\Xi_h$ | - | correction factor for heat flux |
| $[\Gamma]$ | - | thermodynamic correction factor matrix |
| $\nu_{i,j}$ | - | stoichiometric coefficient |
| $\lambda_{eff,s}$ | W/m/K | effective solids heat conductivity |
| $\rho$ | kg/m$^3$ | density |
| $\tau$ | - | particle tortuosity |
| $\omega$ | - | weight fraction |

*Subscripts*

| | |
|---|---|
| g | gas phase |
| i | component i |
| inert | inert porous layer in catalyst particle |
| N | number of components |
| np | number of grid points |
| $N_{reac}$ | number of reactions |
| p | particle |
| OCM | Oxidative Coupling of Methane |
| s | solid phase |
| SRM | Steam Reforming of Methane |

# Appendix 2.A Reaction rate expressions

## 2.A.1 Oxidative coupling

The reaction kinetics for the oxidative coupling of methane was measured by Stansch et al. (1997) on a $La_2O_3$/CaO catalyst in a micro-catalytic fixed bed reactor under a wide range of differential reaction conditions.

**Table A.1:** Reactions for the OCM accounted for by Stansch et al. (1997).

| Reaction | $\Delta H^0_{298}$ kJ/mol | Step |
|---|---|---|
| $CH_4 + 2\,O_2 \longrightarrow CO_2 + 2\,H_2O$ | -803 kJ/mol $CH_4$ | (R1) |
| $2\,CH_4 + \frac{1}{2}\,O_2 \longrightarrow C_2H_6 + H_2O$ | -88 kJ/mol $CH_4$ | (R2) |
| $CH_4 + O_2 \longrightarrow CO + H_2O + H_2$ | -278 kJ/mol | (R3) |
| $CO + \frac{1}{2}\,O_2 \longrightarrow CO_2$ | -283 kJ/mol | (R4) |
| $C_2H_6 + \frac{1}{2}\,O_2 \longrightarrow C_2H_4 + H_2O$ | -106 kJ/mol | (R5) |
| $C_2H_4 + 2\,O_2 \longrightarrow 2\,CO + 2\,H_2O$ | -757 kJ/mol $C_2H_4$ | (R6) |
| $C_2H_6 \longrightarrow C_2H_4 + H_2$ | -136 kJ/mol | (R7) |
| $C_2H_4 + 2\,H_2O \longrightarrow 2\,CO + 4\,H_2$ | 210 kJ/mol $C_2H_4$ | (R8) |
| $CO + H_2O \longleftrightarrow CO_2 + H_2$ | -41 kJ/mol | (R9) |
| $CO_2 + H_2 \longleftrightarrow CO + H_2O$ | 41 kJ/mol | (R10) |

With the next rate equations for step 1, 3-6:

$$r_j = \frac{k_{0,j} e^{-E_{a,j}/RT} p_C^{m_j} p_{O_2}^{n_j}}{(1 + K_{j,CO_2} e^{-\Delta H_{ad,CO_2}/RT} p_{CO_2})^{n_j}} \tag{A.1}$$

And for step 2:

$$r_j = \frac{k_{0,j} e^{-E_{a,j}/RT} p_{CH_4}^{m_j} (K_{j,O_2} e^{-\Delta H_{ad,O_2}/RT} p_{O_2})^{n_j}}{(1 + K_{j,CO_2} e^{-\Delta H_{ad,CO_2}/RT} p_{CO_2} + (K_{j,O_2} e^{-\Delta H_{ad,O_2}/RT} p_{O_2})^{n_j})^2} \tag{A.2}$$

The remaining reaction rates (step 7-10) were described with standard power-law expressions:

$$r_j = k_{0,j} e^{-E_{a,j}/RT} p_C^{m_j} p_H^{n_j} \tag{A.3}$$

The reaction rate constants for the rate equations can be found in Table A.2.

**Table A.2:** Kinetic parameters for oxidative coupling (Stansch et al., 1997).

| Step | $k_0$ [mol/g/s/Pa$^{-(m+n)}$] | $E_a$ [kJ/mol] | $K_{CO_2}$ [Pa$^{-1}$] | $\Delta H_{ad,CO_2}$ [kJ/mol] | $K_{O_2}$ [Pa$^{-1}$] | $\Delta H_{ad,O_2}$ [kJ/mol] | $m_j$ | $n_j$ |
|---|---|---|---|---|---|---|---|---|
| R1 | 0.20 x $10^{-5}$ | 48 | 0.25 x $10^{-12}$ | -175 | | | 0.24 | 0.76 |
| R2 | 23.2 | 182 | 0.83 x $10^{-13}$ | -186 | 0.23 x $10^{-11}$ | -124 | 1.0 | 0.40 |
| R3 | 0.52 x $10^{-6}$ | 68 | 0.36 x $10^{-13}$ | -187 | | | 0.57 | 0.85 |
| R4 | 0.11 x $10^{-3}$ | 104 | 0.40 x $10^{-12}$ | -168 | | | 1.0 | 0.55 |
| R5 | 0.17 | 157 | 0.45 x $10^{-12}$ | -166 | | | 0.95 | 0.37 |
| R6 | 0.06 | 166 | 0.16 x $10^{-12}$ | -211 | | | 1.0 | 0.96 |
| R7 | 1.2 x $10^{7}$ (1) | 226 | | | | | 1.0 | 0 |
| R8 | 9.3 x $10^{3}$ | 300 | | | | | 0.97 | 0 |
| R9 | 0.19 x $10^{-3}$ | 173 | | | | | 1.0 | 1.0 |
| R10 | 0.26 x $10^{-1}$ | 220 | | | | | 1.0 | 1.0 |

(1) Units are mol/s/m$^3$/Pa

## 2.A.2 Steam reforming

The steam reforming reaction rates are calculated with the kinetic model developed by Xu and Froment (1989) for a $Pt/Al_2O_3$ catalyst.

**Table A.3:** Reactions for the SRM accounted for by (Xu and Froment, 1989).

| Reaction | $\Delta H_0^{298}$ [kJ/mol] | Step | $k_0$ [mol/kg/s/bar$^{0.5}$] | $E_a$ [kJ/mol] |
|---|---|---|---|---|
| $CH_4 + H_2O \longleftrightarrow CO + 3\,H_2$ | 206 | (R1) | 1.17 x $10^{15}$ | 240.1 |
| $CO + H_2O \longleftrightarrow CO_2 + H_2$ | -41 | (R2) | 5.43 x $10^{5}$ | 67.1 |
| $C_2H_4 + 2\,H_2O \longrightarrow 2\,CO + 4\,H_2$ | 210 | (R3) | 0.52 x $10^{-6}$ | 68 |
| $C_2H_6 + 2\,H_2O \longrightarrow 2\,CO + 5\,H_2$ | 346 | (R4) | 0.11 x $10^{-3}$ | 104 |

The reaction rates of the equations are:

$$r_1 = \frac{k_{0,1}/p_{H_2}^{2.5}(p_{CH_4}p_{H_2O} - p_{H_2}^3 p_{CO}/K_{eq,1})}{(1 + K_{CO}p_{CO} + K_{H_2}p_{H_2} + K_{CH_4}p_{CH_4} + K_{H_2O}p_{H_2O}/p_{H_2})^2} \quad \text{(A.4)}$$

$$r_2 = \frac{k_{0,2}/p_{H_2}(p_{CO}p_{H_2O} - p_{H_2}p_{CO_2}/K_{eq,2})}{(1 + K_{CO}p_{CO} + K_{H_2}p_{H_2} + K_{CH_4}p_{CH_4} + K_{H_2O}p_{H_2O}/p_{H_2})^2} \quad \text{(A.5)}$$

(A.6)

The reaction rates of the $C_2H_4$ and $C_2H_6$ reaction rates on $Pt/Al_2O_3$ were estimated from data made available by Graf et al. (2007). The activity parameter mentioned in the scheme is approximately equal to 2.

## Appendix 2.B Derivation of diffusivity matrix

For (N-1) components, the diffusion flux according to the generalized Fick formulation is defined by:

$$(J) = -c_t[D](\nabla x) \tag{B.1}$$

Where the diffusivity for (N-1) components, including interaction effects, is calculated by means of Maxwell Stefan's theory of multicomponent diffusion which can be described with a square matrix [D]:

$$[D] = [B]^{-1}[\Gamma] \tag{B.2}$$

For thermodynamically ideal systems the thermodynamic effects matrix [Γ] reduces to the identity matrix [$I$]. The elements of matrix [B] are a function of composition and the binary diffusion coefficients. This matrix follows from the generalized Maxwell Stefan equation, describing diffusion of multiple components in a gaseous mixture.

$$\begin{aligned}
c_t d_i &= \sum_{j=1}^{N} \frac{x_i J_j - x_j J_i}{Đ_{ij}} = \frac{x_i J_N - x_N J_i}{Đ_{iN}} + \sum_{j=1}^{N-1} \frac{x_i J_j - x_j J_i}{Đ_{ij}} \\
&\text{with } J_N = -\sum_{j=1}^{N-1} J_j \\
&= -\frac{x_i}{Đ_{iN}} \sum_{j=1}^{N-1} J_j - \frac{x_N J_i}{Đ_{iN}} + \sum_{j=1}^{N-1} \frac{x_i J_j}{Đ_{ij}} - \sum_{j=1}^{N-1} \frac{x_j J_i}{Đ_{ij}} \\
&= -\sum_{j=1}^{N-1} \frac{x_j J_i}{Đ_{ij}} - \frac{x_N J_i}{Đ_{iN}} + \sum_{j=1}^{N-1} \left( \frac{x_i}{Đ_{ij}} - \frac{x_i}{Đ_{iN}} \right) J_j \\
&= -\sum_{j=1}^{N-1} \frac{x_j J_i}{Đ_{ij}} - \frac{x_N J_i}{Đ_{iN}} + \frac{x_i}{Đ_{ii}} J_i - \frac{x_i}{Đ_{iN}} J_i + \sum_{\substack{j=1 \\ j \neq i}}^{N-1} \left( \frac{x_i}{Đ_{ij}} - \frac{x_i}{Đ_{iN}} \right) J_j \\
&= \left( -\frac{x_i}{Đ_{iN}} - \sum_{j=1}^{N-1} \frac{x_j}{Đ_{ij}} + \frac{x_i}{Đ_{ii}} \right) J_i - \sum_{\substack{j=1 \\ j \neq i}}^{N-1} -x_i \left( \frac{1}{Đ_{ij}} - \frac{1}{Đ_{iN}} \right) J_j \\
&= -\left( \frac{x_i}{Đ_{iN}} + \sum_{\substack{k=1 \\ k \neq i}}^{N-1} \frac{x_k}{Đ_{ik}} \right) J_i - \sum_{\substack{j=1 \\ j \neq i}}^{N-1} B_{ij} J_j = -B_{ii} J_i - \sum_{\substack{j=1 \\ j \neq i}}^{N-1} B_{ij} J_j
\end{aligned} \tag{B.3}$$

The diffusion coefficients of the binary pairs $Đ_{i,j}$ can be estimated with the kinetic theory of gases (Poling et al., 2007).

## Appendix 2.C Conversion between reference velocity frames

Because the mass balances are solved in the mass average reference velocity frame using mass fractions, the diffusion flux of each component should be converted from the molar average reference velocity frame to the mass average velocity frame through the transformation algorithm shown in Table 2.2. The conversion from mass to molar reference velocity frame is especially relevant for the case of non-equimolar diffusion (i.e. $D_i \neq D_j$), which is very common in systems where chemical reactions are taking place. Simplified methods to take the influence of the composition into account are the commonly used equations summarized by Taylor and Krishna (1993), here the Wilke equation is taken as an example:

$$D_{i,eff} = \frac{(1 - x_i)}{\sum_{\substack{j=1 \\ j \neq i}}^{n} \frac{x_j}{Đ_{i,j}}} \tag{C.1}$$

These equations give reasonable results, although the implicit assumption of a single component (i) diffusing through a stagnant gas usually does not hold for reactive systems or diffusive transport with density changes. This is illustrated by means of two simulation results, a case with diffusion of $H_2$, $H_2O$ and $N_2$ through a porous plate and steam reforming occurring in a porous particle. Conditions are listed in Table C.1.

**Table C.1:** Conditions applied for multicomponent diffusion calculations.

| Parameter | Case 1 (*Diffusion*) | | Case 2 (*Reforming*) |
|---|---|---|---|
| | r=0 | r=$r_p$ | |
| $x_{CH_4}$ | - | - | 0.5 |
| $x_{H_2O}$ | 0.0 | 0.5 | 0.4 |
| $x_{H_2}$ | 0.5 | 0.0 | 0.0 |
| $x_{N_2}$ | 0.5 | 0.5 | 0.1 |
| d [mm] | 85.9 | | 3.0 |
| T [K] | 308.35 | | 1073.15 |
| p [kPa] | 101.3 | | 150 |
| $\varepsilon/\tau$ [-] | 0.1 | | |

For diffusion through a porous plate, it is shown in Fig. C.1a that the concentration

profiles calculated with the Wilke equation are significantly different from the solution obtained with the Maxwell-Stefan equations. Because the components differ in molar mass, the corresponding gas density difference will lead to a net molar flux in the porous plate. This contradicts with the Wilke equation which assumes the gases to be stagnant ($N_j$=*0*), so that the solution deviates from result obtained with the Maxwell Stefan equations. The $H_2$ concentration profiles are hardly influenced because its interaction with other components is very low. For the simulation of the case with

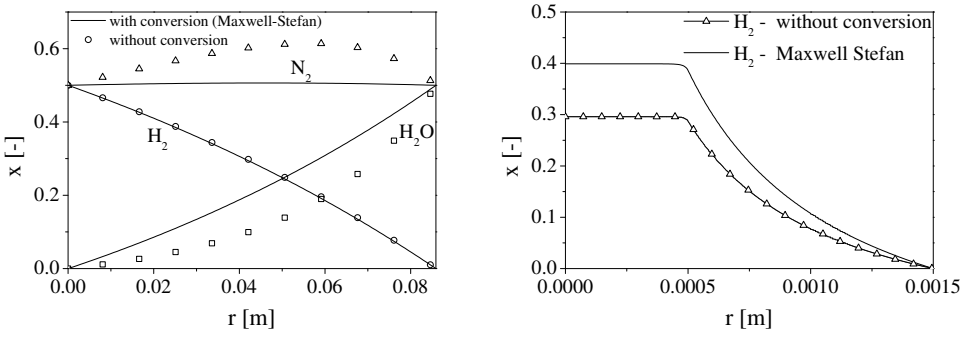


(a) (b)

**Figure C.1:** Influence of using the conversion from molar to mass average reference velocity frame for (a) non-equimolar diffusion in a flat plate (case 1) and (b) steam reforming in a spherical particle (with density changes) (case 2).

steam reforming, a spherical particle with a diameter of 3 mm was used with an active core diameter of 1 mm, which resembles the intended conditions for a dual function catalyst particle. In a system with a chemical reaction occurring (in this case an equilibrium reaction), the difference in concentration profiles is even more pronounced than for the case with diffusion only, which supports the conclusion that the interaction effects between the components should be taken into account properly.

## Appendix 2.D Validation of the particle model

The numerical paricle model was first tested with a non-reactive case, with which the implementation of the Maxwell-Stefan equations could be thoroughly verified. An example was taken from the literature, which describes the diffusion of $H_2$ (1), $N_2$ (2) and $CO_2$ (2) through a porous flat plate (for details see Taylor and Krishna (1993)). First the solution of this problem was calculated under isobaric and isothermal conditions.

**Table D.1:** Mole fractions at the boundary for the validation case (T=308.35 K, p=101.3 kPa).

| | r=0 | r=R |
|---|---|---|
| $H_2$ | 0.0 | 0.50121 |
| $CO_2$ | 0.50086 | 0.49879 |
| $N_2$ | 0.49914 | 0.0 |

The diffusion path length was set to 85.9 mm and the values of the diffusion coefficients of the binary pairs are defined as:

$H_2$ - $N_2$ : $D_{12} = 83.3\ \text{mm}^2/\text{s}$

$H_2$ - $CO_2$ : $D_{13} = 68.0\ \text{mm}^2/\text{s}$

$CO_2$ - $N_2$ : $D_{23} = 16.8\ \text{mm}^2/\text{s}$

In the example, the molar flux was assumed to be zero so the mass density was set constant (similar to constant mole mass). Because the diffusion coefficients vary as function of the composition, the problem cannot be solved analytically. Therefore the model solution was compared with the numerical solution of the same equations obtained with a PDE solver (Matlab). From the mole fraction profile depicted in Fig. D.1 it can be concluded that there is a strong interaction between the components, especially between $N_2$ and $H_2$. Because of the strong interaction, the fluxes of the components are influenced to a large extent. Results confirm that the model equations have been implemented correctly. To verify the correctness of the computed mass fluxes under reactive conditions, the model was validated for both isothermal and non-isothermal cases, with the conditions listed in Table D.2 for a first order irreversible reaction $A \rightarrow P$. The obtained intraparticle concentration profiles can be compared with an analytically derived profile under the assumption of constant mole mass and

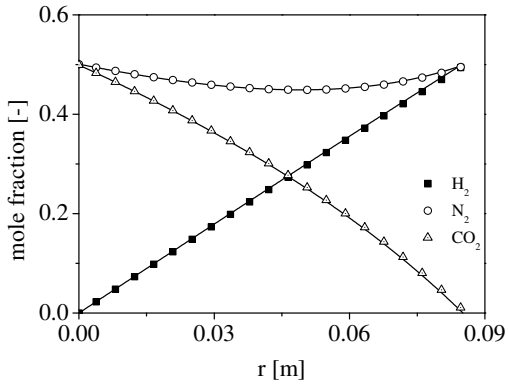


**Figure D.1:** Validation of concentration profiles for case with non-equimolar diffusion in porous plate.

**Table D.2:** Conditions used for verification of the model.

| Reaction data | | Particle properties | |
|---|---|---|---|
| $D_i$ [$m^2/s$] | $1.0 \cdot 10^{-5}$ | $d_p$ [m] | $2 \cdot 10^{-3}$ |
| T [K] | 1000 | $\frac{\epsilon_g}{\tau}$ | 0.25 |
| p [Pa] | $1 \cdot 10^5$ | $\rho_p$ [$kg/m^3$] | $2 \cdot 10^3$ |

constant diffusivity.

$$0 = \frac{d}{dr}\left[r^2 D_i \frac{dC_A}{dr}\right] - r^2 k_1 c_A \tag{D.1}$$

With no gas phase resistance ($k_g=\infty$) and an irreversible reaction ($K_{eq}=\infty$) the solution of D.1 can be calculated analytically (Fogler, 1963; Westerterp et al., 1963).

$$c_A = c_{A,bulk}\left(\frac{r_p}{r}\frac{sinh\left(\frac{r}{r_p}3\phi\right)}{sinh(3\phi)}\right) \qquad with \quad \phi = \frac{r_p}{3}\sqrt{\frac{k_1}{D_i}} \tag{D.2}$$

In Fig. D.2a it is shown that the numerical solution for the concentration profile of component A perfectly agrees with the analytical solution given by equation D.2, for different values of the Thiele modulus $\phi$. Moreover, the computed mass flux at the particle surface agrees very well with the overall reaction rate. The relative error in the calculation of the profiles remains below 0.0005%, which could be even further

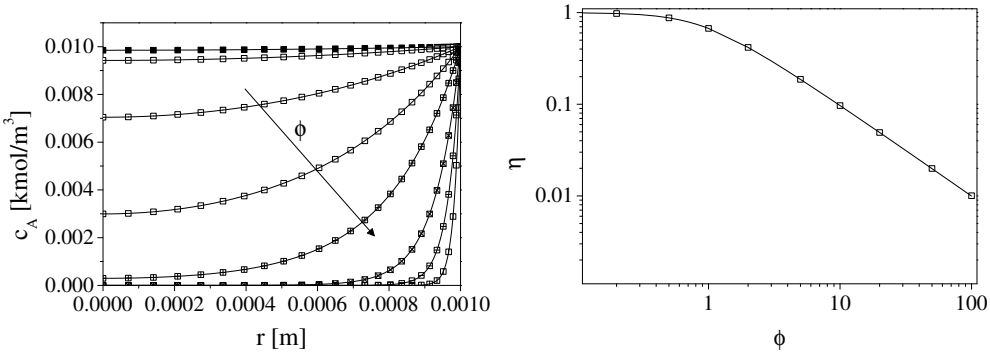


**Figure D.2:** Comparison of radial concentration profiles (a) and effectiveness factors (b) as function of the Thiele modulus calculated with the particle model (points) with the analytical solutions (solid line) for the case of constant diffusivity and gas density.

improved at the cost of more grid cells thereby largely increasing the calculation time. In Fig. D.2b the calculated and analytical effectiveness factors are compared as function of the Thiele modulus. The effectiveness factor for reaction $j$ is here defined as the ratio of the actual reaction rate and the reaction rate at bulk conditions.

$$\eta_j = \frac{\int_{r=0}^{r=r_p} R_{j,local} 4\pi r^2 dr}{R_{j,bulk} V_p} \tag{D.3}$$

At isothermal and isobaric conditions, the effectiveness factor for equation D.3 can be calculated analytically, given by:

$$\eta_{exact} = \frac{1}{3\phi^2}\left(\frac{3\phi - tanh3\phi}{tanh3\phi}\right) \text{ with } \phi = \frac{r_p}{3}\sqrt{\frac{k_1^{"} a_s (K_{eq}+1)}{D_{eff,i} K_{eq}}}$$

The actual reaction rate resulting from the numerical model is calculated by means of Simpson's $1/3^{rd}$ rule and the calculations were carried out with 51 grid cells. By varying the number of cells it was found that applying 51 cells yields a satisfactory balance between accurate solution and calculation speed even for high Thiele moduli ($\phi > 10$). At even higher Thiele moduli with steep gradients prevailing close to the particle surface, the deviation from analytical solution will increase and an increase in the number of cells or a different grid transformation function is needed. For all cases the relative difference between the calculated and analytical solution is smaller than 0.1%, which is very acceptable. It was found that these differences are mainly

caused by the accuracy of the numerical integration near the interface.

Similar to the case of a high Thiele modulus, also for cases with highly exothermic reactions the accurary of the solution should be carefully checked. To illustrate this, a first order irreversible reaction was simulated under isobaric conditions. For non-isothermal systems the Thiele modulus $\phi$ is related to the surface temperature $T_i$ via the reaction rate constant $k_{1i}$.

$$k_1 = k_{1i} exp\left(\frac{E_{act}}{RT_i}\frac{(T-T_i)}{T_i(1+\frac{(T-T_i)}{T_i})}\right) \tag{D.4}$$

Because of temperature gradients prevailing inside the catalyst particle, the reaction rate constant k becomes position dependent, so that effectiveness factors greater than unity are possible because of the Arrhenius dependency of the reaction rate constant. Because of the coupling between the mass and energy balances, the equations can not be solved analytically. Therefore the calculated results from the particle model have been compared with the numerical solution of the same differential equations in Matlab, and found to agree very well.

# 3

# Development of a packed bed membrane reactor with a dual function OCM/SRM catalyst


## Abstract

A numerical feasibility study was performed on the integral performance of dual function catalyst particles, contained in a packed bed reactor equipped with a porous membrane for distributive feeding of oxygen. The exothermic oxidative coupling and the endothermic steam reforming of methane (for simultaneous production of ethylene and synthesis gas) are integrated at the level of a porous catalyst particle with distributed activity, where the presence of the intra-particle heat-sink strongly reduces the total reaction heat and the temperature gradients in the reactor, eliminating the need for expensive conventional cooling of the reactor.

Numerical simulations, with reaction kinetics taken from the literature, revealed that with distributive oxygen feeding via membranes indeed the local oxygen concentration in the packed bed membrane reactor can be kept low, which combined with a high Thiele modulus for oxidative coupling makes dual function catalysis possible. Using a reforming core diameter of approximately 50-100 $\mu$m, the steam reforming and oxidative coupling reaction rates could be effectively tuned to achieve autothermal operation while the methane conversion was enhanced from 44% to 55%. The decrease of the $C_2$ production rates was not detrimental and mainly caused by a lower selectivity of the oxidative coupling catalyst at higher conversions, leading to losses to $C_2$ reforming lower than 40%. In addition, it was shown that the temperature profiles in the reactor can be strongly reduced by employing the dual function catalyst and that the use of axial oxygen membrane flux profiles enables the use of a single particle configuration to approach autothermal operation in the entire reactor.

## 3.1 Introduction

The theoretical feasibility of a dual function OCM/SRM catalyst particle was demonstrated in the previous chapter for various limiting cases of the bulk gas phase compositions and it was shown how autothermal process conditions can be achieved by tuning the catalyst layout and properties. Although the proposed concept with distributed OCM and SRM catalytic activity has been studied in detail on the particle scale, it is important to quantify the process characteristics at the reactor scale because of the changing concentration and temperature profiles along the reactor length. Particularly an increase in the secondary oxidation and $C_2$ reforming reaction rates, results in different criteria for autothermal operation, which requires that the layout of the catalyst particle should be modified accordingly.

This can be achieved by tuning the diffusion limited steam reforming reaction rates at minimal losses to $C_2$ reforming by variation of the diameter of the steam reforming catalytic core, the particle structure (i.e. $\varepsilon/\tau$), the particle diameter or the bulk $H_2O$ and $O_2$ concentrations (see Chapter 2). Although modification of the catalyst for each position in the reactor is attractive to increase energy efficiency, it is undesired to use many different particles with different configurations (i.e. the dimension of $r_{SRM}$) because it makes filling of the reactor unnecessarily complicated and time-consuming. In practice, an average dual function particle design and its properties will be selected and used in the reactor, based on an optimization of the ethylene/ethane yield versus synthesis gas production and overall temperature profiles.

### 3.1.1 Reactor selection

The dual function catalyst particles for this process will be most effective if the reaction heat is rather uniformly generated in the reactor, which is possible with low $O_2$ bulk concentrations and can be realized in two different reactor types. In a fluidized bed reactor, the total reactor volume is nearly at the same temperature because of its excellent mixing properties, but the relatively high degree of back-mixing ($Bo_{max} < 0.01$) compared to fixed bed reactors ($Bo_{max} \rightarrow 2$) is disadvantageous for obtaining a high selectivity of $C_2H_4$ and $C_2H_6$. The influence of back-mixing in bubbling fluidized bed reactors can be reduced to near plug flow behavior by inserting tubes in the reactor which distribute additional gas (e.g. $O_2$) into the reactor (Kunii and Levenspiel (1991), van Swaaij, Jovanovic, van Deemter). Moreover, the presence of internals and the feeding of additional gas at multiple locations strongly limits the down flow of gas and the macroscopic circulation patterns, which reduces unselective (partial, secondary) oxidation reactions (Deshmukh et al., 2005). Hence, the fluidized

bed membrane reactor may be an attractive option to improve heat transfer. However, as described in Chapter 2, the size of the dual function catalyst particles will be in the range of 3-5 mm, which means that the particles are classified as Geldart D spoutable or dense particles. For fluidization in a reactor with inserted (membrane) tubes, this type of particles is less desirable because of possibility for high abrasion rates (of both particles and membranes), slug flow and large degree of back mixing in case spouted beds are used (Kunii and Levenspiel, 1991).

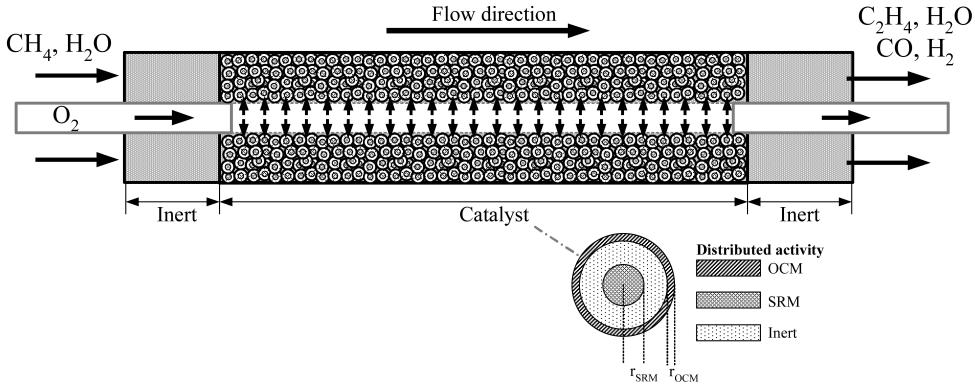


**Figure 3.1:** Schematic of the dual function catalyst particle implemented in a packed bed membrane reactor with distributed $O_2$ feeding.

The fixed bed reactor equipped with (porous) membranes is a better choice for the oxidative coupling of methane, also because the $C_2$ selectivity is high because of the low local $O_2$ concentration in combination with low axial gas back-mixing (see Fig. 3.1). In addition, the concentration of $O_2$ in fixed bed membrane reactors can be controlled by tuning the membrane flux and the reactor length, so that - in contrary to co-fed reactors - higher overall reactant conversion and high product selectivity can be combined with a low $O_2$ bulk concentration level, provided that the selective reaction has a lower reaction order to $O_2$ (Kürten, 2003; Lu, Dixon, Moser and Hua Ma, 2000). In Fig. 3.1 it is shown that in such a reactor the $O_2$ is distributed to the packed bed via a (porous) membrane located in the centerline of the reactor tube and that the dual function catalyst particles are located in the annular space between the membrane and the outer reactor wall. In reactors with small diameter, only one $O_2$ distributor is sufficient but with increasing reactor diameter, radial $O_2$ transport will become limiting, requiring the insertion of multiple $O_2$ distribution membranes into the fixed bed. The major disadvantage of exothermic processes performed in catalytic fixed bed reactors is usually temperature control, but because here the reaction heat

is directly consumed on the particle scale by the integrated steam reforming reactions and the $O_2$ is distributively fed along the reactor length via membranes, the nett heat generation is small resulting in a low adiabatic temperature rise.

The influence of the dual function process on the reactor performance, in terms of $C_2$ yield at a specified $CH_4$ conversion and isothermal operation (overall energy efficiency) was determined by means of detailed reactor modeling of the unsteady-state equations for mass and energy (Bird et al., 2002). To account for the strong intra-particle concentration and temperature profiles typically observed with oxidative coupling of methane, sometimes an analytical approach to solve the reaction diffusion equations is sufficient (e.g. Gosiewski et al., 1999; Smit et al., 2005a; van Sint Annaland et al., 2007a), however with a multi-component mixture and multiple reactions occurring, only idealized modes of operation can be described and heterogeneous reactor modeling is required. The relevance of using heterogeneous reactor models will be made clear during the optimization of the oxidative coupling reactor, when showing the influence of the intra-particle mass and heat transfer limitations on the reactor performance. Furthermore, it is elucidated which particle configuration is most suitable for the combined process by performing detailed reactor simulations at non-isothermal (autothermal) conditions.

## 3.2 Numerical model

The reactor for the dual function process consists of two cylindrical compartments which are separated by a porous ($\gamma$-$Al_2O_3$) wall through which $O_2$ is distributed to the catalyst bed (Fig. 3.1). A heterogeneous reactor model was developed to account for the influence of the intra-particle concentration and temperature profiles on the bulk gas phase composition and temperature. The mass and energy balances describing the axial profiles for both compartments are listed in Table 3.1. The model describing the concentration and temperature profiles on the particle scale, described in detail in Chapter 2, is used to calculate the volumetrically averaged mass and energy source terms at each axial location in the reactor. The main assumptions for the model are:

- Radial temperature differences in the compartments are accounted for via overall wall-to-bed heat transfer coefficients.
- Radial $O_2$ concentration profiles in the compartments are neglected, i.e. absence of concentration polarization is assumed (valid for sufficiently small $d_o - d_i$).
- Gas transport in the axial direction can be described by convective flow with superimposed axial dispersion.

- The governing transport mechanism in the porous catalyst particles is diffusion of mass and energy.
- External mass and heat transfer limitations were neglected. The influence was shown to be small in Chapter 2.

In Table 3.1, the mass convection term can be written in terms of its partial derivatives,

$$\frac{\partial \rho_g v_g \omega_i}{\partial z} = \rho_g v_g \frac{\partial \omega_i}{\partial z} + \omega_i \frac{\partial \rho_g v_g}{\partial z} = \rho_g v_g \frac{\partial \omega_i}{\partial z} + \omega_i \phi''_{m,tot} \tag{3.1}$$

so that the total increase of the mass flux in the reactor compartment due to the membrane flow is directly accounted for.

For the multicomponent gas mixture, the pure component data listed by the Design Institute for Physical Property Data (DIPPD) of the American Institute of Chemical Engineers was used (Daubert and Danner, 1985). The relevant physical properties for the other materials, such as used metals, solid particles and membranes have been summarized in Appendix 3.A.

The pressure differences in the catalyst particle were neglected (following Veldsink et al., 1995) and the axial pressure drop over the packed bed was calculated with the Ergun equation (Ergun, 1952).

$$-\frac{dp}{dz} = 150 \frac{\eta_g v_g}{d_p^2} \frac{(1-\varepsilon_g)^2}{\varepsilon_g^3} + 1.75 \frac{\rho_g v_g^2}{d_p} \frac{(1-\varepsilon_g)}{\varepsilon_g^3} \tag{3.2}$$

The distribution of $O_2$ (or another gas) along the reactor length is governed by the partial pressure difference and the membrane permeability. Ideally, dense membranes are preferred, but here porous tubes are applied. If the pore diameter of these tubes is sufficiently small, the transport can be described by the Dusty-Gas-Model which incorporates a contribution of Knudsen diffusion and viscous flow (Benes, 2000; Krishna and Wesselingh, 1997a; Veldsink et al., 1995).

$$J_{O_2} = \frac{1}{RT} \left( K_0 \frac{4}{3} \sqrt{\frac{8RT}{\pi \langle M \rangle}} + B_0 \frac{\langle P \rangle}{\eta_g} \right) \frac{\Delta p_m}{(r_i + \delta_m) ln \left( \frac{r_i + \delta_m}{r_i} \right)} \tag{3.3}$$

In Equation 3.3 the driving force is the pressure difference between two reactor compartments, hence the exact amount of $O_2$ fed to the reactor will vary with each case simulated because it is dependent on local conditions. Because the exact membrane performance is of less interest here, and the comparison between different cases is much more important, simulations were performed with a fixed overall molar $CH_4/O_2$ feed

**Table 3.1:** Model equations describing concentration and temperature profiles in a reactor compartment.

*Mass conservation equation*

$$\varepsilon_g \frac{\partial \rho_g}{\partial t} = -\frac{\partial \rho_g v_g}{\partial z} - \phi^{\text{“}}_{m,tot} a_m \quad \text{with} \quad a_m = \frac{4 d_i}{d_o^2 - d_i^2}$$

*Component mass balance*

Gas phase:

$$\varepsilon_g \rho_g \frac{\partial \omega_i}{\partial t} = -\frac{\partial \rho_g v_g \omega_i}{\partial z} + \frac{\partial}{\partial z}\left(\rho_g D_{ax} \frac{\partial \omega_i}{\partial z}\right) + n_i a_s + \phi^{\text{“}}_{m,i} a_m$$

$$-D_{ax}\rho_g \left.\frac{\partial \omega_i}{\partial z}\right|_{z=0} + \rho_g v_g \omega_i|_{z=0} = \phi^{\text{”}}_{inlet,i} \qquad \left.\frac{\partial \omega_i}{\partial z}\right|_{z=L} = 0$$

Solid phase:

$$(1-\varepsilon_g)\rho_s \frac{\partial \omega_i}{\partial t} = \frac{1}{r^2}\frac{\partial}{\partial r} r^2 \left(\rho_g \sum_{k=1}^{N-1} d^0_{eff,i,k} \frac{\partial \omega_k}{\partial r} + \omega_i n_{tot}\right) + s_{r,i} M_i$$

$$\text{with: } s_{r,i} = (1-\varepsilon_g)\rho_s \sum_{j=1}^{N_{reac}} \nu_{i,j} r_j \text{ for i = 1..N}$$

$$\left.\frac{\partial \omega_i}{\partial r}\right|_{r=0} = 0 \qquad \rho_g \sum_{k=1}^{N-1} d^0_{eff,i,k} \left.\frac{\partial \omega_k}{\partial r}\right|_{r=r_p} + \omega_i n_{tot}|_{r=r_p} = n_i|_{r=r_p}$$

*Energy balance*

Gas phase:

$$\varepsilon_g \rho_g C_{p,g} \frac{\partial T}{\partial t} = -C_{p,g}\rho_g v_g \frac{\partial T}{\partial z} + \frac{\partial}{\partial z}\left(\lambda_g \frac{\partial T}{\partial z}\right) + \sum_{i=1}^{N} n_i a_s H_i$$

$$+ \sum_{i=1}^{N} \phi^{\text{“}}_{m,i} a_m H_i + \alpha_{b\to w} a_w (T - T_w)$$

$$-\lambda_g \left.\frac{\partial T}{\partial z}\right|_{z=0} + \rho_g v_g C_{p,g} T|_{z=0} = \sum_{i=1}^{N} H_i \phi^{\text{”}}_{inlet,i} \qquad \left.\frac{\partial T}{\partial z}\right|_{z=L} = 0$$

Solid phase:

$$(1-\varepsilon_g)\rho_s C_{p,s} \frac{\partial T}{\partial t} = \frac{1}{r^2}\frac{\partial}{\partial r} r^2 \left(\lambda_{eff,s} \frac{\partial T}{\partial r}\right) + s_h$$

$$\text{with: } s_h = (1-\varepsilon_g)\rho_s \sum_{j=1}^{N_{reac}} r_j \Delta H_{r,j}$$

$$\left.\frac{\partial T}{\partial r}\right|_{r=0} = 0 \qquad \lambda_{eff,s} \left.\frac{\partial T}{\partial r}\right|_{r=r_p} = \left.\sum_{i=1}^{N} n_i H_i\right|_{r=r_p}$$

ratio. A constant flux of $O_2$ is the default setting with which simulations have been performed, but also the influence of a linearly increasing or decreasing flux has been investigated. Particularly the decreasing flux profile, which is quite analogous to the flux expression in Equation 3.3, could decrease the (secondary) oxidation of the highly reactive $C_2H_4$ analogous to ODH of ethane (e.g. Hamel et al., 2008).

Heat and mass transfer correlations describing transport from the gas-phase to the catalyst particle and from the catalyst bed to the (membrane) wall were taken from literature. The heat transfer coefficient for gas-to-particle transport was calculated from the correlation presented by Gunn (1978) and the wall-to-bed heat transport coefficient was taken from Dixon and Cresswell (1979). All the relevant equations have been listed in Appendix 3.B.

The reaction kinetics for the oxidative coupling and steam reforming of methane were also taken from the literature. The kinetic model reported by Stansch et al. (1997) was used to calculate the reaction rates of the oxidative coupling of methane. The reaction rates were measured over a $La_2O_3$/CaO catalyst covering a wide range of feed concentrations at approximately atmospheric pressure and temperatures in the range of 700-955°C (Stansch et al., 1997). The selected $La_2O_3$/CaO catalyst is one of the most active OCM catalysts, resulting in high $C_2$ yields at relatively short reactor lengths and high space time velocities. For the steam reforming of methane, two kinetic models are commonly used both describing the intrinsic reaction rates of steam reforming on $Ni/Al_2O_3$ catalysts (Numaguchi and Kikuchi, 1988; Xu and Froment, 1989). Both models predict very similar results, although at very low $H_2$ pressure and only at initial conditions (i.e. $p_{H_2} \rightarrow 0$), the model of Xu and Froment overestimates the total reforming rate because the denominator in the kinetic model approaches infinity. However, a comparison between the models performed by de Smet et al. (2001) showed that at relevant process conditions both models give nearly identical results. The complete kinetic models are listed in Appendix 2.A (Chapter 2).

### 3.2.1 Numerical solution

In the numerical model, the mass and energy balances (Table 3.1) are simultaneously solved for different reactor compartments using a finite difference technique with higher order discretization schemes and adaptive time-stepping and automatic local grid refinement. To reduce the required calculation time, solving the homogeneous instead of the heterogeneous reactor model is optional for each compartment.

Adaptive time-stepping is especially relevant if accurate solutions during transient operation (such as reverse flow reactors) are required. For the dual function process only the steady state is of primary interest, however, this is computed here via a tran-

sient calculation from a uniform initial condition. Because significant accumulation (and reaction) in the porous particles is taking place, the initial time step should be very low ($t_{min} < 1 \cdot 10^{-5}$ s). The accumulation terms are calculated with an implicit Singly Diagonal Implicit Runge-Kutta (SDIRK) scheme. A spatially averaged tolerance criterion is applied to evaluate whether the current time step should be changed, comparing a solution obtained with time step $\Delta t$ with a solution calculated by means of two consecutive time steps $\Delta t/2$ (following Alexander, 1977; Smit et al., 2005b):

$$tol_t = \frac{1}{L} \sum_{i}^{N} \left( \left( z_{i+1/2} - z_{i-1/2} \right) \left| u_i^{n+1}(t + \Delta t) - u_i^{n+1}(t + 2 \cdot \Delta t/2) \right| \right) \tag{3.4}$$

If the calculated tolerance is higher than the specified maximum error, the time step is decreased with 10%. If it is lower, the time step is increased with 10%. As a consequence of the applied scheme the mass and energy balance have to be solved 3 times for one time step of $\Delta t$, but it was found that the extra computational effort per time step is much lower than the gain in calculation speed because of the larger attainable time steps. For additional information about the accuracy and the validation of the higher order SDIRK schemes, the reader is referred to Smit et al. (2005b).

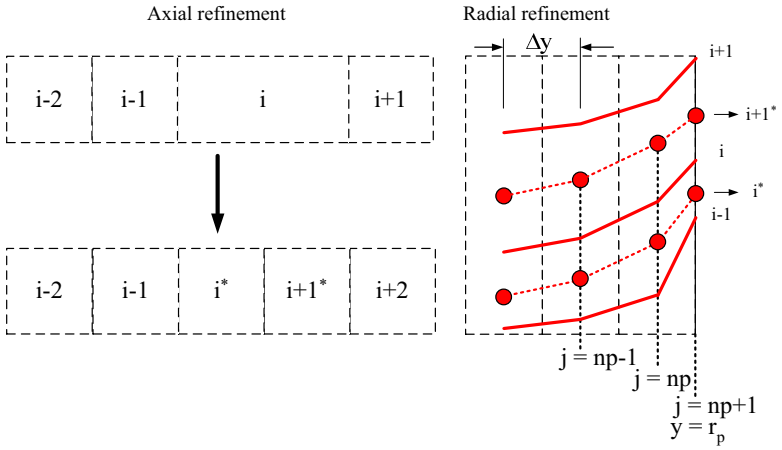


**Figure 3.2:** Local refinement procedure of the axial and radial concentration profiles (cells indicated with * denote the added grid cells).

The dispersion terms are discretized with a conventional 2nd order centered difference scheme, and the convection terms of the mass and energy balances are discretized by means of a higher order WENO35 discretization scheme (Smit et al., 2005a). With

Weighted Essentially Non-Oscillatory (WENO) discretization schemes higher order accuracy for the discretization of the convective terms can be achieved, especially in the case of steep gradients. The principle of the WENO schemes is essentially that higher order interpolating polynomials are combined to approximate the values of the variables at the cell faces in a monotonic fashion. The idea of using these polynomials for local grid adaptation has been developed by Smit et al. (2005a) and it was extended to the heterogeneous model given in Table 3.1. The implementation and validation of the schemes has been described in detail by Smit et al. (2005a).
The decision whether a grid cell should be removed or added is based on the gradient (smoothness) of the axial bulk gas phase profiles in the reactor. If the smoothness of a variable in the axial flow direction exceeds a certain threshold, a grid cell is added with the new value based on the polynomial obtained from the WENO scheme. On the other hand, if the smoothness is lower than the maximum smoothness, a grid cell is removed based on volumetric averaging of the cell values. If a grid cell is added (or removed), in principle information about the radial (intra-particle) profiles of this cell is missing and hence would require (re-)calculation from the initial condition. Because this is very time-consuming, the grid adaptation and interpolation procedure of the axial profiles is also applied to the radial cells (Fig. 3.2). This is a very acceptable assumption, since the radial profiles in different particles are only linked to the bulk gas phase concentration and not via convective transport. Because the WENO coefficients are only dependent on the numerical grid and not determined by the actual value of the variables (i.e. in the bulk gas phase), the grid adaptation and interpolation which is performed on the axial variables can also be applied to the radial cells (provided that the number of radial cells is constant for each particle).

### 3.2.2 Model settings

The reactor compartment, with a typical length of several meters, consists of a $\gamma$-$Al_2O_3$ tube filled with the (dual function) catalyst particles and inert particles at the inlet and oulet. As construction material for this reactor (porous) $Al_2O_3$ was selected, but in principle any other material which does not influence the $C_2$ selectivity too much will suffice. For the distributed feed, $O_2$ is fed via a porous $\gamma$-$Al_2O_3$ membrane with diameter $d_{m,ext}$, which is located at the centerline of the tube (see also Fig. 3.1). The total $O_2$ feed to the membrane tube is just enough to feed the intended amount to the reactor compartment, emulating a dead-end membrane, however for numerical reasons a very small gas stream is kept at the outlet of the shell side. This small exiting shell-side gas stream and the reactor walls will take up some heat from the reactor compartment in the simulations, thereby acting as a small heat sink, but the

influence is small.

The default model parameters have been listed in Table 3.2. A fixed overall $CH_4/O_2$ feed ratio of 4 was selected in this study, to demonstrate the feasibility of the dual function OCM/SRM catalyst in a packed bed membrane reactor. The catalyst bed was taken slightly longer than the length of the porous $Al_2O_3$ membrane (see also Fig, 3.1), to ensure total $O_2$ conversion in the reactor and prevent oxygen slip toward the reactor outlet.

**Table 3.2:** Default parameters for the case studies on OCM and the OCM/SRM process.

| Parameter | Value | Parameter | Value |
|---|---|---|---|
| $L_r$ | 1.0 m | $d_{r,int}$ | 0.05 m |
| $L_m$ | 0.8 m | $d_{m,ext}$ | 0.01 m |
| $L_c$ | 0.8 m | $d_p$ | 0.003 m |
| | | $d_w$ | 0.001 m |
| $\varepsilon_g$ | 0.4 | $\varepsilon_s$ | 0.6 |
| | | $\tau_s$ | 2 |
| $r_{OCM}$ | 250 x $10^{-6}$ m | $r_{SRM}$ | 100-500 x $10^{-6}$ m |

The design of an autothermal membrane reactor for the dual function OCM/SRM process is achieved in two stages. First, the packed bed membrane reactor is optimized for oxidative coupling of methane via modification of the reactor length and/or the membrane flux, so that a high maximized yield to $C_2H_4$ and $C_2H_6$ is obtained, before investigating the effects of introducing steam reforming activity. Next, the advantages of a dual function catalyst over oxidative coupling are illustrated by using the optimized OCM base case as a reference.

With the OCM base case, simulations were performed with the heterogeneous intra-particle model, investigating:

- The advantages of a packed bed membrane reactor, a.o. a better $C_2$ selectivity and heat management (temperature profiles), by comparison of the achievable $C_2$ yield in reactors with pre-mixed and distributed $O_2$ feed at non-isothermal conditions.
- The possibility to describe the results obtained with the intra-particle heterogeneous model by means of a fast short-cut model at isothermal conditions, which speeds up the simulations tremendously.
- Optimization of the $C_2$ product yield, by variation of the $O_2$ membrane flux at

different residence times, total gas throughputs and reactor lengths.

With the optimized OCM base case (i.e. reactor length and optimum $O_2$ membrane flux), the dual function process is tuned to achieve autothermal conditions. The required SRM core radius ($r_{SRM}$) is first based on the overall OCM reaction enthalpy, to formulate an initial particle configuration. The SRM core diameter is varied at both (idealized) isothermal and non-isothermal conditions, and the influence on achieving autothermal operation is studied.

- The influence of the SRM core radius on the reactor performance is studied, by comparing i.e. the $C_2$ losses, $CH_4$ conversion and the local heat production with only oxidative coupling, initially at isothermal conditions.

- The effect of modifying the axial $O_2$ distribution profile on the energy balance and the $C_2$ yield is investigated as well, both for OCM and the dual function OCM/SRM process.

- Finally, the temperature profiles (non-isothermal optimization) of the dual function process are minimized, by varying the SRM core radius ($r_{SRM}$) and assessing the influence on the $C_2$ losses.

For the combined OCM/SRM process, the aim is to achieve autothermal operation and simultaneously producing a mixture of $C_2$ and $CO/H_2$ rich gas. In Table 3.3, the cases are listed that have been used for the optimization of the $C_2$ yield with only OCM, and to achieve autothermal conditions with the dual function OCM/SRM process.

## 3.3 Only oxidative coupling of methane

In this section, the advantages of distributive $O_2$ feeding for the OCM process is demonstrated by comparing simulation results for the performance of a fixed bed reactor with pre-mixed feed with a packed bed membrane reactor at non-isothermal conditions. In addition, a fast (homogeneous) short-cut model is compared with the comprehensive heterogeneous intra-particle reactor model (described in Table 3.1), verifying whether effects of intra-particle concentration gradients can be sufficiently accurately accounted for with a modified Thiele modulus approach. Subsequently, the $C_2$ yield of the packed bed membrane reactor is optimized (e.g. as a function of the oxygen permeation rate) using the extensive heterogeneous model.

**Table 3.3:** Default model settings for the case A (constant feed flow) and case B (constant residence time) on OCM and OCM/SRM process at constant inlet $CH_4$ flow (Overall $CH_4/O_2$=4, $x_{CH_4}$=0.3, $x_{H_2O}$=0.4, $x_{N_2}$=0.3, T=800°C, $p_{in}$=150 kPa, isothermal).

| Case | $\rho_g v_g$ [$kg_{CH_4}/m^2/s$] | $\phi''_{m,O_2}$ [$mol/m^2/s$)] | $L_r$ [m] | GHSV [1/h] |
|---|---|---|---|---|
| A | | 0.0273 | 0.5 | 497 |
| | | 0.0136 | 1.0 | 249 |
| | 0.050 | 0.0068 | 2.0 | 124 |
| | | 0.0045 | 3.0 | 83 |
| | | 0.0034 | 4.0 | 62 |
| B | 0.012 | | 0.5 | 124 |
| | 0.025 | | 1.0 | 124 |
| | 0.050 | 0.0068 | 2.0 | 124 |
| | 0.075 | | 3.0 | 124 |
| | 0.099 | | 4.0 | 124 |

### 3.3.1 Pre-mixed versus distributed feed

With pre-mixed feed of the reactants, a high $CH_4$ conversion (> 30%) can obviously only be achieved if the initial $O_2$ concentration is also high. As a consequence, the adiabatic temperature increase for this scenario is very high, which may be detrimental for the reactor performance (Westerterp et al., 1963):

$$\Delta T_{ad} = \frac{\zeta_{CH_4} \Delta H_{r,av} c_{CH_4,0}}{\rho_g C_{p,g}} \tag{3.5}$$

Based on the initial conditions and an average reaction enthalpy of 200 kJ/mol, it can already be inferred that with an $O_2$ conversion of 100%, the reactor outlet temperature would increase more than 300°C, which is unacceptable. At even higher $O_2$ inlet concentrations, which is required to obtain a high conversion with pre-mixed feed mode of operation, the temperature rise will be even higher.

With the heterogeneous intra-particle reactor model, simulations were performed at an overall $CH_4/O_2$ ratio of 4, and the influence of the temperature profiles on the reactor performance with only oxidative coupling activity is verified at non-isothermal conditions, using pre-mixed feed, with the adiabatic and cooled mode of operation. In all cases, the center tube with an $O_2$ flow was present and the heat exchange via the inner (membrane) wall from the reactor is accounted for and the reaction rates are

corrected for the presence of intra-particle concentration and temperature gradients.

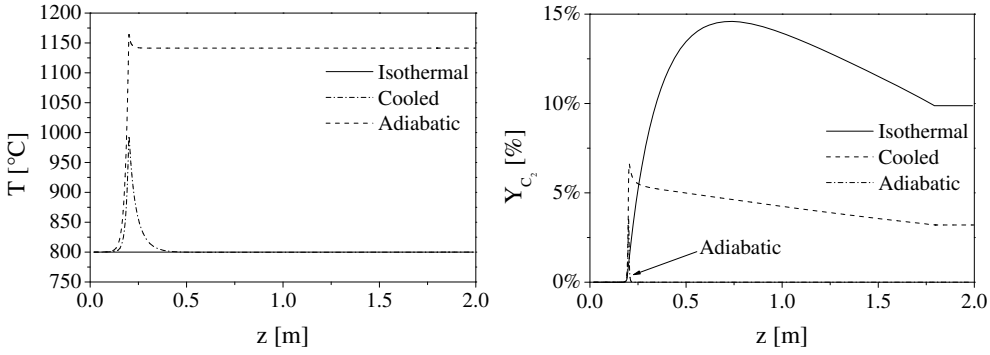


**Figure 3.3:** Comparison of gas phase axial temperature (a) and $C_2$ yield (b) profiles for pre-mixed feed of $O_2$ at isothermal, adiabatic and cooled conditions (conditions are listed in Section 3.2.2, case A with $L_r$=2 m).

The calculated temperature profiles are depicted in Fig. 3.3a. The results for the adiabatic reactor can only be used as indication, as it should be noted that the maximum temperature at which the kinetic model has been validated is 955°C (Stansch et al., 1997). However, it can be concluded from the shown axial temperature profiles for an overall $CH_4/O_2$ feed ratio of 4, that the temperature rise in an adiabatic reactor is very large and almost 300 °C, which has a detrimental influence on the $C_2$ selectivity and yield (Fig. 3.3b). The lower temperature peak observed in the adiabatic simulation results is caused by the energy losses to the membrane tube compartment, which lowers the maximum temperature to some extent. Nevertheless, compared to isothermal operating conditions, nearly all the $C_2$ components have been oxidized and the maximum attained yield of 15% at isothermal conditions, is never reached and the high temperature probably deactivates the OCM catalyst.

Removal of reaction heat can be realized via external interstaged cooling (i.e. using multiple reactors) or by in situ direct cooling of the entire reactor. Assuming a maximum allowable temperature rise of 50 °C, the first option is less desired because 5-6 stages are already required for a relatively small reactor length of 2 m. If the entire reactor outer wall is cooled the temperature can be decreased to approximately 800°C (Fig. 3.3a), however, the maximum temperature peak is still 200 °C higher than the inlet temperature. Further decrease cannot be achieved without the risk of extinction of the reaction and affecting the overall selectivity. Thus, although pre-mixing of

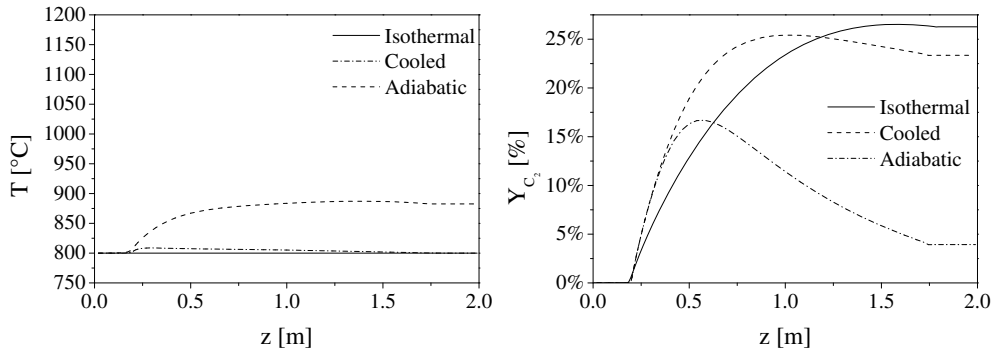


**Figure 3.4:** Temperature (a) and $C_2$ yield (b) axial profiles for isothermal, adiabatic and cooled operation of OCM reactor with distributed feed of $O_2$ (conditions are listed in Section 3.2.2, case A with $L_r$=2 m and overall $CH_4/O_2$ feed ratio = 4).

oxygen and methane might be the most straight-forward, however, temperature control remains difficult because the high initial temperature peak requires the removal of a large amount of heat in a narrow zone in the reactor. The relatively high required $O_2$ inlet concentrations inevitably lead to excessive (adiabatic) temperature increases in the reactor, which limits the allowable reactor diameter and requires complex reactor design to meet cooling demands. As a comparison, the much more moderate temperature profiles obtained by using distributed feed of $O_2$ in an adiabatic or cooled reactor are displayed in Fig. 3.4a. As shown in Fig. 3.4b, the yield of an adiabatic membrane reactor is unacceptably low, but from the much lower maximum temperatures (800 °C versus 1000 °C) and the improved $C_2$ yield (>25% versus 15%) for the isothermal and cooled reactor it can be inferred that by distributing the heat production and by using a cooled reactor the performance increases remarkably. Thus, the use of an integrated heat sink, by means of the dual function OCM/SRM catalyst, it will become possible to remove the excess reaction heat even more efficiently, thereby preventing too high temperatures and unacceptably low $C_2$ selectivities.

### 3.3.2 Short-cut model to approximate intraparticle effects

To account for the presence of intra-particle concentration and temperature profiles, the time-consuming heterogeneous reactor model has to be used. Especially for optimization it is desired to have a model that can predict the reactor performance very fast with reasonable accuracy. With a homogeneous reactor model, the intra-particle

mass transfer limitations were analytically calculated by means of an effectiveness factor $\eta_{O_2}$ obtained from a modified Thiele modulus (van Sint Annaland et al., 2007a,b), see also Chapter 2. The mass and energy balance in this homogeneous model are similar to the equations for the gas phase in Table 3.1, whereas correlations for the effective mass and heat dispersion are listed in Appendix 3.B:

$$\phi'_{O_2} = \frac{r_p}{3}\sqrt{\frac{\sum_{j=1}^{N_{reac}} \frac{n_j+1}{2} k_j c_{O_2,bulk}^{n_j}}{D_{eff,O_2}}} \tag{3.6}$$

It was shown that a parallel-consecutive network of oxidation reactions could be accurately solved with this approach, but that deviations start to occur at higher $CH_4$ conversions. At sufficiently high hydrocarbon concentrations (which is the case for OCM), the effectiveness factor can then be calculated with the well-known expression for first-order irreversible reactions:

$$\eta_{exact,O_2} = \frac{3\phi'_{O_2} - tanh(3\phi'_{O_2})}{3(\phi'_{O_2})^2 tanh(3\phi'_{O_2})} \tag{3.7}$$

The effectiveness factor only takes into account the influence of intra-particle molecular diffusion rates on the overall conversion rate, however, because of the presence of intra-particle concentration profiles, the local oxygen to carbon ratio in the particle and thus the $C_2$ selectivity will also differ from that computed with the bulk gas phase composition. Therefore, the reaction rates which are calculated with the bulk gas phase composition require a correction to account for the change in selectivity, analogous to van Sint Annaland et al. (2007a):

$$\langle\sigma\rangle = 1 - F_{1-\sigma}(1-\sigma_b) \tag{3.8}$$

Where $\langle\sigma\rangle$ represents the averaged selectivity taking into account mass transfer limitations in the catalyst particle and $\sigma_b$ represents the selectivity in the bulk gas phase without diffusion limitations. The factor $F_{1-\sigma}$ depends on the modified Thiele modulus (i.e. the extent of the concentration profiles), the ratio of the (pseudo) first order reaction rate constants ($p_{nm}$) and the $O_2$ reaction order of the unselective and the selective reactions (n,m). For a system of 2 reactions, $F_{1-\sigma}$ was calculated for a wide range of conditions, see van Sint Annaland et al. (2007a). From Fig. 3.5 it is clear that $F_{1-\sigma}$ is lower than unity for the entire range of Thiele moduli, meaning that the selectivity calculated with bulk gas phase conditions underpredicts the actual selectivity based on intra-particle concentration profiles. At higher Thiele moduli and with a larger difference in selective and unselective reaction rates, this effect is even more

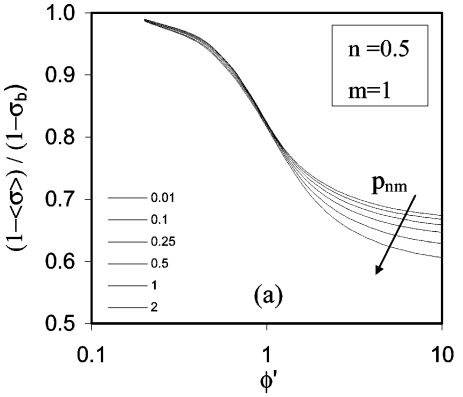


**Figure 3.5:** Influence of intraparticle transport limitations on the average product selectivity as function of the modified Thiele modulus for different values of $p_{nm}$ ($c_b/C_{Ab} = 0.1$ and $c_b/C_{Pb} = 0.1$ and $n = 0.5$, $m = 1$) (reproduced from: van Sint Annaland et al. (2007a))

pronounced. For a multicomponent system with more than two oxidation reactions, like OCM, determining the value of $p_{nm}$ is not straightforward and dependent on the position in the reactor. Based on the calculations performed in Chapter 2, it was determined that the Thiele modulus for oxidative coupling varies between 10 and 20, thus a value for $F_{1-\sigma}$ between 0.5 and 0.7 is anticipated. The axial concentration, yield and conversion profiles are calculated with the settings displayed in Table 3.3 and $F_{1-\sigma} = 0.6$. First, only the correction for the effectiveness factor from Equation 3.7 was used. The decrease in required calculation time from $\approx$ 480 to 10 min is very advantageous, especially for optimization purposes of either OCM or the dual function OCM/SRM process. Clearly, the $CH_4$ conversion of the analytical model is nearly identical to the conversion calculated with the full heterogeneous model taking into account the intra-particle concentration and temperature profiles. However, the selectivity is greatly overestimated, leading to unrealistically high $C_2$ yields at lower $O_2$ fluxes(Fig. 3.6b).

If the selectivity correction factor from Equation 4.5 is also applied, it is shown in Fig. 3.6c that the $CH_4$ conversion profiles can still be quite accurately calculated with this short-cut model and that the $C_2$ yield can be predicted much better (Fig. 3.6d). Toward the end of the reactor and particularly at smaller reactor lengths, the $CH_4$ conversion is slightly underestimated which is related to a lower $CH_4$ reaction rate. From the lower $C_2$ selectivity and the higher bulk gas phase $O_2$ concentration (Fig. 3.6e,f) it can be derived that the secondary oxidation reactions are slightly overestimated at the end of the reactor. Clearly, the $C_2$ yield drops and is lower than

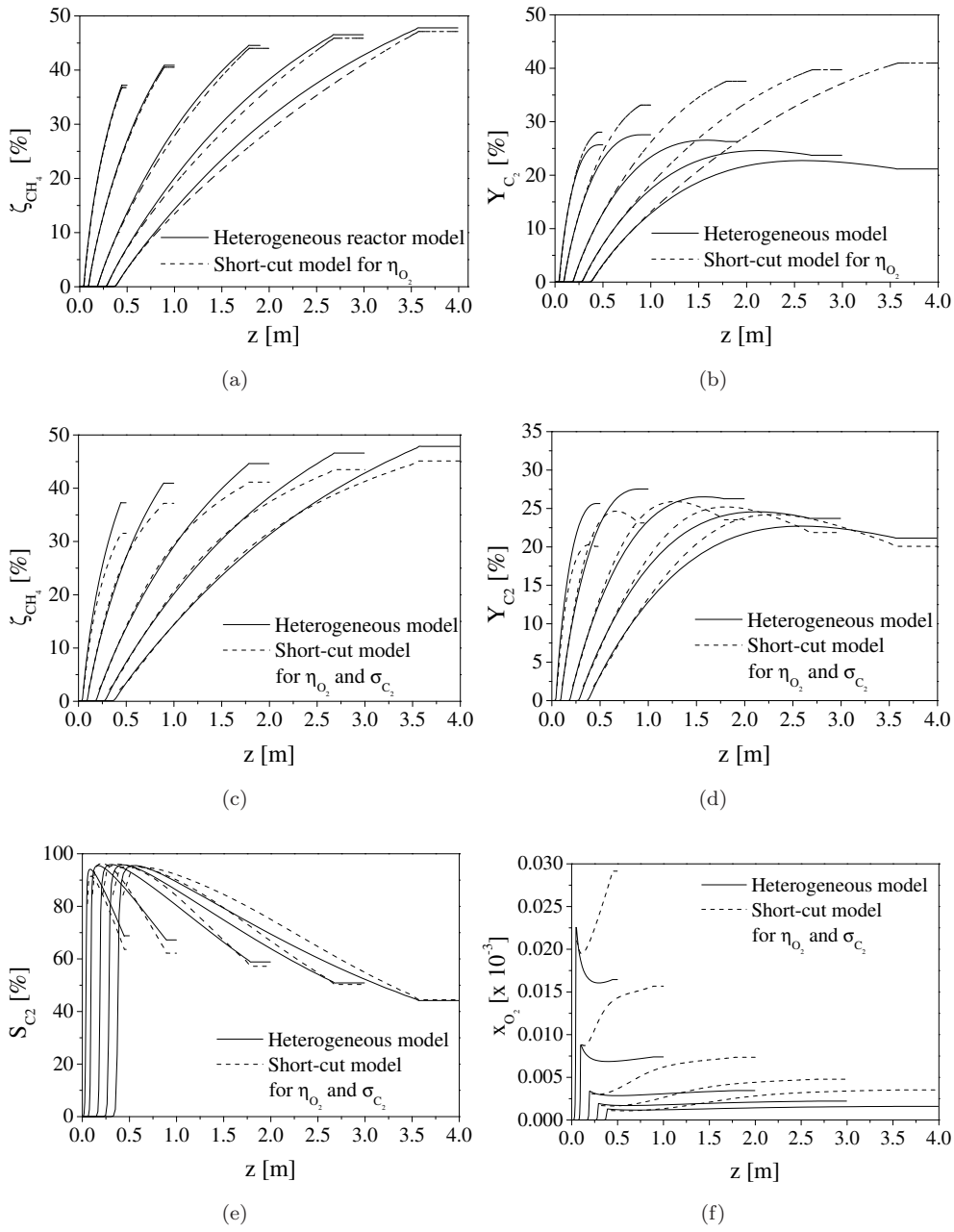


**Figure 3.6:** Comparison of the results from the short-cut model (dashed lines) with the full heterogeneous, intra-particle model (solid lines) without selectivity correction (a-b) and with selectivity correction factor ($F_{1-\sigma} = 0.6$) (c-f) for OCM in a membrane reactor at overall $CH_4/O_2$ ratio of 4 and constant inlet flow (conditions see Section 3.2.2, case A).

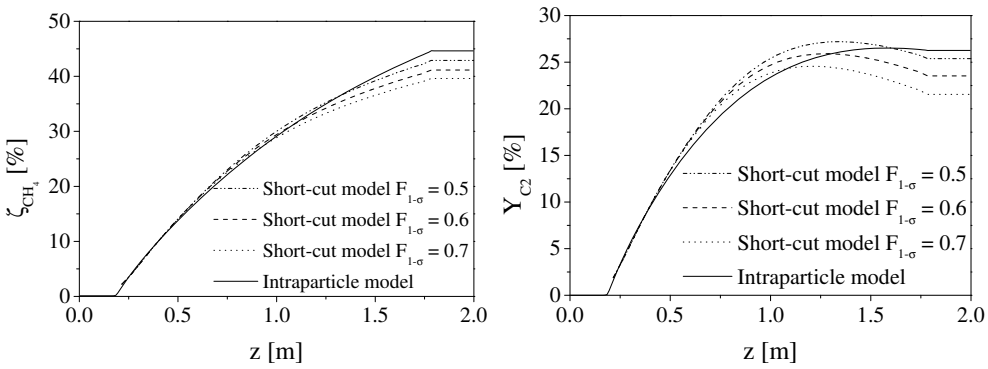


**Figure 3.7:** Sensitivity of analytical reactor model on $F_{1-\sigma}$ for a reactor length of 2 m at overall $CH_4/O_2$ ratio of 4 and constant inlet flow (conditions see Section 3.2.2, case A and $L_r$=2 m).

the yield calculated with intraparticle model, which is related to the assumption that $F_{1-\sigma}$ is constant. The sensitivity of the reactions to $F_{1-\sigma}$ is shown in Fig. 3.7, and it can be seen that a better match between analytical and intraparticle model can be obtained if $F_{1-\sigma}$ would be varied along the reactor length.

For insight in the intra-particle concentration (and if desired, temperature profiles), it is still required to perform simulations with the full intraparticle model, but for a first estimate of the required reactor configuration, the short-cut model can be effectively used.

### 3.3.3 Optimization of product yield

With only oxidative coupling of methane, the extent of intra-particle concentration gradients and their effect on the volumetric conversion rates were investigated by comparing results that were obtained with the heterogeneous, intra-particle model at isothermal conditions (see Table 3.1). Distributed feed of $O_2$ was applied with an overall $CH_4/O_2$ feed ratio of 4, with a constant $O_2$ flux that can be realized by a sufficiently high $O_2$ flow rate through the membrane tube. The residence time in the catalytic reactor compartment was varied by modification of the reactor lengths at a constant inlet flow of $CH_4$ and $O_2$, according to case A (Table 3.3).

The steep intra-particle $O_2$ concentration gradients and concomitantly low catalyst particle utilization (Fig. 3.8), limits the conversion per unit reactor/particle volume. Although this is disadvantageous for the required amount of catalyst, the unselective oxidation reaction rates are decreased and the local, intra-particle $C_2$ selectivity in-

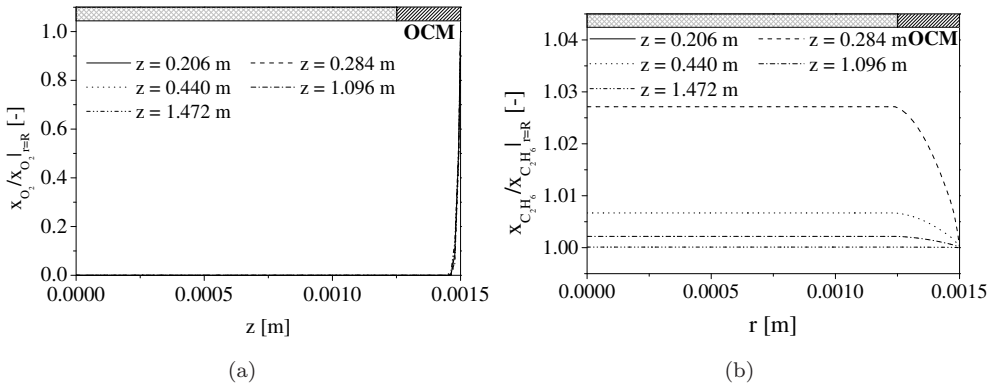


**Figure 3.8:** Normalized radial intra-particle $O_2$ (a) and $C_2H_6$ concentration profiles (b) at different axial locations in the reactor (L=2 m) at constant inlet flow (conditions see Table 3.3, case A).

creases (as shown in Chapter 2), because of the lower intra-particle $O_2$ concentration and the difference in $O_2$ reaction orders. In addition, because of the low catalyst effectiveness factors for OCM, a steam reforming catalyst can be implemented in the particle center and contact of the SRM catalyst with $O_2$ can be prevented. Moreover, the reaction heat for $C_2$ production is also much lower than for $CH_4$ oxidation, because of the higher $C_2$ selectivity, hence one would expect that a higher selectivity also results in a lower temperature rise in case of non-isothermal systems. However, because of the increased $C_2$ oxidation reaction rates due to increasing $C_2$ concentrations downstream, cooling remains required.

If a shorter reactor is used, so that the residence time decreases, the $O_2$ membrane flux increases (satisfying constant inlet flow, case A), so that the local $O_2$ supply rate exceeds the local $O_2$ consumption rates, leading to a higher local $O_2$ concentration, a higher local $O_2/CH_4$ ratio and thus a lower selectivity downstream (Fig. 3.9b). The initial $C_2$ selectivity, however, is for all the cases comparable and higher than 95% because the inlet $CH_4$ concentration remains unaffected by variation of the residence time (Fig. 3.9b). From the conversion and selectivity profiles it can be further noticed that a maximum yield of 28% is achieved if a reactor length of 1 m is applied, corresponding to a membrane flux of approximately 0.01 mol/m$^2$/s (Fig. 3.9a). The maximum obtained yield is currently located in the middle of the reactor instead of at the outlet, because this is determined by the ratio of the $O_2$ flux and the $C_2$ reaction rates. This can be modified by optimizing the $CH_4/O_2$ feed ratio.

It is also investigated whether the $C_2$ yield can be further improved, by repeating the previous simulations for different $O_2$ fluxes but now with a constant residence

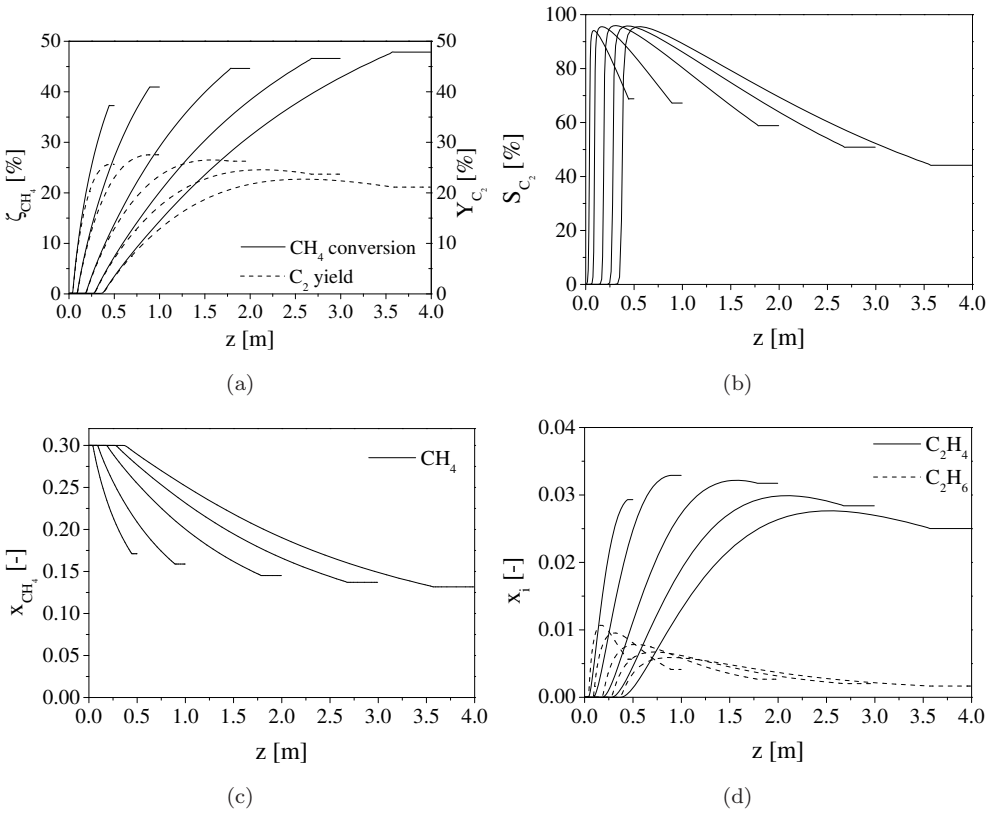


**Figure 3.9:** Axial (a) $CH_4$ conversion and $C_2$ yield profiles, (b) $C_2$ selectivity profiles, (c) $CH_4$ mole fraction and (d) $C_2H_4$ and $C_2H_6$ mole fraction profiles for OCM in a membrane reactor calculated with the full intra-particle heterogeneous reaction model for various reactor lengths (and corresponding $O_2$ fluxes to maintain the overall $CH_4/O_2$ ratio at 4) at constant inlet flow (conditions see Table 3.3, case A).

time, which was achieved by variation of both the reactor length and the total inlet flow (at constant feed ratio, Case B).

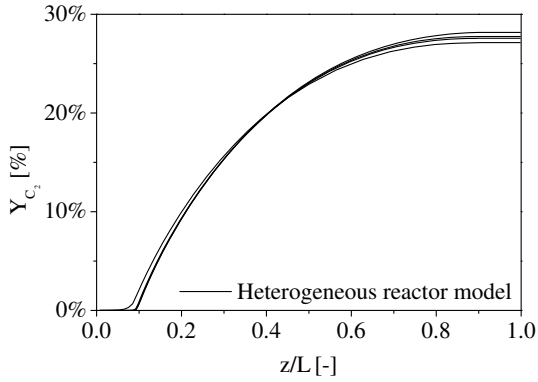


**Figure 3.10:** Influence of the reactor length on the performance of OCM at constant gas residence time in a packed bed membrane reactor using the intra-particle model at an overall $CH_4/O_2$ ratio of 4 (conditions listed in Table 3.3, case B).

In Fig. 3.10 it is shown that unlike the previous calculations, the conversion and yield are hardly influenced by variation of the gas velocity (and reactor length). Because the residence time is kept constant, the gas velocity and the local (volumetric) reaction rates increase proportionally with the reactor length so that the concentration profiles are hardly influenced. As a result, the axial $O_2$ concentration profile is relatively independent of the reactor length and the maximum $CH_4$ conversion of approximately 40-42% and the total $C_2$ yield of 28% can be achieved at all reactor lengths at a relatively constant selectivity to $C_2H_4$ and $C_2H_6$, indicating that the residence time has a strong influence on the results.

The capacity of the reactor can be increased by increasing the gas inlet flow rate. Therefore, the throughput of the reactor was increased up to a factor 4 (compared to base Case A, $L_r$= 1 m) and the influence on the performance was investigated at isothermal conditions. If the $C_2H_4/C_2H_6$ production per $m^3$ reactor can be increased, the construction, catalyst and equipment costs can be decreased. The total pressure drop inevitably increases from 0.003 to 0.03 bar/m, which is however well below the acceptable maximum allowable pressure drop for fixed beds of about 0.1 bar/m. An important issue here is that the trans-membrane pressure drop ($>$ 1 bar) remains much higher than the pressure drop in the fixed bed, because only in this way a controlled dosage of $O_2$ can be accomplished. In Fig. 3.11a it is shown that the amount of

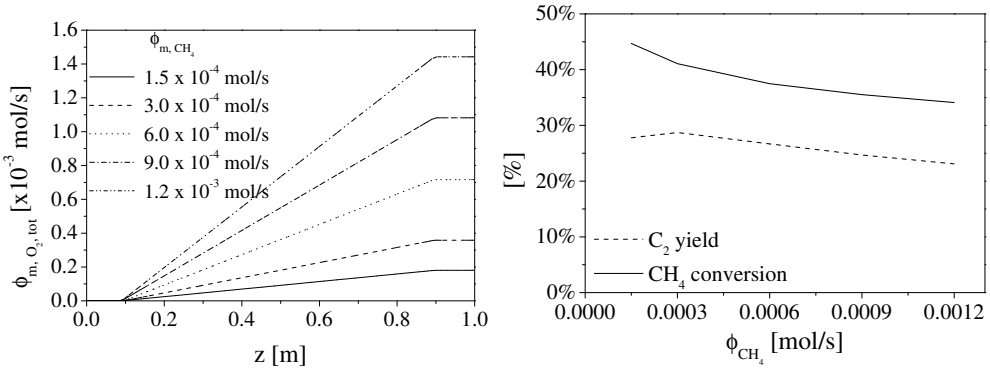


(a) (b)

**Figure 3.11:** (a) Axial $O_2$ membrane flow profile and (b) the influence of the feed flow on the $CH_4$ conversion and $C_2$ yield at overall $CH_4/O_2$ ratio of 4 and $L_r$=1 m (conditions listed in Table 3.3, case B).

$O_2$ added to the reactor (and the flux) increases proportionally with the $CH_4$ inlet flow. As a consequence, the $CH_4$ conversion decreases from 44 to 34% which is caused by the increasing $O_2$ concentration and a concomitant lower $C_2$ selectivity and yield (Fig. 3.11b). Because the unselective ($CH_4$) oxidation reactions consume more $O_2$ per converted mole of $CH_4$, the $C_2$ yield decreased from 28 to 23% although the total productivity per $m^3$ reactor increased with a factor 4. Normally cooling problems will arise with larger volumetric reaction rates, however, in this work the heat sink for the dual function process is integrated in the catalyst particle which strongly reduces cooling issues. It can be argued whether a lower $C_2$ yield at higher production rate is preferred over a slightly higher $C_2$ yield; the differences are relatively small hence a higher production rate may be beneficial. For the demonstration of the dual function process, the low flow case is chosen and the high flow case is used once to demonstrate the feasibility of the process at these conditions.

### 3.3.4 Conclusions OCM

By comparison of OCM with pre-mixed and distributed feeding of $O_2$, it was shown that selective production of $C_2$ products is only possible if the temperature rise in the reactor is low, which can be achieved in a packed bed membrane reactor. With this reactor type, the optimal operating conditions for OCM were determined by investigating the effects of the overall residence time, $O_2$ membrane flux and the total throughput. It was found that the residence time has a large influence on the secondary oxidation reactions of $C_2H_4$ and $C_2H_6$, which can be controlled by the

membrane flux and the reactor length at isothermal conditions. Cooling of this reactor is still required, because at non-isothermal conditions in e.g. an adiabatic reactor, the very exothermic $C_2$ oxidation reactions lead to unacceptably high temperatures. Therefore, the optimized OCM base cases will serve as initial configuration for the dual function process, where the integrated heat sink will be used to minimize the temperature increase in the reactor.
For the calculation of the OCM reaction rates in a packed bed (membrane) reactor, a fast short-cut model which accounts for the intra-particle concentration profiles via effectiveness and selectivity correction factors can be used for optimization. If a more accurate solution of both concentration and temperature profiles is desired, it is essential to use the more time-consuming heterogeneous reactor modeling.

## 3.4 Dual function process

In this section, simulations results for the dual function catalyst implemented in the packed bed membrane reactor are discussed. An initial particle configuration, i.e. the required SRM core radius to achieve autothermal operation, is derived from the overall reaction heat production of the oxidative coupling cases from the previous section. With only oxidative coupling at isothermal conditions, it can be seen in Fig. 3.13a that particularly in shorter reactors, considerable amounts of heat are generated per unit reactor volume because the local reaction rates largely depend on the local $O_2$ flux. For example, with a reactor length of 2 m the heat production amounts approximately 25 kW/m$^3$, whereas about 150 kW/m$^3$ is produced if the reactor length is decreased (with the same inlet flow rate) to 0.5 m. In all cases, the largest heat production will be located at the end of the reactor, which is caused by the relatively high reaction enthalpy of the $C_2$ oxidation reactions ($\Delta H^{298} = 1300 - 1500$ kJ/mol). Acceptable $C_2$ yields with oxidative coupling can however only be achieved if the reactor temperature is maintained around 800°C by efficient cooling of the reactor. This can be partially achieved by reduction of the $O_2$ flux near the end of the reactor (i.e. by using a flux profile), and by applying the dual function catalyst which lowers the heat production rates even more because the local overall reaction heat production is decreased by the integrated steam reforming reactions.

If the reforming reaction rates are totally governed by intra-particle diffusion (see Fig. 3.12), the maximum required steam reforming reaction rate and hence the maximum amount of $CH_4$ that can react to synthesis gas under locally autothermal conditions can be directly estimated from the volumetrically averaged heat liberation of

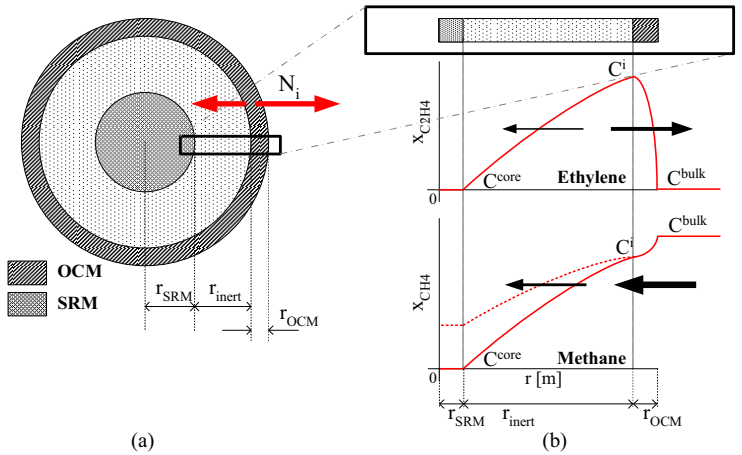


**Figure 3.12:** (a) Schematic layout of dual-function catalyst particle and (b) typical $CH_4$ and $C_2H_4$ intraparticle mole fraction profiles (symbols explained in the symbols list).

oxidative coupling (Fig. 3.13a).

$$r_{SRM} = r_p \frac{Y}{1+Y} \quad \text{with} \quad Y = \frac{-\Delta H_{OCM} R_{OCM}}{\Delta H_{SRM} D_{eff} 4\pi r_p \left(c_{\mathrm{CH_4},b} - c_{\mathrm{CH_4},core}\right)} \tag{3.9}$$

Taking a constant effective diffusion coefficient of $2 \cdot 10^{-5}$ $m^2/s$ and assuming that the driving force is only determined by the $CH_4$ bulk concentration, which is a reasonable assumption, $r_{SRM}$ follows directly from Equation 3.9.

The overall inlet flow rate was kept constant, the heat production rate and therewith $r_{SRM}$ is proportional to the $O_2$ flux, so that the heat production rate for a reactor length of 0.5 m is almost 10 times larger than in a reactor of 4 m length (Fig. 3.13a,b), analogous to Equation 3.9. Compared to the single particle simulations in the previous chapter, the required core radii calculated here (Fig. 3.13b) are much smaller ($r_{SRM} \approx 500$ $\mu$m vs. $r_{SRM} \approx 20$ $\mu$m), which is related to the assumption of isothermal conditions and the much lower steady state $O_2$ bulk gas phase concentration ( 0.1 wt% $O_2$ vs. 0.001 wt% $O_2$) which leads to somewhat higher $C_2$ selectivities and lower heat generation rates.

### 3.4.1 Influence of SRM core diameter

With the SRM core radius obtained from Fig. 3.13b as initial condition ($r_{SRM}$ between $10 - 20\mu$m), simulations were performed with the intra-particle reactor model with the dual function catalyst and real reforming reaction kinetics. The results were

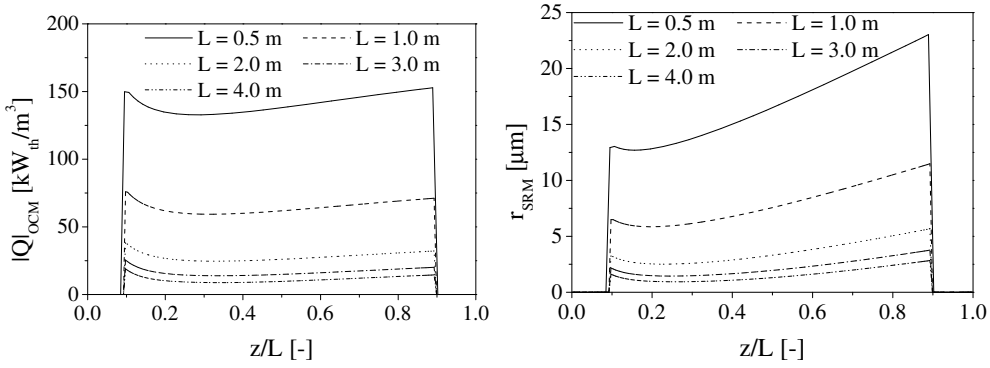


(a) (b)

**Figure 3.13:** Calculated reaction heat production from oxidative coupling (a) and the corresponding required core radius of the steam reforming activity (b) to achieve autothermal conditions (Equation 3.9) at various reactor lengths and $CH_4/O_2$ = 4 (based on Case A, Table 3.3).

compared with the performance of only oxidative coupling of methane, investigating the differences in e.g. $C_2$ production and $CH_4$ conversion. The influence of real steam reforming and water-gas-shift (equilibrium) reaction kinetics and the change of the adsorption isotherms will inevitably lead to a somewhat different catalyst layout than derived with Equation 3.9, hence three cases for the dual function process were calculated with SRM core radius of 10, 15 and 20 $\mu$m, implemented in 3 mm particles that were also used for the OCM base case. The particle porosity was not modified.

Compared to OCM, the $C_2$ yield and selectivity decrease because of the added $CH_4$ and $C_2$ steam reforming reactions (Fig. 3.14a). From the $C_2$ fluxes (Fig. 3.14b) it can be discerned that the actual loss of $C_2$ products due to additional oxidation and reforming remains below 30% and that the largest differences between OCM and the dual function process occur at the end of the reactor (z > 1 m). The additional synthesis gas production, displayed in terms of $CO_x$ (=CO + $CO_2$ ) mole flux, has risen from 0.13 to almost 0.28 mol/m$^2$/s meaning an increase of more than 100% ($r_{SRM} = 15\mu$m). It can be seen that the $CH_4$ conversion has increased compared to OCM (Fig. 3.14c), and that the $CH_4$ steam reforming reactions contribute approximately with 50% to the additional CO and $CO_2$ production and that the remainder of carbon oxides is produced either via primary or secondary oxidation reactions on the OCM catalyst. Reforming reactions of $C_2$ components only plays a small role, which can be concluded from the low driving force for $C_2$ reforming reactions compared to $CH_4$ reforming ($x_{bulk,CH_4}/x_{bulk,C_2}$>10). The concentrations of $CH_4$ and $C_2$ products

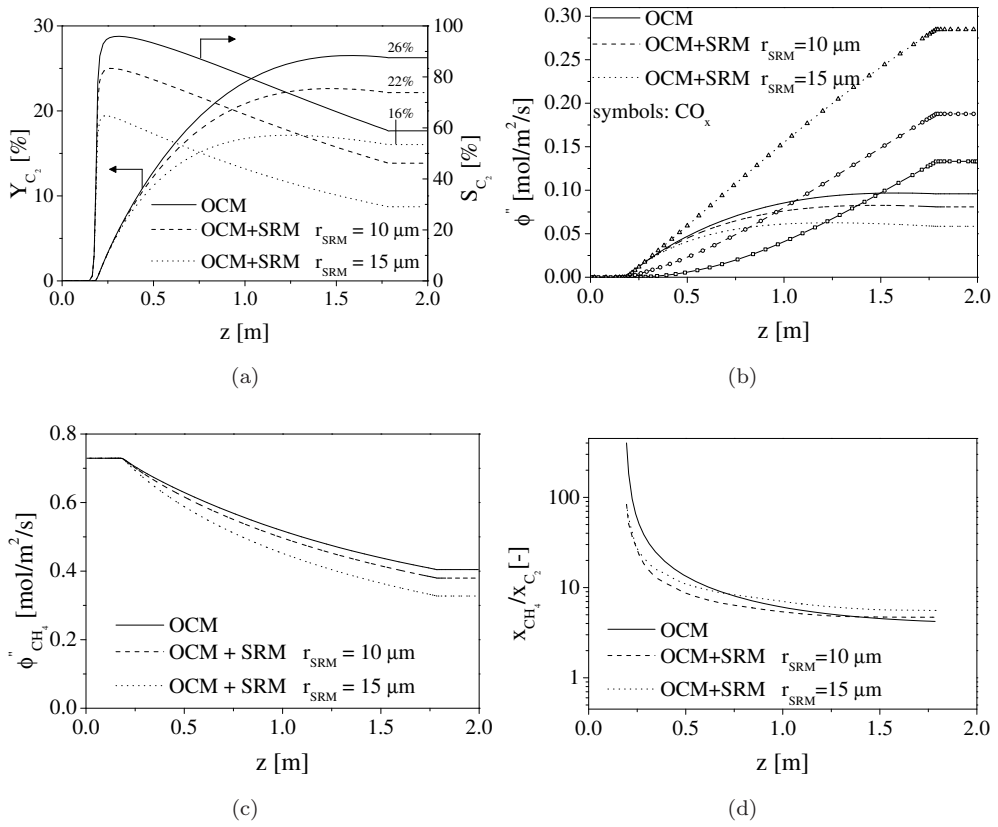


**Figure 3.14:** Comparison of the dual function OCM/SRM process with only OCM in a membrane reactor on the (a) $C_2$ selectivity and yield, (b) $C_2$ and $CO_x$ mole fluxes, (c) $CH_4$ mole flux (conversion) and (d) ratio of $CH_4$ to $C_2$ in gas phase ($x_{CH_4}$=0.3, $x_{H_2O}$=0.4, $CH_4/O_2$=4, other conditions see Table 3.3).

have to be at least of equal magnitude (i.e. $x_{bulk,CH_4}/x_{bulk,C_2}$=1) for a significant contribution of $C_2$ reforming, which is clearly not the case (Fig. 3.14d).

As a consequence of the $CH_4$ reforming reactions, a large part of the OCM reaction heat is consumed by the reforming reactions (Fig. 3.15). The first part of the reactor operates at near autothermal conditions ($|Q| = 0$) if a core radius of 15 $\mu$m is used, however, the dual function process is still quite exothermic at lengths more than 0.75 m, which is caused by the highly exothermic $C_2$ oxidation reactions ($\Delta H_r > 1300 - 1500$ kJ/mol). Thus, the dual function catalyst is able to simultaneously increase the $CH_4$ conversion and to produce more $CO_x$ products while the $C_2$ losses are acceptable. For achievement of autothermal operation efficient cooling near the reactor outlet is required, which means that a larger core radius for reforming is needed

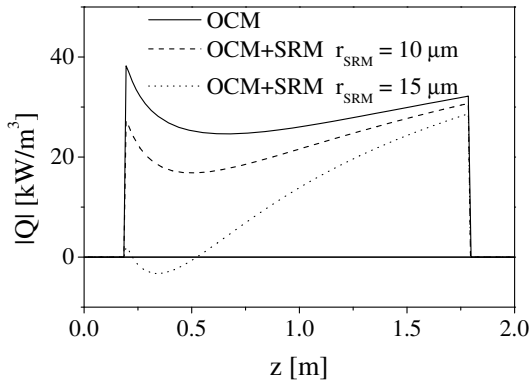


**Figure 3.15:** Calculated nett reaction heat production from simulations with different configurations of the dual function OCM/SRM process ($x_{CH_4}$=0.3, $x_{H_2O}$=0.4, $CH_4/O_2$=4, other conditions see Table 3.3).

and hence non-uniform distribution of catalytic activity throughout the reactor, which is not practical from industrial point of view. The secondary oxidation reactions could also be minimized by e.g. changing the pore structure or by using $O_2$ membrane flux profiles, so that the application of a uniform catalyst configuration becomes more feasible.

### 3.4.2 Influence of oxygen membrane flux profiles

With a high concentration of the selective reaction products at the reactor outlet, the concomitant increase of the reaction heat production makes it increasingly difficult to achieve autothermal conditions without ending up with a complex reactor and particle catalyst bed design.

$$\phi''_{O_2} = \begin{cases} \dfrac{\phi_{O_2,tot}}{\pi d_o \frac{1}{2} (z_r - z_l)^2} (z - z_l) & \text{linearly increasing with z} \\ \dfrac{\phi_{O_2,tot}}{\pi d_o (z_r - z_l)} & \text{constant} \\ \dfrac{\phi_{O_2,tot}}{\pi d_o \frac{1}{2} (z_r - z_l)} \left(1 - \dfrac{z - z_l}{z_r - z_l}\right) & \text{linearly decreasing with z} \end{cases} \tag{3.10}$$

Reduction of the $O_2$ flux at the end of the reactor decreases the local oxidation reaction rates and therewith the losses of $C_2H_4$ and $C_2H_6$ in this part of the reactor. With the total $O_2$ feed kept constant and a reactor length of 1 m, three different $O_2$ flux profiles were examined, given by Equation 3.10.

### Only OCM

The results of linearly increasing and decreasing $O_2$ flux profiles on the oxidative coupling of methane were compared to the already calculated case with a constant $O_2$ flux. Because the distribution profiles directly influence the $O_2$ mole fraction in the

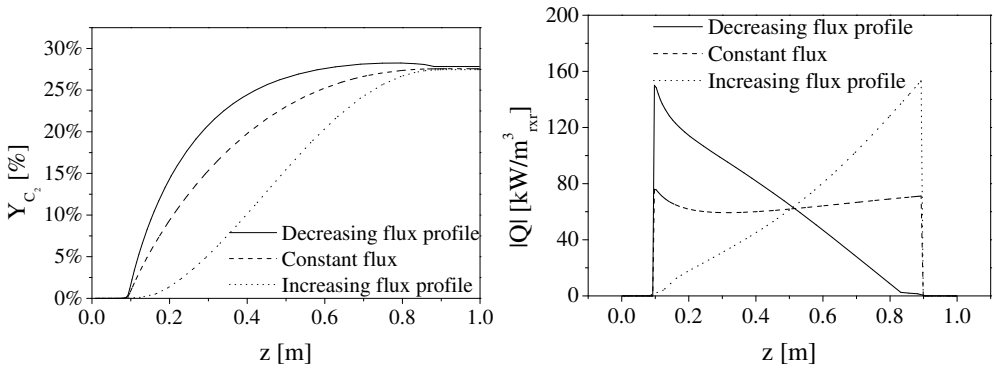


**Figure 3.16:** Influence of $O_2$ flux profiles on the $C_2$ yield (a) and the local (calculated) reaction enthalpy (b) at isothermal operation for oxidative coupling of methane (see Table 3.3, case A, $L_r = 1$ m).

reactor, the local reaction rates are directly proportional to the applied membrane flux. The overall $C_2$ yield for the cases with increasing and decreasing flux profiles is however hardly influenced at ideal isothermal conditions (Fig. 3.16a), because the decrease of the secondary reaction rates (i.e. $C_2H_4$ and $C_2H_6$ oxidation) is compensated by a change of the conversion rate and therefore a higher $C_2$ selectivity at the beginning of the reactor (increased flux profile) or at the end of the reactor (decreased flux profile). The important change compared to the case with constant $O_2$ flux, is that the relatively high heat production at the end of the reactor can be significantly moderated without a decrease of the $C_2$ production (Fig. 3.16b). Obviously, the increasing flux profile is of less interest here, however, the decreasing flux profile offers the opportunity to make the dual function catalyst process autothermal while using a constant particle configuration. With a constant SRM core diameter, the reforming reaction rates are totally governed by the local gas phase composition and temperature. Because the $CH_4$ concentration, which also determines the reforming reaction rate, decreases along the reactor length, the maximum heat consumption rate shows the same trend as the OCM reaction rates, allowing easy tuning to autothermal operation.

It was shown that the performance of the OCM packed bed membrane reactor is hardly influenced if a decreasing flux profile is applied. This is now verified for the packed bed membrane reactor with the dual function catalyst.

#### Dual function catalyst

Catalyst particles with a SRM core diameter of 15 and 20 $\mu$m were used to investigate the effect of the linearly decreasing $O_2$ flux profiles on the performance of the dual function process. A slightly larger SRM core radius was used, so that a case with near autothermal operation can also be shown. Compared to the OCM reference case (without steam reforming), the maximum $C_2$ selectivity and the $C_2$ production rates has decreased because of the added $CH_4$ and $C_2$ reforming reactions (Fig. 3.17a/b), which is comparable to the results shown earlier in Fig. 3.14 with a constant $O_2$ flux. The influence on the $CH_4$ conversion is comparable to the cases simulated with constant $O_2$ flux (Fig. 3.17c). Remarkably, the initial $C_2$ selectivity is higher if a flux profile is used, which is caused by the much lower reaction rates of the uselective reactions at (very) low local $O_2$ concentration, because of the higher $O_2$ reaction order. Particularly the $C_2H_4$ production rate is changed in the beginning of the reactor, which is depicted in Fig. 3.17d where the performance for a constant and decreasing $O_2$ flux profile is compared. It can also be seen that the oxidation reaction rates are only influenced near the reactor outlet, where the $O_2$ concentration is lower.

The major difference between the decreasing and the constant flux profile is, however, that because of the higher maximum $C_2$ selectivity (80% versus 65%, Fig. 3.17e) and the decrease of the $O_2$ flux, the contribution of the very exothermic secondary oxidation has vanished at the reactor outlet while the $C_2$ yield remains nearly unchanged (16% versus 15% at $r_{SRM}$=15$\mu$m, Fig. 3.17e). This leads to less heat formation near the reactor outlet, which has significantly reduced when compared to the constant flux case (Fig. 3.17d). Hence, with a flux profile and the SRM dual function catalyst, the reactor performance can already be tuned to almost autothermal operation. Further optimization of the SRM core diameter, should be done at non-isothermal conditions to account for the important influence of temperature profiles, discussed in the next section.

### 3.4.3 Influence of temperature profiles

Until now the dual function process was evaluated at isothermal operating conditions, so that the particle configuration could be optimized based on the reaction heat production at autothermal conditions. This idealized mode of operation is somewhat

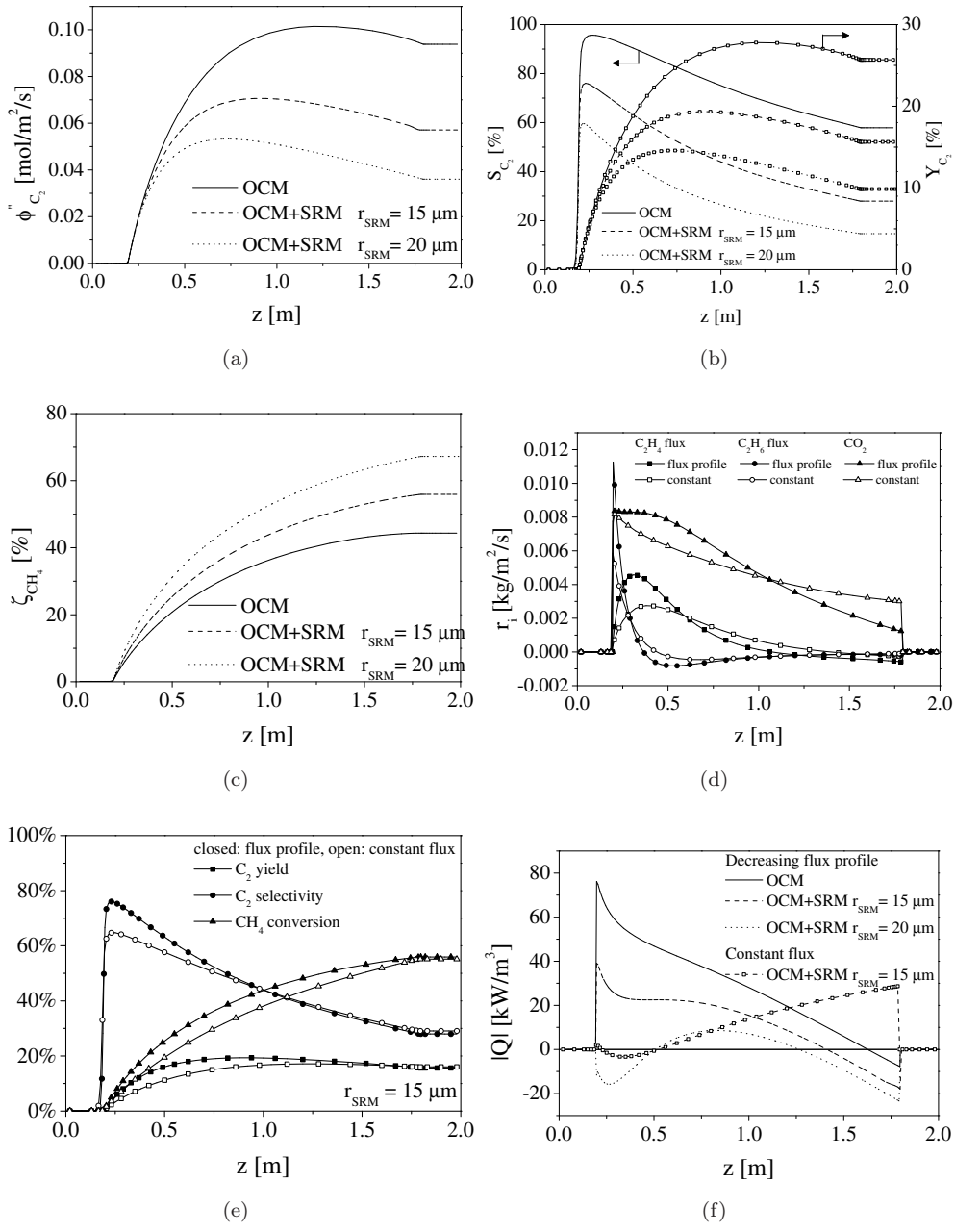


**Figure 3.17:** Comparison of (a) $C_2$ fluxes, (b) $C_2$ selectivity and yield, (c) $CH_4$ conversion, (d) comparison component fluxes, (e) reactor overall performance and (f) calculated reaction heat production rate for the case of a decreasing $O_2$ flux profile with the dual function OCM-SRM catalyst particles (T=800°C, p=150 kPa, other conditions listed in Table 3.3).

artificial, as heat management is of crucial importance for the performance of OCM. The two limiting cases for the packed bed membrane reactor for OCM were presented in Fig. 3.4, with the maximum yield of the optimally cooled reactor at 25% and in an adiabatic (non-cooled) reactor a maximum yield of 17% can be achieved (at a higher $CH_4/O_2$ feed ratio). For OCM, the cooled reactor is preferred because of the higher yields, however at the expense of a much more complicated design and a larger $CH_4$ recycle. In this concept, integrated cooling is applied via the dual function catalyst, leading to a more complicated catalyst, while the reactor can be a fixed bed reactor equipped with porous/dense membranes without additional complex cooling devices. Hence, the reference case should be the adiabatic OCM simulation, with a maximum $C_2$ yield of 17%. In this paragraph, the temperature profile in the reactor with the dual function catalyst is tuned by variation of the core radius of the steam reforming activity between 50 and 100 $\mu$m.

It can be seen in Fig. 3.18 that the dual function catalyst influences both the axial concentration and temperature profiles in the reactor. With an adiabatic OCM reactor, the temperature will easily rise above 850 °C, which caused the overall $C_2$ selectivity to drop below 20% leading to a low performance of the oxidative coupling catalyst. Using a dual function catalyst with a core radius of 75 $\mu$m most of the reaction heat will be removed, and leads to a temperature decrease of 40-50°C compared to the adiabatic reactor (Fig. 3.18d) and a correspondingly better performance of the reactor. A too large core radius, results in an overall decrease of the temperature and the reaction rates because of the relatively high activation energy of >100 kJ/mol. The conversion that can be achieved is for the cooled reactor approximately 41%, whereas the packed bed membrane reactor with the dual function catalyst (75 $\mu$m) can achieve a conversion of nearly 60%, which greatly influences the $C_2$ production rates via the changing methane partial pressure. Comparison of the cases at the same $CH_4$ conversion level of 60% is not possible, because for only OCM the overall $O_2$ feed rate is much higher leading to large secondary reaction rates and hence a decrease of the $C_2$ production rate from $\phi^{"} = 0.085$ mol/m$^2$/s to no $C_2$ yield at all. The conversion for the adiabatic case is somewhat higher (59%) but the $C_2$ production rate of 0.014 mol/m$^2$/s is low (Fig. 3.18a). For the dual function catalyst, the overall $C_2$ production rate has improved much, with production rates varying from 0.02 to 0.04 mol/m$^2$/s. This is a considerable improvement compared to the adiabatic case, because at the same $CH_4/O_2$ feed ratio the $C_2$ production has increased with more than 200%. Next to more $C_2$ products, also the syngas production increased with more than 10%. The $CO/CO_2$ ratio is comparable (because of the shift activity on the OCM catalyst - see Chapter 2), however the $H_2/H_2O$ has increased with

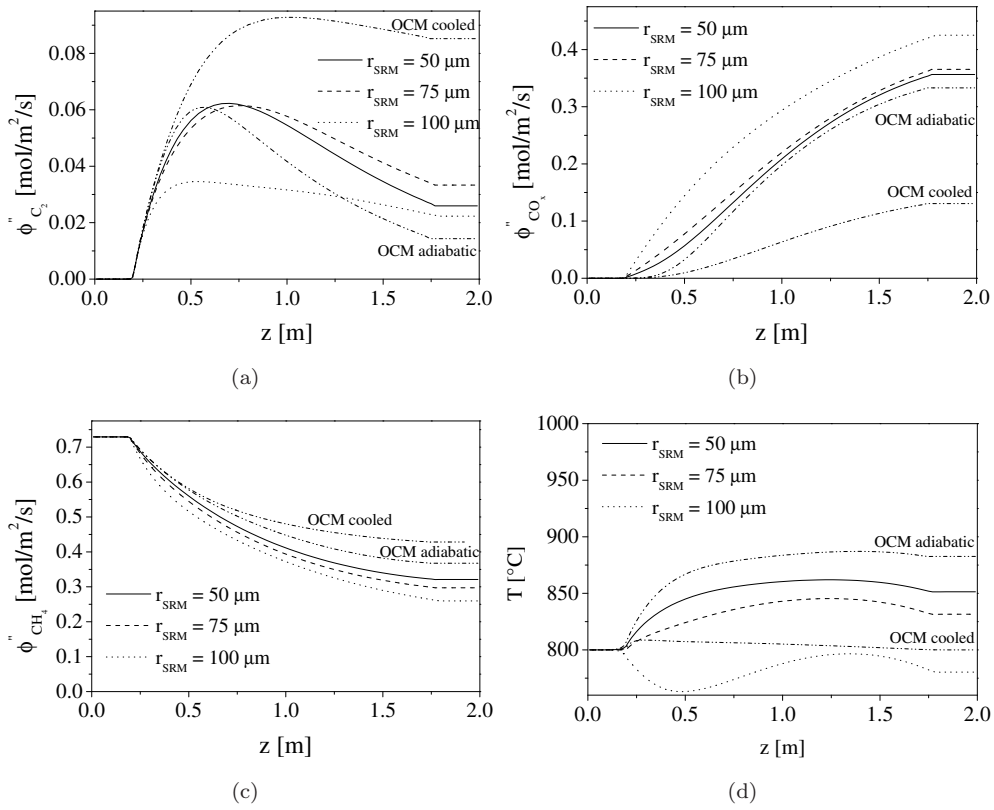


**Figure 3.18:** Axial profiles of the (a) $C_2$ mole fluxes, (b) $CO_x$ mole fluxes, (c) $CH_4$ mole fluxes and (d) gas phase temperature for the packed bed membrane reactor with the dual function catalyst for several SRM core radii, compared with the cooled and adiabatic OCM packed bed membrane reactor cases at non-isothermal conditions (conditions based on Table 3.3, $L_r$= 2m).

approximately 30%.

Because the dual function catalyst increases the $CH_4$ conversion (when the inlet flow rate is kept constant), the reforming reaction rates and the secondary reaction rates will inevitably influence the total $C_2$ production rates of the combined process. Therefore, an optimum $C_2$ production rate is achieved at an axial position between 0.5 and 1.0 m, corresponding to a $CH_4$ conversion between 40-45%, instead of the end of the reactor which was the case for oxidative coupling. Comparing the total $C_2$ production rates and the actual $C_2$ reforming reaction rate in the catalyst particles, it can however be seen that the addition of reforming only influences the total $C_2$ production rate to a small extent (Fig. 3.19a). The largest influence of the reforming

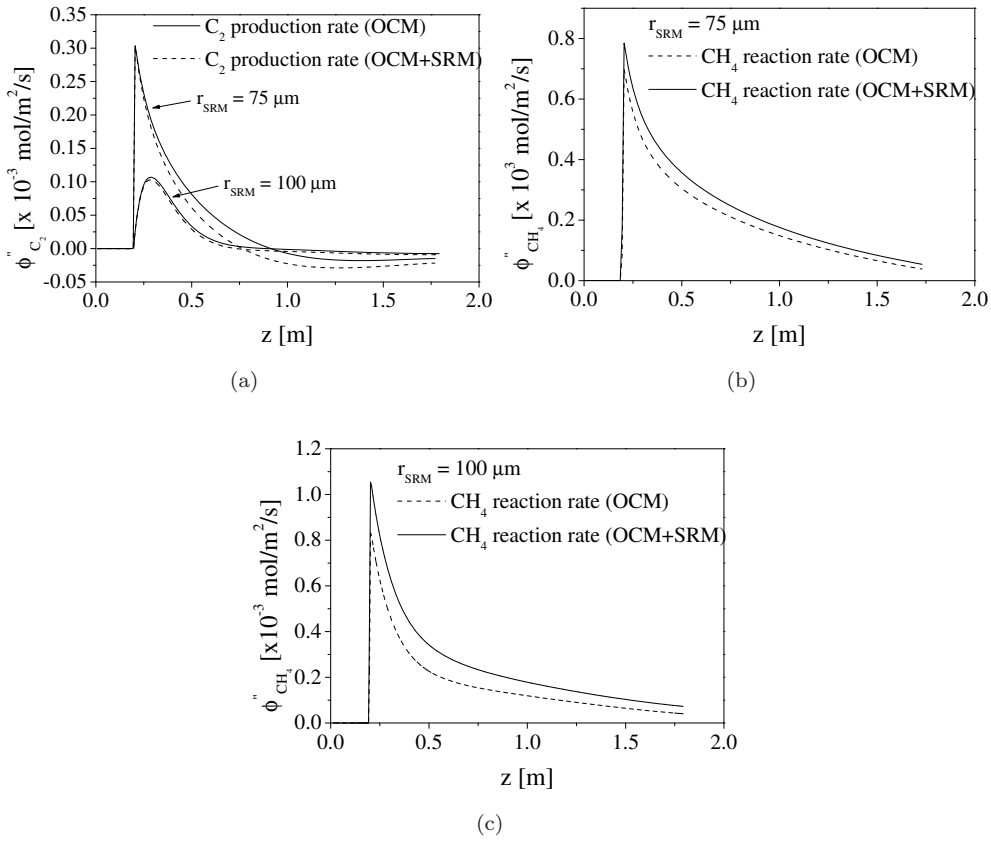


**Figure 3.19:** Influence of the reforming activity on (a) the total $C_2$ production rate, (b)/(c) the $CH_4$ reaction rate at non-isothermal conditions ($r_{SRM} = 75\mu$m and $r_{SRM} = 100\mu$m).

reactions can be noticed at the end of the reactor, where the $C_2$ concentration is the highest. With a core radius of 75 $\mu$m, less than 40% of the produced $C_2$ components are converted into synthesis gas by the reforming catalyst. With a SRM core radius of 100 $\mu$m, it is shown that the total $C_2$ production rate and therefore the losses to $C_2$ reforming is much lower which is related to the very low reaction temperature and lower bulk gas phase concentration (driving force). For both cases, the $CH_4$ reaction rate has however increased with 15-20%, and the reaction heat has therefore decreased significantly (Fig. 3.19b-c).

If the dual function catalyst is compared with adiabatic OCM reactor operating at the point where the optimum $C_2$ yield is achieved, it can be seen that the $CH_4$ conversion has increased from 27% to 34% for the dual function catalyst of 75 $\mu$m.

At this reactor length, the optimum $C_2$ production rates is achieved and it can be seen that the production rate has decreased from 0.085 (cooled) to 0.06 mol/m$^2$/s, while the $CO_x$ production is significantly higher (Fig. 3.18b). Compared to adiabatic conditions, the productivity has also improved because the overall reactor temperature can be maintained at more acceptable levels (at a higher $CH_4$ conversion level). The indirect influence of the added reforming activity on the $C_2$ production rates is that the local $CH_4/O_2$ ratio has changed because of $CH_4$ reforming, leading to somewhat lower production rates than observed with oxidative coupling. With OCM only, high $CH_4$ conversion is not feasible because the high required $CH_4/O_2$ feed ratio leads to excessive temperatures and hence low $C_2$ production, however, the most important advantage of the dual function process is that much higher $CH_4$ conversions can be obtained without additional external heat exchange at near isothermal operation.

## 3.5 Conclusions

The performance of a packed bed membrane reactor with dual function catalyst particles for the simultaneous production of ethylene, carbon monoxide and hydrogen (synthesis gas) was studied. Where conventional membrane reactors used for exothermic reactions mostly require cooling resulting in a complicated and expensive reactor design, this reactor concept efficiently utilizes the endothermic steam reforming (SRM), producing value-added synthesis gas to counteract the heat production by the oxidative coupling (OCM). The membrane reactor, with $O_2$ distributed via a (porous) membrane in the centerline of the packed bed, and the influence of an intra-particle heat-sink, at optimal (autothermal) operating conditions was studied on basis of detailed and extensive numerical simulations.

The performance of a packed bed membrane reactor with only activity for the oxidative coupling of methane was studied first to obtain a good reference case with which the dual function process could be compared. It was found that large temperature excursions in the OCM membrane reactor are caused in particular by the secondary oxidation reactions. If the $O_2$ membrane feed flux at the end of the reactor was lowered, for example by using a linearly decreasing flux profile, the reaction heat can be consumed more easily by the steam reforming reactions. Comparison with a case with constant $O_2$ flux demonstrated that the $CH_4$ conversion and $C_2$ yield are hardly influenced. By tuning the process to mildly exothermic conditions via the SRM core radius ($r_{SRM}$) or distributive addition of $O_2$ ($\phi''_{m,O_2}$), losses of $C_2$ components were minimized and the process was tuned to autothermal operation. Further optimization can be achieved by modification of the catalyst pore structure ($\varepsilon/\tau$), particle diame-

ter ($d_p$) and molar feed ratios. Several catalyst coating and preparation techniques, such as spray coating (Gajda, 2008), washcoating (Caze et al., 2003) and targeted impregnation (Iglesia et al., 1995) can be applied to produce the dual function catalyst particle. By using an average particle configuration ($d_p$=3 mm, $r_{SRM}$=20-100 $\mu$m, $r_{OCM}$=0.25-0.5 mm) it was shown that at a $CH_4/O_2$ ratio of 4, the heat production can be reduced with more than 80% which leads to a maximum temperature in the reactor between 800-900°C which is more than 300°C lower than observed with oxidative coupling at adiabatic conditions. Compared to an adiabatic packed bed membrane reactor with only oxidative coupling, the $C_2$ production rate has slightly increased for the dual function process while the $CO_x$ production and the $CH_4$ has significantly increased without the requirement of additional complex heat exchange.

## Acknowledgement

The authors gratefully acknowledge the financial support by the Netherlands Organisation for Scientific Research (NWO/ACTS) under the research theme of Advanced Sustainable Processes by Engaging Catalytic Technologies (ASPECT) (project 053.62.008).

## Nomenclature

| | | |
|---|---|---|
| *Roman letters* | | |
| $a$ | $m^2/m^3$ | specific surface |
| $Bo$ | - | Bodenstein number = $vd_p/D_{ax}$ |
| $B_0$ | - | |
| $c$ | $mol/m^3$ | concentration |
| $C_p$ | kJ/kg/K | heat capacity |
| $[D_{ax}]$ | $m^2/s$ | axial dispersion coefficient |
| $[D^0_{eff}]$ | $m^2/s$ | effective diffusion matrix in the mass average reference velocity frame |
| $d^0_{eff,i,k}$ | $m^2/s$ | element of matrix $[D^0_{eff}]$ |
| $d$ | m | diameter |
| $d_p$ | m | particle diameter |
| $F_{1-\sigma}$ | - | selectivity correction factor |
| $H_i$ | J/kg | enthalpy of component i |
| $J_i$ | $mol/m^2/s$ | diffusive mole flux of component i |
| $k_j$ | 1/s | first order reaction rate constant |

| | | |
|---|---|---|
| $K_0$ | - | |
| $L$ | m | length |
| $M_i$ | kg/mol | mole mass of component i |
| $n_i$ | kg/m$^2$/s | mass flux of component $i$ |
| $n_j$ | - | reaction order of reaction $j$ |
| $n_{tot}$ | kg/m$^2$/s | drift flux |
| $p, P$ | Pa | (partial) pressure |
| $Q$ | W/m$^3$ | heat |
| $r$ | m | radial coordinate |
| $r_{OCM}$ | m | thickness of the OCM catalytic layer |
| $r_{SRM}$ | m | thickness of the SRM catalytic layer |
| $r_p$ | m | particle radius |
| $r_j$ | mol/kg$_{\text{cat}}$/s | reaction rate of component j |
| $R_j$ | mol/m$^3$/s | reaction rate of component j |
| $R$ | J/mol/K | universal gas constant |
| $s_{r,i}$ | mol/m$^3$/s | source term mass balance |
| $s_h$ | J/m$^3$/s | source term energy balance |
| $t$ | s | time |
| $T$ | K | temperature |
| $v$ | m/s | velocity |
| $x$ | - | mole fraction |
| $y$ | - | dimensionless radial coordinate |
| $Y$ | - | yield |
| $z$ | m | axial coordinate |

*Greek letters*

| | | |
|---|---|---|
| $\alpha_{b\rightarrow w}$ | W/m$^2$/K | bed-to-wall heat transfer coefficient |
| $\delta$ | m | thickness |
| $\varepsilon$ | - | porosity |
| $\phi_{i,tot}$ | - | total mass flow of component i |
| $\phi_i^{'}$ | - | Thiele modulus of component i |
| $\phi^{"}$ | kg/m$^2$/s | mass flux |
| $\Delta H_{r,j}$ | J/mol | reaction enthalpy of reaction j |
| $\Delta T_{ad}$ | K | adiabatic temperature rise |
| $\eta$ | kg/m/s | dynamic viscosity |
| $\eta_{exact,i}$ | - | analytical effectiveness factor |
| $\nu_{i,j}$ | - | stoichiometric coefficient |

| | | |
|---|---|---|
| $\lambda_g$ | W/m/K | gas phase heat conductivity |
| $\lambda_{eff,s}$ | W/m/K | effective solids heat conductivity |
| $\rho$ | kg/m$^3$ | density |
| $\tau$ | - | particle tortuosity |
| $\omega$ | - | weight fraction |
| $\sigma$ | - | selectivity |
| $\zeta$ | - | conversion |

*Subscripts*

| | |
|---|---|
| c | catalyst bed |
| g | gas phase |
| i | inner |
| inert | inert porous layer in catalyst particle |
| m | membrane |
| N | number of components |
| $N_{reac}$ | number of reactions |
| o | outer |
| p | particle |
| OCM | Oxidative Coupling of Methane |
| r | reactor |
| s | solid phase |
| SRM | Steam Reforming of Methane |
| w | wall |

# Appendix 3.A Physical properties

Most physical properties displayed in the table are a function of temperature, but the temperature dependency is weak. An average value of the solid heat capacities was used in the temperature range of 800-1200 K, which are listed in the Table. For all cases it was verified that the standard deviation of the average values in the range of investigated temperatures did not exceed 2%.

**Table A.1:** Properties of the (porous) solids used for the simulations of the packed bed membrane reactor equipped with dual function catalyst particles (Daubert and Danner, 1985).

| $\rho_s$ [kg/m$^3$] | Equation | Used value |
|---|---|---|
| CaO (bulk) | - | 1978 |
| $Al_2O_3$ (bulk) | - | 2170 |
| Steel | - | 7870 |
| $\lambda_s$ [W/m/K] | Equation | Used value |
| CaO | $7.2309 \cdot 10^{-9} \cdot T^3 + 2.5453 \cdot 10^{-5} \cdot T^2 - 3.0426 \cdot 10^{-2} \cdot T + 19.537$ | - |
| $Al_2O_3$ | $33.222 \cdot exp^{-1.3323 \cdot 10^{-3} \cdot T}$ | - |
| Steel | $1.52976 \cdot 10^{-2} \cdot T + 9.01905$ | - |
| $C_{p,s}$ [J/kg/K] | Equation | Used value |
| CaO | $4.7250 \cdot 10^4 + 6.8T - 5.6700 \cdot 10^{-4}T^2$ | 964 |
| $Al_2O_3$ | $4.33 \cdot 10^2 + 1.94T - 1.71 \cdot 10^{-3}T^2 + 6.94 \cdot 10^{-7}T^3 - 1.03 \cdot 10^{-10}T^4$ | 2360 |
| Steel | $3.65435 \cdot 10^2 + 4.06488 \cdot 10^{-1}T - 1.73214 \cdot 10^{-4}T^2$ | 596 |

# Appendix 3.B Heat and mass transfer coefficients

**Table B.1:** Effective heat and mass transfer coefficients for the short-cut and the full intra-particle (heterogeneous) reactor model.

Bed conductivity ($\lambda_{bed,0}$) is calculated according to Zehner and Schlünder (1970).

$$\frac{\lambda_{bed,0}}{\lambda_g} = \left(1-\sqrt{1-\varepsilon_g}\right)\left(1+\frac{\lambda_{rad}}{\lambda_g}\right) + \sqrt{1-\varepsilon_g}\left(\frac{2}{1-\frac{\lambda_g}{\lambda_s}B}\left[\frac{(1-\frac{\lambda_g}{\lambda_s}B)}{(1-\frac{\lambda_g}{\lambda_s}B)^2} ln\left(\frac{\lambda_s}{\lambda_g B}\right) - \frac{B+1}{2} - \frac{B-1}{1-\frac{\lambda_g}{\lambda_s}B}\right] + \frac{1}{\frac{\lambda_g}{\lambda_{rad}}+\frac{\lambda_g}{\lambda_s}}\right)$$

$$\text{With: } \lambda_{rad} = d_p \frac{0.23}{2/\varepsilon_{rad}-1}\left(\frac{T}{100}\right)^2$$

$$B = 1.25 * \left(\frac{1-\varepsilon_g}{\varepsilon_g}\right)^{10/9}$$

For the short-cut model, the effective axial heat dispersion was then calculated by (Vortmeyer and Berninger, 1982):

$$\lambda_{eff} = \lambda_{bed,0} + \frac{RePr\lambda_g}{Pe_{ax}} + \frac{Re^2 Pr^2 \lambda_g}{6(1-\varepsilon_g)Nu}$$

In which $Pe_{ax}$ is calculated according to Gunn and Misbah (1993):

$$Pe_{ax} = \frac{2p}{1-p} \qquad p = 0.17 + 0.33\exp^{\frac{-24}{Re}}$$

Gas-to-particle heat transfer coefficient (Gunn, 1978):

$$Nu = \left(7-10\varepsilon_g+5\varepsilon_g^2\right)\left(1+0.7Re^{0.2}Pr^{1/3}\right) + \left(1.33-2.4\varepsilon_g+1.2\varepsilon_g^2\right)Re^{0.7}Pr^{1/3}$$

Axial mass dispersion (Edwards and Richardson, 1968):

$$\frac{D_{ax}}{v_g d_p} = \frac{0.73}{ReSc} + \frac{0.5}{\varepsilon_g\left(1+\frac{9.7\varepsilon_g}{ReSc}\right)}$$

**Table B.2:** Wall-to-bed heat and gas-to-particle transfer coefficients.

Wall to bed heat transfer coefficient in a packed bed (Dixon and Cresswell, 1979):

$$\frac{1}{\alpha_{wall\rightarrow bed}} = \frac{1}{\frac{Nu_w \lambda_g}{d_p} + \alpha_{rad}} + \frac{r_i Pe_{er}}{3\lambda_g RePr}\frac{Bi+3}{Bi+4}$$

In which $Pe_{er}, Nu_w$ are dependent on the Reynolds number:

| $\mathrm{Re} > 50$ | $\mathrm{Re} < 50$ |
|---|---|
| $Bi_f = \frac{Nu_{wf} r_i Pe_{rf}}{d_p RePr}$ | $Bi_s = 2.41 + 0.156\left(\frac{2r_i}{d_p} - 1\right)^2$ |
| $Bi = \frac{Nu_w r_i Pe_{er}}{d_p RePr}$ | $Pe_{rf} = \frac{12}{1 + 8\frac{\varepsilon_g}{RePr}}$ |
| $Nu_{wf} = \left(1 - \frac{d_p}{2r_i}\right) Re^{0.6} Pr^{1/3}$ | |
| $N_s = 1.5\,(1-\varepsilon_g)\left(\frac{2r_i}{d_p}\right)^2 \frac{\lambda_g}{\lambda_{bed}} \frac{1}{\frac{1}{Nu} + \frac{\lambda_g}{10\lambda_s}}$ | $N_f = 1.5\,(1-\varepsilon_g)\left(\frac{2r_i}{d_p}\right)^2 \frac{Pe_{rf}}{RePr} \frac{1}{\frac{1}{Nu} + \frac{\lambda_g}{10\lambda_s}}$ |
| $Pe_{er} = \frac{1}{\frac{1}{Pe_{rf}} + \frac{\lambda_{bed}}{\lambda_g RePr} + \frac{Bi_f + 4}{Bi_f\left(\frac{8}{N_s} + \frac{Bi_s+4}{Bi_s}\right)}}$ | $Pe_{er} = \frac{1}{\frac{1}{Pe_{rf} Bi_s}\frac{Bi_s+4}{\left(\frac{8}{N_f} + \frac{Bi_f+4}{Bi_f}\right)} + \frac{\lambda_{bed}}{\lambda_g RePr}}$ |
| $Nu_w = \frac{Bi_f d_p RePr}{r_i Pe_{er}}$ | $Nu_w = \frac{Bi_s d_p RePr}{r_i Pe_{er}}$ |

Gas-to-particle heat transfer coefficient (Gunn, 1978):

$$Nu = \left(7 - 10\varepsilon_g + 5\varepsilon_g^2\right)\left(1 + 0.7 Re^{0.2} Pr^{1/3}\right) + \left(1.33 - 2.4\varepsilon_g + 1.2\varepsilon_g^2\right) Re^{0.7} Pr^{1/3}$$

# Appendix 3.C Validation heterogeneous model

The full intra-particle heterogeneous reactor model was validated with an irreversible first order reaction and constant physical properties. The reference case to check whether the intra-particle concentration and temperature profiles are correctly accounted for, was the homogeneous reactor model where the reaction rates are corrected with well-known effectiveness factors from the literature. The applied operating conditions are listed in Table C.1.

**Table C.1:** Model settings for validation of isothermal and non-isothermal first-order irreversible reaction.

| Parameter | Value | Parameter | Value |
|---|---|---|---|
| $p_{in}$ | 1.5 bar | $x_{A,in}$ | 0.15 |
| $T_{in}$ | 800 °C | $x_{\mathrm{N}_2,in}$ | 0.85 |
| $\rho_g v_g$ | 1 kg/m$^2$/s | $M_{av}$ | 0.015 kg/mol |
| L | 0.25 m | $\varepsilon_s/\tau_s$ | 0.3 |
| $d_p$ | 0.003 m | $\mathcal{D}$ | $1 \cdot 10^{-3}$ m$^2$/s |

## Isothermal case

The first order irreversible reaction rate expression for the conversion of A into B is given by:

$$r_A = k_0 c_A \quad \text{mol/m}^3\text{/s} \tag{C.1}$$

Several isothermal cases with constant physical properties and with different fixed reaction rate constants $k_0$ were performed, to verify whether the model can accurately solve both slow and fast reactions:
$k_0 = 150, 300, 600, 1200, 2400, 4800$ s$^{-1}$.

The solutions obtained with the heterogeneous (intra-particle) reactor model were compared with a homogeneous reactor where the intra-particle diffusion limitations were accounted for via an effectiveness factor. For simple first-order irreversible reactions, the analytical expression for the catalyst effectiveness factor is given by (Westerterp et al., 1963):

$$\eta_{exact} = \frac{3\phi - tanh(3\phi)}{3(\phi)^2 tanh(3\phi)} \tag{C.2}$$

Where the Thiele modulus is defined as:

$$\phi = \frac{d_p}{6}\sqrt{\frac{k_0}{D_{eff}}} \tag{C.3}$$

The settings in Table C.1 were used and the resulting mole fractions for component A are plotted as function of the reactor length (Fig. C.1). It is shown that the weight fractions calculated by the heterogeneous reactor model exactly match the concentration profiles obtained with the concentration profiles obtained with the homogeneous reactor model with the reaction rates corrected via Equation C.2/C.3. Hence, with

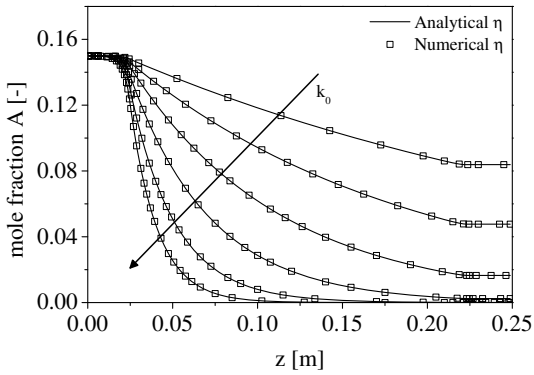


**Figure C.1:** Influence of reaction rate constant on the numerical and analytical solution for first order isothermal reaction (conditions see Table C.1).

these cases it is shown that the particle model is successfully integrated in the packed bed reactor model, however, the implementation of the energy balances still needs to be verified. This is done for an exothermic combustion reaction, where the adiabatic temperature rise is compared with the analytical solution.

## Non-isothermal case

The reaction rate expression for the non-isothermal conversion of A into B is given by:

$$r_A = k_0 \cdot e^{-E_a/RT} c_A \quad \text{mol/m}^3\text{/s} \tag{C.4}$$

Determination of an effectiveness factor for a non-isothermal catalyst particle requires a simultaneous solution of the mass and energy balances. Because the Arrhenius type dependency of the reaction rate constant has a strong non-linear influence on the

energy balance, comparison with an analytical expression of the effectiveness factor is no longer possible. Hence, the simulation results of the combined reactor-particle model are compared with numerical representations derived by other researchers.

For the first order irreversible reaction, Liu et al. (1970) determined the following empirical formula to describe the effectiveness factor while taking into account the influence of the reaction heat (Aris, 1975; Westerterp et al., 1963):

$$\eta = e^{0.14\phi\delta^{1.6}} - 1 + \frac{tanh(\phi)}{\phi} \qquad \begin{cases} \delta > 2.5, \phi < 1.235 - 0.094\delta \\ \delta \leq 2.5, \phi < 1.820 - 0.328\delta \end{cases} \tag{C.5}$$

In the equation, $\delta$ represents the influence of the heat of reaction:

$$\delta = \beta \cdot \gamma \quad \beta = \frac{-\Delta H D_{eff} c_A}{\lambda_{eff} T} \quad \gamma = \frac{E_a}{RT}$$

With a $\Delta H$ of 10 kJ/mol and solid effective conductivity of 10 W/m/K, the concentration and temperature profiles are calculated. The following reaction rate constants were taken: $k_0 = 150, 300, 600, 1200, 2400, 4800 \cdot 10^4$ s$^{-1}$ and $E_a$=100 kJ/mol. From

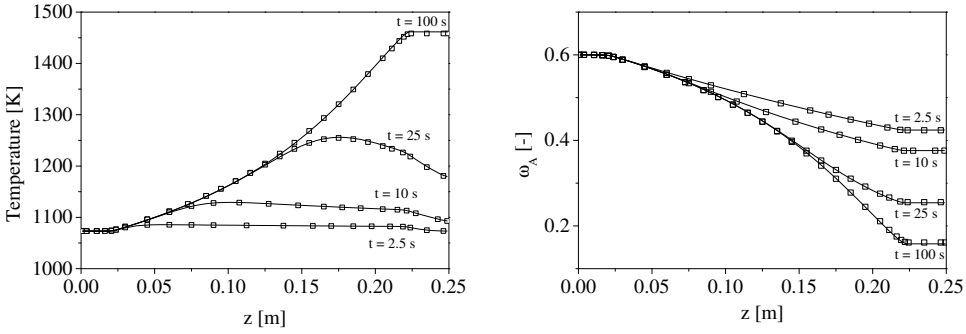


(a) (b)

**Figure C.2:** Comparison of numerical and analytical solution for first order non-isothermal reaction. $\delta = 0.07$

Fig. C.2 it can be discerned that the solution proposed in the literature and the numerical solution of the heterogeneous reactor model show an exact match for this first order reaction.

# 4

# Development of a novel reactor concept for thermally coupled OCM/SRM


## Abstract

A novel reactor concept with autothermal operation has been developed for the simultaneous production of ethylene by oxidative coupling (OCM) and synthesis gas by steam reforming of methane (SRM). A detailed reactor model was developed and used to gain insight in the complex behavior of the reactor comprising two separate reaction chambers which are thermally coupled. The OCM is carried out in packed bed reverse flow membrane reactor tubes submerged in a fluidized bed where the unconverted methane and by-products, from which the valuable $C_2$ components have been separated, are reformed together with some additional steam, thus producing synthesis gas and consuming the reaction heat liberated by the exothermic OCM. On basis of detailed simulations it has been shown that indeed the exothermic OCM and endothermic SRM can be very efficiently coupled permitting autothermal operation with cyclic steady state $C_2$ yields up to 30% at full methane conversion with a $CH_4/O_2$ ratio of 2-2.5 and a $H_2O/CH_4$ ratio of 3 in the SRM fluidized bed reactor.

## 4.1 Introduction

In the first part of this thesis, it was investigated how catalytic functions for OCM and SRM can be integrated in a single bi-functional catalyst particle, which offers several advantages such as optimal heat transfer between the two reactions and a relatively simple reactor configuration. The main disadvantages of this concept are related to the complicated and probably expensive catalyst configuration and inevitable lower $C_2$ production. On the reactor scale, integration of exo- and endothermic processes in a single multifunctional reactor to achieve autothermal operation can be realized with many different configurations. For each reaction (exo- or endothermic), the most suitable reactor should be selected and possibilities to realize efficient thermal coupling (i.e. maximize the exchange of reaction heat between two different reactor chambers) should be evaluated.

A simplified process scheme, depicted in Fig. 4.1, shows that $CH_4$ is first fed to the OCM reactor, producing the desired higher hydrocarbons, and sequentially the product gas is led to a steam reforming reactor. The excess reaction heat from OCM is consumed by the steam reforming reactions, while simultaneously valuable synthesis gas is produced. To reduce or eliminate the interference between both processes, $C_2H_4$ (and $C_2H_6$) should be separated from the OCM process stream before feeding it into the SRM reactor compartment, preventing excessive consecutive reforming reactions of $C_2H_4$.

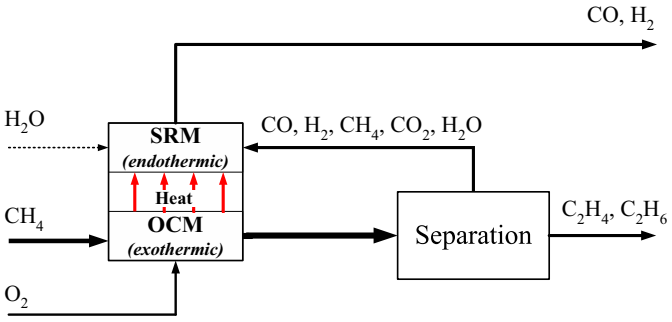


**Figure 4.1:** Schematic of thermally coupled oxidative coupling and steam reforming of methane with intermediate $C_2H_4/C_2H_6$ separation.

An important aspect of this configuration is the choice of the separation technique for the removal of $C_2$ components, which can be realized via either reactive

or physical separation. A process stream consisting of $C_1$ and $C_2$ components can be separated via a reaction which selectively consumes $C_2H_4$, e.g. via benzene alkylation as proposed by Graf (2008). It was experimentally demonstrated that $C_2H_4$ can indeed be separated from the OCM reaction mixture with high selectivity via benzene alkylation over a ZSM-5 zeolite catalyst at 450°C to ethylbenzene (a precursor for styrene/polystyrene). Although this technique is a promising alternative to physical separation, it also links the $C_2H_4$ production capacity almost exclusively to the styrene market which is relatively small compared to the total ethylene market. The global demand for ethylene derivatives such as high and low density polyethylene (LDPE/HDPE) represents more than 70-80% of the global $C_2H_4$ production, whereas less than 10% of $C_2H_4$ is used for the ethylbenzene/styrene (Sundaram et al., 2001). In addition, the larger market and applicability of synthesis gas for various bulk chemicals and fuels also makes conversion of $C_2H_4$ into ethylbenzene less attractive. For the separation of ethylene via physical methods, several options have been investigated, such as the removal of ethylene via chromotographic methods in a recycle reactor (Makri and Vayenas, 2003), large-scale (cryogenic) distillation (Mleczko and Baerns, 1995), or absorption of the selective products in a gas/liquid $AgNO_3$ membrane contactor (Chilukuri et al., 2007). A more detailed market analysis and a first cost comparison of both options may be decisive for the type of technology, but is not evaluated here. In this chapter, the $C_1/C_2$ separation is outside the scope and the focus is on the development of a novel reactor concept for the simultaneous production of ethylene and synthesis gas by thermally coupling the OCM and SRM.

First, it is elucidated that optimal $C_2$ yields and optimal energy integration can be achieved by performing the OCM in a reverse flow packed bed membrane reactor submerged in a SRM fluidized bed reactor. Subsequently, a numerical simulation study has been carried out to investigate the reactor behavior in more detail and to demonstrate whether energy efficient autothermal operation can indeed be achieved.

## 4.2 Novel reactor concept

For the oxidative coupling of methane, efficient heat removal from the reactor is critical for the $C_2$ selectivity, catalyst life and membrane stability. At laboratory scale, temperature excursions in the reactor can be largely circumvented by operation at highly diluted and thus isothermal conditions (e.g. Lu et al., 1999), however, at higher $CH_4$ concentrations and larger reactor volumes the large adiabatic temperature rise becomes detrimental for the reactor performance. To circumvent large temperature gradients in the reactor, the reactor concept presented here is equipped with porous

membranes for distributive $O_2$ feeding, so that the reaction heat is generated along the reactor length, increasing the heat transfer area. In addition:

- The OCM packed bed membrane reactor is immersed in a fluidized bed SRM reactor, in which the by-products and unconverted $CH_4$ of OCM are converted into synthesis gas. Due to the integrated heat exchange the excess OCM reaction heat can be easily transported via the reactor wall to the SRM reactor, enabling autothermal operation.

- Distributed feed of $O_2$ is beneficial to increase the $C_2$ selectivity. An important feature which is common for many selective oxidations is that the reaction order in $O_2$ for the selective reaction is lower than for the unselective reaction, so that the $C_2$ selectivity can be increased by lowering the $O_2$ concentration via the application of distributed feeding of $O_2$.

- Reverse flow operation with integrated heat exchange is used for the OCM reactor; periodic reversal of the flow direction in the reactor ensures 1) that the inlet and outlet temperatures are below the ignition temperature of the unselective homogeneous gas phase reactions and 2) that expensive, high temperature external heat exchangers are not required for recuperative heat exchange.

For the oxidative coupling of methane, the available catalysts developed since the 1980's are ranging from lanthanoids to alkali metals (Choudhary and Uphade, 2004). Although there are more active catalysts available, such as $La_2O_3$, one of the best and stable catalysts with moderate activity, $Mn/Na_2WO_4$ on $SiO_2$, with the highest $C_2$ yield (25-28%) is selected in this study (e.g. Pak and Lunsford, 1998). In this section, the advantageous aspects of distributed $O_2$ feed and reverse flow operation for autothermal operation of the thermally coupled novel OCM/SRM reactor concept are discussed.

### 4.2.1 Distributed feeding of oxygen

To study the expected beneficial influence of distributed $O_2$ feed for the OCM on $Mn/Na_2WO_4$ supported on silica, the $O_2$ dependency of the primary reaction rates ($CH_4$ oxidation and coupling) was determined at 800°C under differential conditions in a micro-catalytic fixed bed reactor.

The experimental results (summarized in Fig. 4.2) confirm that the reaction order in $O_2$ is indeed lower for the OCM reaction (n=0.36) than for the methane combustion reaction (n=1). The lower reaction order in $O_2$ results in an increase of the overall $C_2$ selectivity at low $O_2$ concentration (as high as 85% at $p_{O_2} < 5$ kPa)

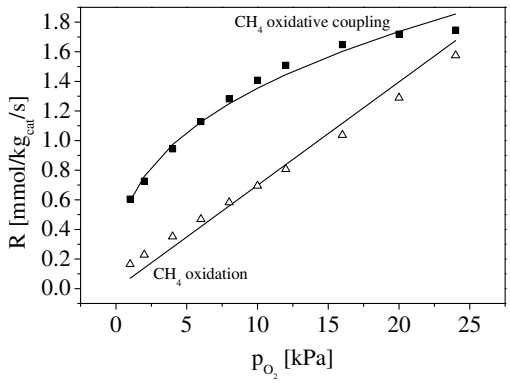


**Figure 4.2:** Reaction rates for the oxidative coupling and combustion of methane on a 5% $Mn/Na_2WO_4$ supported on silica catalyst measured under differential conditions in a micro-catalytic fixed bed reactor ($\zeta_{O_2,max}$=5%, T=800°C, $p_{tot}$=200 kPa, $p_{CH_4}$=50 kPa, $m_{cat}$=0.25 g, $\phi_v$=250 Nml/min).

at the expense of a lower $CH_4$ conversion rate (i.e. more catalyst required).
Operation at low $O_2$ concentration levels can be combined with higher methane conversion via distributive feeding of $O_2$/air along the reactor, so that much higher $C_2$ yields can be realized compared to co-feed reactors. The advantageous effect of a distributed feed of $O_2$/air has been demonstrated with experiments in an isothermal packed bed membrane reactor, where porous $Al_2O_3$ membranes were applied to distributively feed air to a diluted $CH_4$ stream over a $Mn/Na_2WO_4$ catalyst at 800°C (Coronas et al., 1994a,b; Lu et al., 1999; Lafarga et al., 1994). An additional advantage of distributively dosing of $O_2$ is that the reaction heat is released along the reactor length, leading to a more uniform temperature profile avoiding hot spots and providing better options for heat removal.
In addition, the relatively low catalytic activity of this catalytic system is actually an advantage from a reaction engineering point of view. Large reaction rates in a small reaction volume lead to a high heat generation per unit volume and to increasingly difficult heat removal, which may result in an unwanted temperature rise which is detrimental for the $C_2$ selectivity because unselective reactions prevail at higher temperatures.

### 4.2.2 Reverse flow operation

Since the oxidative coupling of methane is carried out at high temperatures (T > 850°C), efficient use of the energy contained in the reaction products exiting the reactor at this temperature requires expensive external high temperature gas-gas heat exchangers for recuperative heat exchange. Additionally, unselective reactions occurring downstream of the reactor are detrimental for the hydrocarbon yield, making fast quenching of the products to low temperatures (T < 500°C) essential.

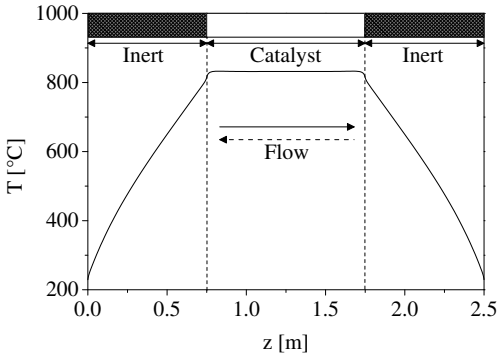


**Figure 4.3:** Cyclic steady state trapezoidal like temperature profile observed in reverse flow reactors with inert sections.

Integration of recuperative heat exchange inside the reactor and fast quenching of the product stream can be achieved via reverse flow operation (i.e. dynamic operation by periodically switching the flow direction through the packed bed membrane reactor). By positioning inert bed sections at the OCM reactor inlet and outlet (Fig. 4.3) and periodically switching of the flow direction, the heating of the feed stream and the cooling of the product stream is integrated in the reactor, using the solid particles as an energy repository: the cold feed gas is pre-heated with energy that was stored in the inert particles during the previous flow cycle when the hot product gas was cooled down over this bed. After many flow cycles a cyclic steady state is attained and a trapezoidal like temperature profile will move back and forth in the inert sections (see Fig. 4.3).

In autothermal reverse flow reactors with thermally coupled endo- and exothermic reactions, temperature and concentration fronts of both reaction sections need to be tuned very carefully to maximize energy exchange and achieve stable reactor operation. In counter-currently operated packed bed reactors with thermally coupled reactor compartments (Fig. 4.4a), a real steady state can be achieved (acting

as a counter-current heat exchanger), with recuperative heat exchange integrated in the reactor. Tuning of the processes to satisfy the overall energy balance and to achieve steady state, however, is only possible if the heat front velocities are of equal magnitude, which is realized by adjusting the ratio of the gas velocities to each compartment (assuming that the overall process is autothermal), see van Sint Annaland et al. (2002).

$$\Phi^{"endo}_{m,in} \approx \Phi^{"exo}_{m,in} \frac{C^{exo}_{p,g}}{C^{endo}_{p,g}} \left(1 - \frac{\omega^{exo}_{g,in}(-\Delta H^{exo}_r)}{C^{exo}_{p,g}(T_{max} - T_{g,in})}\right) \tag{4.1}$$

If the reaction heats of the exothermic and the endothermic reaction are not of equal magnitude, a high degree of dilution of one of the process streams is required. This was confirmed by van Sint Annaland et al. (2002), who demonstrated that counter-current operation in the case of thermal dehydrogenation of propane combined with combustion of a suitable fuel (such a methane) is only feasible, if very diluted streams are used for the exothermic reactions (in order to match the reaction heat of the exo- and endothermic processes). Because pre-mixed feed was used the reaction zone are narrow and located near the reactor inlet, which led to large convective heat losses and a low reaction coupling energy efficiency. Inert sections located at inlet and outlet of the reactor will lead to an increase of the maximum temperature in the catalytic compartment, however, the use of this configuration with a counter-currently operating reactor results in even higher degree of complexity (Kolios et al., 2002).

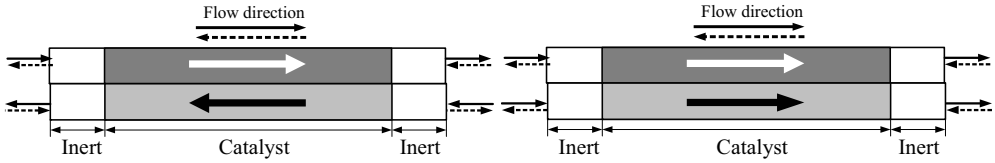


**Figure 4.4:** Configurations for (a) counter-current and (b) co-current operated reverse flow reactors for combination of exo- and endothermic reactions and their corresponding temperature profiles.

If co-current operation is used instead (Fig. 4.4b), the ratio of the gas velocities is adjusted according to the ratio of the Damköhler numbers because the reactions need to take place at the same axial position in the reactor (relative to the front) in order to efficiently exchange reaction heat (van Sint Annaland et al., 2002).

$$Da_I = \frac{k_r a_v \rho_g L_r}{\Phi^{"}_{m,in}} \quad \longrightarrow \quad \frac{Da^{exo}_I}{Da^{endo}_I} = \frac{\Phi^{"endo}_{m,in} k^{exo}_r}{\Phi^{"exo}_{m,in} k^{endo}_r} = 1 \tag{4.2}$$

In membrane reactors, the (methane) gas velocity for the exothermic reaction ($v_g^{exo}$) is determined by the $O_2$ membrane flux, in order to satisfy an overall $CH_4/O_2$ feed ratio and selectivity. Matching of the Damköhler can therefore only be achieved by adjusting the gas velocity of the endothermic reactions ($v_g^{endo}$), although the gas velocity of the endothermic reaction is limited by the conversion and selectivity of the exothermic reaction (Fig. 4.1).

In addition, the use of a distributed $O_2$ feed results in a rather uniform heat generation along the entire reactor length instead of a traveling heat front in the reactor, which may easily lead to unacceptably high temperatures (Smit et al., 2004). Therefore, a maximum exchange of energy from OCM to SRM requires a uniform heat sink which makes co-current operation difficult to implement. The operating window (and hence the maximum overall conversion and energy integration) for autothermal operation is for both modes further limited by additional constraints such as the maximum pressure drop, maximum reactor temperature (reaction kinetics and catalyst stability) and inlet concentrations. In addition, to maximize energy exchange and achieve stable reactor operation special design of inert sections (Nieken et al., 1994a) and complex process control is required (Stitt, 2004).

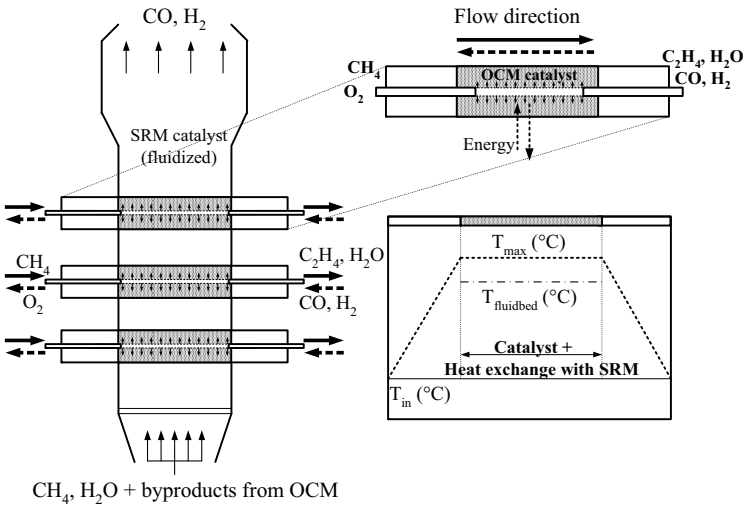


**Figure 4.5:** Novel reactor concept of a reverse flow OCM fixed bed membrane reactor submerged in a fluidized bed SRM reactor.

To obtain much better temperature control and remove the excess heat from the

OCM reactor with maximized cooling efficiency, it is proposed here to immerse the reverse flow fixed bed membrane reactor tubes for OCM in a fluidized bed reactor where SRM is performed. The excellent heat transfer characteristics in the fluidized bed ensure a virtually uniform operating temperature (750-800°C), enabling the SRM reactor to act as a uniform heat sink for the reaction heat produced inside the OCM reactor tubes (Fig. 4.5). In contrast to conventional cooled reverse flow reactors, possibilities for thermal runaway as observed by a.o. Khinast et al. (1998, 1999); Kolios et al. (2000) can be strongly reduced because 1) the reaction heat is generated uniformly along the reactor length, thereby reducing the possibility of hot-spot formation and 2) the steam reforming reactions act as a non-linear heat-sink, because of the Arrhenius-type dependency of the reaction rates, which can accurately be controlled by adding additional $H_2O$ and/or $CH_4$. In addition, the catalytic activity of the SRM process (i.e. dilution of the catalyst) can be applied as an extra degree of freedom to optimize the reactor performance.
In this chapter, this novel reactor concept for thermally coupled OCM and SRM is studied numerically.

## 4.3 Reactor model

A detailed pseudo-homogeneous 1-D reactor model was developed for the OCM packed bed membrane reactor operated in reverse flow, solving the unsteady multi-component mass and energy balances taking into account heat transfer from the OCM reactor compartment to the SRM fluidized bed. The SRM fluidized bed is considered to be at thermodynamic equilibrium which is a very reasonable assumption when a very active noble metal based catalyst is employed, so that the heat transfer can be modeled as a heat sink with a fixed temperature.

The main conservation equations have been listed in Table 4.1. The mass and energy balances are solved for the catalytic reactor compartment and the membrane tube through which $O_2$ is dosed to the catalytic reactor (the heat capacity and the heat transfer resistance of the reactor wall was neglected). To account for the heat transfer to the SRM fluidized bed reactor, transport coefficients from the literature were used. For the transport from the catalyst bed to the reactor (solid) wall, numerous correlations are available such as (e.g. Dixon and Cresswell, 1979), however with these correlations the heat transfer coefficients are usually overestimated at relatively low $d_t/d_p$. Based on experimental findings and a modeling study, Nusselt numbers varying from 10-20 have been determined, hence the $\alpha_{bed \rightarrow wall}$ was assumed to be constant at 160 W/m$^2$/K. The heat transfer coefficient $\alpha_{wall \rightarrow fb}$ is mostly much

**Table 4.1:** Model equations for the 1-D pseudohomogeneous reactor model of the OCM compartment.

*Component mass balances*

$$\varepsilon_g \rho_g \frac{\partial \omega_i}{\partial t} = -\frac{\partial \rho_g v_g \omega_i}{\partial z} + \frac{\partial}{\partial z}\left(\rho_g D_{ax} \frac{\partial \omega_i}{\partial z}\right) + s_{r,i} M_i + \phi^{\text{“}}_{mem,i} a_m$$

with: $s_{r,i} = \rho_{s,bulk} \sum_{j=1}^{N_{reac}} \nu_{i,j} r_j$ for i = 1..N

*Energy balance (reactor compartment)*

$$\begin{aligned}(\varepsilon_g \rho_g C_{p,g} + \rho_{s,bulk} C_p)\frac{\partial T}{\partial t} &= -C_{p,g}\rho_g v_g \frac{\partial T}{\partial z} + \frac{\partial}{\partial z}\left(\lambda_{eff}\frac{\partial T}{\partial z}\right) + s_h + \sum_{i=1}^{N} \phi^{\text{“}}_{mem,i} a_m H_i \\ &+ \alpha_{b\rightarrow fb} a_w (T - T_{fb}) + \alpha_{m\rightarrow b} a_m (T - T_m)\end{aligned}$$

with: $s_h = \rho_{s,bulk} \sum_{j=1}^{N_{reac}} r_j \Delta H_{r,j}$

*Energy balance (membrane compartment)*

$$\begin{aligned}(\varepsilon_g \rho_g C_{p,g} + \rho_{s,bulk} C_p)\frac{\partial T_m}{\partial t} &= -C_{p,g}\rho_g v_g \frac{\partial T_m}{\partial z} + \frac{\partial}{\partial z}\left(\lambda_{eff}\frac{\partial T_m}{\partial z}\right) - \sum_{i=1}^{N} \phi^{\text{“}}_{mem,i} a_m H_i \\ &- \alpha_{m\rightarrow b} a_m (T - T_m)\end{aligned}$$

higher. With conventional Geldart A type particles ($d_p = 100\mu$m) and a fluidization velocity of at least $2u_{mf}$, a heat transfer coefficient of 350 W/m$^2$/K can be easily achieved. An extensive description of the additional equations for the pressure drop, transport parameters, physical properties and initial and boundary conditions can be found in Smit et al. (2005a). For information on the numerical solution strategy with adaptive meshing and time stepping, the interested reader is referred to Smit et al. (2005b).

**Table 4.2:** Operating conditions and reactor dimensions of the base case.

| Parameter | Value | Parameter | Value |
|---|---|---|---|
| $T_{in}$ | 200°C | $\Phi_{CH_4,in}$ | 0.0034 mol/s |
| $T_{fluidbed}$ | 780°C | $\Phi_{CH_4}/\Phi_{O_2}$ | 1-5 |
| p | 120 kPa | $d_r$ | 0.025 m |
| $L_{catalyst}$ | 1 m | $d_{mem}$ | 0.013 m |
| $L_{reactor}$ | 2 m | $d_p$ | 0.002 m |
| $L_{mem}$ | 0.8 m | $\alpha_{b\rightarrow fb}$ | 160 W/m$^2$/K |
| $t_{switch}$ | 1000 s | $\alpha_{m\rightarrow b}$ | 150 W/m$^2$/K |

To reduce heat losses, both the membrane and the reactor compartment are filled with (inert) particles. For the selected $Mn/Na_2WO_4$ catalyst used in the reactor compartment, there is no detailed kinetic model available. Therefore, the most complete kinetic model for OCM published in the literature, developed by Stansch et al. (1997) on a $La_2O_3/CaO$ catalyst, has been used instead, but a with a lower catalytic activity, so that calculated reaction rates resemble those measured on the $Mn/Na_2WO_4$ catalyst. Note that this kinetic model will somewhat underpredict the $C_2$ selectivity of the $Mn/Na_2WO_4$ catalyst. To account for the presence of intra-particle concentration and temperature profiles, the short-cut model demonstrated in Chapter 3, analogous to van Sint Annaland et al. (2007a) was implemented with the modified Thiele modulus calculated from:

$$\phi'_{O_2} = \frac{d_p}{6}\sqrt{\frac{\sum_{j=1}^{N_{reac}} \frac{n_j+1}{2} k_j c_{O_2,bulk}^{n_j}}{D_{eff,O_2}}} \tag{4.3}$$

where the rate constants in 4.3 are based on the pseudo n$^{th}$ $O_2$ order reaction rates, calculated from the reaction kinetic model (Stansch et al., 1997). At sufficiently high hydrocarbon concentrations (which is the case for OCM), the effectiveness factor can

then be calculated with the well-known expression for first-order irreversible reactions:

$$\eta_{O_2} = \frac{3\phi'_{O_2} - tanh(3\phi'_{O_2})}{3(\phi'_{O_2})^2 tanh(3\phi'_{O_2})} \tag{4.4}$$

The effects of the intra-particle concentration profiles, on the $C_2$ selectivity are also corrected, see van Sint Annaland et al. (2007a):

$$\langle\sigma\rangle = 1 - F_{1-\sigma}(1 - \langle\sigma_b\rangle) \tag{4.5}$$

Because the intra-particle temperature profiles in a packed bed membrane reactor for OCM are relatively small (<10 °C), this method can be readily applied to account for the particle effectiveness, although non-isothermal conditions are assumed for the gas phase.

## 4.4 Results

The influence of distributive feeding of $O_2$/air, operating temperature of the fluidized bed and overall heat transfer coefficients between the compartments on the overall reactor performance have been investigated. The operating conditions and dimensions of the reactor used in the simulations to investigate the novel reactor concept have been listed in Table 4.2. First, the influence of reverse flow operation on the OCM reactor performance will be evaluated, followed by a discussion on the operating conditions required to achieve overall autothermal operation.

### 4.4.1 Influence of reverse flow operation

The performance of the OCM reverse flow packed bed membrane reactor has first been investigated at different overall $CH_4/O_2$ feed ratios at isothermal reactor conditions. The length of the membrane was taken slightly shorter than the catalyst section, to ensure that all $O_2$ fed via the membrane is converted in the catalytic bed and that unselective gas-phase reactions with $O_2$ in the post catalytic section are prevented. First, the influence on the $C_2$ selectivity and the $C_2$ yield of increasing the reactor length and increasing the total flow rate while keeping the overall $CH_4/O_2$ ratio constant at 2.5 is studied. In these simulations the flow rate was adjusted so that the overall residence time was constant and that optimal $C_2$ yield was achieved at the reactor outlet (Fig. 4.6 - dotted lines).

The results, presented in Fig. 4.6, show that indeed very high $C_2$ selectivities and yields can be achieved because of distributive $O_2$ feeding. Because the overall

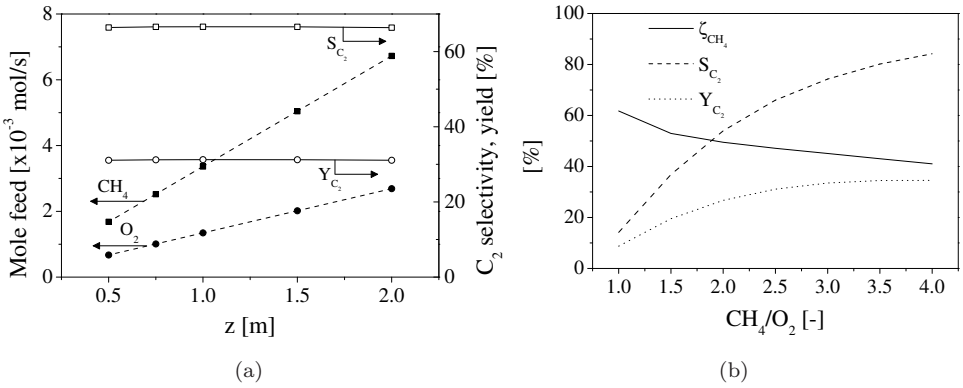


**Figure 4.6:** (a) Total $C_2$ yield, $C_2$ selectivity and mole feed flux under isothermal conditions (T=780°C) at a constant $CH_4/O_2$ ratio of 2.5 as a function of the reactor length and (b) dependency of $CH_4$ conversion, $C_2$ selectivity and yield on the overall $CH_4/O_2$ ratio (see Table 4.2 for other conditions).

residence time was kept constant, the performance of the reactor is nearly unchanged if the length is changed. Under these conditions and if temperature effects are ignored, the overall $C_2$ yield is mainly determined by the $CH_4/O_2$ feed ratio. For example, with a $CH_4/O_2$ ratio of 2.5 a $C_2$ yield of 30% can be achieved while with a $CH_4/O_2$ of 4 the $C_2$ yield slightly increases to 34%, but drops below 10% at an overall $CH_4/O_2$ ratio of 1. With a reactor length of 1 m at the selected operating conditions sufficient heat transfer area with the SRM fluidized bed can be realized (see also Fig. 4.8 and 4.9).

At non-isothermal conditions, the influence of periodically changing the flow direction can be discerned from Fig. 4.7. At the end of each semi-cycle, a nearly symmetric temperature profile exists in the reactor. For a reverse flow reactor operated in adiabatic mode, i.e. without heat exchange with the fluidized bed, the time-averaged outlet temperature rise equals the adiabatic temperature rise. However, in the OCM/SRM reactor, a large part of the reaction heat is transferred to the fluidized bed reactor, the outlet temperature is actually lower.

In contrast to conventional (adiabatic) reverse flow reactors, the temperature plateau in the reaction zone is mainly determined by the fluidized bed reaction temperature, the overall heat exchange coefficient for the heat transfer between the OCM/SRM compartments and the $O_2$ membrane flux. If the amount of $O_2$ fed to the reactor is changed from a $CH_4/O_2$ ratio of 2.0 to 3.0, it is demonstrated in Fig. 4.8a that the maximum temperature in the reaction section decreases with the reduction of the overall reaction heat released by the oxidative coupling reactions.

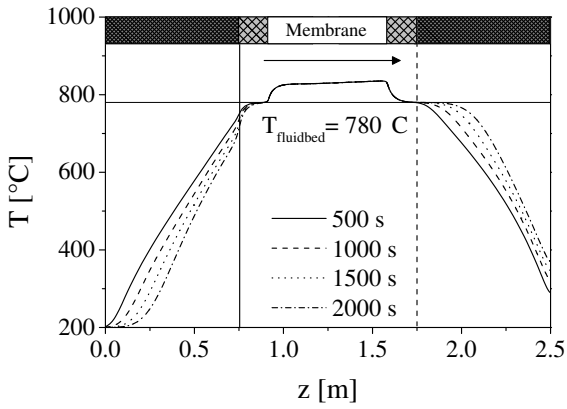


**Figure 4.7:** Axial temperature profile at the end of a semi-cycle with a $CH_4/O_2$ feed ratio of 2.5 ($L_{reactor}$=2.5 m, $t_{cycle}$=1000 s, see Table 4.2 for other conditions).

At the lowest $CH_4/O_2$ ratio, i.e. at the highest $CH_4$ conversion, the temperature increase relative to the fluidized bed temperature is maximum 50°C, which is still acceptable to prevent catalyst deactivation or membrane deterioration (via sintering). In practice, somewhat lower feed ratios will be applied, because the $C_2$ yield is higher when a lower local $O_2$ concentration is applied.

The corresponding axial product mole fraction profiles in Fig. 4.8b show that at higher $CH_4$ conversions the formation of CO and $CO_2$ via oxidation of $CH_4$ is slightly gaining importance, while the $C_2H_4/C_2H_6$ ratio is strongly influenced due to the increased relative importance of the oxidative dehydrogenation of $C_2H_6$ at low $O_2$ concentrations (low reaction order in $O_2$).

### Heat transfer effects

In Fig. 4.8a it was shown that in the cyclic steady state the increase of the plateau temperature in the OCM reactor section is smaller than 50 °C, due to the excellent heat transfer to the fluidized bed reactor operating at 780 °C where the external heat transfer coefficient in the SRM fluidized bed was assumed at 350 $W/m^2/K$ (e.g. Kunii and Levenspiel, 1991). When the temperature limit in the OCM reactor needs to be decreased, the external heat transfer coefficient in the SRM fluidized bed can be increased by e.g. applying higher fluidization velocities or using smaller catalyst particles or operation of the SRM fluidized at lower temperatures. This was confirmed by performing a sensitivity study on the influence of the external heat transfer coefficient $\alpha_{wall \rightarrow fb}$. In the case that $\alpha_{wall \rightarrow fb}$ is lower than 350 $W/m^2/K$, which is highly

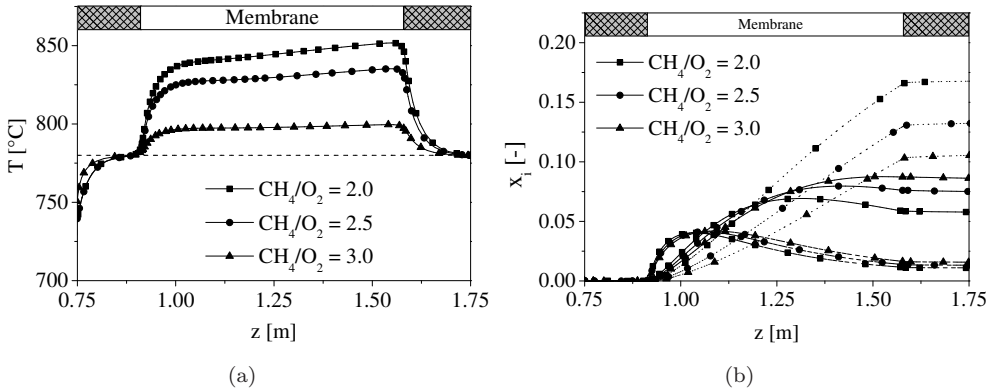


(a) (b)

**Figure 4.8:** Cyclic steady state axial temperature profiles in the OCM packed bed membrane reverse flow reactor (L=2.5 m) at the end of the forward flow cycle ($t_{cycle}$=1000 s) (a) and axial mole fraction profiles in the catalytic reactor section (L=1.0 m) (b) for a $CH_4/O_2$ ratio of 2.5 (solid lines) and 3 (dotted lines) (see Table 4.2 for other operating conditions).

unlikely with fluidized bed reactors, it was observed with $\alpha_{wall \rightarrow fb}$ being 20% of its original value the maximum temperature in the reactor is approximately 860 °C. The product distribution is not severely influenced (the $C_2$ yield is slightly lower because of unselective oxidation reactions) and the $CH_4$ conversion does not differ more than 1% over the range evaluated. The heat transfer coefficient for transport from packed bed to the tube wall ($\alpha_{b \rightarrow wall}$) is of similar magnitude as $\alpha_{wall \rightarrow fb}$ and because the inner surface of the tube is of similar magnitude as the outer surface, similar effects on the results were observed.

### Flow switching time

With a catalytic reactor length of 1 m, it was found that with inert sections of 0.75 m at both reactor ends all the heat can efficiently be kept inside the reactor, while the outlet temperature remains below 400 °C (Fig. 4.9). The maximum outlet temperature in a (cooled) reverse flow reactor of given size is determined by the time at which the flow direction is switched. At an overall $CH_4/O_2$ feed ratio of 2.5, the reaction heat of oxidative coupling is efficiently transported to the SRM fluidized bed reactor compartment, so that the temperature profile and thus the $C_2$ selectivity is hardly influenced by the switching time (see Fig. 4.9). This in contrary to conventional (adiabatic) reverse flow reactors with inert sections, where decrease of the switching time inevitably leads to a lower plateau temperature (Nieken et al., 1994b).

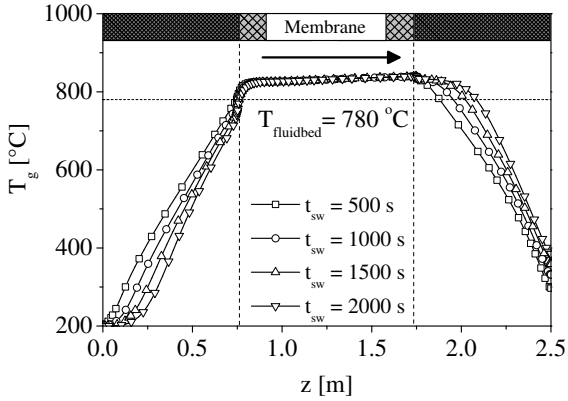


**Figure 4.9:** Cyclic steady state axial temperature profiles in the OCM packed bed membrane reverse flow reactor (see Table 4.2 for operating conditions).

Increasing the switching time from 500 to 2000s, the reactor outlet temperature in the cyclic steady state increases to maximum 400 °C. The maximum allowable switching time is constrained by the inlet temperature of the catalytic reactor section, which should be at least 700 °C in order to start the oxidative coupling reactions, but also by the fact that fast quenching should still be possible. On the other hand, the application of a switching time lower than 1000 s decreases the time-averaged outlet temperature to approximately 200 °C, but this will lead to an increase in the undesired switching losses of valuable $C_2$ hydrocarbons.

### 4.4.2 Autothermal operation

To establish the operating conditions to achieve overall autothermal operation, the reaction enthalpy of the OCM reactions in a single reactor tube was calculated for different $CH_4/O_2$ feed ratios at isothermal reaction conditions (which can be considered as a limiting case for $\alpha_{fb} \rightarrow \infty$). Ethylene and ethane were removed from the OCM product mixture and the by-products and unconverted methane from OCM were used as a feedstock for the steam reforming reactions. Additional steam was added until an overall $H_2O/CH_4$ ratio of 3 was reached, which is typically used to prevent deposition of carbonaceous species. The enthalpy change in the SRM compartment to reach thermodynamic equilibrium was calculated. Figure 4.10 shows the (absolute) enthalpy change in the OCM and SRM compartments for different $CH_4/O_2$ ratios.

With increasing $CH_4/O_2$ ratio, the overall process becomes less exothermic because first a relatively smaller amount of $O_2$ is fed to the reactor decreasing the $CH_4$ conversion and second improving the $C_2$ selectivity and yield due to the lower reaction

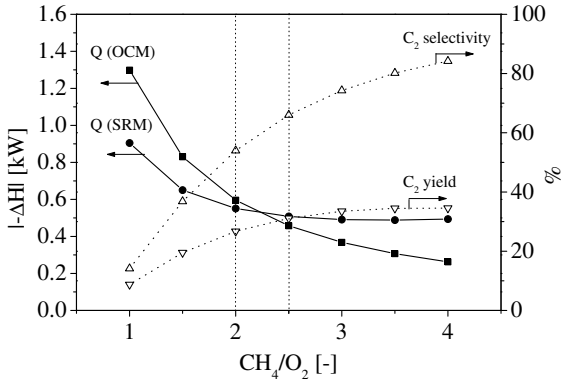


**Figure 4.10:** Influence of the $CH_4/O_2$ ratio on the (absolute) enthalpy change in the OCM and SRM compartments and the overall $C_2$ selectivity and yield at isothermal conditions (T=780°C, p=120 kPa, $H_2O/CH_4$=3).

order in $O_2$ where the reaction enthalpy of oxidative coupling ($\Delta H_{r,0}$ = -88 kJ/mol $CH_4$) is much smaller compared to methane combustion ($\Delta H_{r,0}$ = -802 kJ/mol $CH_4$). The concomitant effect of lower $CH_4$ conversions and higher $C_2$ selectivities in the OCM compartment, is a nett decrease of the energy consumption required in the SRM compartment despite the fact that more $CH_4$ is available, due the water-gas-shift reaction. With a total $CH_4/O_2$ ratio in the range of 2-2.5, as can be discerned from Fig. 4.10, the energy production and consumption nearly match each other and the overall process can be operated autothermally.
The preferred reaction product of SRM reactions is CO and $H_2$, and with a $CH_4/O_2$ ratio in the autothermal operating range (2-2.5), synthesis gas yields of approximately 60-70% can be achieved. Higher synthesis gas yields could be realised by decreasing the $H_2O/CH_4$ ratio, which would suppress $CO_2$ formation via the water-gas-shift reaction. However, a $H_2O/CH_4$ ratio of about 3 is typically required to prevent the formation of carbonaceous species.

The important conclusion is that (near) autothermal operation can be achieved at a $C_2$ yield of approximately 30% corresponding to a $CH_4/O_2$ ratio between 2-2.5 and a $CH_4$ conversion of approximately 45%. Although this should be realizable in an optimally designed and operated packed bed membrane reactor, the $C_2$ yield is still somewhat higher than the currently experimentally maximally achieved yield of about 27.5% by a.o. Lu et al. (1999) in a lab reactor. At a lower $C_2$ yield and a concomitant higher heat production in the OCM compartment, this reactor concept can still be operated autothermally, by feeding additional $CH_4$ and/or $H_2O$ to the

SRM compartment to increase the heat consumption.

## 4.5 Conclusions

For the simultaneous autothermal production of ethylene and synthesis gas directly from methane in a single multifunctional system, a novel reactor concept is proposed where the oxidative coupling (OCM) and steam reforming (SRM) processes are performed in different reactor compartments which are thermally coupled. A fixed bed reverse flow membrane reactor was used for the exothermic OCM, which is immersed in a fluidized bed reactor where the endothermic SRM reactions are carried out, consuming the reaction heat of OCM while producing synthesis gas. With this reactor concept optimal $C_2$ yield (because of the distributive oxygen feeding via the membrane and fast quenching of the reaction products thanks to the reverse flow concept) and optimal energy efficiency due to process intensification (because of the integration of recuperative heat exchange via the reverse flow concept and thermal coupling of endothermic and exothermic reactions) are combined in an autothermal reactor.

Numerical simulations have demonstrated that in the cyclic steady state, the reaction enthalpy can indeed be efficiently transferred from the OCM packed bed membrane reactor to the fluidized bed compartment and that $C_2$ yields up to 30% with approximately 100% methane conversion are possible in an overall autothermal operation mode, when using an overall $CH_4/O_2$ ratio of 2-2.5 and with a $H_2O/CH_4$ ratio of 3 in the SRM fluidized bed reactor.

## Acknowledgement

The author wishes to thank T. Kolkman for his valuable contribution to the modeling work. The financial support by the Netherlands Organisation for Scientific Research (NWO/ACTS) under the research theme of Advanced Sustainable Processes by Engaging Catalytic Technologies (ASPECT) (project 053.62.008) is gratefully acknowledged.

# Nomenclature

| | | |
|---|---|---|
| *Roman letters* | | |
| $a$ | $m^2/m^3$ | specific surface area |
| $d$ | m | diameter |
| $Da_I$ | - | Damköhler number |
| $D_{eff}$ | $m^2/s$ | effective diffusivity |
| $D_{ax}$ | $m^2/s$ | axial dispersion coefficient |
| $c_i$ | $mol/m^3$ | concentration of component i |
| $C_p$ | J/kg/K | heat capacity |
| $F_{1-\sigma}$ | - | selectivity correction factor |
| $H_i$ | J/mol | enthalpy |
| $k_j$ | 1/s | first order reaction rate constant |
| $L$ | m | length |
| $M_j$ | kg/mol | mole mass |
| $n_j$ | - | reaction order of reaction j |
| $p$ | Pa | pressure |
| $Q$ | W | heat |
| $r$ | m | radius |
| $r_j$ | $mol/kg_{cat}/s$ | reaction rate |
| $s_{r,i}$ | $mol/m^3/s$ | source term mass balance |
| $s_h$ | $J/m^3/s$ | source term energy balance |
| $t$ | s | time |
| $T$ | K | temperature |
| $u_{mf}$ | m/s | minimum fluidization velocity |
| $v$ | m/s | superficial velocity |
| $z$ | m | axial coordinate |
| *Greek letters* | | |
| $\alpha$ | $W/m^2/K$ | heat transfer coefficient |
| $\varepsilon_g$ | - | bed void fraction |
| $\phi_i^{'}$ | - | Thiele modulus |
| $\Phi_i$ | mol/s | inlet mole flow |
| $\Phi^{"endo}_{m,in}$ | $kg/m^2/s$ | inlet mass flux (gas velocity) |
| $\Phi^{"}_{mem,i}$ | $kg/m^2/s$ | membrane mass flux of component i |
| $\eta$ | - | effectiveness factor |
| $\Delta H_{r,j}$ | J/mol | reaction enthalpy of reaction $j$ |

| | | |
|---|---|---|
| $\nu_{i,j}$ | - | stoichiometric coefficient |
| $\lambda_{eff}$ | W/m/K | effective bed conductivity |
| $\rho$ | kg/m$^3$ | density |
| $\sigma$ | - | selectivity |
| $\omega$ | - | weight fraction |

*Subscripts*

| | |
|---|---|
| b, bulk | bulk solid property |
| endo | endothermic |
| exo | exothermic |
| fb | fluidized bed |
| g | gas phase |
| i | inner |
| m | membrane |
| max | maximum |
| N | number of components |
| $N_{reac}$ | number of reactions |
| o | outer |
| s | solid phase |
| t | tube |
| w | wall |

# 5

# OCM kinetics on a $Mn/Na_2WO_4/SiO_2$ catalyst


## Abstract

The rates of the reactions prevailing during the oxidative coupling of methane (OCM) were measured under differential conditions in a quartz micro-catalytic fixed bed reactor on a $Mn/Na_2WO_4/SiO_2$ catalyst. Because the catalyst is a reducible metal oxide, it was found with Thermal Gravity Analysis (TGA) that catalyst pre-treatment with oxygen is required to obtain a high $C_2$ selectivity of about 85%, and that a low oxygen partial pressure during the OCM reactions is already sufficient to maintain the catalyst stable in the oxidized state.

Because the kinetic models for OCM over a $Mn/Na_2WO_4/SiO_2$ in the literature are not suitable for application in numerical reactor models, the overall reaction orders and rate constants of the primary reactions were determined by measuring the intrinsic reaction rates at different methane and oxygen inlet concentrations. The reaction rate constants of the secondary ethane and ethylene oxidation reactions were estimated assuming first order in both the hydrocarbon and in oxygen from the experimental data published by Takanabe and Iglesia (2008) for the same catalyst. It was found that the reaction order in oxygen for the coupling reaction is 0.38, while the reaction order in oxygen for ethylene oxidation approaches unity, indicating that low oxygen concentration levels are beneficial for obtaining a high $C_2$ selectivity (up to 80-90%). Based on the experiments and least-squares minimization, a simplified reaction mechanism is proposed, where the dependency of the ethane (coupling) and carbon dioxide (oxidation) production rates and the secondary ethylene production and $C_2$ oxidation rates are described with power-law type reaction rate expressions.

## 5.1 Introduction

During the 1980's pioneering research was carried out on the oxidative coupling of methane (OCM) by several research groups (Keller and Bhasin, 1982; Ito et al., 1985) and since then the production of ethylene and ethane directly from natural gas became a widely investigated topic. Because the selective production of $C_2H_4$ and $C_2H_6$ from methane also suffers from the typical problems encountered in many partial oxidation reaction systems, namely acceptable $C_2$ selectivities at low $CH_4$ conversions, but low $C_2$ selectivities at high $CH_4$ conversions resulting in a low $C_2$ yield, many different materials were investigated for their catalytic activity and selectivity for OCM. A widely investigated catalyst for OCM is Li/MgO (Korf et al., 1989), which is already active and selective at reaction temperatures of 750 °C but is inherently unstable because of the loss of active components. For both the packed bed membrane reactor concepts in which OCM and SRM are combined on the scale of the dual function catalyst particle (Chapter 2 & 3) and on the scale of separate compartments in a heat exchange reactor (Chapter 4), long-term catalyst stability is essential. In the dual function catalyst particle, contact of oxygen with the SRM catalyst is prevented by total conversion of $O_2$ in the outer part of the OCM catalyst, which can only be achieved if a very active catalyst such as the $La_2O_3/CaO$ catalyst is used (Sofranko et al., 1987; Stansch et al., 1997). For the packed bed membrane reactor with separate OCM and SRM compartments, too high catalyst activity will inevitably lead to undesired concentration polarization and concomitant radial temperature profiles. Therefore the $Mn/WO_4/SiO_2$ catalyst, with a somewhat lower activity than $La_2O_3/CaO$, but with good selectivity and stability was used for application in the packed bed membrane reactor.

Usually the research is limited to study the catalyst performance and the determination of a reaction mechanism, however, for reactor modeling and design of a new process involving oxidative coupling of methane, possibly combined with steam reforming, an accurate description of the most important reaction rates is required. A quantitative description of the reaction rates of the most important reactions on a $Mn/WO_4/SiO_2$ catalyst by means of a relatively straightforward kinetic study is the objective of the research described in this chapter. A simplified kinetic model is presented, describing the rates of the primary and secondary reactions prevailing during the oxidative coupling of methane over a $Mn/Na_2WO_4/SiO_2$ catalyst. The primary reaction rates were measured in a micro-catalytic fixed bed reactor under differential operating conditions, while the secondary reaction rate constants were derived from a kinetic study by Takanabe and Iglesia (2008) in which the first order rate constants were determined by means of isotopic labeling of $CH_4$, $C_2H_4$ and $C_2H_6$. The obtained

reaction rates were described via conventional power-law reaction rate expressions.

This chapter starts with a short review of the available catalysts for oxidative coupling and two promising catalysts are discussed in more detail. The preparation of the best performing catalyst, the experimental setup and the procedures followed during the experimental program are described. The composition of the selected catalyst is compared with available data from the literature by analyzing the elements in a small amount of catalyst via X-ray fluorescence (XRF) spectroscopy. Subsequently, it was shown that the (redox) catalyst remains in the oxided state and the percentage of the oxides on the catalyst that can be reduced is measured by means of thermogravimetric analysis. Finally, the homogeneous reaction rates (mostly occuring in the pre- and post-catalytic sections) and the catalytic reaction rates during the oxidative coupling were determined in a micro-catalytic fixed bed reactor by investigating the dependency of the conversion rates on the partial pressures of methane, oxygen, ethylene and ethane. The reaction rates of the relevant reactions are described using power-law reaction rate expressions in a simplified kinetic model.

## 5.2 Review on OCM catalysts

A large number of unsupported and supported catalysts, mostly elements from Group I-II of the Periodic Table, was developed and tested for their catalytic activity and stability for methane coupling reactions. In a comprehensive review of catalytic materials for oxidative coupling, it was shown that for alkaline earth metal (e.g. Mg, Ca, Sr) and promoted rare earth (e.g. La, Ce, Nd) oxide catalysts the performance can be modified by adding an alkaline earth promoter (Choudhary and Uphade, 2004). Unsupported catalysts with a better activity and selectivity are for example lanthanide oxides $Nd_2O_3$, $Eu_2O_3$ and $La_2O_3$ (Kus et al., 2003), where the strong basic sites of e.g. La and Nd oxides result in improved catalytic activity. The activity can be increased by doping with Ce or Nd, addition of 10 wt% ceria showed an increase in the $C_2$ yield to 20-22% (Dedov et al., 2003). The Sr-promoted $La_2O_3$ showed however the best performance according to Choudhary and Uphade (2004). The $C_2$ yield (15-20%) of these catalysts is acceptable, however, unsupported catalysts are less applicable in industrial environment due to their weak mechanical strength and limited reaction rate per unit catalyst volume.

The best supported catalysts for OCM usually consist of similar elements as the unsupported catalysts, although an additional degree of freedom (the support material) is used for further optimization. Numerous studies have been performed to determine which is the best catalyst/support combination for OCM and some of the highlights

**Table 5.1:** Reactivity and performance of supported OCM catalysts ($CH_4/O_2$ ratio = 2-10, p = 1 bar).

| Catalyst | $CH_4/O_2$ (-) | T (°C) | $\zeta_{CH_4}$ (%) | $S_{C_2+}$ (%) | $Y_{C_2+}$ (%) | $r_{CH_4}$ ($\mu$mol/g/s) | $m_{cat}$ (g) | GHSV (ml/g/h) | Reference |
|---|---|---|---|---|---|---|---|---|---|
| *Unsupported* | | | | | | | | | |
| La/CaO | 4 | 800 | 28 | 56 | 16 | | 1 | | Dedov et al. (2003) |
| Ce/MgO | 4 | 800 | 28 | 50 | 14 | | 1 | | Dedov et al. (2003) |
| $Sr/La_2O_3$ | 4 | 800 | 29 | 59 | 17 | | 1 | | Stansch et al. (1997) |
| $La_2O_3$ | 5.4 | 800 | 24.0 | 65.0 | 15.6 | 49.6 | 0.3 | 19977 | Conway et al. (1992) |
| La/CaO | 8 | 800 | 19.8 | 67.2 | | | 1 | | [8MJ] |
| *Supported* | | | | | | | | | |
| Li/MgO | 2 | 750 | 37.8 | 50.3 | 19.0 | 0.268 | 4 | 747 | Ito et al. (1985) |
| $Pb/SiO_2$ | 6 | 750 | 13.0 | 58.2 | 7.6 | 57.2 | 0.1 | 119880 | DeBoy et al. (1988) |
| $Mn/Na_2WO_4/MgO$ | 7.4 | 800 | 20.0 | 80.0 | 16.0 | 6.9 | 2.1 | 3212 | Wang et al. (2006) |
| Li/Sn/MgO | 9.6 | 680 | 14.3 | 84.0 | 12.0 | 18.7 | 0.75 | 15984 | Korf et al. (1989) |
| *The $Mn/Na_2WO_4$ catalyst* | | | | | | | | | |
| 1.9% Mn/5% $Na_2WO_4$ | 4.5 | 850 | 33 | 80 | 26 | 2.8 | 0.40 | 2700 | Palermo et al. (1998) |
| 2% Mn/x% Na/3% $WO_4$ | 3.0 | 800 | 33 | 59 | 19 | 2.1 | 0.10 | 70560 | Ji et al. (2002, 2003) |
| 2% $Mn_2O_3$/5% $Na_2WO_4$ | 4.0 | 780 | 33 | 37 | 12 | 6.3 | 0.40 | 196110 | Chou et al. (2003) |
| 2% Mn/5% $Na_2WO_4$ | 7.4 | 800 | 20 | 80 | 16 | 2.8 | 0.51 | 12917 | Pak et al. (1998) |
| 2% Mn/5% $Na_2WO_4$ | 3.0 | 800 | 36.8 | 64.9 | | | | | Jiang et al. (1993) |
| $Mn/Na_2WO_4/SiO_2$ | 4 | 820 | 30 | 68 | 21 | | 0.2 | 30000 | Wang et al. (2006) |

have been listed in Table 5.1, for several inlet $CH_4/O_2$ concentrations. Most of the catalysts were tested in a micro-catalytic fixed bed reactor under differential conditions at a molar $CH_4/O_2$ ratio ranging from 2-10 (undiluted). The $C_2$ yield that can be achieved with supported catalysts varies between 12-21%, at relatively similar temperatures. Comparison of the performance of the catalysts is, however, difficult because the inlet $CH_4$ and $O_2$ concentration ($CH_4/O_2$ ratio), and the flow rate (i.e. $CH_4$ conversion) was not the same in all these tests, although it is assumed that the catalyst were tested at nearly optimal conditions. In addition, the catalytic activity should also be taken into account (represented by the $CH_4$ reaction rate), because it determines the required reactor volume and the volumetric heat generation. For example, the Li/MgO catalyst has a relatively low activity (also at higher GHSV), but a very acceptable $C_2$ yield of 19%. Next to selectivity and activity, another important issue for OCM catalysts is the long-term stability; because of the high operating temperature and the prevailing exothermic reactions, the active catalytic components tend to migrate or even evaporate from the catalytic surface leading to deactivation of the catalyst. For catalysts, such as the Li/MgO catalyst, the high mobility of Li limits the lifetime and thus the industrial applicability. The problem can be partially solved by using excess catalyst, thereby decreasing the utilization of the catalytic bed, and by selecting a catalyst with high activity such as $La_2O_3$. If the catalyst gradually deactivates, the remaining catalyst will be used until the overall activity becomes unacceptable, however at the expense of throughput. Another method is to apply a catalyst with better stability and lower activity, such as the $Mn/Na_2WO_4$ catalyst. The properties and performance of these two catalysts are discussed in somewhat more detail below.

### 5.2.1 The $La_2CO_3$/CaO catalyst

In the literature it is found that if OCM catalysts are promoted by lanthanoids or alkali metals, additional activity and selectivity is observed during kinetic experiments (Choudhary and Uphade, 2004). For example, lithium-doped magnesium oxide (Li/MgO) has been subject of investigation of many researchers because of its relatively high activity towards $C_2$ formation. Although this catalyst is very promising, its lack of long-term stability due to evaporation/migration of active material makes it less suitable for larger scale application. A catalyst showing a great thermal and hydrothermal stability is the $La_2CO_3$ catalyst which was tested on oxidative coupling activity for periods up to 500 h on stream (Conway et al., 1992). High $C_2$ yields were experimentally observed with the use of rare earth oxides promoted with alkaline earth metals as catalyst. As shown in Table 5.1, the Sr-promoted $La_2O_3$ with a

Sr/La ratio of 0.1 showed good results at an $CH_4/O_2$ inlet ratio of 4.0 and a temperature of 800 °C, at which a $CH_4$ conversion of approximately 28-29% and a yield around 18% could be obtained (Choudhary and Uphade, 2004).

The support of this catalyst is equally important, because it partially determines the catalytic performance because of its surface basicity, larger surface area and lower cost. In addition, when catalysts are applied in industrial scale reactors the support provides mechanical strength (crushing strength) and a lower pressure drop across the catalyst bed. The activity and selectivity of Li/MgO catalysts were drastically reduced when they were supported on different catalyst carriers due to formation of metal oxides containing Li and Mg, because the basicity of the active sites was strongly influenced by the origin of the support and the deactivation because of chemical interactions between support and catalyst. However, the most active catalysts reported for oxidative coupling of methane is the $La_2O_3$ catalyst supported on CaO, which has been proposed by a.o. Becker and Baerns (1991). As mentioned before, unsupported Sr-promoted $La_2O_3$ already shows a high catalytic activity and $C_2$ selectivity, also on different supports like commercially available macro-porous silica-alumina (Choudhary and Uphade, 2004). On CaO an even higher activity was found, however, high space time yields with this catalyst may be difficult because of the large temperature increases caused by the exothermic reactions. Temperature increases of more than 100 °C are already observed during kinetic experiments and it is very likely that this will increase even further at larger reactor scale and higher $CH_4$ conversions (Stansch et al., 1997). Therefore, a catalyst with a lower reaction rate per unit catalyst mass is preferred for better thermal control of the oxidative coupling of methane, unless special measures are taken for heat removal, such as in the packed bed membrane reactor with a dual function catalyst, described in Chapter 3.

### 5.2.2 The $Mn/Na_2WO_4/SiO_2$ catalyst

With most catalysts, the overall $C_2$ product yield obtained in single pass operation mode does not exceed 25-30%, which is the generally considered lower limit for commercialization of OCM (Choudhary and Uphade, 2004; Lunsford, 1990, 2000). In the 1990's, however, an active and stable catalyst has been developed by Fang et al. (1992), who identified sodium-promoted manganese oxides as promising catalysts for the oxidative coupling of methane. Catalysts based on manganese oxides were already suggested as good OCM catalysts by Sofranko et al. (1987), who measured methane conversion rates over various transition metal oxides in a redox cyclic mode of operation. From the investigated transition metal oxides, only manganese and tin oxides remained stable, while an overall $C_2$ selectivity of more than 75% was achieved on the

more stable and less volatile manganese oxides supported on $SiO_2$ at temperatures around 800°C (Jones et al., 1987; Sofranko et al., 1987). By addition of alkali metals or alkaline earth metals, the surface basicity and the interaction between the alkali metal ions and the manganese oxides leads to suppression of carbon oxide formation (Sofranko et al., 1988), which was further developed by Fang et al. (1992) into a catalyst containing 2 wt% Mn/5 wt% $Na_2WO_4$ supported on $SiO_2$, which appeared to have a much higher stability probably thanks to by the presence of tungsten.

Further optimization of a x%Na-3.1%W-2%Mn/$SiO_2$ catalyst (x varying from 0 to 7.8 wt%) indicates that a good catalytic performance can only be obtained if all 3 metals of this trimetallic system are present at the catalyst surface (Ji et al., 2002). For example, there is an optimum Na-concentration at the catalyst surface, which influences the near-surface composition of W and Mn. The addition of Na decreases the CO selectivity; with sodium free catalyst a CO selectivity of approximately 61% is realized but this value decreases to about 13% on a catalyst containing 0.8wt% Na. A strong correlation exists between the surface Mn concentration and the catalyst performance, hence, a too high Na load will cause enrichment of Na near the surface resulting in a decrease of the surface Mn concentration, directly affecting the $CH_4$ conversion and $C_2$ selectivity, see Ji et al. (2002). By doping the catalyst with $SnO_2$, a significant increase of the $CH_4$ conversion up to 33% and a corresponding $C_{2+}$ selectivity of approximately 73% can be achieved. Cofeeding oxygen and methane without diluent at elevated pressure (6-10 bar), $CH_4/O_2$ ratio of 6 and high GHSV resulted in much higher $C_{2+}$ selectivity mainly because of the production of $C_3$ (30%) and $C_4$ (4%) components, which is remarkably higher than found with other investigated catalysts (Chou et al., 2003). The reason for the remarkable increase in conversion and selectivity is thought to be the improvement in $O_2$ storage capacity due to the addition of $SnO_2$, while the migration of catalytic species to the catalyst surface is also enhanced (Chou et al., 2003). This behavior was also observed with the addition of $Na_2WO_4$ to a catalyst consisting of Mn/$SiO_2$ (Ji et al., 2002).

The stability of the Mn/$Na_2WO_4$ catalyst on $SiO_2$ and MgO was investigated in the cofeed and pulsed feed mode in a fixed bed microreactor (alumina tubes) at temperatures varying from 750-800°C and $CH_4/O_2$ ratios between 5 and 10 (integral operation). During an on-stream time of at least 30 hours, the $CH_4$ conversion and $C_2$ selectivity could be maintained at constant values of respectively 20% and 80%, with both the Mn/$Na_2WO_4$/$SiO_2$ and the Mn/$Na_2WO_4$/MgO catalyst (Wang et al., 1995). The activity of the MgO based catalyst could however not be retained because of a significant decrease in surface area during the operation. The $SiO_2$ based catalyst appeared to be stable under integral and differential conditions, showing that $O_2$

deficiency does not play a role in the deactivation. In contrast to other researchers who all conclude that the catalyst is highly stable during very long operating time (>500h), Pak et al. (1998) concluded that the $Mn/Na_2WO_4/SiO_2$ catalyst gradually deactivates over time, but that this effect is partially compensated or masked by the observed hot spots in the reactor, which they confirmed by investigating the temperature profiles along the axial reactor coordinate. Experimental results performed by different research groups hence showed that the catalyst shows excellent overall $C_2$ selectivity (80%) at moderate $CH_4$ conversions (20-25%), especially under oxygen limiting conditions (Wang et al., 1995). Long-term experiments under OCM conditions also demonstrated that the initial activity coud be retained for periods up to 97h in a small fixed bed reactor (Pak et al., 1998) and even up to 450h in a fluidized bed reactor (Kou et al., 1998). For this reason the $Mn/Na_2WO_4/SiO_2$ catalyst is one of the best and most promising catalysts available for the oxidative coupling of methane, especially in packed bed membrane reactors.

Another advantage is the easy preparation of this catalyst. The $Mn/Na_2WO_4/SiO_2$ catalyst can be very easily prepared from readily available chemicals. The most common way to produce $Mn/Na_2WO_4$ catalyst on $SiO_2$ is incipient wetness impregnation with aqueous solutions of $Mn(NO_3)_2$ and $Na_2WO_4$ at 85-90°C (Ji et al., 2002, 2003; Palermo et al., 1998; Wang et al., 1995; Zhang et al., 2006) followed by drying in air or $O_2$ at 80-130°C. Although 50-90°C is the most often used impregnation temperature, some researchers also appear to carry out this step at room temperature (Palermo et al., 1998). Calcination of the catalyst is carried out under flowing air/oxygen at temperatures in the range of 800-900°C. Chou et al. (2003) applied equal volume impregnation at 54°C and subsequent impregnation with toluene solutions containing 5% di-n-butyltin dilaurate to obtain ($SnO_2$ doped) $Mn_2O_3$/5% $Na_2WO_4/SiO_2$. The composition of the catalyst was optimized to a large extent by Fang et al. (1992) and it was found that a catalyst with a loading of 2 wt% Mn and 5 wt% $Na_2WO_4$ results in high selectivity and methane conversion. This was confirmed by other researchers, who determined an optimal catalyst composition of 0.8 wt% Na/3.1 wt% W/1.2 wt% Mn on $SiO_2$ (Fang et al., 1992; Ji et al., 2002; Lunsford, 1990).

## 5.3 Review on reaction mechanism and influence of operating conditions

It is generally accepted that the heterogeneously catalytized oxidative coupling reaction involves the abstraction of a H-atom from methane by the adsorbed $O_2$ species, leading to the formation of methyl radicals at the catalyst surface. The generated intermediate methyl radicals then react further to form the primary reaction products, ethane and carbon oxides in the gas phase via branched chain reactions in the pores of the catalyst and in the void space between the catalyst pellets (Couwenberg et al., 1996a). The reaction mechanism of OCM on $Mn/Na_2WO_4/SiO_2$ appears to be similar to that of other OCM catalysts (Pak et al., 1998). The reaction network is complex involving many heterogeneous surface and homogeneous gas phase reactions. Many kinetic models have been developed with varying complexity, depending on whether surface and gas phase reactions have been accounted for separately (e.g. Stansch et al., 1997; Takanabe and Iglesia, 2008; Couwenberg et al., 1996a,b; Roos et al., 1989). In this study, where the quantitative description of the consumption and production rates of the main gas phase components is the primary objective, some relatively unimportant reactions were ignored and other reactions lumped together, so that the reaction rate expressions are simplified and the kinetic model is determined based on the most important primary and secondary reactions.

### 5.3.1 Primary reactions

During the initial stage of the reaction, the methyl radicals are coupled near the catalytic surface to form $C_2H_6$, CO and/or $CO_2$ (Choudhary and Uphade, 2004; Hoogendam, 1996; Stansch et al., 1997).

$$2\,CH_4 + \tfrac{1}{2}\,O_2 \longrightarrow C_2H_6 + H_2O \qquad \Delta H^0_{298} = -88.3 \text{ kJ/mol } CH_4 \qquad (1)$$

$$CH_4 + 2\,O_2 \longrightarrow CO_2 + 2\,H_2O \qquad \Delta H^0_{298} = -802 \text{ kJ/mol } CH_4 \qquad (2)$$

$$CH_4 + H_2O \rightleftharpoons CO + 3\,H_2 \qquad \Delta H^0_{298} = -200 \text{ kJ/mol } CH_4 \qquad (3)$$

$$CH_4 + O_2 \longrightarrow CO + H_2O + H_2 \qquad \Delta H^0_{298} = -277.8 \text{ kJ/mol } CH_4 \qquad (4)$$

At differential operating conditions, ethylene is only formed in very small quantities as a primary product, whereas at higher $CH_4$ conversion the bulk of $C_2H_4$ is formed via either oxidative or thermal dehydrogenation reactions (Pak et al., 1998). Carbon dioxide is considered as both a primary and secondary reaction product, and it was found that the origin of $CO_2$ of the primary reaction is the combustion of methane. A simplified scheme of the reaction network was presented (in slightly different forms)

(e.g. Stansch et al., 1997; Takanabe and Iglesia, 2008).

### 5.3.2 Secondary reactions

A good OCM catalyst should generate sufficient methyl radicals (activity) and take care that these radicals couple to form $C_2H_6$ before unselective or secondary reactions take place. Increase in the rate of secondary reactions, which occurs at increasing $O_2$ and $C_2$ concentration levels, will inevitably lead to loss of selectivity and additional heat production (Martin and Mirodatos, 1995).

$$C_2H_6 + \tfrac{1}{2}O_2 \longrightarrow C_2H_4 + H_2O \qquad \Delta H^0_{298} = -105.5 \text{ kJ/mol } C_2H_6 \qquad (5)$$
$$C_2H_6 \longrightarrow C_2H_4 + H_2 \qquad \Delta H^0_{298} = +136 \text{ kJ/mol } C_2H_6 \qquad (6)$$
$$C_2H_6 + \tfrac{7}{2}O_2 \longrightarrow 2\,CO_2 + 3\,H_2O \qquad \Delta H^0_{298} = -1428.7 \text{ kJ/mol } C_2H_6 \qquad (7)$$
$$C_2H_6 + \tfrac{5}{2}O_2 \longrightarrow 2\,CO + 3\,H_2O \qquad \Delta H^0_{298} = -757 \text{ kJ/mol } C_2H_6 \qquad (8)$$
$$C_2H_4 + 3\,O_2 \longrightarrow 2\,CO_2 + 2\,H_2O \qquad \Delta H^0_{298} = -1323.2 \text{ kJ/mol } C_2H_4 \qquad (10)$$
$$C_2H_4 + 2\,O_2 \longrightarrow 2\,CO + 2\,H_2O \qquad \Delta H^0_{298} = -757.2 \text{ kJ/mol } C_2H_4 \qquad (11)$$
$$CO + H_2O \rightleftharpoons CO_2 + H_2 \qquad \Delta H^0_{298} = -41 \text{ kJ/mol CO} \qquad (13)$$
$$CO + \tfrac{1}{2}O_2 \longrightarrow CO_2 \qquad \Delta H^0_{298} = -283 \text{ kJ/mol CO} \qquad (14)$$
$$H_2 + \tfrac{1}{2}O_2 \longrightarrow H_2O \qquad \Delta H^0_{298} = -241 \text{ kJ/mol } H_2 \qquad (15)$$

Ethylene is considered as a secondary product formed by oxidative dehydrogenation or thermal cracking of ethane, which was demonstrated by Pak et al. (1998) who compared the $C_2H_4$ formation rate under differential and integral conditions. The subsequent oxidation reactions will only be prominent if the concentration of $C_2H_4$ is sufficiently high, which is typically downstream in the reactor. The first reaction leading to $C_2H_4$ formation is the oxidative dehydrogenation of ethane (reaction 5), while the second reaction is the thermal dehydrogenation of ethane (reaction 6). It was found that co-feeding ethane with methane and oxygen to a reactor in the absence of a catalyst leads to a greatly increased overall conversion, because it led to an increased radical concentration and hence higher branching rates ($C_2H_6$ has a lower C-H bond energy than $CH_4$). Although this beneficial effect disappears when the ethane-to-methane inlet ratio exceeds 0.04 (Chen et al., 1994), it increases the opportunity of using natural gas as a carbon source (well-head quality natural gas typically contains some ethane). Cofeeding of ethane in the presence of a Sn/Li/MgO catalyst during the OCM reaction resulted in a higher ethylene concentration combined with a lower methane conversion, and measurement of the $^{13}C$ content in both ethylene and ethane confirmed that the main source of ethylene is ethane (Martin and Mirodatos, 1995).

Although both CO and $CO_2$ are considered as primary reaction products (Couwenberg, 1995; Nelson and Cant, 1990; Shi et al., 1994), a large part of carbon oxides is

also formed via combustion of $C_2H_4$ (Pak et al., 1998). However, it was also found during studies into the source of $CO_x$ that at lower temperatures deep oxidation mainly occurs via methane combustion. As the temperature increases, at which OCM is favored, the primary source of $CO_x$ products is predominantly the combustion of ethylene and ethane (Martin and Mirodatos, 1995).

### 5.3.3 Influence of operating conditions

The critical parameter which determines the performance of oxidative coupling of methane clearly is the oxygen concentration in the reactor. Because $O_2$ is involved as a surface species, oxygen needs to be present in sufficient amounts to provide a continuous supply of $O_2$ to the OCM reaction on the catalyst surface (Pak et al., 1998). The range in which the oxygen inlet concentration can be varied is at least limited by 2 constraints. First, because of the highly exothermic reactions a relatively high methane-to-oxygen ratio is required to overcome heat removal problems and to keep the (local) methane conversion sufficiently low. When pre-mixed feed is applied, the lower a $CH_4/O_2$ ratio is determined by the upper flammability limit of methane-oxygen mixtures, which amounts approximately 60-65 mol% $CH_4$ at atmospheric conditions (Couwenberg, 1995). Distributed feed of $O_2$ can be applied to have sufficiently low local $O_2$ concentrations to overcome too high reactor temperatures and to remain below the flammability limits.

Because $O_2$ is a surface species, and many OCM catalysts are redox type catalysts, the performance of the OCM process with pre-mixed feed of oxygen and methane was compared with operation in the cyclic mode, in which oxygen and methane are sequentially fed to the reactor (avoiding direct contact between gaseous oxygen and methane). During this reaction, lattice oxygen is the main reactant in the coupling reaction instead of gaseous/molecular $O_2$. It was shown that with longer reduction time ($CH_4$ cycle) the overall time-averaged methane conversion drops significantly while the $C_2$ selectivity increases at temperatures varying from 800-850 °C. Because of the limited run time lengths of only 0 to 5 min, the overall yield per time is low. In large (industrial) reactors the presence of gaseous $O_2$ is preferred for maximizing conversion and selectivity (Jones et al., 1987).

The oxygen concentration has a large influence on the $C_2$ selectivity that can be obtained. The decreased $C_2$ selectivity at high $O_2$ concentrations was for observed on any OCM catalyst, see e.g. (Hoogendam, 1996; Korf et al., 1989; Pak et al., 1998). Because of the lower $O_2$ reaction order for the OCM reaction ($C_2H_6$ production), a high $C_2$ selectivity will be achieved at lower $O_2$ levels at the expense of a lower methane conversion at increasing methane-to-oxygen ratio. This does not necessarily

mean that the highest $C_2$ yield is also obtained at a low $O_2$ concentration, because a higher methane conversion is usually more important than a lower selectivity. Using a too low $O_2$ concentration might however lead to extinction of the reaction, as observed by Sofranko et al. (1987) who identified that molecular oxygen should always be present in order to achieve sufficient $CH_4$ conversion (15-20%) at high $C_2$ selectivity (80-90%). Hence, there will be an optimum $O_2$ concentration for maximum $C_2$ yield.

#### Reactor pressure

The effect of the total pressure on the reaction rates of OCM was investigated over a wide range varying from 100-800 kPa. For a catalyst with a relatively low catalytic activity, such as the $Mn/Na_2WO_4/SiO_2$ catalyst, and especially at higher pressures (>600 kPa) the influence of gas phase reactions becomes important. At high pressure and high residence time, it was found that the only significant effect of the catalyst is the conversion of CO into $CO_2$ and the selectivity towards $C_2$ products decreases (Couwenberg, 1995; Ekstrom et al., 1990). In addition, gas-phase reactions in the pre- and post catalytic space can become dominant at pressures above 1000 kPa, which can lead to uncontrollable selectivity. The contribution of the pre- and postcatalytic volume to the OCM process can be minimized by reduction of the available volume and the temperature in this zone (by introducing e.g. steep temperature gradients).

The effect of elevated reactor pressures on the catalytic reaction rates was investigated with a $SiO_2$ based catalyst at a constant space velocity and a $CH_4/O_2$ ratio of 10. The influence on $CH_4$ conversion and $C_2$ selectivity was very small, which indicated that the productivity of $C_2$ hydrocarbons per unit mass of catalyst is higher, because of the higher mass velocity at elevated pressure (Wang et al., 1995). Similar data was also reported by other researchers, however, they also discussed the thermal effects which accompany the coupling and combustion reactions. Although only 20-40 mg catalyst was used at differential operating conditions, a temperature increase of almost 82°C over a length of approximately 6 mm was measured during experiments for both MgO and $SiO_2$ based catalysts in the unsteady state; the large temperature gradient can be partially attributed to the high initial activity of the catalyst (Pak et al., 1998; Wang et al., 1995).

#### Reactor temperature

The influence of the operating temperature on oxidative coupling is significant, although bound to maximum temperatures because of catalyst stability and selectivity problems. Because the activation energy of the selective coupling reaction is typically higher than for the primary reactions, the selective reaction is much more sensitive

to temperature variations. Therefore, a high temperature is desired for maximum reaction rate. Although at reactor temperatures in the range from 675-750 °C the selectivity towards $C_2$ products keeps increasing with rising temperature, already at 750°C the contribution of homogeneous gas-phase reactions can be relatively high. The gas phase reaction play an important role in oxidative coupling (increase in the yield of $C_2$ products). At temperatures above 825 °C and a pressure of 130 kPa it was found that a $C_2$ yield of 20% could reached over a Sn/Li/MgO catalyst and on a Li/MgO catalyst it was concluded that the higher yield is partially achieved due to thermal cracking of ethane to ethylene (Couwenberg, 1995; Korf et al., 1989). If the reactor temperature, however, becomes too high, the contribution of non-selective gas-phase reactions becomes important. Moreover, most OCM catalysts deactivate at a faster rate at higher temperatures, which makes it difficult to maintain steady state operation for the endurance of an experiment. Typically the lifetime of a Li/MgO catalyst is limited to 100 hours, but this can be enhanced by limiting the reactor temperature (Hoogendam, 1996; Korf et al., 1989) and doping of the Li/MgO catalyst with e.g. tin. Other catalysts, such as the $Mn/Na_2WO_4$ catalyst, can perform at much higher temperatures (850-900 °C), which allow the use of a higher temperature and simultaneously producing sufficient $C_2$ products.

## 5.4 Experimental

The reaction rates of the primary reactions prevailing during OCM over a $Mn/Na_2WO_4/SiO_2$ catalyst were measured under differential conditions. The experimental set-up, contains a feed section, a micro-catalytic fixed bed reactor and an analysis section. In the feed section, the desired feed gas flow rate and composition are controlled by mass flow controllers (Brooks 5850S) for methane, air and nitrogen, as well as ethane or ethylene.

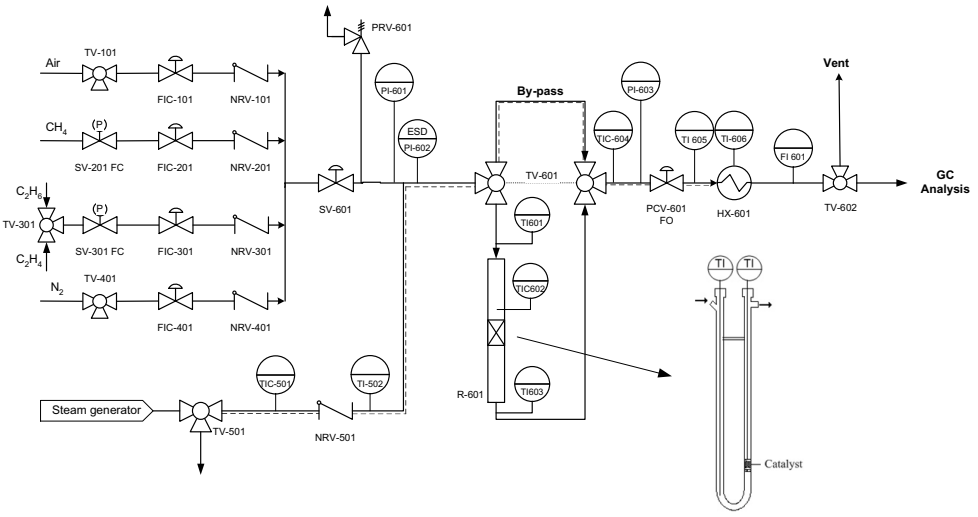


**Figure 5.1:** Process flow diagram of the experimental setup with the micro-catalytic fixed bed reactor.

The feed mixture can be sent over a bypass to measure the exact feed composition or fed to the reactor. The reactor is a micro-catalytic fixed bed reactor (ID = 5 mm) made of quartz in which the inlet and outlet temperatures are measured. It is positioned inside a fluidized sand bed oven, resulting in very high external heat exchange and virtual isothermal operation. The feed and product streams are analyzed by online gas chromatography (GC), with a Varian Micro-GC 4900 containing three columns, two 5Å molsieve columns to separate oxygen, nitrogen, methane, carbon monoxide and hydrogen and a PoraPLOT Q column to separate $H_2O$, $CO_2$, $C_2$ and $C_3$ components. The columns are equipped with thermal conductivity detectors. Most water is condensed after the reactor, in order to protect the molsieve columns. Nitrogen balance is used to calculate outlet mole fractions and the amount of condensed water is computed from the hydrogen atom balance. Resulting errors in

oxygen and carbon atom mass balances are within 1% and in most cases even within 0.5%. In this work, the $Mn/Na_2WO_4$ on $SiO_2$ catalyst is prepared by the two-step incipient wetness impregnation using solutions of pure $Mn(NO_3)_2$ and $Na_2WO_4$ obtained from Sigma Aldrich. The carrier is commercially available silica, Sigma Aldrich grade 10181. The impregnated silica is then calcined at 850 or 900 °C in air, resulting in a catalyst containing approximately 2 wt% Mn and 5 wt% $Na_2WO_4$, which was caracterized by means of XRF analysis (see Table 5.2).

**Table 5.2:** Measured composition of the $Mn/Na_2WO_4/SiO_2$ catalyst by X-Ray Fluorescence analysis (XRF).

| Analysis | $m_{sample}$ (mg) | Na (wt%) | Mn (wt%) | W (wt%) |
|---|---|---|---|---|
| 1 | 614.9 | 0.95 | 2.47 | 2.78 |
| 2 | 532.7 | 0.95 | 2.49 | 2.80 |
| Average | | 0.95 | 2.48 | 2.79 |

### 5.4.1 Stability and reproducibility (TGA)

Before the kinetic experiments were performed, it was verified that the catalyst preparation method is reproducible and that the activity and the selectivity are comparable with results published in literature. With a calcination temperature of 900 °C a $C_2$ yield of 20% could be obtained at a $CH_4$ conversion of 30%, the small obtained differences with the reported literature data can be attributed to the use of air in this work instead of pure oxygen often used in the literature. The observed reactions rates are very similar to published values (e.g. Wang et al., 1995). During the explorative experiments, however, under differential conditions, at various flow rates and reaction temperatures, it was found that the reaction rates are slowly decreasing with time on stream, which could indicate catalyst deactivation by either migration of active components, sintering of the structure or blocking of the active sites (e.g. by carboneaceous species or reaction products).

The possibility of migration of active components, which increases at higher operating temperatures, was excluded by an experiment where the flow of methane and oxygen to the reactor was switched off (after a short purge with $N_2$), and switched back after a couple of minutes. If the loss of active components would be the main reason for the decreasing reaction rates, it is expected that reaction rates will be at the same level again after switching back to the reactor mode. However, after switching back to the feed flow the activity was only partially restored, from which

it is concluded that migration is not the main mechanism for the decrease in catalytic activity at this short time scale. Adsorption of species (such as $C_2H_4$ and $C_2H_6$) at the catalyst surface could also be a possibility, although under the applied conditions the formation of carbonaceous species on the catalyst surface is thermodynamically possible and therefore much more likely. When the reactor flow is stopped, the carbonaceous deposits can possibly disappear during the period of no feed flow by reaction with the remaining oxygen. This was verified with Thermal Gravity Analysis (TGA) by switching flow between a methane rich flow (50% $CH_4$/50% $N_2$) and an air flow. During the period of reduction, however, the sample mass decreased to a constant value whereas coke formation would have led to an increase of the sample mass. After oxidation in air, the original sample mass was retained thus there is another mechanism responsible for the changes in the activity.

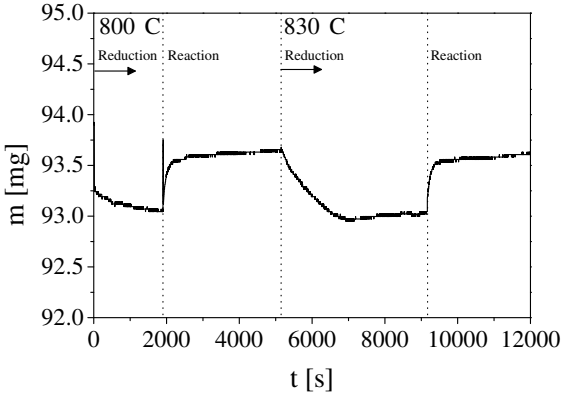


**Figure 5.2:** Mass of a $Mn/Na_2WO_4/SiO_2$ sample obtained with Thermal Gravity Analysis (TGA) at different temperatures with a reduction cycle with $H_2$ and oxidation cycle with an OCM reaction mixture of 4% $O_2$, 25% $CH_4$, balance $N_2$.

It was found that after oxidation with air (and a short flush of the reactor with $N_2$), the $C_2$ selectivity was significantly improved from 60% to 70% if a reaction mixture was fed to the sample container. Apparently, the oxidation state of the catalyst is important for the performance of oxidative coupling. Oxidation of the $Mn/Na_2WO_4$ catalyst is possible, Mn for example can exist as Mn, MnO, $Mn_3O_4$ or $MnO_2$. A possible occurring transition might be the oxidation of MnO to $Mn_3O_4$. XRF measurements have shown that the catalyst contains 2.48 wt% Mn, if this is present as MnO the oxidation of MnO to $Mn_3O_4$ will theoretically result in a mass increase of 0.45 mg. TGA experiments were performed at 800 and 830 °C by first fully reducing a catalyst sample under $H_2$, followed by switching to a feed mixture which equals

the feed composition used in the kinetic set-up. In Fig. 5.2 it is shown that feeding a reaction mixture to a fully reduced catalyst sample causes the reduced catalyst to increase in weight with 0.54 mg from approximately 93 to 93.5 mg, which is in the same order of magnitude as the theoretical calculation. Furthermore, from the relatively stable operation during OCM it can be concluded that the catalyst remains sufficiently oxidized under reaction conditions to maintain a good OCM performance, which is surprising, because the $CH_4$ concentration is a factor 6 higher than oxygen. This result is however supported by different TGA experiments, with a mixture containing oxygen fractions of 0.5% and 1%, which are still able to oxidize the catalyst. It can be concluded that the long time required for steady state is caused by slowly oxidizing the catalyst and this can be resolved by flushing the reactor with air before starting the kinetic experiments.

### 5.4.2 Absence of mass and heat transfer limitations

For kinetic measurements, it should be ensured that mass and heat transfer limitations are absent so that differential conditions can be attained and that the intrinsic reaction kinetics can be measured. Temperature and concentration gradients can occur inside the catalyst particle, between the particle surface and surrounding gas film as well as between the particles and the bulk gas phase. Several analytical criteria have been reported to check for these limitations, which have been listed in Table 5.3.

**Table 5.3:** Diagnostic criteria for checking absence of mass and heat transfer limitations (Mears, 1971a,b).

| | | | | |
|---|---|---|---|---|
| Intraparticle | Mass | $\frac{n+1}{2}\frac{R_i \cdot (d_p/6)^2}{D_{eff} \cdot c_i^0}$ | $<$ | $0.25$ |
| | Heat | $\frac{\lvert\Delta H\rvert \cdot R_i \cdot d_p^2}{\lambda_s \cdot T_s}$ | $<$ | $3 \cdot \frac{T_s \cdot R_g}{E_a}$ |
| Interphase | Mass | $\frac{c_{bulk} - c_{surface}}{c_{bulk}}$ | $<$ | $0.05$ |
| | Heat | $\frac{\lvert\Delta H\rvert \cdot R_i \cdot d_p^2}{\alpha \cdot T}$ | $<$ | $0.3 \cdot \frac{T_s \cdot R_g}{E_a}$ |
| Isothermal | Radial | $\frac{\lvert\Delta H\rvert \cdot R_i \cdot d_p^2}{\lambda_{e,r} \cdot T}$ | $<$ | $1.6 \cdot \frac{T \cdot R_g}{E_a \cdot (1 + 8 \cdot (d_p/d_r \cdot Bi_w))}$ |

It was found that none of these criteria becomes limiting under the conditions investigated, however, care must be taken because the criteria for mass transport limitations usually concern limitations for reactants and products because the catalytic reaction intermediates only exist on the catalytic surface. During high temperature

reactions such as oxidative coupling, however, the catalyst produces methyl radicals which react further in the gas phase to ethane or are oxidized to carbon oxides. It has been reported that transport of these radicals could also become rate determining (Couwenberg et al., 1996a). Therefore limitations will also be verified experimentally in this chapter.

### Intra-particle limitations

To check for intra-particle limitations, measurements with different particle sizes have been performed. If no limitations occur, the observed reaction rate should be independent of the particle diameter. Catalyst particles of 300-600 $\mu$m have been partly crushed and sieved to a fraction of 100-300 $\mu$m. Reaction rates were measured for both catalyst fractions.

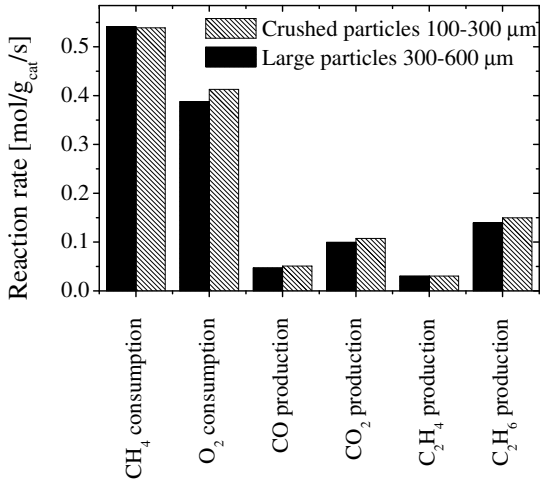


**Figure 5.3:** Reaction rates for different catalyst particle sizes ($p_{O_2}$=8.1 kPa, $p_{CH_4}$=49.6 kPa, T=800°C, p=200 kPa, $\phi_{v,tot}$=200Nml/min, $m_{cat}$=0.25 g)

Fig. 5.3 shows only slightly reduced reaction rates for the larger particles, so that it can be concluded that intra-particle mass transfer limitations do not play a significant role. Analytical evaluation of the criterion for intra-particle heat transfer already showed that isothermicity inside the catalyst particle is satisfied, therefore it can be concluded that intra-particle limitations are not significant.

### External limitations

External mass transport occurs in a stagnant layer around the particles through which reactants and products will diffuse. At higher flow rates the thickness of this stagnant film will be reduced and measured reaction rates will be higher if external mass transport limitations will play a role. If no limitations occur, measured rates must be equal for both flow rates at the same gas residence time. External mass transport limitations can be verified experimentally by measuring reaction rates at different flow rates and catalyst amounts, keeping the GHSV (contact time) unchanged. In Fig. 5.4 the results of four cases are shown.

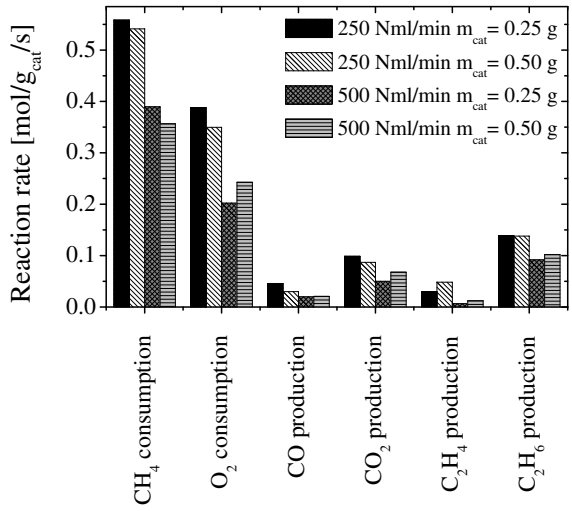


**Figure 5.4:** Reaction rates at different flow rates ($p_{O_2}$=8 kPa, $p_{CH_4}$=50 kPa, T=800°C, p=200 kPa, $\phi_{v,tot}$=250-500Nml/min, $m_{cat}$=0.25-0.50 g)

The figure shows slightly lower reaction rates at 500 ml/min (for both amounts of catalyst). This result is remarkable, considering the fact that a higher rate was expected if a transport limitation prevails, because the stagnant film layer thickness should decrease. Therefore it can be concluded that external mass transport limitations do not play a significant role. The lower reaction rates at higher flow rates can possibly be explained by a reduction of gas phase reactions, as the residence time in pre and post catalytic zones is reduced.

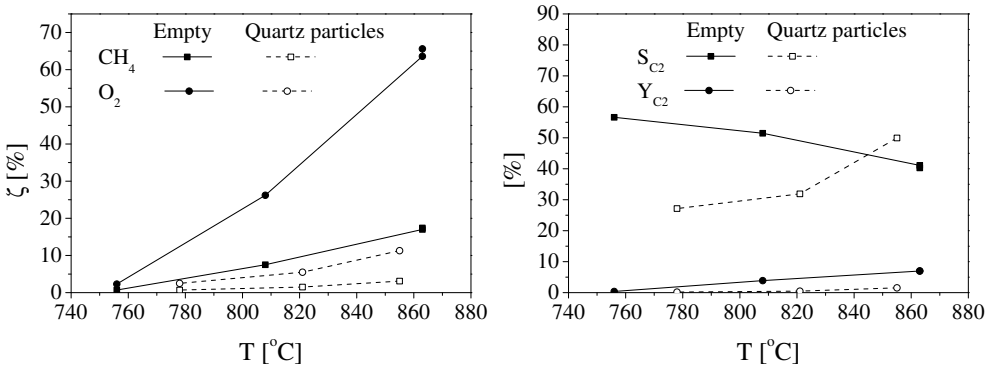


(a) (b)

**Figure 5.5:** Extent of gas phase reactions at different temperatures in an empty tube and in a reactor filled with quartz particles ($d_p = 1 - 2$ mm) on (a) conversion and (b) selectivity and yield ($CH_4/O_2/N_2$=4:1:4, $\phi$=250 Nml/min, p=200 kPa).

### 5.4.3 Extent of homogeneous reactions

It is expected that without a catalyst present, gas phase reactions will occur due to the prevailing high temperatures in the OCM process. This was confirmed with experiments at different temperatures, where the contribution of gas phase reactions was measured in an empty tube reactor. Two reactor materials have been used; stainless steel and quartz. With the stainless steel tube unacceptably high $CH_4$ and $O_2$ conversions of 54% and 100% respectively at 810 °C were found and significant amounts of carbonaceous products were formed. With quartz as a reactor material, it is shown that conversion of $CH_4$ and $O_2$ takes place significantly, especially at higher temperatures (see Fig. 5.5). For accurate determination of the reaction kinetics it is however necessary to minimize the influence of gas phase reactions as much as possible, which was realized by reduction of the void space by filling the pre- and post-catalytic volume with inert quartz particles (1-2 mm). It can be seen that the reaction rates have decreased with a factor 5, so that the $O_2$ conversion is less than 3%, which is an acceptable level for measuring the reaction rates at 800 °C.

### 5.4.4 Experimental procedure

For the kinetic measurements, the post- and pre-catalytic reactor volume was filled with quartz chips of 1-2 mm and a catalyst mass up to 0.5 g was used. The reactor inlet and outlet temperature was measured with two K-type thermocouples.

Prior to the experiments, the setup was tested for leaks with $N_2$ at an operating

pressure of 2 bar, first at room temperature and then at process temperature. First, the homogeneous gas phase reactions were measured at 800°C and 2 bar, with different mixtures of $CH_4$, air and $N_2$ at a total flow rate of 250 ml/min. Subsequently, the reactor was filled with the $Mn/Na_2WO_4/SiO_2$ catalyst (max. 0.5 g, $d_p$ = 0.5 mm) and heated until process temperature with a ramp rate of 5-10 °C/min under a flow of air to ensure the catalyst is in the oxidized state. Before starting the kinetic measurements, the reactor was purged with $N_2$ for at least 10 min to ensure all air has been removed. The feed composition for each test was measured with the flow by-passing the reactor (see Fig. 5.1). After the flow was switched to the reactor, the outlet composition was measured on the GC and process parameters were logged.

It was shown that the gas-phase reactions cannot be completely prevented from occurring in pre- and post-catalytic zone during experiments with catalyst. To get insight into solely the heterogeneous reactions, the rates measured during experiments without catalyst present are subtracted from the rates from experiments with catalyst, assuming there is no interaction between heterogeneous and gas-phase reactions. Because the rates are not exactly obtained at the same partial pressures, the experimental results are fitted, with linear, power law or polynomial trends and subsequently the catalytic contribution is calculated.

## 5.5 Results

The kinetic measurements have been carried out at a constant temperature of 800 °C and a pressure of 2 bar. Different $CH_4$ and $O_2$ inlet concentrations were applied, to investigate the influence of the concentrations on the intrinsic reaction rate and to determine the reaction orders. Differential operating conditions were used, so that the overall $O_2$ conversion was always below 25% and the $CH_4$ conversion below 6.5%.

**Table 5.4:** Operating conditions used in the kinetic experiments.

| Description | Value | Unit |
|---|---|---|
| Particle size | 0.3-0.5 | mm |
| Temperature | 800-900 | °C |
| Total pressure | 200 | kPa |
| Catalyst mass | 0.25-0.50 | g |
| $O_2$ partial pressure | 0.7-28.2 | kPa |
| $CH_4$ partial pressure | 9.7-89.6 | kPa |
| Total flow rate | 250 | Nml/min |

### 5.5.1 Primary reaction rates

The primary reaction rates were measured under differential conditions, first to determine the contribution of homogeneous gas phase reactions (also in the pre- and post catalytic sections) using the reactor filled with only quartz particles and subsequently for the reactor filled with the $Mn/Na_2WO_4/SiO_2$ catalyst. In Fig. 5.6 and 5.7, the influence of the $O_2$ partial pressure on the gas phase and the total reaction rates is plotted. The calculated heterogeneous contribution (substracting the gas phase reaction rate from the total measured reaction rate) is also displayed.

Comparing the extent of gas phase reactions to the total reaction rate, it can be concluded that at low $O_2$ partial pressures, the most interesting concentration range for OCM, there is hardly any influence of gas phase reactions on the total reaction rate and the $C_2$ selectivity is high (Fig. 5.6 and 5.7). Above an oxygen partial pressure of 10 kPa, however, it can be seen that particularly carbon monoxide and hydrogen are almost entirely generated in the gas phase, while $CO_2$ is only produced in small amounts over the entire range of $O_2$ partial pressures investigated. It can be concluded that the contribution of the catalyst to $H_2$ and CO production is nihil. Ethane is only

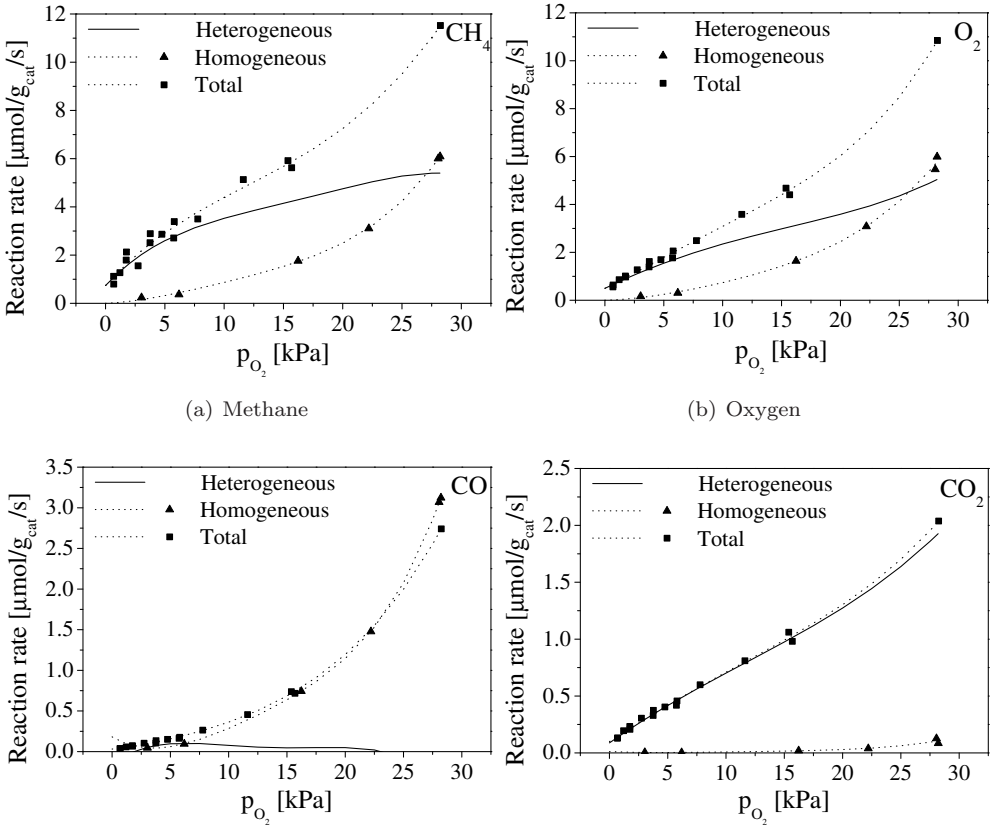


(a) Methane

(b) Oxygen

(c) Carbon monoxide

(d) Carbon dioxide

**Figure 5.6:** Influence of the $p_{O_2}$ on the $CH_4$ and $O_2$ consumption rates and the CO and $CO_2$ production rates ($p_{CH_4}$=50 kPa, T=800°C and p=200 kPa, $m_{cat}$=0.25 g, $\phi_v$=250 Nml/min).

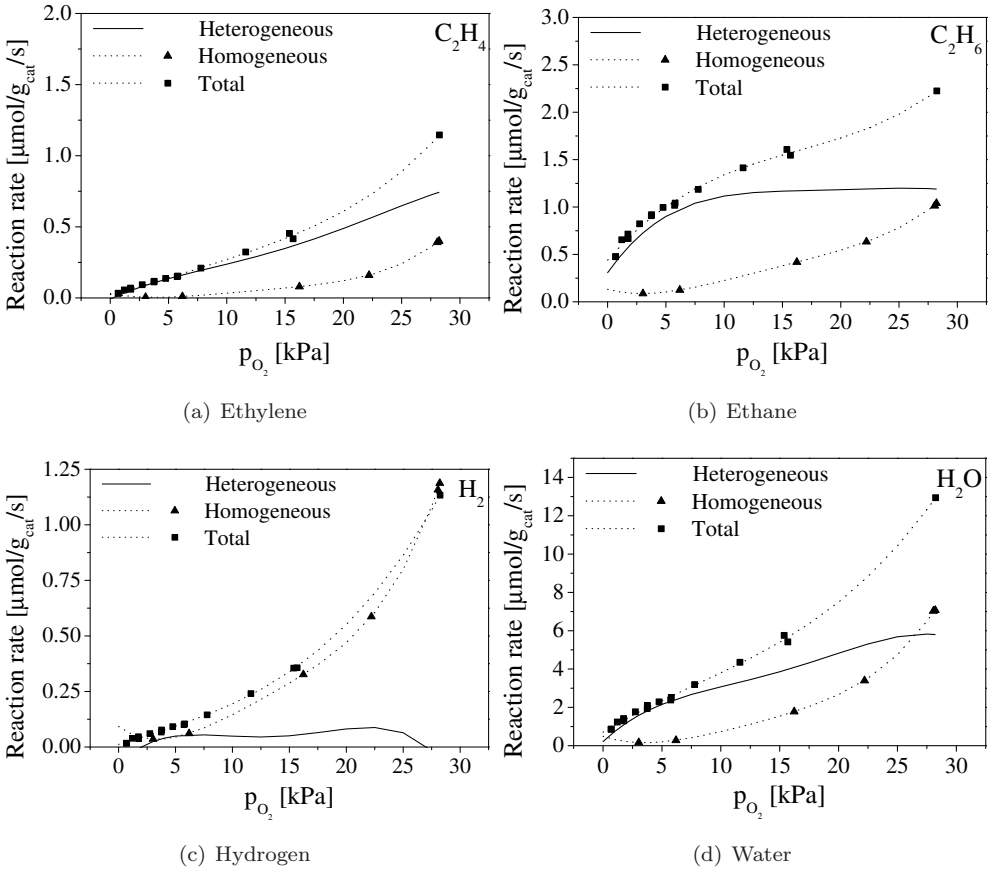


(a) Ethylene (b) Ethane

(c) Hydrogen (d) Water

**Figure 5.7:** Influence of the $p_{O_2}$ on the $C_2H_4$, $C_2H_6$, $H_2$ and $H_2O$ production rates ($p_{CH_4}$=50 kPa, T=800°C and p=200 kPa, $m_{cat}$=0.25 g, $\phi_v$=250 Nml/min).

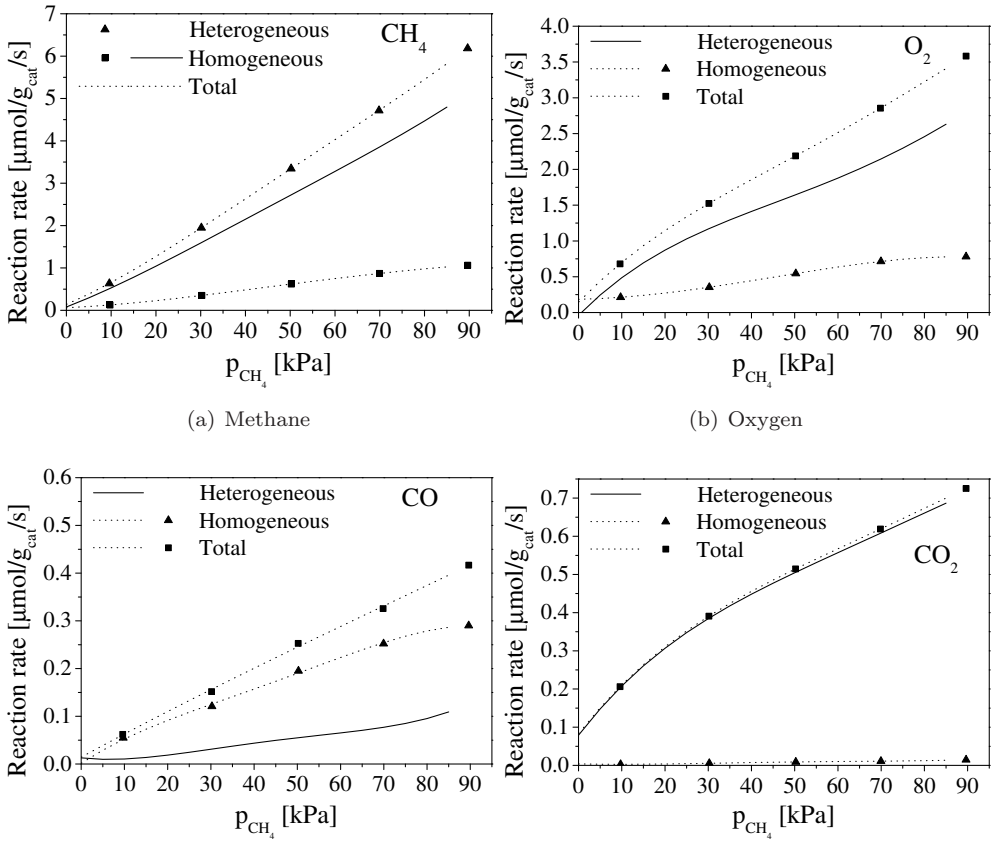


(a) Methane

(b) Oxygen

(c) Carbon monoxide

(d) Carbon dioxide

**Figure 5.8:** Influence of the $p_{CH_4}$ the $CH_4$ and $O_2$ consumption rates and the CO and $CO_2$ production rates ($p_{O_2}$=8 kPa, T=800°C and p=200 kPa, $m_{cat}$=0.25 g, $\phi_v$=250 Nml/min).

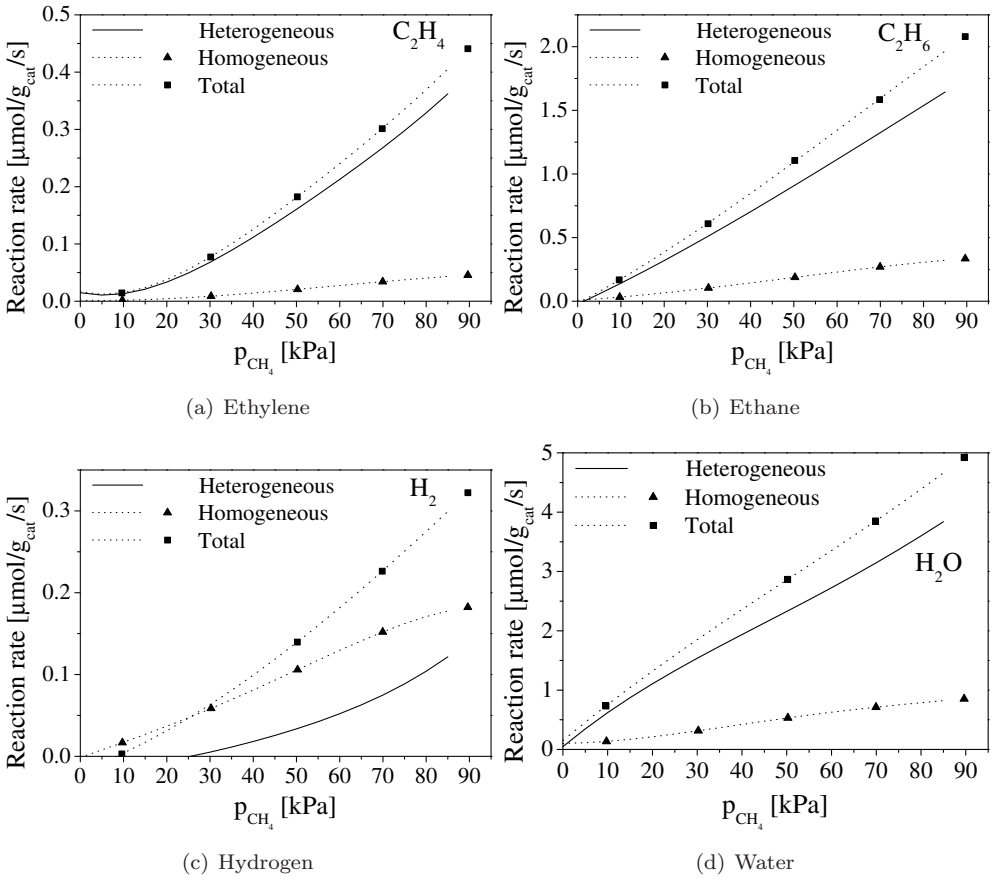


(a) Ethylene

(b) Ethane

(c) Hydrogen

(d) Water

**Figure 5.9:** Influence of the $p_{CH_4}$ on the $C_2H_4$, $C_2H_6$, $H_2$ and $H_2O$ production rates ($p_{O_2}$=8 kPa, T=800°C and p=200 kPa, $m_{cat}$=0.25 g, $\phi_v$=250 Nml/min).

formed in the gas phase at $p_{O_2}$ higher than 7-10 kPa due to coupling reactions, while $C_2H_4$ can be considered as a secondary product which will only be generated in sufficient amounts at higher $CH_4$ conversions. The catalyst clearly leads to selective $C_2H_6$ formation, already at low $O_2$ pressures, but the net generation rate is decreasing at higher $O_2$ pressures because a part of $C_2H_6$ is likely to be dehydrogenated to $C_2H_4$. It can be seen that the overall reaction order for each component is slightly different in the gas phase, particularly for the CO formation rate the $O_2$ reaction order is rather high, while the other components show reaction orders in $O_2$ slightly higher than 1, which results in a decreasing $C_2$ selectivity at higher $O_2$ concentrations. A second set of experiments was performed, but in this series a constant $O_2$ partial pressure of 8 kPa was used while the $CH_4$ inlet partial pressure was varied. From Fig. 5.8 and 5.9 it can be inferred that nearly all components show first order dependency on the $CH_4$ concentration. Products of the gas phase reactions are mainly CO and $C_2H_6$, as also observed before in the experiments when varying the $O_2$ concentration. At higher $CH_4$ partial pressures, it seems that the catalytic partial oxidation to CO and $H_2$ is gaining some importance, as can be inferred from the increasing catalytic contribution to CO production. The contribution is however still small, as the catalytic production rate of $C_2H_6$ is much higher. The large difference between $C_2H_6$ and $C_2H_4$ generation rates (note the different scales in Fig. 5.9a and b) again confirms that $C_2H_4$ can be considered as mostly a secondary product.

## 5.6 Kinetic model

The derivation of the kinetic model is also split into two parts. During the measurements at differential conditions, the secondary reaction rates can be neglected and the reaction rate constants of the primary reactions can directly be determined. The kinetic model for the primary reactions then serves as a basis for the calculation of the secondary reaction rate constants from the literature.

### 5.6.1 Assumptions

The measurements at various $CH_4$ and $O_2$ inlet concentrations at differential operating conditions have led to experimental data which can be used to derive a simplified kinetic model. The following preliminary conclusions can be made:

- The oxidation reaction to CO proceeds mainly in the gas phase.
- The origin of $CO_2$ is mainly $CH_4$ at the used differential conditions.
- The oxidative coupling reaction produces the primary reaction product $C_2H_6$.
- Ethylene is mainly generated via $C_2H_6$ oxidative dehydrogenation.
- The secondary oxidation reactions can be neglected at the used conditions.

These observations will be shortly discussed in the following sections.

#### (Oxidative) dehydrogenation of ethane

Two pathways exist for $C_2H_4$ formation, the oxidative (reaction 5) and the thermal (reaction 6) dehydrogenation reaction. Experiments with a feed of 50 kPa $C_2H_6$ without and with 1 kPa $O_2$ have been carried out in a reactor with 0.25 g of catalyst at 800°C at 200 kPa to examine the relative rates of these reactions. The experiment with $O_2$ showed 50% $C_2H_6$ conversion and almost 100% conversion of $O_2$. Most $C_2H_6$ is converted to $C_2H_4$ (selectivity 98.6%) and all $O_2$ reacted to $CO_2$. Also traces of $CH_4$ were found in the product stream, but this reaction is neglected due to the low significance. The experiment without $O_2$ showed similar $C_2H_6$ conversion and $C_2H_4$ formation and the temperature inside the reactor dropped slightly when the mixture was fed to the reactor, indicating that the endothermic thermal dehydrogenation reaction took place and not the exothermic oxidative dehydrogenation. At higher $O_2$ concentrations, however, it is expected that the oxidative dehydrogenation has a more important contribution, therefore the reaction will be incorporated in the kinetic model.

### Hydrogen oxidation

Partial oxidation of $CH_4$ and $C_2$ and the dehydrogenation of $C_2H_6$ lead to $H_2$ formation. It is likely that $H_2$ will react fast with $O_2$ to form water (reaction 15). Several studies on the reaction mechanism of $H_2$ oxidation have been reported in the literature (O'Conaire et al., 2004; Mueller et al., 1999) and it is believed that it consists of 19 elementary steps. The behavior is complex, as the reaction rates are dependent of three explosion limits. The exact location of the explosion limits depends on various factors such as the size of the reaction vessel, the surface-to-volume ratio, and the initial reactant concentrations (including inert components, such as $N_2$ etc.) (Veser, 2001). Impurities and the reactor surface (even quartz) will influence reaction rates, so that it is difficult to determine the reaction rates of $H_2$ oxidation at OCM conditions. Furthermore there is no information in the literature whether $Mn/Na_2WO_4/SiO_2$ will catalyze this reaction. The experimental results show that $H_2$ formation in the presence of this catalyst is similar to that in the gas-phase. At first sight it might be concluded that the catalyst has no influence on hydrogen oxidation. However, in the presence of the catalyst much higher $C_2H_4$ reaction rates are measured, which are formed by dehydrogenation of ethane. The accompanied $H_2$ production is not measured at the reactor outlet. Additional difficulty is that most dehydrogenation will take place in the post-catalytic zone. The most probable explanation for the observed results is that the hydrogen produced during gas-phase partial oxidation of $CH_4$ in the pre-catalytic zone is (partly) catalytically oxidized to water, followed by $H_2$ production in the post-catalytic zone by dehydrogenation. This might be the reason why the net hydrogen production is similar for experiments with and without catalyst. To enhance the understanding of the later proposed mechanism, it is assumed that all $H_2$ formed during catalyzed reactions and the dehydrogenation of ethane is converted to water.

### Ethane and ethylene oxidation

To get insight into the primary and secondary reactions of OCM, it is important to know the origin of the unselective products CO and $CO_2$. Next to CO being a primary and secondary oxidation product, it has been reported that good coupling catalysts generally are also effective for the conversion of CO to $CO_2$ (Shi et al., 1994). Thus, although the catalytic contribution to CO formation seems negligible, it might be produced much faster in the experiments with a catalyst, but is converted at a similar rate in a consecutive reaction to $CO_2$ (reaction 13 and 14). However, here it is assumed that the $CH_4$ conversion to CO is not catalyzed. Experimental verification of the origin of the carbon oxides, was carried out with $C_2H_6$ in the feed at an $O_2$

partial pressure of 15 kPa. The inlet concentration of 0.5 kPa $C_2H_6$ was based on the average concentration measured in the reactor outlet during differential measurements of OCM. Surprisingly, in experiments without and with 0.25 g catalyst, in both cases it was found that $C_2H_6$ is totally converted and CO and $CO_2$ are formed at 1.86 x $10^{-6}$ and 2.05 x $10^{-6}$ mol/g/s respectively, which is higher than the measured rates at the experiments with only $CH_4$ and $O_2$ in the feed (Fig. 5.6 and 5.7). The results can be explained by considering the fact that if $CH_4$ is not present in the feed streams, which has been reported to have an inhibiting effect on $C_2H_6$ and $C_2H_4$ oxidation in the gas phase (Pak et al., 1998; Roos et al., 1989).

It was also attempted to determine the $C_2$ secondary oxidation reaction rates in the micro-catalytic reactor by co-feeding $C_2H_4$ or $C_2H_6$ at different $O_2$ and $CH_4$ inlet concentrations, however, this resulted in an unacceptable error in the carbon mole balance and differential conditions could not be obtained ($C_2H_6$ conversion of more than 40%). In addition, a significant deviation from isothermal operation was observed because of the strongly exothermic reactions. Furthermore, it can not be excluded that part (or all) of the $C_2$ products are already converted prior to reaching the catalyst bed in the pre-catalytic zone, which inevitably results in large inaccuracies in the determination of the kinetic parameters of secondary reactions.

Because the secondary oxidation reactions of $C_2H_4$ and $C_2H_6$ could not be measured and the source of $CO_x$ could not be elucidated, the influence of $C_2H_4$ and $C_2H_6$ oxidation was estimated by comparing the obtained experimental results with the reaction rate constants determined by Takanabe and Iglesia (2008). They recently measured the first order rate constants on a $Mn/Na_2WO_4/SiO_2$ catalyst in a recirculating batch reactor at differential operating conditions. Isotopic labeling of $CH_4$, $C_2H_4$ and $C_2H_6$ allowed for accurate determination of the rate constants, unraveling the complex catalyzed reactions in the OCM process, which was also performed by other researchers (Pak et al., 1998; Shi et al., 1994; Takanabe and Iglesia, 2008). It was found that the contribution of secondary oxidation of $C_2$ components to carbon oxides depends on many parameters, and it appears that the rate constant for $CO_2$ formation from $C_2H_4$ is 68 times larger than that for $CH_4$ oxidation, while $C_2H_6$ combustion plays no significant role (Pak et al., 1998). Takanabe and Iglesia (2008) found a ratio between the reaction rate constant of $C_2H_4$ and $CH_4$ oxidation of 4.3, which confirms the measurements of Pak et al. (1998). In contrary to other researchers, they also found that the ratio between $C_2H_6$ and $CH_4$ oxidation is 2.7, which suggests that $C_2H_6$ oxidation cannot be neglected in the kinetic model if it is kept in mind that typically the $C_2H_6$ concentration is much larger than that of $C_2H_4$, particularly at higher $CH_4$ concentrations (see also Fig. 5.9a-b). At the differential conditions used

in the experiments, however, the total contribution of $C_2H_4$ and $C_2H_6$ to $CO_2$ formation is in general lower than from $CH_4$ oxidation, because $CH_4$ conversion is typically lower than about 30-50% because of the desired high $CH_4/O_2$ ratios. Therefore, it can be assumed that the contribution of $C_2H_4$ and $C_2H_6$ oxidation to the $CO_2$ formation rate can be mostly neglected for the derivation of the primary reaction rate constants. Furthermore, it is assumed that CO formed on the catalyst surface is immediately converted to $CO_2$, which probably is a catalyzed reaction as described above. To simplify the mechanism further, it is assumed that CO formed in the gas phase will not react on the catalyst to $CO_2$.

### 5.6.2 Proposed simplified mechanism

Based on the analysis of the obtained experimental results and relevant publications in the literature, the next simplified reaction mechanism for the heterogeneous reaction rates (corrected for gas-phase reactions) is proposed:

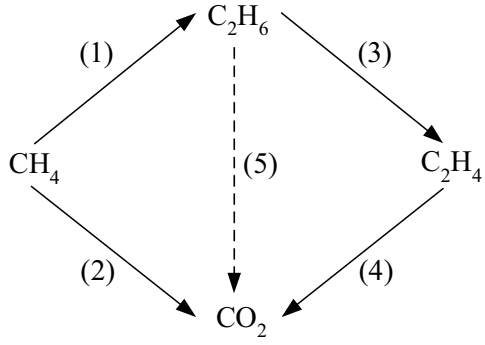


**Figure 5.10:** Schematic simplified reaction scheme for the oxidative coupling of methane on $Mn/Na_2WO_4/SiO_2$.

Because no inhibition effects have been identified, the rates will be represented by simple power-law or linear relations. Only the total conversion rates were derived from the experimental results, and the reaction rates of the individual reactions (1-5) were calculated based on the reaction stoichiometry and the assumptions that CO and $H_2$ are not generated catalytically and that there is no interaction with gas phase reactions. Because the gas phase reactions in the post-catalytic zone will be influenced by the higher concentrations of the reaction products ($C_2H_6$), there will be some additional dehydrogenation and oxidation reactions, but here it is assumed that the influence on the overall reaction rate is low.

The result of the calculated reaction rates from the experimental data for the individual reactions in the proposed reaction scheme is displayed in Fig. 5.11a-b (markers). Clearly, the secondary oxidation of $C_2H_4$ (reaction 4) can be neglected, because the calculated reaction rate of this reaction is much lower than the other reactions at differential conditions, as was concluded earlier. Hence, for the determination of the reaction rate constants and reaction orders, only reactions 1, 2 and 3 have been taken into account. The kinetic parameters were calculated, by fitting the calculated reaction rates to the suggested power-law rate expression (Table 5.5), based on least squares minimization:

$$\varepsilon = \sum^{datapoints} \left( \frac{r_{measured} - r_{fit}}{r_{measured}} \right)^2 \tag{5.1}$$

As shown in Fig. 5.11a-b, it can be seen that the fitted reaction rates are in quite reasonable agreement with the rates actually observed and therefore it can be concluded that the proposed mechanism is describing the experimental results adequately. The

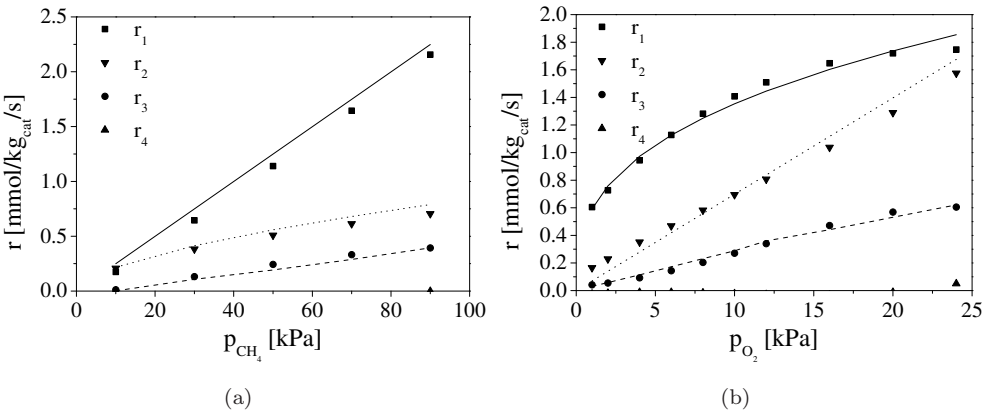


**Figure 5.11:** Comparison of the kinetic model fit with the measured reaction rates (a) $CH_4$ partial pressure and (b) $O_2$ partial pressure.

results of the error minimization are summarized in Table 5.5. Reaction (4) and (5) were omitted in the minimization, because of the negligible reaction rates in these experiments. However, assuming first order in $O_2$, $C_2H_6$ and $C_2H_4$, the reaction rate constants can be roughly estimated if the ratio $k_4/k_1$ is equal to 4.3 and $k_5/k_1$ equal to 2.7, which is based on the data published by Takanabe and Iglesia (2008).

Based on the experimental results in Fig. 5.11a-b, it was assumed that the reaction orders in $CH_4$ for reaction 1 and 3, and the $O_2$ reaction order of reaction 3 were equal to 1.0. This result is well in agreement with earlier obtained results from e.g.

**Table 5.5:** Kinetic parameters obtained via the least squares minimization of the OCM experiments at differential conditions (with $k_i$ in mmol/kg/s/kPa$^{m_i+n_i}$).

| i | Reaction | Expression | $k_i$ | $n_i$ | $m_i$ |
|---|---|---|---|---|---|
| *Based on measurements* | | | | | |
| (1) | $2\,CH_4 + \frac{1}{2}\,O_2 \longrightarrow C_2H_6 + H_2O$ | $r_1 = k_1 p_{CH_4}^{n_1} p_{O_2}^{m_1}$ | 0.0118 | 1.0 | 0.36 |
| (2) | $CH_4 + 2\,O_2 \longrightarrow CO_2 + 2\,H_2O$ | $r_2 = k_2 p_{CH_4}^{n_2} p_{O_2}^{m_2}$ | 0.00702 | 0.59 | 1.0 |
| (3) | $C_2H_6 + \frac{1}{2}\,O_2 \longrightarrow C_2H_4 + H_2O$ | $r_3 = k_3 p_{C_2H_6}^{n_3} p_{O_2}^{m_3}$ | 0.2008 | 1.0 | 0.58 |
| *Based on (Takanabe and Iglesia, 2008)* | | | | | |
| (4) | $C_2H_4 + 3\,O_2 \longrightarrow 2\,CO_2 + 2\,H_2O$ | $r_4 = k_4 p_{C_2H_4}^{n_4} p_{O_2}^{m_4}$ | 0.0520 | 1.0 | 1.0 |
| (5) | $C_2H_6 + \frac{7}{2}\,O_2 \longrightarrow 2\,CO_2 + 3\,H_2O$ | $r_5 = k_5 p_{C_2H_6}^{n_5} p_{O_2}^{m_5}$ | 0.0331 | 1.0 | 1.0 |

Stansch et al. (1997) on a different catalyst. The reaction order of 1.0 for $O_2$ for reaction (2) was also observed by Stansch. Clearly, it can be seen that while reaction (1) and (3) have a reaction order of approximately 1.0 to the hydrocarbons, a lower reaction order in $CH_4$ was found for the methane oxidation (reaction 2), which is also observed by Stansch. An important result is that the reaction order in $O_2$ for the coupling and dehydrogenation reaction is lower than unity, while the reaction in methane combustion is equal to one, which results in a higher $C_2$ selectivity at lower $O_2$ partial pressures. Over the entire range of reactants pressures it is observed that the primary OCM reaction rates can be predicted well by the developed power-law reaction rate equations.

## 5.7 Conclusions

In this chapter, the performance of the $Mn/Na_2WO_4/SiO_2$ for oxidative coupling of methane was investigated because it was found that this catalyst has excellent long-term stability and moderate catalytic activity, which is especially important for avoiding radial concentration and temperature gradients in the combined OCM/SRM process presented in Chapter 4, in which OCM is performed in a packed bed membrane reactor operated in reverse flow. The objective was to characterize the behavior of the catalyst and to obtain a kinetic model which can describe the reaction rates with sufficient accuracy for reactor modeling studies. First, the catalyst was prepared and experiments in a micro-catalytic fixed bed reactor under integral conditions have confirmed that $C_{2+}$ yields of more than 20% can be obtained in the oxidative coupling of methane using a $Mn/Na_2WO_4/SiO_2$ catalyst at 830 °C, which is in agreement with results reported in literature.

By means of Thermal Gravity Analysis (TGA) it was determined that the catalyst, which is a reducible metal oxide, requires pretreatment with oxygen/air to obtain a high $C_2$ selectivity and stable reactor performance. The intrinsic catalytic reaction rates were calculated from the measured reaction rates with and without catalyst at differential operating conditions. At a $CH_4$ partial pressure in the range of 1090 kPa and a $O_2$ partial pressure in the range of 0.730 kPa at 800 °C and 200 kPa, the reaction rates for the reactions (oxidative coupling, total oxidation of $CH_4$ and oxidative dehydrogenation of $C_2H_6$) were derived from the experimental data and fitted with power-law reaction rate expressions. It was found that $C_2H_6$ formation is linearly dependent on the $CH_4$ concentration, while the dependency on the $O_2$ partial pressure can be described by a power law function with a reaction order in $O_2$ of 0.36, confirming observations of other researchers. At differential operating conditions, the secondary $C_2H_4$ reaction rates could not be determined, however, reaction rates can be well described with data available in the literature, in which it was found that the reaction rate of $C_2H_4$ oxidation is 2−8 times larger than for $CH_4$ oxidation. These results signify that highest $C_2$ selectivities can be obtained at high $CH_4$ and low $O_2$ partial pressures, best achieved in reactor systems with distributed oxygen feed.

## Acknowledgement

The author wishes to thank M.J. Tuinier for his significant contribution to the development of the kinetic model and M. Baltussen for performing the explorative measurements on the secondary oxidation reactions. The financial support by the Netherlands Organisation for Scientific Research (NWO/ACTS) under the research theme of Advanced Sustainable Processes by Engaging Catalytic Technologies (ASPECT) (project 053.62.008).

## Nomenclature

*Roman letters*

| | | |
|---|---|---|
| $Bi_w$ | | Biot number wall $= \alpha r_p/\lambda$ |
| $c$ | $mol/m^3$ | concentration |
| $D_{eff}$ | $m^2/s$ | effective diffusivity |
| $d_r$ | m | reactor diameter |
| $d_p$ | m | particle diameter |
| $E_a$ | J/mol | activation energy |
| $k_j$ | $mmol/kg_{cat}/s/kPa^{m_i+n_i}$ | reaction rate constant |

| | | |
|---|---|---|
| $m$ | kg | mass |
| $n$ | - | reaction order |
| $p, P$ | Pa | (partial) pressure |
| $r_j$ | $\mathrm{mol/kg_{cat}/s}$ | reaction rate of component j |
| $R_j$ | $\mathrm{mol/m^3/s}$ | reaction rate of component j |
| $R_g$ | J/mol/K | universal gas constant |
| $S$ | % | product selectivity |
| $T$ | K | temperature |
| $Y$ | % | product yield |

*Greek letters*

| | | |
|---|---|---|
| $\alpha$ | $\mathrm{W/m^2/K}$ | heat transfer coefficient |
| $\varepsilon$ | - | residual |
| $\phi_v$ | $\mathrm{Nm^3/min}$ | volumetric flow rate |
| $\Delta H^0_{298}$ | J/mol | reaction enthalpy |
| $\lambda_{e,r}$ | W/m/K | effective radial heat conductivity |
| $\lambda_s$ | W/m/K | particle heat conductivity |
| $\zeta$ | - | conversion |

*Subscripts*

| | |
|---|---|
| cat | catalyst |
| s | solid phase |

# 6

# Experimental demonstration of a packed bed membrane reactor for OCM


## Abstract

This chapter describes an experimental study on the oxidative coupling of methane (OCM) on a $Mn/Na_2WO_4/SiO_2$ catalyst in an inorganic ($Al_2O_3$) packed bed membrane reactor to support the novel reactor concept developed in Chapter 4 in which OCM and SRM are thermally coupled in a single reactor with separate compartments. The effects of distributed feed of oxygen on the hydrocarbon yield and the axial temperature profiles were studied in a reactor with a relatively large amount of catalyst, so that effects of larger scale could be studied. The fluidized bed reactor, in which steam reforming reactions are performed, was emulated by a fluidized sand bed which was heated by means of an electrical oven.

Two packed bed membrane reactors of different size equipped with a modified $Al_2O_3$ membrane were used, based on its relatively good stability at high temperatures and its low fluxes. Prior to reactive experiments, the membrane was subjected to flux tests by which the permeability parameters were determined and experiments by which the operating conditions were determined to have negligible influence of back-permeation. Experiments with OCM and distributed feed of air, demonstrated that a $C_2$ yield of 25-30 % can be achieved, which is comparable with results published in the literature. Comparison with OCM experiments with pre-mixed feed of air showed that the obtained yield in a packed bed membrane reactor is significantly higher provided that the oxygen flux is sufficiently low to operate at low oxygen concentrations and that near isothermal conditions can be achieved (either via dilution of the feed or increase of the membrane length). The strong influence of the temperature profiles was also confirmed by simulations with a reactor model that included the reaction rate expressions which were experimentally determined in Chapter 5.

## 6.1 Introduction

Membrane reactors are used in a wide range of applications including the selective withdrawal of reaction products, for example selective hydrogen removal extraction for dehydrogenation reactions (Hamel et al., 2008) or hydrogen production for fuel cells (Patil et al., 2006), and the (selective) addition of reactants, particularly for oxygen addition for partial oxidation reaction systems. The application of distributed feed of oxygen in high temperature reactors has been an emerging field in scientific research since the early 1990's, for example for the production of synthesis gas, formaldehyde, carbon monoxide, methanol or ethylene (Smit et al., 2005a; Deshmukh et al., 2005; Kürten et al., 2004; Saracco et al., 1999). By adding $O_2$ locally along the reactor length, the low oxygen concentrations that can be achieved with distributed feed are advantageous for most of the catalytic (partial) oxidation reactions, including oxidative coupling of methane, because the secondary oxidation of the more reactive selective (desired) reaction products is suppressed. Moreover, the $O_2$ reaction order for the selective reaction is typically lower than that for the total oxidation reaction, which results in overall higher selectivities of the desired products.

In this work, two different packed bed membrane reactor concepts have been developed for the combined oxidative coupling of methane (OCM) and steam reforming of methane (SRM). In the first concept the integration is achieved on the particle scale using dual function OCM/SRM catalyst (see Chapters 2 and 3). Distributive feeding of $O_2$ is essential for the feasibility of this concept, because the OCM reaction rates and hence the heat production rate is controlled by the $O_2$ flux and needs to be moderated along the reactor length. Because both OCM and SRM products are generated in the same reactor compartment (on the dual function catalyst), dense membranes with integrated air separation are preferred to prevent dilution of ethylene and synthesis gas with inert nitrogen. The second reactor concept thermally couples the OCM and SRM, on the reactor scale. The combined heat exchange reactor (presented and studied in Chapter 4) consists of separate compartments for the OCM and SRM which exchange energy and the oxidative coupling process is performed in reverse flow so that the reaction feed stream is effectively heated with the reaction energy stored in (inert) particles located at the in- and outlet of the reactor. The feasibility of the latter concept is experimentally studied in this chapter using a packed bed membrane reactor for OCM (without reverse flow), equipped with porous membranes to distribute air to the reactor. The fluidized bed reactor, in which SRM should be performed to consume the generated OCM reaction heat, was replaced by a fluidized sand bed which was kept at constant temperature (emulating SRM).

In the previous chapter, it was demonstrated experimentally in a micro-catalytic

fixed bed reactor that a higher $C_2$ selectivity is favored at low $O_2$ concentrations and low $CH_4$ conversions. Although this indicates directly that higher $C_2$ yields should be possible by using membrane reactors, it is necessary to understand the influence of lower $O_2$ concentrations, particularly at higher concentrations of valuable ethylene and ethane. In this chapter, the influence of distributed feed of $O_2$ on the performance of oxidative coupling of methane is therefore studied at higher $CH_4$ conversions. First, the available membrane types and the catalytic membrane reactors used for OCM are shortly reviewed, followed by an experimental study of the main characteristics of oxidative coupling of methane in two different membrane reactors. First, the applied porous membranes were characterized via measurements of the pore size and mole fluxes. During the experimental study, the influence of several relevant parameters on oxidative coupling of methane was investigated in a small scale membrane reactor, with a limited amount of catalyst. In another, larger, membrane reactor similar experiments were performed, and the obtained results were compared with conventional pre-mixed feed experiments, and with model simulations using the determined kinetic model from Chapter 5.

## 6.2 Membranes for distributive feed of $O_2$

Ideally, an inorganic membrane for the addition of $O_2$ to a reactor compartment should be stable for long-term operation and have sufficient oxygen permeability for the OCM reaction. Two different classes of membranes can be identified, namely permselective and porous membrane which will be briefly reviewed and discussed next.

### 6.2.1 Permselective membranes

Dense oxygen permselective membranes consist of materials that can conduct oxygen ions ($O^{2-}$, $O^{-}$) via an oxygen ion and electron conduction mechanism at high temperatures. Because the selectivity for $O_2$ transport is >99%, it makes this type of membrane inherently suitable for in-situ air separation and therefore has great potential for many (partial) oxidation reactions. Early developments focussed on pure oxygen ion conductors, the so-called Electrochemical Oxygen Pump (EOP), which requires an external (electronic) circuit to transport the electrons (e.g. Eng and Stoukides, 1991). The mixed oxygen ion and electron conducting membrane (MIEC) reactor is more promising, because it can generate higher oxygen fluxes without the requirement of external electrical power, making it is easier to integrated these membranes in a reactor system.

The perovskite oxides which are often used for permselective membranes, usually consist of lanthanoids (La, Nd but also Ba), transition elements (Ca, Sr, Ba) and alkaline earth metals (Co, Fe, Mg, Cr). The permeability, stability and the conductivity strongly depends on the combination of these components. The optimization of the oxygen fluxes of the most important perovskites versus their stability is reviewed by Yang et al. (2005). Typical $O_2$ fluxes range from 0.004-0.02 mol/m$^2$/s, which are obtained at temperatures above 850°C. The long term operational stability of these membranes was tested in a strongly reducing environment (partial oxidation of methane) for periods up to 1000 hours.

The perovskite oxide membranes usually exhibit some catalytic activity for oxidative coupling of methane, hence since the 1990s continuous improvements on the OCM catalytic performance have been reported. In the past years, more than 80 papers have been published and in Table 6.1 some highlights on dense (catalytic) membrane reactors for OCM are listed.

Dense membranes possess some catalytic activity for oxidative coupling of methane, which was demonstrated by a.o. Zeng et al. (1998) who tested a disk-shaped membrane without catalyst. Due to the low available surface area and the low $O_2$ fluxes, it is required to use very diluted inlet feed streams and low $CH_4$ flow rates (2 ml/min) to obtain a reasonable $C_2$ selectivity. In a tubular membrane reactor, the reaction rates measured over 1 month slightly increase at diluted conditions, however, as the $O_2$ membrane flux increases, gas phase oxidation reactions prevail which hamper the $C_2$ yield (Lu, Dixon, Moser, Ma and Balachandran, 2000). The highest yield of 35% ever measured with OCM was obtained by Akin and Lin (2002), who used a BYS membrane. Although this is a promising result (very high selectivity), the $O_2$ flux and the corresponding productivity was very low. Particularly at higher $CH_4$ partial pressures, the yield drops, because the oxygen permeation flux is limiting the reaction rate. In membrane reactors without catalyst, a high oxygen vacancy concentration leads to a large $O_2$ flux and a high methyl radical generation rate, resulting in an increased (catalytic) contribution of the membrane to the OCM reactions. Without catalyst, however, the $C_2$ yield is quite low because of the low $CH_4$ conversion (typically <10%). Wang et al. (2005) tested the well known La/Sr/CaO catalyst with a tubular perovskite membrane, which improves the $C_2$ yield from 4% (no catalyst) to approximately 15% (with catalyst). Comparison with a co-feed packed bed reactor demonstrated that very high $C_2H_4/C_2H_6$ ratios can be achieved, because of the small $C_2H_4$ oxidation rates. Even higher yields can be expected if $Sr/La_2O_3$ is used as a catalyst, however, Guo et al. (1997) applied a solid oxide membrane reactor with an Ag-YSZ tube which limits the $O_2$ flux and therewith the reaction rates. In more

**Table 6.1:** Performance of OCM in dense and porous (catalytic) membrane reactors.

| Membrane type | Catalyst | Reactants | T (°C) | $\zeta_{CH_4}$ | $S_{C_2+}$ | $Y_{C_2+}$ | Reference |
|---|---|---|---|---|---|---|---|
| *Dense (air as $O_2$ source)* | | $CH_4$:He | | | | | |
| $La_{0.8}Sr_{0.2}Co_{0.6}Fe_{0.4}O_{3-\delta}$ | - | 1:60 | 900 | 18.1 | 70.8 | 12.8 | Zeng et al. (1998) |
| $BaCe_{0.8}Gd_{0.2}O_3$ | - | 1:44 | 780 | 26.4 | 62.5 | 16.5 | Lu et al. (2000a) |
| $Bi_{1.5}Y_{0.3}Sm_{0.2}O_3$ | - | | 900 | 64.8 | 54 | 35 | Akin and Lin (2002) |
| $Ba_{0.5}Sr_{0.5}Co_{0.8}Fe_{0.2}O_{3-\delta}$ | La/Sr/CaO | 1:5 | 850 | 24 | 63 | 15 | Wang et al. (2005) |
| $Bi_2O_3$/YSZ and Ag | $Sr/La_2O_3$ | 1:4 | 730 | 10 | 60 | 6 | Guo et al. (1997) |
| $Ba_{0.5}Sr_{0.5}Co_{0.8}Fe_{0.2}O_{3-\delta}$ | La/Sr/CaO | 1:9 | 950 | 28 | 66 | 18 | Olivier et al. (2009) |
| $Ba_{0.5}Ce_{0.4}Gd_{0.1}Co_{0.8}Fe_{0.2}O_{3-\delta}$ | Na-W-Mn | 1:1 | 800 | 51.6 | 67.4 | 34.7 | Bhatia et al. (2009) |
| *Porous (pure $O_2$ as feed)* | | | | | | | |
| $Al_2O_3/SiO_2$ | Li/MgO | $CH_4$ | 750 | 37 | 56 | 21 | Coronas et al. (1994a) |
| $Al_2O_3/SiO_2$ | Li/MgO | $CH_4$ | 750 | - | 97 | 12.8 | Coronas et al. (1994b) |
| $LaOCl/Al_2O_3$ | - | $CH_4$ | 750 | - | - | - | Chanaud et al. (1995) |
| Vycor glass | $Sm_2O_3$ | 1:5 ($N_2$) | 800 | 30 | 36 | 10 | Ramachandra et al. (1996) |
| $\gamma$-$Al_2O_3$ | Mn-W-Na-$SiO_2$ | 1:33 | 800 | 47 | 58 | 27.5 | Lu et al. (2000b) |
| Ceramic | Li/MgO | $CH_4$ | 750 | 57 | 53 | 30 | Kao et al. (2003) |

recent work Olivier et al. (2009) use the same catalytic material, however, with a $Ba_{0.5}Sr_{0.5}Co_{0.8}Fe_{0.2}O_{3-\delta}$ membrane tube which results in more than 18% $C_2$ yield at methane inlet concentrations of 10%. Other materials such as Pt/MgO, Sr/$La_2O_3$ were tested next to LaSr/CaO. Similar OCM performance is obtained with the (well-known) Na-W-Mn/$SiO_2$ catalyst coated on the membrane wall (Bhatia et al., 2009). The results summarized here demonstrate the potential of oxygen permeable membranes for OCM. Because the $O_2$ flux is limited, the oxygen deficient conditions prevent the presence of (molecular) oxygen and the highest $C_2$ yields can be obtained with these membrane types (Yang et al., 2005). In addition, the possibility of integrated air separation avoid the use expensive air separation unit (using cryogenic technology), while the reaction products in the reactor are not diluted with inert nitrogen. The production of the membrane is relatively easy, because it relies on conventional techniques such as dissolving, drying and extrusion (tubes) or isostatic pressing (discs). The main challenge with dense (catalytic) membranes is, however, to obtain a material that remains mechanically and chemically stable in a strong reducing atmosphere, has sufficient (mechanical) strength so that it can be connected to the reactor, and which possesses sufficient catalytic performance and $O_2$ flux at the optimal reaction temperature for oxidative coupling of methane.

### 6.2.2 Porous membranes

An attractive (mechanically and chemically more stable) membrane for OCM is a porous membrane, which usually consists of inorganic (ceramic) materials like $Al_2O_3$ or $SiO_2$ and is produced via controlled extrusion and consequent sintering of small particulates at high temperature. A distinction can be made between the membranes consisting of one layer with constant pore size, produced via extrusion, and the so-called asymmetric multilayer membranes with varying pore size, which have to be produced in multiple production steps. Both the monolayer and multilayer types are currently successfully applied on commercial scale, mainly for purification of water via microfiltration and ultrafiltration (Mulder, 2000), see Fig. 6.1. The multilayer membranes usually have much smaller pore size ($d_{pore} < 10$ nm) which enables the separation of gas (or liquid) mixtures, based on size exclusion. If the pore size is sufficiently small, mixtures like $CH_4$ and $H_2$ can be successfully separated by means of microporous silica and alumina membranes (Benes, 2000; Nijmeijer, 1999). The smaller the pore size, the larger the separation factors (for filtration) that can be obtained, however the (temperature and steam) stability of these membranes is still limiting commercial application.

Inorganic $Al_2O_3$ membranes can resist relatively high temperatures, hence in the

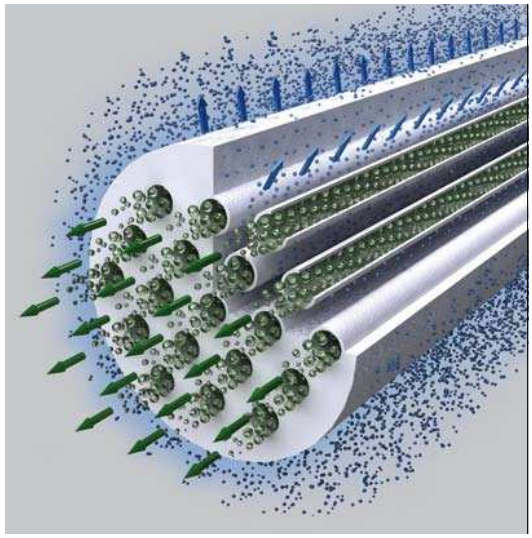

**Figure 6.1:** Cross flow ceramic membrane module for ultrafiltration (source GEA Westfalia Separator (2009)).

1990's the materials were also found suitable for the addition of $O_2$ to a (catalytic) reactor compartment, and since then numerous studies have been published on the advantageous properties of this reactor type (see e.g. Coronas et al., 1994a; Kao et al., 2003; Kiatkittipong et al., 2005; Lafarga et al., 1994; Lu, Dixon, Moser, Ma and Balachandran, 2000; Ramachandra et al., 1996). Because the $O_2$ fluxes are much higher compared to perovskite type membranes, at a relatively high trans-membrane pressure drop, the back-permeation of valuable hydrocarbons is low. The drawback of a somewhat higher $O_2$ flux obviously is that the $C_2$ selectivity is somewhat lower, however, at a higher $CH_4$ conversion than observed with perovskite type membranes. Moreover it is possible to use pure methane as reactor feed, instead of highly diluted feed streams. In Table 6.1 the highlights on membrane reactor development for OCM are listed.

Several researchers have attempted to influence the permeation fluxes by modification of the porous membrane tubes. Lafarga et al. (1994) modified an alumina membrane by depositing small $SiO_2$ particulates in the pores to increase the trans-membrane pressure drop and lower the flux, with different reactor configurations. This membrane type was tested with a fixed bed of $Li_2O_3$ catalyst in either the centerline or annular space of the reactor, while a part of the catalyst was impregnated in the membrane pore structure. The performance of the reactor was studied with pure $O_2$ and $CH_4$ as feed and it was found that considerable improvement can be

achieved compared to a co-feed reactor, and that axial temperature profiles are moderated. Particularly the use of a non-uniform $O_2$ permeation pattern increased the $C_2$ selectivity (Coronas et al., 1994a,b). This conclusion is supported by the modeling study performed in Chapter 3, in which the effect of non-uniform permeation patterns on the temperature profiles and $C_2$ yield was studied. However, because the $O_2$ mole fluxes remain rather high with porous membranes, using a catalyst with high activity is beneficial (Chanaud et al., 1995), however, this also might lead to high reactor temperatures. Ramachandra et al. (1996) applied a Vycor glass membrane with a $Sm_2O_3$ catalyst bed but observed no significant improvement of the $C_2$ yield compared to co-feed reactors. Another point of attention is the long-term stability of these membranes. Although the fluxes can be sufficiently decreased for application with OCM, the severe operating temperatures to which the membrane is exposed will influence the pore structure. It was found by Nijmeijer et al. (2001) that impregnation of the porous structure with $LaNO_3$ stabilizes the structure, which is advantageous for lower temperature applications. At high temperatures, this is only a temporary solution and eventually the fluxes will increase. Although stability is also important, it is evident that the main bottleneck of porous membrane reactors for OCM is the requirement of a high trans-membrane pressure drop (to avoid back-permeation) and simultaneously a sufficiently low $O_2$ flux (because of temperature control). A straightforward solution to overcome this problem is to dilute the $O_2$ flux with an inert. With this method, $C_2$ yields of 27% can be obtained using an $Al_2O_3$ membrane (Lu, Dixon, Moser and Hua Ma, 2000). However, for industrial application this is not a feasible solution.

### Transport in porous membranes

The driving force for transport of gas through porous structures is a (partial) pressure difference, which can be subdivided in a contribution of viscous flow and diffusion. With sufficiently large (cylindrical) pores (macropores, $d_{pore} > 50$ nm), gas is transported mainly via viscous (Poiseuille) flow. The flux through the membrane is inversely proportional to the gas viscosity, and the total flux of a (pure) gas through the membrane can be described with Darcy's law (Benes, 2000).

$$N_{visc} = -\frac{B_0}{\eta}\frac{p}{RT}\frac{\partial p}{\partial z} \tag{6.1}$$

The permeability of gases is greatly influenced by the membrane structure, which can be mathematically described by the parameter $B_0$. Different expressions were defined for $B_0$, for example for cylindrical (straight) pores the contribution of viscous flow can be described using the Hagen-Poiseuille equation, while for other (less ideal) structures

different types of expressions of $B_0$ are available (see e.g. Krishna and Wesselingh, 1997b). Contrary to viscous flow, the extent and type of diffusive transport determines whether gas separation is possible. Three types of diffusive transport are distinguished for porous structures, which are bulk (molecular), Knudsen and surface diffusion. Molecular diffusion dominates particularly at higher pressures, because the chance of molecular collisions increases with the system pressure. Surface diffusion, i.e. when adsorbed molecules move along the pore walls, has only a significant contribution to the total flux if the membrane is microporous ($d_{pore} < 2nm$) and for strongly adsorbed species such as $H_2S$ (Krishna and Wesselingh, 1997b). For the current application, surface diffusion can be safely neglected. Knudsen diffusion becomes dominant if the mean free path of the molecules over the pore size is large, which typically occurs if the pore size becomes smaller (mesoporous $2 < d_{pore} < 50$ nm). The ratio between the mean free path and the pore diameter can be calculated with the following equation (Mulder, 2000).

$$\frac{\lambda}{d_{pore}} = \frac{k_B T}{\pi d_{gas}^2 p \sqrt{2} d_{pore}} \tag{6.2}$$

For $O_2$ at a temperature of 800°C, Knudsen diffusion becomes important if the pore diameter is typically lower than 10 nm. If Knudsen diffusion determines the membrane flux, separation of gases with (very) different molecular weights is possible because the separation factor is proportional to the square root of the mole weights (Benes, 2000; Krishna and Wesselingh, 1997b; Takht Ravanchi et al., 2009).

$$N_{Kn} = -\frac{1}{RT}\frac{4}{3} K_0 \upsilon_m \frac{\partial p}{\partial z} \tag{6.3}$$

Typically, it cannot be determined beforehand which transport mechanism determines the overall membrane flux and the viscous flow, bulk diffusion and Knudsen diffusion can occur simultaneously. For a pure gas, the expressions from Equation 6.1 and 6.3 can be combined into a single equation. For a multicomponent mixture, however, the mathematical description of gas transport becomes slightly more complicated, and involves the application of the well-known Maxwell Stefan equations, also known as the Dusty Gas Model (Benes, 2000; Mason and Malinauskas, 1983; Veldsink et al., 1995).

$$\sum_{\substack{j=1 \\ j \neq i}}^{N} \frac{x_i N_j - x_j N_i}{p D_{ij}^{eff}} - \frac{N_i}{p K_0 \upsilon_m} = \frac{1}{RT}\frac{\partial x_i}{\partial z} + \frac{x_i}{RT}\left(1 + \frac{B_0 p}{\eta K_0 \upsilon_m}\right)\frac{\partial p}{\partial z} \tag{6.4}$$

Because the pores are not ideal, the structure parameters $B_0$ and $K_0$ have to be determined experimentally by flux measurements.

## 6.3 Membrane reactor setup

The oxidative coupling of methane was studied in a catalytic fixed bed reactor, equipped with a single porous $Al_2O_3$ membrane tube to distribute the $O_2$ over the reactor length. Two different reactor sizes were used, the first reactor (Fig. 6.2a) is used to study the effects of distributed $O_2$ feed at near isothermal conditions, with a relatively small amount of catalyst ($m_{cat} < 5$ g). To study in particular the effects of temperature profiles, a second somewhat larger reactor was constructed (Fig. 6.2b), carrying approximately 10 times the amount of catalyst ($m_{cat} < 50$ g). The $Mn/Na_2WO_4$ catalyst supported on $SiO_2$ with a particle size distribution between 0.3-0.5 mm was used, which was prepared as described in Chapter 5 following (Pak et al., 1998).

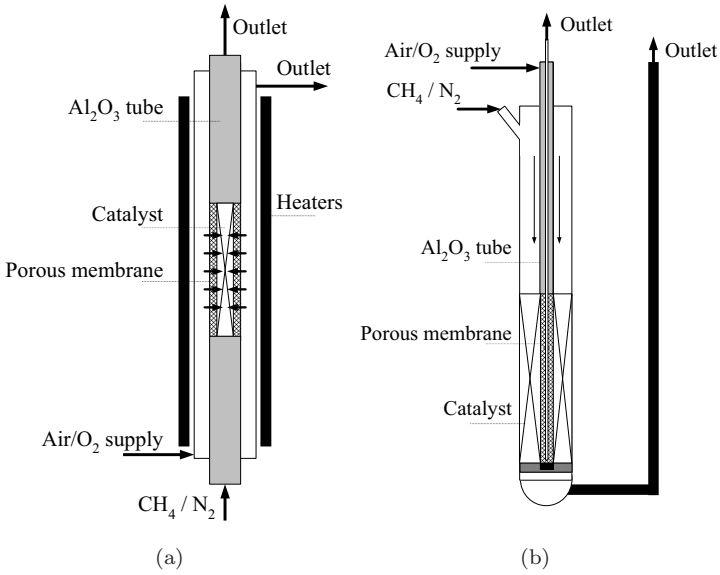


**Figure 6.2:** Schematic of the (a) tube-in-tube packed bed membrane reactor (Reactor A) and (b) U-tube membrane reactor submerged into a fluidized bed oven (Reactor B).

Both reactors can be mounted in a fully automated experimental set-up, which facilitates the feed of reactants, pressure regulation, sampling and data acquisition from the pressure and temperature sensors. Reactor A, shown in Fig. 6.2a, is heated via a tubular electrical furnace (Elicra), Reactor B (Fig. 6.2b) is immersed in a fluidized bed sand oven, which represents the SRM fluidized bed reactor in the combined con-

cept (Chapter 4), which is heated by an electrical heating oven (Westeneng). The gas feed flow rates were controlled with thermal mass flow controllers (Brooks Instrument, type 5850S). The total length of both reactor tubes equals approximately 0.3 m and the inert sections are filled with quartz particles to reduce the influence of unselective gas-phase reactions in the pre- and post catalytic sections. Because the reactor size is constrained by the pressure drop over the fixed bed, a maximum membrane length of 0.1 m was used. In both reactors, the inlet and outlet temperatures are monitored by thermocouples (Rössel Messtechnik model STE, K-type). In addition, in reactor B it is possible to measure the axial temperature profile in the center of the membrane tube and along the outer reactor wall by moving the thermocouples to different positions. A process flow diagram of the used setup (in this case with reactor B), is depicted in Fig. 6.3.

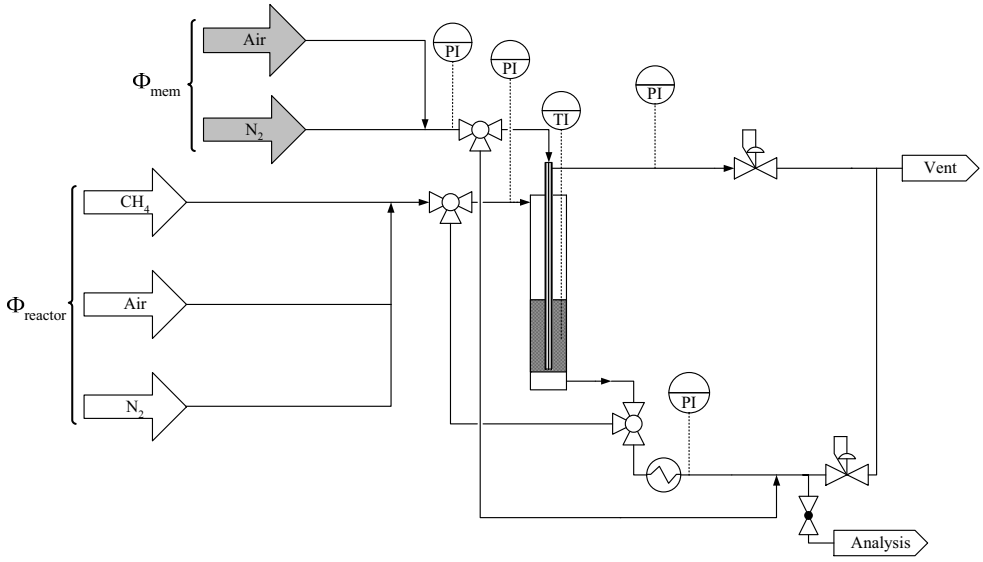


**Figure 6.3:** Process flow diagram of the experimental setup used for the tube-in-tube packed bed membrane reactor (Reactor A) and the U-tube membrane reactor (Reactor B).

Before the experiment, the reactor compartment is filled with $Mn/Na_2WO_4/SiO_2$ catalyst (0.3-0.5 mm) and the pre- and postcatalytic volume with inert quartz or alumina particles of appropriate size ($d_p$ =0.3-0.5 mm). Subsequently, first the reactor and then the membrane sealing is tested for gas leaking, by measuring the transmembrane flux at a fixed pressure drop. During each experiment, the reactor is heated under constant flow of $N_2$, while before each OCM run the catalyst is oxidized

by flowing air for 15 minutes through the reactor. After it is ensured that the catalyst is in the oxidized state, the inlet and outlet composition is analyzed by means of gas chromatography on a Varian Micro-GC 4900 (details can be found in Chapter 5).

## 6.4 Membrane characterization

Porous membrane tubes used for feeding the $O_2$/air to the OCM reactor consist of a macro-porous support tube made of 99.7 wt% $Al_2O_3$ with a thin meso- or macroporous layer coated on the inside of the tube with an average pore diameter ranging from 5-1400 nm. In this study, membrane tubes procured from two manufacturers were tested.

**Table 6.2:** Properties of the membrane.

| Description | Membraflow GmbH | Pervatech BV |
|---|---|---|
| material | $\alpha$-$Al_2O_3$ meso/macro-porous layer | $\gamma$-$Al_2O_3$ meso-porous layer |
| $< d >_{\text{pore}}$ | 20, 100, 200, 1000, 1400 nm | 5-10 nm |
| $d_i$ | 6.9 mm | 6.9 mm |
| $\delta_w$ | 1 mm | 1.5 mm |
| $L_{\text{tube}}$ | 0.1 m | 0.3 m (0.1 m effective) |

From the membrane properties shown in Table 6.2, it can be seen that the Membraflow tubes are available with a large range of pore diameters. In addition, the meso-porous layer is made of $\alpha$-$Al_2O_3$, meaning that the tubes can withstand temperatures up to 1000°C without significant change of the pore structure. Because the actual reactor length is much longer than the membrane (and catalyst bed), the 10 cm membrane was connected to two non-porous 99.7 wt% $Al_2O_3$ tubes obtained from Gimex BV. The standard membranes produced by Pervatech BV consist of the same support tube, however the meso-porous layer is made of $\gamma$-$Al_2O_3$ which is less stable at high temperatures causing the pores to grow. To increase the stability, the membrane was impregnated with 5 wt% $La_2O_3$, following the method described by (Nijmeijer et al., 2001) and (Lu, Dixon, Moser, Ma and Balachandran, 2000). A tube length of 30 cm was used, of which one side was closed (dead-end configuration), and 20 cm of the tube was coated with glass and calcined at 850°C, leaving an available permeation area of 10 cm length.

### 6.4.1 Flux measurements

For oxidative coupling with a $CH_4$ flow rate of 500 Nml/min and a $CH_4/O_2$ feed ratio of 4, an $O_2$ flow rate of 125 Nml/min would suffice. With a membrane length of 0.1 m and diameter of approximately 0.01 m, this results in an air mole flux of approximately 0.10-0.15 mol/m$^2$/s. A high trans-membrane pressure difference is required to reduce back-permeation of reactants or valuable hydrocarbons to the membrane side, however this also demands that the glass membrane sealing with the solid alumina tubes is sufficiently leak tight. The experimental setup displayed in Fig. 6.2 was used to measure the membrane flux as a function of the membrane pressure difference, which is indicative for the applicability of the membranes. Membraflow membranes with pore diameters of 20, 500, 1000 and 1400 nm were tested at a temperature of 800°C. In dead-end configuration, the total gas feed was forced through the membrane and the pressure drop was measured. In Fig. 6.4a, it can be discerned that with large pore diameters >1000 nm the pressure drop remains constant as function the volumetric flow rate, because the membrane resistance is mainly determined by its support structure. For smaller pore diameter, the flux drops proportionally, however, compared to the desired flux for the OCM reaction of 0.1 mol/m$^2$/s, the fluxes measured with these tubes are still quite high.

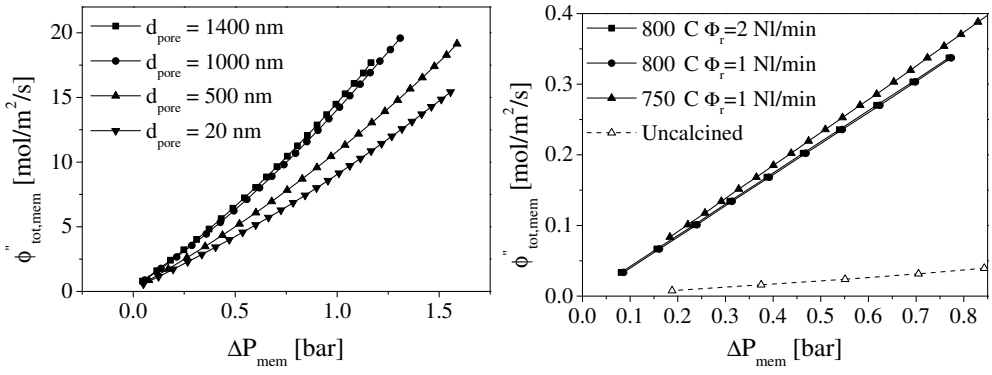


(a) (b)

**Figure 6.4:** Flux test of (a) Membraflow membranes ($L_{mem}$=0.1 m, T=800°C, $\phi_{reactor}$=1000 Nml/min) and (b) Pervatech membranes with 5 nm top layer ($L_{mem}$=0.1 m, T=750-800°C, $\phi_{reactor}$=1000 or 2000 Nml/min).

The flux through the 5 nm Pervatech membrane was also measured, at temperatures of 750 and 800°C. In the reactor compartment, a $N_2$ gas flow of 1000 and 2000 Nml/min was used while adding air via the membrane. From the results listed in

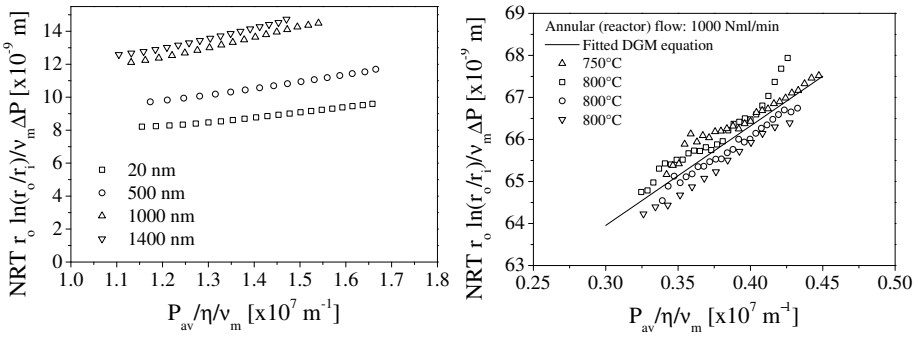


(a) (b)

**Figure 6.5:** Dusty-gas model for (a) Membraflow membrane and (b) Pervatech membrane.

Fig. 6.4b it can be seen that the membrane fluxes for the Pervatech membranes are much smaller, because of the much lower pore diameter. The main difference with the results obtained with the Membraflow tubes is that at low fluxes, the trans-membrane pressure drop is for all cases larger than 0.2-0.4 bar which is sufficient to prevent back permeation of hydrocarbons to the membrane side as will be shown in the next section. The flux measurements of both membranes were used to determine the Dusty Gas Model parameters.

By rewriting Equation 6.4 for a pure gas, the influence of both viscous flow ($B_0$) and Knudsen diffusion ($K_0$) can be determined from the experimental data:

$$N_i = \frac{1}{RT}\left(K_0 \upsilon_m + B_0 \frac{P_t + P_s}{2\eta_g}\right)\frac{\Delta P}{r_s ln\frac{r_s}{r_t}} \tag{6.5}$$

By plotting the linearized version of the equation, the parameters can be obtained from the slope and intercept of the plot. As can be discerned from Fig. 6.5, the resulting plot is for all tested temperatures (up to 800°C) and membranes an almost linear function of the modified pressure difference. The determined parameters and the contribution of viscous flow and Knudsen diffusion are displayed in Table 6.3.

The large contribution of Knudsen flow to the flux through the porous membrane and the relatively high trans-membrane pressure drop accompanied with the gas flows indicates some permselectivity, however, because of the small difference in molecular weight between $O_2$ and $N_2$ selective permeation of $O_2$ (and also back-permeation) is not significant.

**Table 6.3:** Dusty gas model parameters.

| Description | Membraflow (20 nm) | Pervatech (5 nm) |
|---|---|---|
| $B_0$ | $3.42 \cdot 10^{-16}$ | $2.39 \cdot 10^{-15}$ |
| $K_0$ | $3.94 \cdot 10^{-9}$ | $5.70 \cdot 10^{-08}$ |
| Viscous flow (6.1) | 21% | 12% |
| Knudsen diffusion (6.3) | 79% | 88% |

### 6.4.2 Back-permeation measurements

At lower trans-membrane pressure drops and membrane fluxes, back-permeation of valuable hydrocarbon feedstock or products can occur countercurrently to the permeation of $O_2$/air, leading to a reduced carbon efficiency. With perm-porometry measurements it was determined that the average pore radius of the Pervatech membrane is about 2.7 nm, and with the dusty-gas model it can be verified that back-permeation could be significant. Therefore, the influence back-permeation was tested at a temperature of 150°C (to prevent undesired reactions) by feeding pure $CH_4$ to the reactor tube and pure $N_2$ to the membrane side. The gas composition of the membrane and reactor outlet was monitored by gas chromatography, and the extent of some back-permeation was calculated with the overall mass balance. Fig. 6.6a il-

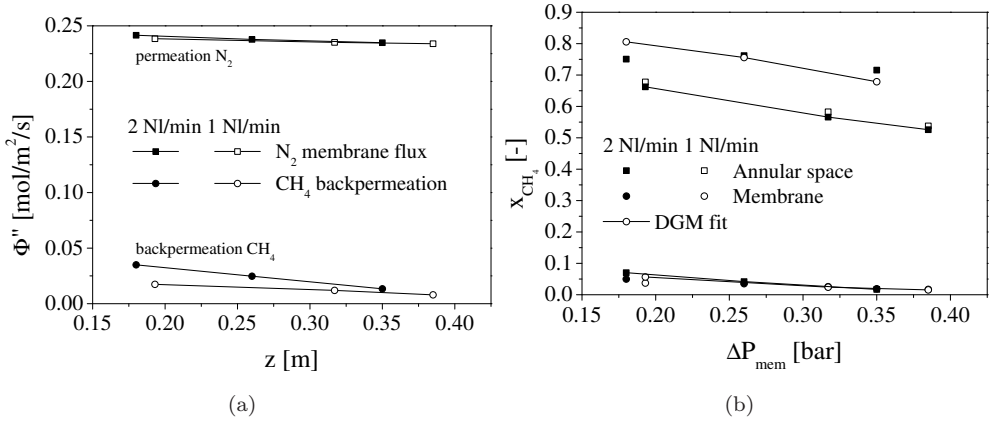


(a) (b)

**Figure 6.6:** (a) Influence of $CH_4$ flow and transmembrane pressure difference on $N_2$ permeation and methane backpermeation fluxes and (b) comparison of the Dusty-Gas-Model with the $CH_4$ mole fraction at the membrane and reactor outlet during backpermeation experiments (T=150°C, $p_{reactor}$=1.7 bar, $\phi_{mem}$=1000 Nml/min $N_2$ , $\phi_{reactor}$=1000 and 2000 Nml/min $CH_4$, $< d_{pore} >$=5.44 nm).

lustrates that indeed back-permeation of $CH_4$ through the membrane can be observed at a flow rate of 1000 Nml/min, however, the total $CH_4$ losses to the membrane side are limited to maximum 2.5%. The actual losses during an OCM experiment will be much lower, because at reaction conditions the concentrations of the relevant components are lower, so the results depicted in Fig. 6.6a can be considered as a limiting case. Hence, losses due to back-permeation can be safely neglected. The measured $CH_4$ concentrations were compared with the Dusty-Gas-Model for exactly the same reactor configuration. In the emtpy reactor and membrane compartments, the transient equations for convection and dispersion were solved where the axial dispersion was represented by a cascade of 3 ideally stirred sections. The extent of gas backmixing was estimated using the well-known Aris-correlation for laminar flow through a cylindrical tube (Westerterp et al., 1963):

$$\frac{1}{Bo} = \frac{1}{ReSc} + \frac{ReSc}{192} \qquad \mathrm{Re} < 2000 \tag{6.6}$$

With a Reynolds number of 450 and Schmidt number being approximately 1.2, the resulting Bodenstein number is about 0.36, so that the Peclet number ($Pe = Bo\frac{L_{mem}}{d_t}$) is approximately 5.1. This corresponds to approximately 3 to 4 ideally stirred tanks in series ($N \approx 1 + Pe/2$). The trans membrane transport in the porous membrane was also calculated with the Dusty Gas Model using three ideally stirred sections in series. In Fig. 6.6b it is shown that with the average membrane parameters listed in Table 6.3 the outlet mole fraction of $CH_4$ (and also $N_2$) can be well described for both the reactor flow of 1000 and 2000 Nml/min at flow conditions deviating from plug flow behavior. It can be expected that with catalyst particles present in the reactor, the back-permeation will be even lower because of the increased gas velocity. Hence, it can be inferred that at a membrane pressure difference of 0.2-0.3 bar, the losses due to back-permeation can be safely neglected.

## 6.5 Experimental results from a small membrane reactor (A)

The main characteristics of oxidative coupling of methane were investigated first with Reactor A (Fig. 6.2a), in which the effect of distributed feed of $O_2$ on the OCM reactor performance was studied at different residence times and reactant concentrations. A 20 nm $Al_2O_3$ membrane (Membraflow) was used to distribute the $O_2$ feed, which was connected to solid $Al_2O_3$ tubes.

### 6.5.1 Space velocity

For a future industrial application of OCM, a high space time yield of the valuable hydrocarbons is essential. Therefore, reactor A was filled with 0.5 g of $Mn/Na_2WO_4$ catalyst ($d_p$=0.3-0.5 mm) and the influence of the gas hourly space velocity (GHSV) was tested first with pre-mixed feed of air and consequently with distributed feed of $O_2$ (air) at an oven temperature of 800°C. In the pre-mixed reactor, an overall $CH_4/O_2$ feed ratio of 1 is selected so that acceptable $C_2$ yields could be achieved.

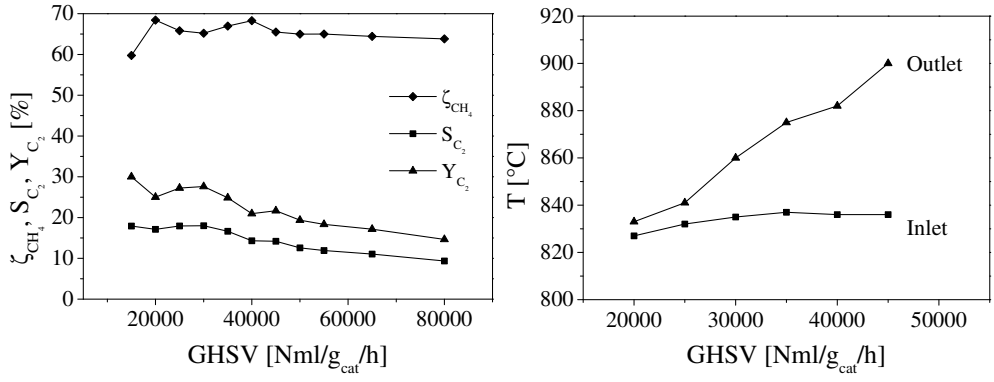


**Figure 6.7:** (a) $C_2$ selectivity and yield and (b) reactor inlet and outlet temperature for oxidative coupling on $Mn/Na_2WO_4$ with pre-mixed feed of $O_2$ (air) ($m_{cat}$=0.5 g, $x_{CH_4}$=0.16, $CH_4/O_2$= 1, $p_{in}$=2 bar).

For pre-mixed feed of air, the expected decrease of the $C_2$ yield at increasing space time follows clearly from Fig. 6.7a. Although the methane conversion is higher than 60%, which is related to the high oxygen inlet concentration, the high selectivity to total oxidation products results in a poor yield in higher hydrocarbons. Especially

at higher space times (shorter residence times) the heat production rates become too large, so that the selectivity to the $C_2$ products decreases even more. The selectivity mainly decreases because of the higher secondary oxidation reaction rates, which firstly decreases the $C_2$ yield but more importantly it leads to a stronger temperature effect. At the highest gas flow rate measured, the temperature increase over the small catalyst bed was more than 70 °C (Fig. 6.7b), which is unacceptable for long-term catalyst and reactor stability. In order to arrive at an acceptable temperature rise at larger scale operation, such that the $C_2$ yield is not affected too much, it is therefore essential to provide sufficient heat transfer (cooling) area.

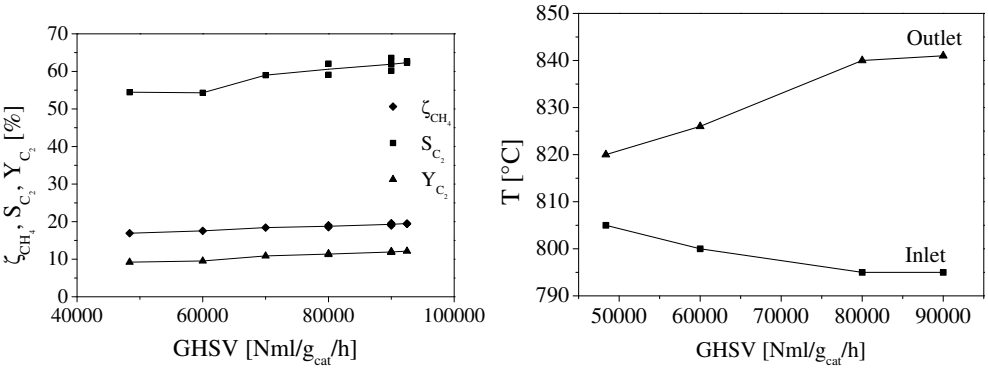


(a) (b)

**Figure 6.8:** (a) $C_2$ selectivity and yield and (b) reactor inlet and outlet temperature for oxidative coupling on $Mn/Na_2WO_4$ with distributed feed of $O_2$ (air) ($m_{cat}$=0.5 g, $L_{mem}$=5 cm, $x_{CH_4}$ =0.16, $CH_4/O_2$= 6, $p_{in}$=2 bar).

Distributed feed of air and increasing the $CH_4/O_2$ feed ratio will lead to an increase of the $C_2$ selectivity (because of the lower $O_2$ concentration) and a decrease of the temperature gradients (less $O_2$ converted). Variation of the residence time (Fig. 6.8a) then shows that the $C_2$ selectivity and yield slightly increase with increase of the space time. Because of the gradual addition of gas along the reactor length, it must be noted that the residence time in a membrane reactor can be defined in different ways. In this work, the axial gas velocity is scaled proportionally with the membrane flux so that the overall reactant feed ratios remain constant at $CH_4/O_2$ of 6, and the space velocity is based on the total gas flow to the reactor. The overall $CH_4$ conversion remains relatively constant, because the ratio between the total $O_2$ membrane flux and the $CH_4$ feed flow rate remains the same. The slightly higher $C_2$ selectivity is caused by the somewhat shorter contact times of the selective products (either in the post-

catalytic volume or in the reactor), which limits the extent of the secondary oxidation reaction somewhat. Because air is used as membrane feed, the diluting influence of $N_2$ might also be beneficial for the $C_2$ selectivity. In addition, as a result of distributed feed of air the reactor temperature (Fig. 6.8b) remains far below the 900°C that is obtained with pre-mixed feed of air. However, these experiments demonstrate that even with relatively small amounts of catalyst, removal of the reaction heat is essential in order to obtain an acceptable $C_2$ yield.

### 6.5.2 Dilution with nitrogen

In many publications an inert diluent like He or $N_2$ is added to increase the $C_2$ selectivity and to control the reactor temperature. This (undesired) effect was measured in a membrane reactor with 2.5 g catalyst and a membrane length of 8.5 cm. A constant reactant flow was used, while additional $N_2$ was added via the reactor inlet and via the membrane, to increase the overall space velocity. It was ensured that the $O_2$ conversion in all experiments was 99% or higher.

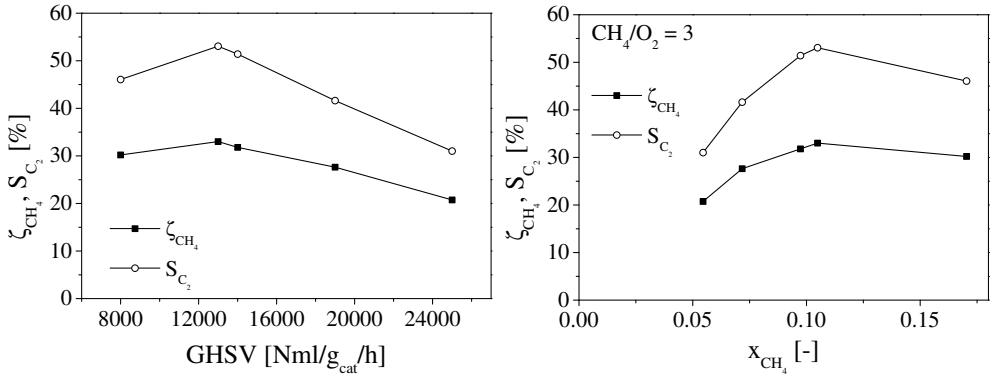


**Figure 6.9:** Effect of dilution of the $CH_4$ inlet flow with $N_2$ at constant feed ratio ($L_{mem}$=0.1 m, $m_{cat}$=2.2 g, $CH_4/O_2$=3, $\phi_{v,CH_4}$=50 Nml/min, $p_{in}$ = 2 bara, $T_{oven}$=800 °C)

It can be seen in Fig. 6.9a/b that because of the increased overall gas flow, the $CH_4$ inlet concentration decreases which results in a proportional decrease of the total reaction rate. Only at the highest concentrations, the conversion remains nearly constant while the $C_2$ selectivity decreases. This is explained as follows: because of the constant overall $CH_4/O_2$ feed ratio, the $O_2$ concentration has increased, which

caused the $C_2$ selectivity to decrease related to the different reaction stoichiometry of the oxidation reactions and more importantly the difference of $O_2$ reaction orders of the oxidation and coupling reactions. An optimum operating condition for this reactor can be observed, which lies at an inlet $CH_4$ concentration between 10 and 12 vol% and an overal GHSV of 12000 Nml/g/h. It must be noted that if for other reactor configurations, e.g. with larger membrane tubes and larger catalyst amounts, the actual optimum operating conditions are likely to deviate from the conditions determined in this section because of the changed temperature and concentration gradients in the reactor.

### 6.5.3 Reactant concentration

From the kinetic studies performed in Chapter 5, it is already expected that the effect the inlet $CH_4$ concentration on the $C_2$ selectivity will be significant. Measurements to elucidate the effect of the reactant concentrations were performed with constant space velocity (contrary to the previous section where GHSV was varied), with diluted reactant flow to minimize temperature effects. The experiments with pre-mixed feed were carried out with $N_2$ flowing via the membrane so that the flow pattern is comparable with the distributed feed experiments in which air was fed via the membrane. In Fig.

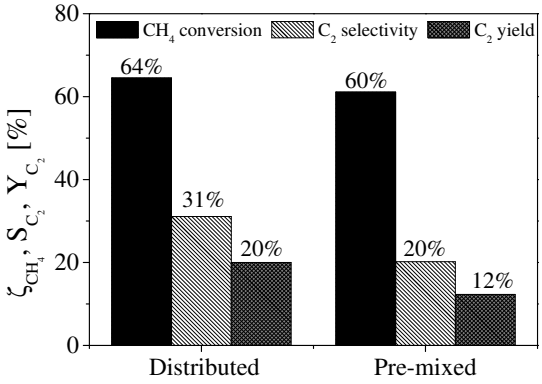


**Figure 6.10:** Performance of OCM with distributed and pre-mixed feed of $O_2$ at diluted conditions ($L_{mem}$=0.1 m, $m_{cat}$=2.2 g, $CH_4/O_2$=1, $\phi_{v,CH_4}$=50 Nml/min, $p_{in}$ = 2 bara, $T_{oven}$=800 °C, GHSV = 20000 Nml/$g_{cat}$/h)

6.10 it is obvious that the reactor with distributed feed of $O_2$ performs better than the reactor with pre-mixed feed. The $C_2$ selectivity under these conditions is more than 10% better, which leads to an improvement of the hydrocarbon yield to 20%.

Clearly, the lower $O_2$ reaction order for the oxidative coupling reaction combined with the low $O_2$ concentration leads to an increase in the $C_2$ production rate compared to the $CO_x$ production rate. It is concluded that in principle distributed feed of $O_2$ is beneficial in order to obtain a higher $C_2$ selectivity and yield, however, provided that temperature effects are low, which can be achieved via dilution with an inert gas.

## 6.6 Experimental results from a larger reactor (B)

Now that the advantageous influence of distributed feed of $O_2$ on the performance of OCM was experimentally determined on small scale under better controlled circumstances, the somewhat larger reactor B (Fig. 6.2b) is used with a larger quantity of the $Mn/Na_2WO_4/SiO_2$ catalyst ($\rho_{cat}$=800 kg/m$^3$, $m_{cat}$=46 g) to study the OCM reaction. The reactor tube was placed in the center of a fluidized bed of sand particles, which was heated with 5 °C/min to an operating temperature of 800 °C. After the reactor has reached the desired operating temperature, the catalyst was oxidized with an air flow of 500 Nml/min, after which the reactor was again flushed with $N_2$. The composition of the feed was measured on the micro-GC, and consequently the gas mixture was fed to the reactor and the outlet concentration of all the relevant components was monitored.

### 6.6.1 Concentration effects

Similar to reactor A, the effect of an increased reactor throughput was investigated by increasing the reactant inlet concentrations at a constant overall $CH_4/O_2$ feed ratio, while keeping the overall reactor and membrane feed flow rate constant by adding balance $N_2$ (constant overall space velocity). First, the influence of the $CH_4$ inlet concentration is elucidated.

As already observed in the previous chapters during the modeling of membrane reactors and the determination of reaction kinetics, the secondary oxidation of the valuable $C_2H_4$ and $C_2H_6$ plays a significant role in the overall $C_2$ yield, but also the reactor temperature is a critical parameter. Particularly, because the membrane in this reactor is located in the center of the fixed bed, at some distance of a heat sink, corresponding to the likely configuration of an industrial scale reactor, an increase in the temperature near the membrane can be expected. Hence, if the $CH_4$ concentration increases from 5 vol% to 30 vol% (Fig. 6.11), it can be seen that the $C_2$ selectivity drops because of the higher local $O_2$ concentration and probably a higher temperature. Hence, a higher $CH_4$ inlet concentration leads to a larger contribution of the unselective oxidation reactions. The effect of varying the most important parameter

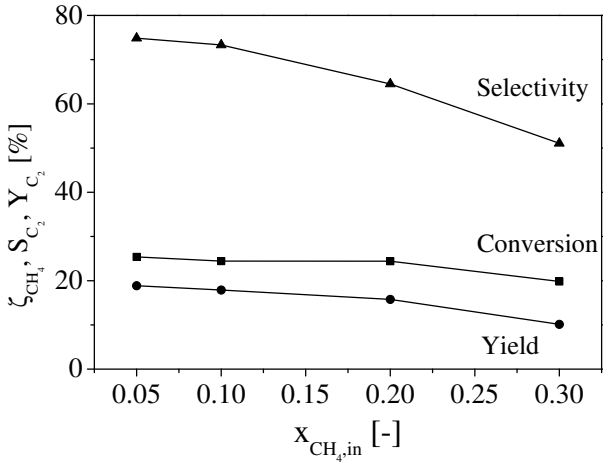


**Figure 6.11:** Effect of the $CH_4$ inlet mole fraction on the OCM performance at a constant $CH_4/O_2$ feed ratio of 4 ($T_{fb}$=800 °C, $p_{reactor,in}$=2 bar, $\Delta p_{mem}$=0.4 bar, $\phi_{reactor}$=1000 Nml/min, $x_{reactor,\ CH_4}$=0.05-0.3, $x_{reactor,\ N_2}$=balance, air as $O_2$ source).

for OCM, the $O_2$ concentration, was studied by changing the overall $CH_4/O_2$ feed ratio between 1 and 4. The $CH_4$ conversion and hydrocarbon yield was calculated. In view of minimization of temperature effects, a low $CH_4$ feed flow rate of 50 Nml/min diluted with $N_2$ was taken as the base case.

The addition of more $O_2$ results in a higher methane conversion, and generally a lower $C_2$ selectivity. This is illustrated in Fig. 6.12a, in which it can be seen that the $C_2$ selectivity decreases as the $CH_4$ conversion increases. Interestingly, however, the total $C_2$ yield slightly increases to more than 25% because of the stronger increase of the conversion rate compared to decrease in the selectivity. If these results are compared with a co-feed reactor, it can be seen that lowering of the $O_2$ concentration at a constant space velocity clearly leads to an improvement of the $C_2$ yield, but there is no difference with the selectivity of a co-feed reactor at these operating conditions (Fig. 6.12b). It can be concluded that on the small scale a reactor with distributed feed outperforms a reactor with pre-mixed feed of $O_2$, however in somewhat larger systems in which non-isothermal reaction conditions influence the reaction rates, the differences become smaller.

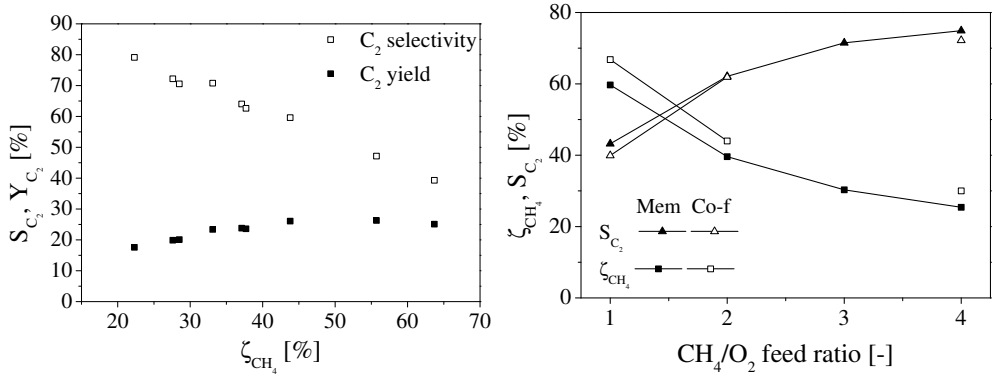


**Figure 6.12:** Effect of the $O_2$ inlet mole fraction on the OCM performance in (a) the membrane reactor and (b) in reactor with pre-mixed feed compared with distributed feed at a $CH_4/O_2$ feed ratio of 1-4 ($T_{fb}$=800 °C, $p_{reactor,in}$=2 bar, $\Delta p_{mem}$=0.4 bar, $\phi_{reactor}$=1000 Nml/min, $x_{reactor,\ CH_4}$=0.05, $x_{reactor,\ N_2}$=balance, air as $O_2$ source).

## 6.6.2 Temperature effects

It was observed in the experiments with the variation of the reactant concentrations that the non-isothermal operating conditions influence the reactor performance. Because the currently used reactor is somewhat larger than the previous reactor A, it is anticipated that because of the strongly exothermic reactions, temperature profiles will emerge along the axial and radial direction in the reactor. Therefore, the temperature profiles were measured along the axial direction in the center of the membrane tube and at the outer reactor wall. An impression of the temperature profile was obtained by positioning the thermocouples at different locations along the reactor length. This procedure was performed for the experiments in which the $O_2$ concentration was varied, for both pre-mixed feed and distributed feed of $O_2$.

In Fig. 6.13 two important phenomena can be discerned, which are characteristic for the mode of $O_2$ distribution. Because in the co-feed reactor all $O_2$ is available at the reactor inlet, it can be seen that only a limited part of the catalyst bed is utilized for the exothermic OCM reactions, but that the maximum temperature is rather high. For a lower $CH_4/O_2$ ratio and hence a higher $O_2$ concentration levels, the temperature in the center of the reactor becomes more than 850 °C, while it was found that the wall temperature is nearly equal or slightly above the fluidized bed oven temperature of 800 °C. The presence of radial heat transport limitations

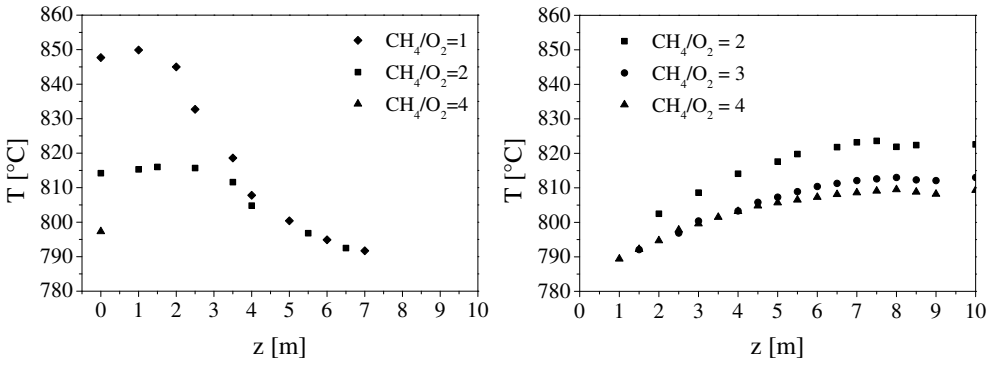


**Figure 6.13:** Measured temperature profile in the center of Reactor B for (a) co-feeding of $O_2$ and (b) distributed feed of $O_2$ ($T_{fb}$=800 °C, $p_{reactor,in}$=2 bar, $\Delta p_{mem}$=0.7 bar, $\phi_{reactor}$=1000 Nml/min, $x_{reactor,\ CH_4}$=0.05, $x_{reactor,\ N_2}$=0.95, air as $O_2$ source)

will inevitably lead to a lower catalyst bed utilization and decrease of the long-term catalyst stability. With distributed feed, it can be seen from Fig. 6.13b for the same overall $CH_4/O_2$ feed ratio that the maximum temperature in the membrane reactor ($T_{max}$<830 °C) is not much lower than observed in the co-feed reactor ($T_{max}$<830 °C). In the membrane reactor, the higher temperature observed at the end of the reactor is caused by increased $C_2H_4$ and $C_2H_6$ oxidation rates, of which the reaction enthalpy is much higher.

It can be concluded that in somewhat larger packed bed membrane reactors for OCM, radial temperature profiles are present in the reactor but that an increase of the observed 30 °C is not detrimental for the $C_2$ yield. Currently, the heat produced by the OCM reactions is transported to the fluidized bed reactor, which represents the SRM fluidized bed reactor in the combined OCM/SRM process demonstrated in Chapter 4. From the results it can be inferred that this method of heat removal is effective, because the measured reactor wall temperature remained below 805 °C while the fluidized bed temperature was 800 °C. However, heat removal from the OCM packed bed membrane reactor should be optimized if larger reactor tubes are selected or if the $CH_4$ inlet concentration is increased. The use of axial $O_2$ mole flux profiles might be considered, which can be achieved by depositing glass particulates in the pores following e.g. Coronas et al. (1994a). If a reverse flow packed bed membrane reactor for OCM is required, like with the reactor concept demonstrated in Chapter 4, the first solution is not possible, however the axial $O_2$ dosing profile might be realized

by creating axial pressure profiles at the membrane side by adding a packed bed with sufficiently small particles.

## 6.7 Model verification

The membrane length used in the experimental setup was limited to 0.1 m, however, for somewhat larger-scale applications tubes up to 0.5 m or even longer may be used. Somewhat longer membranes and possibly lower $O_2$ fluxes are required, to be able to incorporate reverse flow operation with longer flow direction switching times. In addition, because the heat production rates are somewhat lower in these longer reactor, the methane inlet fraction might be increased thereby increasing the reactor capacity. In this section, oxidative coupling on the $Mn/Na_2WO_4$ catalyst is studied in a packed bed membrane reactor with longer membrane lengths by means of numerical modeling. The packed bed membrane reactor model used for the combined OCM/SRM reactor concept in Chapter 4 was extended with the simplified kinetic model, derived for OCM on the $Mn/Na_2WO_4/SiO_2$ catalyst in Chapter 5, summarized in Table 6.4.

**Table 6.4:** Reaction rate constants for OCM on $Mn/Na_2WO_4/SiO_2$ (with $k_i$ in mmol/kg/s/kPa$^{m_i+n_i}$ and $E_a$ in kJ/mol).

| i | Reaction | Expression | $k_i$ | $E_a$ [1] |
|---|---|---|---|---|
| *Based on measurements* | | | | |
| (1) | $2\,CH_4 + \frac{1}{2}O_2 \longrightarrow C_2H_6 + H_2O$ | $r_1 = k_1 p_{CH_4}^{1.0} p_{O_2}^{0.36}$ | 0.0118 | 182 |
| (2) | $CH_4 + 2\,O_2 \longrightarrow CO_2 + 2\,H_2O$ | $r_2 = k_2 p_{CH_4}^{0.59} p_{O_2}^{1.0}$ | 0.00702 | 28 |
| (3) | $C_2H_6 + \frac{1}{2}O_2 \longrightarrow C_2H_4 + H_2O$ | $r_3 = k_3 p_{C_2H_6}^{1.0} p_{O_2}^{0.58}$ | 0.2008 | 157 |
| *Based on (Takanabe and Iglesia, 2008)* | | | | |
| (4) | $C_2H_4 + 3\,O_2 \longrightarrow 2\,CO_2 + 2\,H_2O$ | $r_4 = k_4 p_{C_2H_4}^{1.0} p_{O_2}^{1.0}$ | 0.0520 | 166 |
| (5) | $C_2H_6 + \frac{7}{2}O_2 \longrightarrow 2\,CO_2 + 3\,H_2O$ | $r_5 = k_5 p_{C_2H_6}^{1.0} p_{O_2}^{1.0}$ | 0.0331 | 150 |

In the kinetic study, the activation energy was not determined, therefore the activation energies determined by Stansch et al. (1997) on a $La_2CO_3/CaO$ catalyst were assumed, to get some (approximate) insight in the behavior of the OCM packed bed membrane reactor at non-isothermal conditions. For the $C_2H_6$ oxidation reaction, an activation energy of 150 kJ/mol was assumed which is comparable with $C_2H_4$ oxidation. With the assumed activation energies and the reaction rate constants $k_i$ of the

[1] obtained from (Stansch et al., 1997)

different reactions (listed in Table 6.4), the pre-exponential reaction rate constants were calculated. First, the simulation results were compared with the obtained experimental results at diluted $CH_4$ flow, which were shown in Fig. 6.12. In order to investigate the influence of the catalytic activity, the calculated reaction rates were multiplied with an activity parameter that was varied from 1-5. It was ensured that the total amount of $CH_4$ and $O_2$ fed to the reactor was the same as in the experiments.

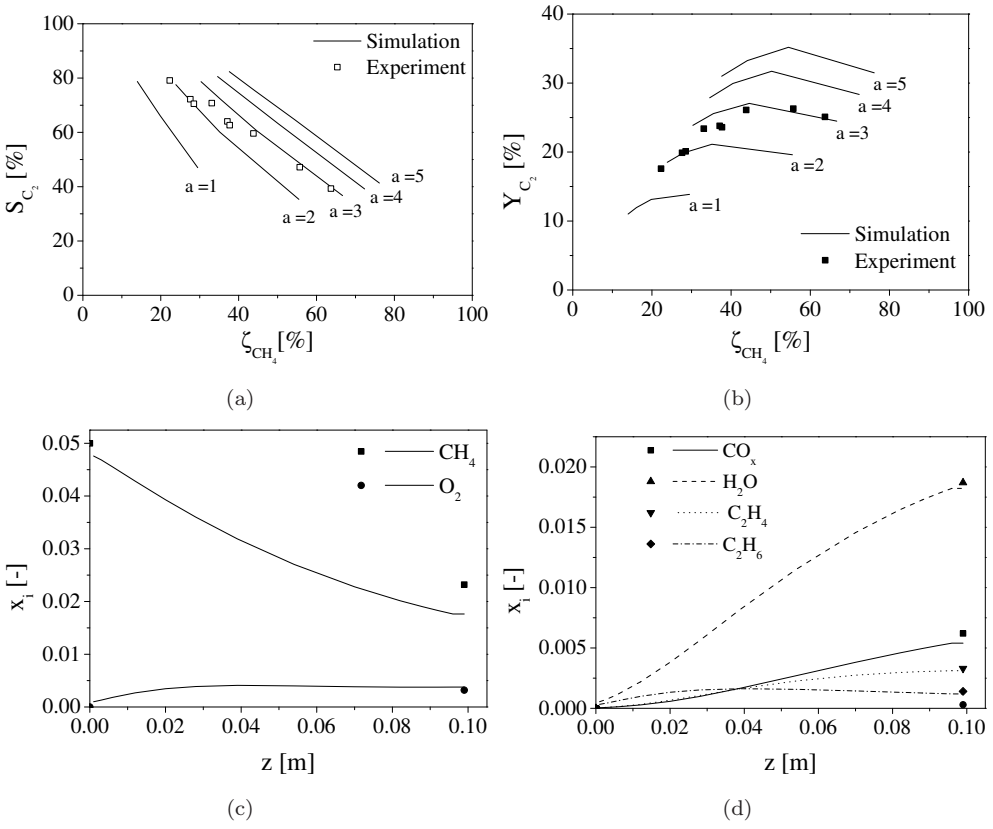


**Figure 6.14:** Simulated $C_2$ selectivity (a) and yield (b) as function of $CH_4$ conversion for different OCM catalytic activities ($a$=1-5) compared with the measured selectivity and yield in the packed bed membrane reactor and (c, d) axial mole fraction profiles at $CH_4/O_2$ ratio of 2 at a catalyst activity factor of 3, compared with the measured component mole fractions in the packed bed membrane reactor (Reactor B) ($T_{fb}$=800 °C, $p_{reactor,in}$=2 bar, $\Delta p_{mem}$=0.7 bar, $\phi_{reactor}$=1000 Nml/min, $x_{reactor,\ CH_4}$=0.05, $x_{reactor,\ N_2}$=0.95, air as $O_2$ source).

From the results depicted in Fig. 6.14a/b, it is shown that the $C_2$ selectivity and

yield calculated with the reactor model are strongly dependent on the activity factor. With an activity factor of 1, which represents the uncorrected reaction rates of the kinetic model, it is shown that the experimental selectivity and yield is much higher than predicted. Although the activity of the catalyst used in this study could have been slightly more active than the catalyst batch used in the kinetic study, it is anticipated that the main reason for the observed higher activity is related to temperature profiles in the catalyst bed. Because of the high activation energies, and expected strong temperature profiles in the reactor, the reaction rates are underestimated so that the total yield and also the $CH_4$ conversion is underpredicted. By using an activity factor between 2 (at lower $CH_4$ conversions) and 3 (at higher $CH_4$ conversions), the model can reasonably describe the experimental results. This is also illustrated by the plotted axial mole fraction profiles, which are shown in Fig. 6.14c/d. If the catalytic activity is multiplied with a factor of 3, reasonable agreement with the experimental results can be obtained. To illustrate the impact of the catalyst activity (activation energy) on the simulated reactor performance, some qualitative simulations were carried out by increasing the reactor length while the feed flow rates were kept constant.

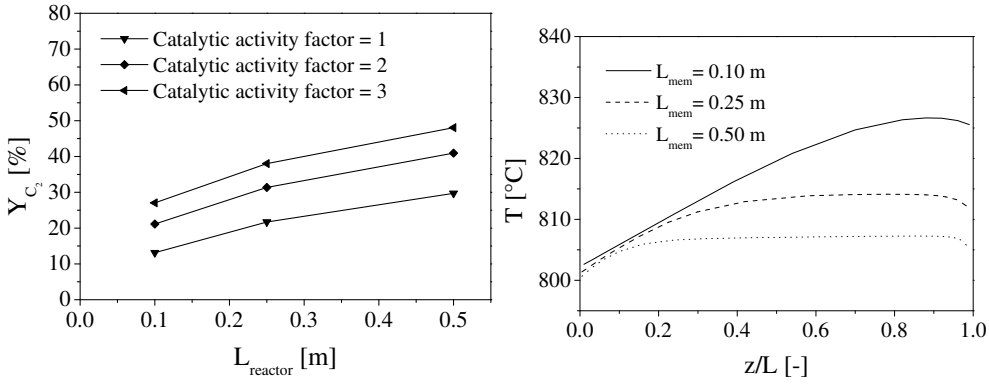


(a) (b)

**Figure 6.15:** Influence of the reactor length on (a) the performance of OCM and catalyst activity factor of 1-3 and (b) axial temperature profiles at a catalyst activity of 2 at $CH_4/O_2$ ratio of 2 (Reactor B) ($T_{fb}$=800 °C, $p_{reactor,in}$=2 bar, $\Delta p_{mem}$=0.7 bar, $\phi_{reactor}$=1000 Nml/min, $x_{reactor,\ CH_4}$=0.05, $x_{reactor,\ N_2}$=0.95, air as $O_2$ source)

In Fig. 6.15a it can be seen that with an increased reactor length the $C_2$ yield can be strongly increased, because of the lower local $O_2$ fluxes and $O_2$ concentrations (at

constant activity). As a result of the lower $O_2$ concentration, the local heat production rate is also lower, which obviously results in a smaller temperature increase (see Fig. 6.15b). It can be concluded that with a packed bed membrane reactor for OCM in principle very high $C_2$ yield should become possible provided that a sufficiently active and selective catalyst and sufficiently long membranes are used, because of the necessary removal of the reaction heat. For accurate predictions of the reaction rates at non-isothermal conditions further experimental studies are required to determine the activation energies for the reactions on the $Mn/Na_2WO_4$ catalyst.

## 6.8 Conclusions

In this chapter, the feasibility of using a membrane reactor for oxidative coupling of methane was investigated experimentally. The catalyst which was tested in the previous chapter, $Mn/Na_2WO_4/SiO_2$, was used as catalyst and porous inorganic $Al_2O_3$ membranes were selected for the distribution of oxygen along the reactor length. From the experimental results it is concluded that indeed operation with a lower local oxygen concentration improves the $C_2$ selectivity and yield to 25-30%, however, only under diluted conditions and on small scale. Although in principle distributed feed of oxygen can thus outperform a reactor with pre-mixed feed, it can be inferred that with the diluted conditions applied, the advantageous properties of the membrane reactor disappear somewhat which is supported by results found in the literature.

The performance of oxidative coupling of methane was studied by using two different reactor sizes, the first reactor was used to study the effects of distributed oxygen feed and dilution with nitrogen at near isothermal conditions, with a relatively small amount of catalyst. The effects of temperature profiles, the methane inlet concentration and the oxygen concentration were also studied in a second somewhat larger reactor, carrying approximately a 10 times larger amount of catalyst than the smaller reactor.

It was found that the temperature effects in the membrane reactor can be moderated somewhat by application of distributed feed, although the measured difference with the maximum temperature in a pre-mixed reactor is not large. Because of the porous membranes, the oxygen flux at the end of the reactor is relatively high, resulting in higher secondary oxidation reaction rates and concomitant temperature rise. In order to minimize the temperature increase downstream, a non-uniform flow pattern could be applied. For larger scale application, the use of pure methane as a reactor feed is only possible if the membrane is modified such that the maximum achievable membrane flux is decreased, meaning that OCM with pure methane feed

is only feasible at low space time which is less desired from an industrial point of view. By selecting a better method of heat removal, i.e. by application of longer membrane tubes with lower fluxes, the increase of the temperature can be moderated even further. It was found that with the kinetic model describing the reaction rates on the $Mn/Na_2WO_4$ catalyst, the experimental results can be reasonably reproduced if an activity correction factor was applied probably because of radial temperature profiles. Experimental determination of the activation energies of the prevailing reactions is required to increase the accuracy. Finally it should be noted that for industrial application, in which mechanical stability and performance becomes increasingly important, it is necessary to develop an oxygen distributor which can resist the severe operating conditions on the long-term.

## Acknowledgement

The author wishes to thank M. Patel and P.W. Spek for their contribution to the experimental work. H. Kruidhof is acknowledged for his advice on membrane selection, M. Luiten for the permporometry measurements. The financial support by the Netherlands Organisation for Scientific Research (NWO/ACTS) under the research theme of Advanced Sustainable Processes by Engaging Catalytic Technologies (ASPECT) (project 053.62.008).

## Nomenclature

*Roman letters*

| | | |
|---|---|---|
| $Bo$ | - | Bodenstein number $= vd_t/D_{ax}$ |
| $B_0$ | $m^2$ | structure parameter of Dusty Gas Model |
| $D_{ij}^{eff}$ | $m^2/s$ | effective diffusivity |
| $d$ | m | diameter |
| $d_p$ | m | particle diameter |
| $d_{gas}$ | m | kinetic diameter |
| $E_a$ | J/mol | activation energy |
| $k_B$ | J/K | Boltzmann constant ($=1.3806504 \cdot 10^{-23}$) |
| $k_j$ | $mmol/kg_{cat}/s/kPa^{m_i+n_i}$ | reaction rate constant |
| $K_0$ | m | structure parameter of Dusty Gas Model |
| $L$ | m | length |
| $m$ | kg | mass |
| $N_i$ | $mol/m^2/s$ | mole flux of component $i$ |

| | | |
|---|---|---|
| $p, P$ | Pa | (partial) pressure |
| $Pe$ | - | Peclet number = $Bo\frac{L_{mem}}{d_t}$ |
| $r$ | m | radius |
| $r_j$ | mol/kg$_{\text{cat}}$/s | reaction rate of component j |
| $R$ | J/mol/K | universal gas constant |
| $Re$ | - | Reynolds number (= $\frac{\rho v d}{\eta}$) |
| $S$ | % | product selectivity |
| $Sc$ | - | Schmidt number (= $\frac{\nu}{D}$) |
| $T$ | K | temperature |
| $x$ | - | mole fraction |
| $Y$ | % | product yield |
| $z$ | m | axial coordinate |

*Greek letters*

| | | |
|---|---|---|
| $\delta$ | m | thickness |
| $\phi_{reactor}$ | Nml/min | volumetric inlet flow rate at reactor side |
| $\eta$ | kg/m/s | dynamic viscosity |
| $\lambda$ | m | mean free path |
| $\rho$ | kg/m$^3$ | density |
| $\zeta$ | % | conversion |
| $\upsilon_m$ | m/s | mean molecular velocity (= $\sqrt{\frac{8RT}{\pi M}}$) |

*Subscripts*

| | |
|---|---|
| cat | catalyst |
| g | gas phase |
| i | inner |
| mem | membrane |
| p | particle |
| t | tube/reactor side |
| s | shell/membrane side |
| w | wall |

# Bibliography


Akin, F. T. and Lin, Y. S.: 2002, Oxidative coupling of methane in dense ceramic membrane reactor with high yields, *AIChE Journal* **48**(10), 2298–2306.

Alexander, R.: 1977, Diagonal implicit runge-kutta methods for stiff O.D.E.'s, *SIAM Journal on Numerical Analysis* **14**(6), 1006–1021.

Anderson, J. B.: 1963, A criterion for isothermal behaviour of a catalyst pellet, *Chemical Engineering Science* **18**(2), 147.

Apecetche, M. A., Gonzalez, M. G., Williams, R. J. J. and Cunningham, R. E.: 1973, Viscous and diffusive transport with simultaneous chemical reaction in non-isobaric porous catalyst particles, *Journal of Catalysis* **29**(3), 451.

Aris, R.: 1975, *The mathematical theory of diffusion and reaction in permeable catalysts*, Clarendon Press, Oxford.

Baerns, M. and Buyevskaya, O.: 1998, Simple chemical processes based on low molecular-mass alkanes as chemical feedstocks, *Catalysis Today* **45**(1-4), 13.

Becker, S. and Baerns, M.: 1991, Oxidative coupling of methane over $La_2O_3$/CaO catalysts. Effect of bulk and surface properties on catalytic performance, *Journal of Catalysis* **128**(2), 512.

Benes, N. E.: 2000, *Mass Transport in Thin Supported Silica Membranes*, PhD thesis, University of Twente.

Bhatia, S., Thien, C. Y. and Mohamed, A. R.: 2009, Oxidative coupling of methane (OCM) in a catalytic membrane reactor and comparison of its performance with other catalytic reactors, *Chemical Engineering Journal* **148**(2-3), 525–532.

Bird, R. B., Stewart, W. E. and Lightfoot, E. N.: 2002, *Transport Phenomena*, 2nd edn, John Wiley & Sons.

BP: 2009, *BP Statistical Review of World Energy June 2009*, Beacon Press, London.

Caze, P., Didier, L., Marques, P., Remy, C. and Woehl, P.: 2003, Structured catalysts incorporating thick washcoats and method of preparation thereof.

Chanaud, P., Julbe, A., Larbot, A., Guizard, C., Cot, L., Borges, H., Fendler, A. G. and Mirodatos, C.: 1995, Catalytic membrane reactor for oxidative coupling of methane. part 1: Preparation and characterization of LaOCl membranes, *Catalysis Today* **25**(3-4), 225.

Chen, Q., Couwenberg, P. M. and Marin, G. B.: 1994, Oxidative coupling of methane with cofeeding of ethane, *Catalysis Today* **21**(2-3), 309–319.

Chilukuri, P., Rademakers, K., Nymeijer, K., van der Ham, L. and van den Berg, H.: 2007, Propylene/propane separation with a gas/liquid membrane contactor using a silver salt solution, *Industrial and Engineering Chemistry Research* **46**(25), 8701–8709.

Chou, L., Cai, Y., Zhang, B., Niu, J., Ji, S. and Li, S.: 2003, Influence of $SnO_2$-doped W-Mn/$SiO_2$ for oxidative conversion of methane to high hydrocarbons at elevated pressure, *Applied Catalysis A: General* **238**(2), 185.

Choudhary, V. R. and Uphade, B. S.: 2004, Oxidative conversion of methane/natural gas into higher hydrocarbons, *Catalysis Surveys from Asia* **8**(1), 15–25.

Conway, S. J., Greig, J. A. and Thomas, G. M.: 1992, Comparison of lanthanum oxide and strontium-modified lanthanum oxide catalysts for the oxidative coupling of methane, *Applied Catalysis A: General* **86**, 199–212.

Coronas, J., Menéndez, M. and Santamaria, J.: 1994a, Development of ceramic membrane reactors with a non-uniform permeation pattern. Application to methane oxidative coupling, *Chemical Engineering Science* **49**(24A), 4749–4757.

Coronas, J., Menéndez, M. and Santamaria, J.: 1994b, Methane oxidative coupling using porous ceramic membrane reactors-II. reaction studies, *Chemical Engineering Science* **49**(12), 2015–2025.

Couwenberg, P. M.: 1995, *Gas-phase chain reactions catalyzed by solids: the oxidative coupling of methane*, PhD thesis, Eindhoven University.

Couwenberg, P. M., Chen, Q. and Marin, G. B.: 1996a, Irreducible mass-transport limitations during a heterogeneously catalyzed gas-phase chain reaction: Oxidative coupling of methane, *Industrial & Engineering Chemistry Research* **35**(2), 415.

Couwenberg, P. M., Chen, Q. and Marin, G. B.: 1996b, Kinetics of a gas-phase chain reaction catalyzed by a solid: The oxidative coupling of methane over Li/MgO-based catalysts, *Industrial & Engineering Chemistry Research* **35**(11), 3999–4011.

Daubert, T. E. and Danner, R. P. (eds): 1985, *Data compilation tables of properties of pure compounds*, Design Institute for Physical Property Data, American Institute of Chemical Engineers.

de Smet, C. R. H., de Croon, M. H. J. M., Berger, R. J., Marin, G. B. and Schouten, J. C.: 2001, Design of adiabatic fixed-bed reactors for the partial oxidation of methane to synthesis gas. Application to production of methanol and hydrogen-for-fuel-cells, *Chemical Engineering Science* **56**, 4849–4861.

DeBoy, J. M. and Hicks, R. F.: 1988, The oxidative coupling of methane of alkali, alkaline earth, and rare earth oxides, *Industrial Engineering Chemistry Research* **27**, 1577–1582.

Dedov, A. G., Loktev, A. S., Moiseev, I. I., Aboukais, A., Lamonier, J. F. and Filimonov, I. N.: 2003, Oxidative coupling of methane catalyzed by rare earth oxides: Unexpected synergistic effect of the oxide mixtures, *Applied Catalysis A: General* **245**(2), 209–220.

Deshmukh, S. A. R. K., Laverman, J. A., Van Sint Annaland, M. and Kuipers, J. A. M.: 2005, Development of a membrane-assisted fluidized bed reactor. 2. experimental demonstration and modeling for the partial oxidation of methanol, *Industrial and Engineering Chemistry Research* **44**(16), 5966–5976.

Dixon, A. G. and Cresswell, D. L.: 1979, Theoretical prediction of effective heat-transfer parameters in packed-beds, *AIChE Journal* **25**(4), 663–676.

Dry, M. E.: 2002, The fischer-tropsch process: 1950-2000, *Catalysis Today* **71**, 227–241.

editor Verein Deutscher Ingenieure, V.-G. V. u. C. G.: 1993, *VDI Heat Atlas*, VDI Verlag, Düsseldorf.

Edwards, M. F. and Richardson, J. F.: 1968, Gas dispersion in packed beds, *Chemical Engineering Science* **23**, 109–123.

EIA: 2009, *International Energy Outlook 2009*, US Department of Energy, Washington.

Ekstrom, A., Regtop, R. and Bhargava, S.: 1990, Effect of pressure on the oxidative coupling reaction of methane, *Applied Catalysis* **62**(2), 253–269.

Eng, D. and Stoukides, M.: 1991, The catalytic and electrocatalytic coupling of methane over yttria-stabilized zirconia, *Catalysis Letters* **9**(1-2), 47–54.

Ergun, S.: 1952, Fluid flow through packed columns, *Chemical Engineering Progress* **48**(2), 89–94.

Fang, X., Li, S., Gu, J. and Yang, D.: 1992, *J. Mol. Catal. (China)* **6**, 427.

Fogler, S.: 1963, *Elements of chemical reactor design and operation*, 1 edn, John Wiley & Sons Ltd.

Gajda, G. J.: 2008, Selective hydrogenation process using layered catalyst composition and preparation of said catalyst.

GEA Westfalia Separator: 2009, `http://www.westfalia-separator.com`.

Gosiewski, K., Bartmann, U., Moszczynski, M. and Mleczko, L.: 1999, Effect of the intraparticle mass transport limitations on temperature profiles and catalytic performance of the reverse-flow reactor for the partial oxidation of methane to synthesis gas, *Chemical Engineering Science* **54**(20), 4589–4602.

Graf, P. O.: 2008, *Combining oxidative coupling and steam reforming of methane: Vision or Utopia?*, Phd thesis, University of Twente.

Graf, P. O., Mojet, B. L., van Ommen, J. G. and Lefferts, L.: 2007, Comparative study of steam reforming of methane, ethane and ethylene on Pt, Rh and Pd supported on yttrium-stabilized zirconia, *Applied Catalysis A: General* **332**(2), 310–317.

Gunn, D. J.: 1978, Transfer of heat or mass to particles in fixed and fluidized beds, *International Journal of Heat and Mass Transfer* **21**(4), 467–476.

Gunn, D. J. and Misbah, M. M. A.: 1993, Bayesian estimation of heat transport parameters in fixed beds, *International Journal of Heat and Mass Transfer* **36**(8), 2209–2221.

Guo, X. M., Hidajat, K., Ching, C. B. and Chen, H. F.: 1997, Oxidative coupling of methane in a solid oxide membrane reactor, *Industrial and Engineering Chemistry Research* **36**(9), 3576–3582.

Hamel, C., Tóta, A., Klose, F., Tsotsas, E. and Seidel-Morgenstern, A.: 2008, Analysis of single and multi-stage membrane reactors for the oxidation of short-chain alkanes - simulation study and pilot scale experiments, *Chemical Engineering Research and Design* **86**(7), 753 – 764.

Hoogendam, G. C.: 1996, *The oxidative coupling of methane over doped Li/MgO catalysts*, PhD thesis, University of Twente.

IEA: 2009, *World Energy Outlook 2009*, OECD/IEA, Paris.

Iglesia, E., Soled, S. L., Baumgartner, J. E. and Reyes, S. C.: 1995, Synthesis and catalytic properties of eggshell cobalt catalysts for the Fischer-Tropsch synthesis, *Journal of Catalysis* **153**, 108–122.

Iordanidis, A. A.: 2002, *Mathematical modeling of catalytic fixed bed reactors*, PhD thesis, University of Twente.

Ito, T., Wang, J., Lin, C. and Lunsford, J. H.: 1985, Oxidative dimerization of methane over a lithium-promoted magnesium oxide catalyst, *Journal of the American Chemical Society* **107**, 5062–5068.

Ji, S., Xiao, T.-c., Li, S.-b., Xu, C.-z., Hou, R.-l., Coleman, K. S. and Green, M. L. H.: 2002, The relationship between the structure and the performance of Na-W-Mn/$SiO_2$ catalysts for the oxidative coupling of methane, *Applied Catalysis A: General* **225**(1-2), 271.

Ji, S., Xiao, T., Li, S., Chou, L., Zhang, B., Xu, C., Hou, R., York, A. P. E. and Green, M. L. H.: 2003, Surface $WO_4$ tetrahedron: the essence of the oxidative coupling of methane over Mn/$SiO_2$ catalysts, *Journal of Catalysis* **220**(1), 47.

Jiang, Z. C., Yu, C. J., Fang, X. P., Li, S. B. and Wang, H. L.: 1993, Oxide support interaction and surface reconstruction in the $Na_2WO_4/SiO_2$ system, *Journal Of Physical Chemistry* **97**(49), 12870–12875.

Jones, C. A., Leonard, J. J. and Sofranko, J. A.: 1987, The oxidative conversion of methane to higher hydrocarbons over alkali-promoted Mn/$SiO_2$, *Journal of Catalysis* **103**(2), 311.

Kao, Y. K., Lei, L. and Lin, Y. S.: 2003, Optimum operation of oxidative coupling of methane in porous ceramic membrane reactors, *Catalysis Today* **82**(1-4), 255–273.

Keller, G. E. and Bhasin, M. M.: 1982, Synthesis of ethylene via oxidative coupling of methane: I. determination of active catalysts, *Journal of Catalysis* **73**(1), 9–19.

Khinast, J., Gurumoorthy, A. and D., L.: 1998, Complex dynamic features of a cooled reverse-flow reactor, *AIChE Journal* **44**(5), 1128–1140.

Khinast, J., Jeong, Y. O. and Luss, D.: 1999, Dependence of cooled reverse-flow reactor dynamics on reactor model, *AIChE Journal* **45**(2), 299–309.

Kiatkittipong, W., Tagawa, T., Goto, S., Assabumrungrat, S., Silpasup, K. and Praserthdam, P.: 2005, Comparative study of oxidative coupling of methane modeling in various types of reactor, *Chemical Engineering Journal* **115**(1-2), 63–71.

Kolios, G., Frauhammer, J. and Eigenberger, G.: 2000, Autothermal fixed-bed reactor concepts, *Chemical Engineering Science* **55**, 5945–5967.

Kolios, G., Frauhammer, J. and Eigenberger, G.: 2002, Efficient reactor concepts for coupling endothermic and exothermic reactions, *Chemical Engineering Science* **57**, 1505–1510.

Korf, S. J., Roos, J. A., Veltman, L. J., van Ommen, J. G. and Ross, J. R. H.: 1989, Effect of additives on lithium doped magnesium oxide catalysts used in the oxidative coupling of methane, *Applied Catalysis* **56**, 119–135.

Kou, Y., Zhang, B., Niu, J., Li, S., Wang, H., Tanaka, T. and Yoshida, S.: 1998, Amorphous features of working catalysts: XAFS and XPS characterization of $Mn/Na_2WO_4/SiO_2$ as used for the oxidative coupling of methane, *Journal of Catalysis* **173**(2), 399.

Krishna, R. and Wesselingh, J. A.: 1997a, The Maxwell-Stefan approach to mass transfer, *Chemical Engineering Science* **52**(6), 861–911.

Krishna, R. and Wesselingh, J. A.: 1997b, The Maxwell-Stefan approach to mass transfer, *Chemical Engineering Science* **52**(6), 861–911.

Kunii, D. and Levenspiel, O.: 1991, *Fluidization Engineering*, 2nd edn, Butterworth-Heinemann.

Kürten, U.: 2003, *Modeling of packed bed membrane reactors: Impact of oxygen distribution on conversion and selectivity in partial oxidation systems*, PhD thesis, University of Twente.

Kürten, U., van Sint Annaland, M. and Kuipers, J. A. M.: 2004, Oxygen distribution in packed bed membrane reactors for partial oxidation systems and its effect on product selectivity, *International Journal of Chemical Reactor Engineering* **2**.

Kus, S., Otremba, M. and Taniewski, M.: 2003, The catalytic performance in oxidative coupling of methane and the surface basicity of $La_2O_3$, $Nd_2O_3$, $ZrO_2$ and $Nb_2O_5$, *Fuel* **82**(11), 1331–1338.

Lafarga, D., Santamaria, J. and Menendez, M.: 1994, Methane oxidative coupling using porous ceramic membrane reactors-1. reactor development, *Chemical Engineering Science* **49**(12), 2005.

Levenspiel, O.: 2005, What will come after petroleum?, *Industrial and Engineering Chemistry Research* **44**(14), 5073–5078.

Lu, Y., Dixon, A. G., Moser, W., Ma, Y. H. and Balachandran, U.: 2000, Oxygen-permeable dense membrane reactor for the oxidative coupling of methane, *Journal of Membrane Science* **170**(1), 27–34.

Lu, Y., Dixon, A. G., Moser, W. R. and Hua Ma, Y.: 2000, Oxidative coupling of methane in a modified $\gamma$-$Al_2O_3$ membrane reactor, *Chemical Engineering Science* **55**(21), 4901.

Lu, Y., Dixon, A. G., Moser, W. R. and Ma, Y. H.: 1999, Oxidative coupling of methane in a modified $\gamma$-alumina membrane reactor, *Chemical Engineering Science* **55**, 4901–4912.

Lunsford, J.: 1990, The catalytic conversion of methane to higher hydrocarbons, *Catalysis Today* **6**(3), 235.

Lunsford, J.: 2000, Catalytic conversion of methane to more useful chemicals and fuels: A challenge for the 21st century, *Catalysis Today* **63**(2-4), 165–174.

Makri, M. and Vayenas, C. G.: 2003, Scale-up of gas recycle reactor-separators for the production of $C_2H_4$ from $CH_4$, *Applied Catalysis A: General* **244**, 301–310.

Martin, G. A. and Mirodatos, C.: 1995, Surface chemistry in the oxidative coupling of methane, *Fuel Processing Technology* **42**(2-3), 179–215.

Mason, E. A. and Malinauskas, A. P.: 1983, Gas transport in porous media: the dusty gas model, *Chemical Engineering Monograph* **17**.

Mears, D. E.: 1971a, Diagnostic criteria for heat transport limitations in fixed bed reactors, *Journal of Catalysis* **20**, 127–131.

Mears, D. E.: 1971b, Tests for transport limitations in experimental catalytic reactors, **10**(4), 7.

Mears, D. E.: 1973, On the relative importance of intraparticle and interphase transport effects in gas-solid catalysis, *Journal of Catalysis* **30**, 283–287.

Mleczko, L. and Baerns, M.: 1995, Catalytic oxidative coupling of methane - reaction engineering aspects and process schemes, *Fuel Processing Technology* **42**(2-3), 217.

Mueller, M. A., Kim, T. J., Yetter, R. A. and Dryer, F. L.: 1999, Flow reactor studies and kinetic modeling of the $H_2/O_2$ reaction, *International Journal of Chemical Kinetics* **31**(2), 113–125.

Mulder, M.: 2000, *Basic Principles of Membrane Technology*, 2nd edn, Kluwer Academic Publishers.

Nakamura, D. N. e.: 2007, Ethylene report, *Oil and Gas Journal* **105**(27), 46.

Nelson, P. F. and Cant, N. W.: 1990, Oxidation of $C_2$ hydrocarbon products during the oxidative coupling of methane over a lithium/magnesia catalyst, *Journal of Physical Chemistry* **94**(9), 3756–3761.

Nieken, U., Kolios, G. and Eigenberger, G.: 1994a, Control of the ignited steady state in autothermal fixed-bed reactors for catalytic combustion, *Chemical Engineering Science* **49**(24), 5507–5518.

Nieken, U., Kolios, G. and Eigenberger, G.: 1994b, Fixed-bed reactors with periodic flow reversal: experimental results for catalytic combustion, *Catalysis Today* **20**, 335–350.

Nijmeijer, A.: 1999, *Hydrogen-selective membranes for use in membrane steam reforming*, PhD thesis, University of Twente.

Nijmeijer, A., Kruidhof, H., Bredesen, R. and Verweij, H.: 2001, Preparation and properties of hydrothermally stable $\gamma$-alumina membranes, *Journal of the American Ceramic Society* **84**(1), 136–140.

Numaguchi, T. and Kikuchi, K.: 1988, Intrinsic kinetics and design simulation in a complex reaction network: steam-methane reforming, *Chemical Engineering Science* **43**, 2295–2301.

O'Conaire, M., Curran, H. J., Simmie, J., Pitz, W. J. and Westbrook, C. K.: 2004, A comprehensive modeling study of hydrogen oxidation, *International Journal of Chemical Kinetics* **36**(11), 603–622.

Olivier, L., Haag, S., Mirodatos, C. and van Veen, A. C.: 2009, Oxidative coupling of methane using catalyst modified dense perovskite membrane reactors, *Catalysis Today* **142**(1-2), 34–41.

Pak, S. and Lunsford, J. H.: 1998, Thermal effects during the oxidative coupling of methane over $Mn/Na_2WO_4/SiO_2$ and $Mn/Na_2WO_4/MgO$ catalysts, *Applied Catalysis A: General* **168**(1), 131.

Pak, S., Qiu, P. and Lunsford, J. H.: 1998, Elementary reactions in the oxidative coupling of methane over $Mn/Na_2WO_4/SiO_2$ and $Mn/Na_2WO_4/MgO$ catalysts, *Journal of Catalysis* **179**(1), 222–230.

Palermo, A., Vazquez, J. P. H., Lee, A. F., Tikhov, M. S. and Lambert, R. M.: 1998, Critical influence of the amorphous silica-to-cristobalite phase transition on the performance of $Mn/Na_2WO_4/SiO_2$ catalysts for the oxidative coupling of methane, *Journal of Catalysis* **177**(2), 259.

Patil, C. S., Van Sint Annaland, M. and Kuipers, J. A. M.: 2006, Experimental study of a membrane assisted fluidized bed reactor for $H_2$ production by steam reforming of $CH_4$, *Chemical Engineering Research and Design* **84**(5A), 399–404.

Poling, B. E., Prausnitz, J. M. and O'Connell, J. P.: 2007, *The properties of gases and liquids*, McGraw-Hill, New York.

Ramachandra, A. M., Lu, Y., Ma, Y. H., Moser, W. R. and Dixon, A. G.: 1996, Oxidative coupling of methane in porous vycor membrane reactors, *Journal of Membrane Science* **116**(2), 253–264.

Roos, J. A., Korf, S. J., Veehof, R. H. J., van Ommen, J. G. and Ross, J. R. H.: 1989, Kinetic and mechanistic aspects of the oxidative coupling of methane over a Li/MgO catalyst, *Applied Catalysis* **52**(1), 131.

Saracco, G., Neomagus, H. W. J. P., Versteeg, G. F. and Van Swaaij, W. P. M.: 1999, High-temperature membrane reactors: Potential and problems, *Chemical Engineering Science* **54**(13-14), 1997–2017.

Shi, C., Rosynek, M. P. and Lunsford, J. H.: 1994, Origin of carbon oxides during the oxidative coupling of methane, *Journal of Physical Chemistry* **98**(34), 8371–8376.

Smit, J., van Sint Annaland, M. and Kuipers, J. A. M.: 2004, Development of a novel reactor concept for the partial oxidation of methane to syngas, *Chemical Engineering Research and Design* **82**(2), 245–251.

Smit, J., van Sint Annaland, M. and Kuipers, J. A. M.: 2005a, Feasibility study of a reverse flow catalytic membrane reactor with porous membranes for the production of syngas, *Chemical Engineering Science* **60**(24), 6971–6982.

Smit, J., van Sint Annaland, M. and Kuipers, J. A. M.: 2005b, Grid adaptation with WENO schemes for non-uniform grids to solve convection-dominated partial differential equations, *Chemical Engineering Science* **60**(10), 2609–2619.

Sofranko, J. A., Leonard, J. J. and Jones, C. A.: 1987, The oxidative conversion of methane to higher hydrocarbons, *Journal of Catalysis* **103**(2), 302.

Sofranko, J. A., Leonard, J. J., Jones, C. A., Gaffney, A. M. and Withers, H. P.: 1988, Catalytic oxidative coupling of methane over sodium-promoted $Mn/SiO_2$ and Mn/MgO, *Catalysis Today* **3**(2-3), 127.

Stansch, Z., Mleczko, L. and Baerns, M.: 1997, Comprehensive kinetics of oxidative coupling of methane over the $La_2O_3/CaO$ catalyst, *Industrial & Engineering Chemistry Research* **36**(7), 2568–2579.

Stewart, W. E. and Prober, R.: 1964, Matrix calculation of multicomponent mass transfer in isothermal systems, *Industrial & Engineering Chemistry Fundamentals* **3**(3), 224–235.

Stitt, E. H.: 2004, Multifunctional reactors? 'up to a point lord copper', *Chemical Engineering Research and Design* **82**(A2), 129–139.

Sundaram, K. M., Shreehan, M. M. and Olszewski, E. F.: 2001, *Kirk-Othmer Encyclopedia of Chemical Technology*, John Wiley & Sons, Inc., chapter Ethylene.

Takanabe, K. and Iglesia, E.: 2008, Rate and selectivity enhancements mediated by OH radicals in the oxidative coupling of methane catalyzed by $Mn/Na_2WO_4/SiO_2$, *Angewandte Chemie International Edition* **47**, 7689–7693.

Takht Ravanchi, M., Kaghazchi, T. and Kargari, A.: 2009, Application of membrane separation processes in petrochemical industry: a review, *Desalination* **235**(1-3), 199–244.

Taylor, R. and Krishna, R.: 1993, *Multicomponent Mass Transfer*, John Wiley & Sons, Inc., New York.

Toor, H. L.: 1964a, Solution of the linearized equations of multicomponent mass transfer: I, *AIChE Journal* **10**(4), 448–455.

Toor, H. L.: 1964b, Solution of the linearized equations of multicomponent mass transfer: II, *AIChE Journal* **10**(4), 460–465.

Trimm, D. L. and Lam, C. W.: 1980, The combustion of methane on platinum-alumina fibre catalysts - i, *Chemical Engineering Science* **35**, 1405–1413.

van Sint Annaland, M., Kürten, U. and Kuipers, J. A. M.: 2007a, Effect of mass-transport limitations on the performance of a packed bed membrane reactor for partial oxidations. Intraparticle mass transport, *Industrial and Engineering Chemistry Research* **46**(23), 7513–7523.

van Sint Annaland, M., Kürten, U. and Kuipers, J. A. M.: 2007b, Effect of mass-transport limitations on the performance of a packed bed membrane reactor for partial oxidations. Transport from the membrane to the packed bed, *Industrial and Engineering Chemistry Research* **46**(23), 7524–7534.

van Sint Annaland, M., Scholts, H. A. R., Kuipers, J. A. M. and van Swaaij, W. P. M.: 2002, A novel reverse flow reactor coupling endothermic and exothermic reactions. Part I: comparison of reactor configurations for irreversible endothermic reactions, *Chemical Engineering Science* **57**, 833–854.

Veldsink, J. W., Versteeg, G. F., van Swaaij, W. P. M. and van Damme, R. M. J.: 1995, The use of the dusty-gas model for the description of mass transport with chemical reaction in porous media, *The Chemical Engineering Journal and the Biochemical Engineering Journal* **57**(2), 115.

Veser, G.: 2001, Experimental and theoretical investigation of $H_2$ oxidation in a high-temperature catalytic microreactor, *Chemical Engineering Science* **56**(4), 1265–1273.

Vortmeyer, D. and Berninger, R.: 1982, Comments on the paper 'theoretical prediction of effective heat transfer parameters in packed beds' by Anthony Dixon and D.L. Cresswell [AIChE J., 25, 663, (1979)], *AIChE Journal* **28**(3), 508–510.

Wang, D. J., Rosynek, M. P. and Lunsford, J. H.: 1995, Oxidative coupling of methane over oxide-supported sodium-manganese catalysts, *Journal of Catalysis* **155**(2), 390.

Wang, H., Cong, Y. and Yang, W.: 2005, Oxidative coupling of methane in $Ba_{0.5}Sr_{0.5}Co_{0.8}Fe_{0.2}O_{3-\delta}$ tubular membrane reactors, *Catalysis Today* **104**(2-4), 160–167.

Wang, J., Chou, L., Zhang, B., Song, H., Zhao, J., Yang, J. and Li, S.: 2006, Comparative study on oxidation of methane to ethane and ethylene over $Na_2WO_4Mn/SiO_2$ catalysts prepared by different methods, *Journal of Molecular Catalysis A: Chemical* **245**, 272–277.

Weisz, P. B. and Hicks, J. S.: 1962, The behaviour of porous catalyst particles in view of internal mass and heat diffusion effects, *Chemical Engineering Science* **17**(4), 265.

Wesseling, P.: 2001, *Principles of computational fluid dynamics*, Springer-Verlag, New York.

Westerterp, K. R., van Swaaij, W. P. M. and Beenackers, A. A. C. M.: 1963, *Elements of chemical reactor design and operation*, 1st edn, John Wiley & Sons Ltd.

Xu, J. and Froment, G. F.: 1989, Methane steam reforming, methanation and water-gas shift: I. intrinsic kinetics, *AIChE Journal* **35**(1), 88–96.

Yang, W., Wang, H., Zhu, X. and Lin, L.: 2005, Development and application of oxygen permeable membrane in selective oxidation of light alkanes, *Topics in Catalysis* **35**(1-2), 155–167.

Zehner, P. and Schlünder, E. U.: 1970, Thermal conductivity of granular materials at moderate temperatures, *Chemie Ingenieur Technik* **42**, 933–941.

Zeng, Y., Lin, Y. S. and Swartz, S. L.: 1998, Perovskite-type ceramic membrane: Synthesis, oxygen permeation and membrane reactor performance for oxidative coupling of methane, *Journal of Membrane Science* **150**(1), 87–98.

Zhang, H., Wu, J., Xu, B. and Hu, C.: 2006, Simultaneous production of syngas and ethylene from methane by combining its catalytic oxidative coupling over $Mn/Na_2WO_4/SiO_2$ with gas phase partial oxidation, *Catalysis Letters* **106**(3 - 4), 161.

Zimmermann, H. and Walz, R.: 2006, *Ullmann's Encyclopedia of Industrial Chemistry.*, John Wiley & Sons, Inc., New York., chapter Ethylene.

# Epilogue and outlook

In this thesis, two integrated autothermal membrane reactor concepts for combining the exothermic oxidative coupling of methane (OCM) with the endothermic steam reforming of methane (SRM) were studied. In the first concept, the integration is achieved on the catalyst particle scale and in the second concept on the reactor scale. By integrating OCM, which has a inherently limited hydrocarbon yield (<35%), with SRM, significant improvements in the overall $CH_4$ conversion can be realized at autothermal operating conditions, circumventing large $CH_4$ recycle streams and simultaneously producing valuable ethylene and synthesis gas. The implementation of OCM and SRM on a single catalyst particle was considered, in which the steam reforming reaction rates were controlled by utilizing intentionally created intra-particle mass transfer limitations. The behavior of this dual function catalyst particle was investigated by means of numerical simulations in a packed bed membrane reactor, in which oxygen was added distributively along the reactor length to improve the OCM selectivity and to create a relatively uniform temperature profile in the reactor. The integration of OCM and SRM on the reactor scale can be realized by performing the OCM and SRM reactions in separate sections of a heat exchange reactor, which was studied by numerical simulations and experiments. It is concluded that the OCM process can be effectively cooled and that the generated reaction heat is efficiently used to produce synthesis gas. The thermal coupling can be achieved on the reactor scale, but is most optimally achieved on the catalyst particle scale.

To the author's knowledge, the use of a dual function catalyst particle to combine OCM and SRM in a packed bed membrane reactor is a new concept. Although the feasibility of the dual function catalyst particle has been demonstrated for various operating conditions by means of numerical simulations, the development of a real dual function OCM/SRM catalyst particle could not be realized within this joint research project and the preparation of the dual function catalyst is still a major scientific and technological challenge. In this work, spherical dual function catalyst particles have been considered for OCM and SRM, although it is expected that the control of reaction rates via diffusional limitations and the separation of catalytic activities can also be interesting for different combinations of exothermic and endothermic processes, and in other catalyst geometries, for example, by controlled deposition of thin layers of OCM and SRM catalyst in a structured monolith reactor. Application of this reactor type avoids the requirement of controlled preparation of bulk quantities of small dual function catalyst particles, but demands other concepts for distributing the oxygen along the reactor length. For the preparation of dual function catalyst particles,

specific knowledge on the coating and preparation of layered catalysts is available in the literature, however, this technology needs to be developed and applied to the high temperature OCM/SRM dual function process, which requires further study of the long-term chemical, mechanical and thermal performance of the catalyst. The potential of this solution is high, since it enables the use of membrane reactors with higher throughput, yield and reactant conversion without the requirement for expensive heat exchange equipment and in particular if dense $O_2$ perm-selective membranes can be integrated.

For industrial application of oxidative coupling, an important problem is the relatively low yield of hydrocarbons. It cannot be expected that new catalysts for OCM are to be discovered in the coming years, realizing that the newest catalysts date back from the 1990's. With packed bed membrane reactors, it is shown that the overall performance can be improved and that significant advantages over conventional reactors can be achieved at the laboratory scale, such as improvement of the $C_2$ selectivity and temperature control via distributive production of the reaction heat along the reactor length. Despite the fact that multi-tubular packed bed reactors are well-known and widely applied in the process industry, the application of membrane reactors on industrial scale is still limited (especially for high temperature applications such as OCM), because the use of porous or dense membranes for distributive oxygen feeding adds additional complexity to these reactors which are already quite capital intensive in terms of construction and maintenance. It is expected that industrial application of high temperature membrane reactors requires further development of long-term mechanically stable and robust membranes and better and cheaper sealing techniques. In addition, less labor-intensive, large-scale production methods need to be developed in order to meet the demand for large numbers of affordable membrane tubes with the appropriate flux and sufficiently high trans-membrane pressure drop. Despite the many difficulties which still have to be overcome, it can be concluded that distributed feeding of oxygen is in principle the best technology available to cope with selective oxidation processes in packed bed reactors.

As a consequence of the process integration, a crucial factor for the feasibility of both reactor concepts remains the availability of (cheap) technology for separation of the hydrocarbons and synthesis gas from the product stream. Currently, the energy intensive cryogenic separation of ethylene and ethane from synthesis gas and/or methane is the technology of choice, although selective reactive separation of ethylene to produce ethylbenzene has been proposed (Graf, 2008). Finally, for both the developed integrated OCM/SRM processes, a major challenge still lies in the larger scale testing of the reactor concepts and further improvement of OCM, because on the

larger scale concentration and temperature profiles may limit the overall performance, as was demonstrated experimentally in this work. Nevertheless, it can be concluded the combined OCM/SRM process is a promising additional ethylene production alternative, but developments in catalyst and membrane preparation are required to optimally benefit from the advantages on the reactor scale.

# Dankwoord

Het sluitstuk in een bouwwerk heeft in het algemeen als taak om de constructie bij elkaar te houden en ervoor te zorgen dat het geheel niet instort. Het zorgt voor samenhang. Voor een proefschrift als dit is niet het sluitstuk, maar de inhoud veel belangrijker en zorgt het oorspronkelijke idee voor de rode draad in het verhaal. Het dankwoord mag dan niet de sluitsteen zijn, het voelt in ieder geval wel als zodanig. Met het symbolisch plaatsen van de sluitsteen in dit Magnum Opus is het proefschrift na veel zweten dan bijna klaar. Laat ik de laatste pagina's aanwenden om de mensen te bedanken die in meer of mindere mate hebben bijgedragen aan het tot stand komen van dit proefschrift.

Als eerste wil ik mijn promotor Hans Kuipers en assistent-promotor Martin van Sint Annaland bedanken voor het mogelijk maken van dit project en voor de kans en vrijheid die zij mij hebben geboden om dit onderzoek uit te voeren. Hans, ondanks je drukke dubbele baan als hoogleraar van de vakgroep en wetenschappelijk directeur van het IMPACT instituut was er altijd tijd voor de maandelijkse besprekingen, die vaak nuttige en bruikbare inzichten hebben opgeleverd om het project naar een hoger niveau te tillen. Het enthousiasme en je kritische, open houding waarmee nieuwe ideeën werden onthaald hebben altijd gezorgd voor een goede samenwerking. Tevens was het altijd erg prettig om op korte termijn verbeteringen en commentaar op artikelen en hoofdstukken te ontvangen. Martin, je tomeloze drive naar wetenschappelijke perfectie hebben een grote inhoudelijke bijdrage geleverd aan dit proefschrift. Ik heb ontzettend veel geleerd van je kennis van numerieke modellen, waardoor we in staat zijn geweest de deeltjes- en reactormodellen verder te ontwikkelen en te verfijnen. De randvoorwaarden en het oplossen van de vergelijkingen in het deeltjesmodel hebben vele uren gekost en me grijze haren bezorgd, maar ik ben je zeer erkentelijk voor het feit dat de deur altijd openstond om hierover te discussiëren. Verder was het altijd zeer prettig om met je te kunnen klankborden over verkregen resultaten, problemen met opstellingen en rapportage.

Het onderzoek beschreven in dit proefschrift was onderdeel van een gedeeld project, waarbij kennis van katalytische materialen en processen werd uitgewisseld voor toepassing in reactorconcepten en vice versa. Leon Lefferts wil ik daarom van harte bedanken voor zijn aandeel in dit werk en voor het participeren in de promotie-commissie. Een woord van dank gaat eveneens naar Barbara Mojet, onder meer voor de hulp en de interpretatie van het gedrag van de OCM katalysator. Een gezamenlijk project wordt tot een succes gemaakt door de mensen die er aan werken. Patrick, onze samenwerking was altijd zeer goed en ik wil je dan ook bedanken voor

de vele discussies die we hebben gehad over de resultaten en de voortgang van de verschillende deelonderzoeken. De presentaties die we samen hebben gegeven vond ik altijd erg prettig, ik denk dat hierdoor het totale project zeer sterk uit de verf is gekomen op conferenties en voortgangsbesprekingen. Daarnaast was het altijd zeer gezellig op sociaal vlak, ik zal het conferentiediner in Delft nooit vergeten.

Het experimentele werk zou zeker minder kans van slagen hebben gehad, zonder de aanwezigheid van een goede werkplaats met zeer kundige technici. Gerrit Schorfhaar, Erik Analbers, Johan Agterhorst en Wim Leppink zijn onmisbaar geweest bij de realisatie van verschillende opstellingen en het oplossen van de bijbehorende problemen. Tevens was de kennis van Robert Meijer op het gebied van elektronika, sensortechniek en elektronische schakelingen zeer welkom. Onze vele discussies over programmeren in Labview en de vele mogelijkheden van dit programma zal ik niet vergeten (veel succes met het geautomatiseerde gasdetectie-systeem). Nicole Haitjema zorgde dat alles administratief in orde was, regelde afspraken, declaraties, hotels en nog veel meer. Mieke Luijten wil ik bedanken voor de metingen aan de aangeschafte membranen. Henk Kruidhof voor de discussies en adviezen over de keuze van het juiste membraan voor deze toepassing. Jan van Veen, Dick Witteveen en Joop Snoeyenbos ben ik zeer erkentelijk voor het vervaardigen van de kwartsglas-reactoren en het prepareren van de alumina buizen en membranen, zodat de voortgang van de experimenten niet in gevaar kwam.

Met name op het experimentele vlak hebben enkele studenten hun tanden stukgebeten op de oxidatieve koppeling van methaan. Het klinkt allemaal heel mooi, totdat je gaat proberen etheen te maken. Mahal Patel kwam hier als rookie op het gebied van experimenteel werk en vertrok als veteraan. Hij was de eerste student die zich bezig mocht gaan houden met de membraanreactor. De vele data die hij heeft verzameld over het prepareren van membranen en het (soms onvoorspelbare) gedrag van de reactor, zijn van groot nut geweest. Zijn opvolger Wessel Spek had als taak om het gedrag van de kleine membraanreactor in kaart te brengen. Hij heeft een grote hoeveelheid gegevens achtergelaten die zeer bruikbaar zijn geweest bij het tot stand komen van dit werk. Martin Tuinier was verantwoordelijk voor de uitvoering van de kinetiekmetingen en het bepalen van reactiensnelheidsvergelijkingen van de primaire reacties van oxidatieve koppeling. Het werken met een opstelling op zeer hoge temperatuur is niet eenvoudig gebleken, maar het resultaat is daar. Maike Baltussen heeft vervolgexperimenten uitgevoerd waarbij de verbranding van etheen en ethaan is onderzocht. Op het gebied van numerieke simulaties is de hulp van Tom Kolkman erg belangrijk geweest voor de ontwikkeling en haalbaarheidsstudie van het gecombineerde reactorconcept. Tom wist het model zodanig te optimaliseren dat de

simulatietijd is verkort van “zo, nu eerst een kop koffie” naar “klaar terwijl u wacht”. Heren en dame, ik ben zeer dankbaar voor jullie hulp en bijdrage aan dit werk.

Gedurende de ruim vier jaar die ik heb gewerkt bij de vakgroep FCRE, is er niet een dag geweest dat ik met tegenzin naar het werk ging, eerst in Langezijds en later in de Meander. De aanwezigheid van de soms wat lawaaiige kantoortuin, die uniek was op de UT (het concept wordt nu overgenomen door andere groepen), zorgt voor een zeer plezierige werksfeer en heeft ervoor gezorgd dat problemen sneller opgelost konden worden. Daarnaast was het altijd handig om collega’s te hebben (Statler en Waldorf) die alles in de gaten houden, zodat je van alles op de hoogte wordt gehouden zonder daarvoor al te veel moeite te hoeven doen. De vele borrels, de AIO-uitjes zal ik tevens niet vergeten. Een woord van dank is gericht aan Sander Noorman, de vele keren dat we weer discussies moesten voeren over het deeltjesmodellen, opstellingen of practicum FTV liggen inmiddels achter ons. Lange tijd waren we de enige chemical brothers in de groep, en onze samenwerking heb ik als zeer prettig en constructief ervaren. Tevens wil ik mijn paranimfen, Martin Tuinier en Tom Kolkman, alvast bedanken voor het assistenteren tijdens de verdediging en aansluitend de komende festiviteiten.

Als bijna laatste wil ik ook mijn ouders bedanken. Jullie hebben het altijd mogelijk gemaakt om te kunnen studeren, stonden altijd voor me klaar en hebben me altijd gesteund, wat ervoor heeft gezorgd dat ik dit proefschrift en nu dit dankwoord kan schrijven. Femke en Jim, schoonouders en familie wil ik eveneens bedanken voor hun steun en interesse. Tot slot wil ik mijn lief Maureen bedanken voor haar geduld tijdens het schrijven van dit werk. Je bent mijn steun en toeverlaat. Het heeft een vakantie en vele weekenden gekost, maar dan heb je ook wat.

Hartelijk dank!

Tymen

Foto: Gijs van Ouwerkerk © UT Nieuws

Tymen Tiemersma werd op 14 januari 1979 geboren in Kollumerzwaag (Friesland). Daar groeide hij ook op en volgde hij basisonderwijs op de toenmalige Ds. Griffijnschool. In juni 1997 nam hij het VWO diploma in ontvangst op het Lauwers College te Buitenpost, waarna hij in september 1997 begon aan de opleiding Chemische Technologie aan de Hanzehogeschool in Groningen. Gedurende deze opleiding werden stages gevolgd bij Akzo Nobel MPP Systems, Forbo Flooring en Akzo Nobel Chemicals Research. Na voltooiing van de HTS, volgde hij de opleiding Chemische Technologie aan de Universiteit Twente en werkte hij als deeltijd onderzoeker bij Akzo Nobel Chemicals in Arnhem. In augustus 2004 studeerde hij af bij de vakgroep Fundamental Aspects of Chemical Reaction Engineering op een onderzoek getiteld: “Two-dimensional packed bed membrane reactor model for autothermal reforming of methane”.

Na de ingenieursopleiding trad hij in dienst van dezelfde vakgroep om als promovendus de combinatie van oxidatieve koppeling en het reformen van methaan te onderzoeken. De resultaten van dit onderzoek staan beschreven in dit proefschrift. Sinds begin 2009 werkt Tymen bij het Teijin Aramid Research Institute als Senior Researcher op de afdeling Monomers & Polymers.

ISBN 978-90-365-2985-3